Self healing in Fe-based systems
From model alloys to designed steels

Fu, Y.

Important note
To cite this publication, please use the final published version (if applicable).
Please check the document version above.

Self Healing in Fe-based Systems:
from Model Alloys to Designed Steels

SELF HEALING IN FE-BASED SYSTEMS:
FROM MODEL ALLOYS TO DESIGNED STEELS

Proefschrift

ter verkrijging van de graad van doctor
aan de Technische Universiteit Delft,
op gezag van de Rector Magnificus Prof. dr. ir. T. H. J. J. van der Hagen,
voorzitter van het College voor Promoties,
in het openbaar te verdedigen op
donderdag 15 september 2022 om 15.00 uur

door

Yifan FU

Master of Engineering in Materials Science,
Dalian University of Technology, Dalian, China
Master of Science in Advanced Materials,
University of Nottingham, Nottingham, UK

geboren te Benxi, China

Dit proefschrift is goedgekeurd door de promotoren.
 Prof. dr. dr.h.c. ir. S. van der Zwaag, Prof. dr. E.H. Brück en Dr. ir. N. H. van Dijk

Samenstelling promotiecommissie:

Rector magnificus,	voorzitter
Prof. dr. dr.h.c. ir. S. van der Zwaag	Technische Universiteit Delft, promotor
Prof. dr. E. H. Brück	Technische Universiteit Delft, promotor
Dr. ir. N. H. van Dijk	Technische Universiteit Delft, promotor

Onafhankelijke leden:

Prof. dr. M.J. Santofimia Navarro	Technische Universiteit Delft
Prof.dr.ir. H.E.J.G. Schlangen	Technische Universiteit Delft
Prof. dr. A. Simar	Université catholique de Louvain, Belgium
Prof. dr. Y. T. Pei	Rijksuniversiteit Groningen
Prof. dr. ir. R. Benedictus	Technische Universiteit Delft, reservelid

TUDelft

Delft University of Technology

To my family

CONTENTS

1

INTRODUCTION

'As flame of fire as we gather; as skyful of starts as we scatter.'

In memory of Lao Song (Minqiu Song)

1.1 SELF-HEALING MATERIALS

Self-healing materials, defined by the name, present a new class of smart materials which can fully or partially repair themselves when damaged. In contrast to the traditional 'damage prevention' paradigm (the materials are designed such that the occurrence of damage is delayed as much as possible), the development of self-healing materials is guided by the 'damage management' principle [1, 2]. That is, the formation of damage is tolerable, as long as the damage can be fully or partially erased by the accumulation of healing agents and/or removal of the damage. Inspired by nature, the self-healing behaviour is generally achieved by the local migration of the healing agents [3], i.e. a fraction of the material is mobile, and once the damage takes place and the repair is required, the mobile phase can be triggered (either externally triggered by certain external stimulations or internally triggered by the damage itself) resulting in transfer towards the damage sites, where the healing takes place subsequently and the mobile phase becomes immobilised again. In the field of self-healing materials, the dominating sub-field has been the study of self-healing polymers [4, 5], where the self-healing capacity is provided by the discharge of encapsulated healing agents and/or the

incorporation of dynamic bonds. Given the relative effective chemical reactions, the large volume of mobile molecules and the fast diffusion, self healing in polymers is feasible even at room temperature. Another widely-studied self-healing system is concrete [6], where the healing agent is the mineral generated by the bacteria, which are previously embedded in the concrete and can be activated by the water through the load-induced cracks. Other examples include self-healing composites [7, 8], asphalts [9], ceramics [10], etc. Regardless of the varying details of healing mechanism, the existence of local mobility is required.

1.2 Self-healing metals

The realisation of self healing in metals is, however, more difficult than in polymers, mainly because of: (1) the relatively low mobility of metallic atoms resulting from the strong atomic bonding and (2) the relatively small size of the metallic atoms acting as the healing agents. Due to these intrinsic limitations, the application of self-healing metals is usually restricted to either the systems that require assisted healing or systems that operating at elevated temperatures with small initiating damage [11, 12]. For the former category, external triggers like electric field [13] and local melting [14] are commonly used to provide a higher mobility, so that healing can be achieved for cracks in the range of mm's. For the latter category, the healing agents are generally provided by the autonomous nucleation of nano-sized or micro-sized precipitates that exclusively form at the damage sites at high temperatures [15, 16]. The precipitates are capable of healing the microscopic damage, and since the accumulation of microscopic damage can lead to macroscopic damage and subsequently to catastrophic failure, the healing of the damage at its initial stage can effectively prolong the lifetime of the metal.

One potential application lies in the field of creep-resistant alloys. This is for two reasons. Firstly, creep damage takes place at elevated temperatures, which can provide mobility for the metallic atoms. In addition, creep-induced damage is initially small (in the range of tens of nm) and therefore relatively easy to be filled by the also small healing atoms. Since the accumulation of small scale damage can ultimately result in the final failure, the self healing of early stage damage is of great importance.

1.3 SELF HEALING OF CREEP-INDUCED DAMAGE

When exposed to a combination of a high temperature and constant stress levels (even below the quasi-static yield stress), metals experience time-dependent plastic deformation, known as creep. Creep damage often begins with the nucleation of grain-boundary cavities, which further grow and coalesce into larger cracks, and ultimately leads to failure [17]. To improve the creep resistance, the traditional mechanism is to tune the microstructure and composition of the metals such that the initiation of the cavities is postponed as long as possible [18-20]. However, since nucleation of the cavities has been regarded as being unavoidable, the concept of self healing [3, 11, 12] has been proposed as an alternative strategy. In the self-healing creep-resistant alloys, the healing agents are provided by supersaturated solute atoms pre-dissolved in matrix that show a tendency to precipitation. The healing is autonomous, i.e. the trigger for the healing is the damage itself, instead of some external assist. The high temperature, where creep takes place, provides a relatively high mobility for the transport of the healing agents. To summarise, during creep, the occurrence of cavities triggers the migration of solute atoms (previously immobilised in the matrix) towards the damage sites, where the healing subsequently takes place by precipitation. Thereby the continuous growth and the more catastrophic coalesce of the cavities can be postponed, if not prevented.

In recent years, the concept of self healing has been verified as being effective in prolonging creep lifetimes in multiple metallic systems. For austenitic stainless steels (i.e. steels having an fcc lattice structure at the operating temperature), Laha and co-workers [15, 21] reported that the combined addition of boron and nitrogen is effective in reducing the cavity growth rate, as well as increasing the creep rupture strength. Lumley and co-workers [22, 23] demonstrated that underaged Al alloys showed a lower strain rate, and thus a longer lifetime, compared to a fully-aged counterparts. The improvement in the creep performance after an under-ageing heat treatment is achieved by the dynamic precipitation of free solute atoms and the subsequent retardation of dislocation motion during the creep test. In a systematic study on ferritic steels (i.e steels or alloys with a bcc lattice structure at the operating temperature), a series experiments on binary Fe-X alloys, including Fe-Cu [24-26], Fe-Au [16, 27-30], Fe-Mo [31] and Fe-W [32],

as well as simulation studies [33-35] have been conducted to reveal the healing mechanism during creep. For these model alloys, the grain-boundary cavities (that serve as triggers) are expected to be autonomously filled gradually by the formation of solid precipitates (that serve as healing agents). The composition of these alloys are selected such that at the operating temperature 1 at.% of supersaturated solute atoms are immobilised in the matrix. Several criteria are fundamental in order to achieve autonomous site-selective healing: (i) an extra amount of solute atoms (typically 1 at. % supersaturation at the creep temperature) need to be present into the matrix, providing the driving force for the formation of precipitates; (ii) the nucleation energy barrier at free creep cavity surfaces need to be sufficiently lower than the energy barrier for nucleation in the matrix, assuring the site selectively; (iii) the solute atoms should have a higher diffusivity compared to the host atoms, so that the cavity can shrink during filling by precipitation as the vacancies diffuse outward due to the Kirkendall effect; and (iv) the solute atoms should not react with other microstructural components and thereby not be consumed before reaching the damage sites. Guided by the findings from the model alloys, a series of ferritic chrome steels with a combination of decent high-temperature mechanical properties and self-healing potential have been designed [36]. In these steels other alloying elements than the healing element, W, such as C, Cr, Ni are added to achieve decent mechanical properties, but as in the model alloys, the healing is due to only one solute element (i.e. the healing agent).

So far, the self healing of creep damage in ferritic Fe-based alloys by precipitation has only been demonstrated for systems with one healing element (for both the model alloys and for the designed alloys). It is of great interest to introduce a ternary Fe-X-Y system with two healing elements, which can (1) provide insight in the interplay between two separate healing agents in the same system and (2) be used to explore the potential of effective healing on different time scales. This thesis starts with studying the precipitation behavior at the surface of creep-induced grain boundary cavities in a Fe-Au-W ternary model alloy. Both Au and W serve as healing agents, and at the operating temperature, both elements are in a supersaturated state with approximately 1 at.% of supersaturation. Since the diffusivity of Au is approximately two orders of magnitude higher than that of W, it can be expected that the two healing agents operate on different time scales, which can further extend the functioning time of self healing. Following the first step

from the binary Fe-X and the ternary Fe-X-Y self-healing model alloys towards multi-component industrial steels, this thesis also test evaluates the creep and self-healing behaviourbehavior in custom the designed ferritic 12Cr steels alloys [36] and gives suggestions for follow-up experiments and the design of the next generation of self-healing creep-resistant steels.

1.4 SCOPE OF THIS THESIS

In **Chapter 2**, autonomous healing of creep-induced grain boundary cavities by Au-rich and W-rich precipitates was studied in a Fe-3Au-4W (wt.%) alloy at a fixed temperature of 550 °C with different applied stresses. The ternary alloy, with two supersaturated healing solutes with a concentration comparable to previously studied Fe-3Au and Fe-4W alloys, serves as a model system to study the interplay between two separate healing agents. The creep properties are evaluated and compared with those of the previously studied Fe-Au and Fe-W binary systems. The microstructures of the creep-failed samples are studied by electron microscopy to investigate the cavity filling behavior and the mass transfer of supersaturated solute to the defect sites. A model is proposed to describe the competitive healing behavior of the Au-rich and W-rich precipitates.

One of the challenges in studying the healing of the creep-induced defects lies in the observation of both the creep cavities and the precipitation inside these cavities at different stages of the creep life. In **Chapter 3**, the study of precipitation of supersaturated solutes in *bcc* iron at free surfaces for ternary Fe-3Au-4W and related binary Fe-3Au and Fe-4W alloys (all in wt.%) is proposed as a complimentary method to understand and predict the precipitation behaviour and the mass transfer of supersaturated solutes. The time evolution of the surface precipitation is compared among the three alloys to investigate the interplay between the Au and W solutes in the ternary system. The kinetics of the precipitation on the external free surface for the ternary Fe-Au-W alloy is compared to the previously studied precipitation on the internal surfaces of the grain-boundary cavities during creep loading of the same alloy.

To better understand the microstructure development at different stages of creep, in **Chapter 4**, synchrotron X-ray holotomography is applied as a powerful tool to visualise the evolution of both the grain-boundary cavities

and the precipitates within the cavities. The damage and healing behaviour in a Fe-3Au-4W (wt.%) ternary system is studied by performing creep experiments with a constant stress of 145 MPa at 550 °C. The creep experiments are stopped after different times to investigate the microstructure development at different stages of creep. With two voxel sizes of 100 and 30 nm, Au-rich and W-rich precipitates can be segmented. The segmentation results are compared with the SEM results from a previous research on the same ternary system. The growth of cavities and the mass transfer of solute towards the damage sites are also compared with the previously studied two binary counterparts.

Self healing of creep-induced cavities is achieved by the removal of vacancies from the cavities due to the inverse Kirkendall effect. In **Chapter 5,** a set of numerical and analytical models is presented to predict the growth and contraction of grain-boundary creep cavities in binary self-healing alloys. The inward vacancy flux is driven by the stress distribution along the grain boundary, while the time-dependent outward vacancy flux results from the solute segregation on the cavity surface. Both the stress distribution and the solute flux are calculated with a multi-physics finite element package COMSOL® [37]. The time evolution of the filling ratio, and the resulting critical stress, are calculated based on the accumulated inward and outward vacancy fluxes. The influences of the grain-boundary to bulk diffusivity ratio, the level of solute supersaturation, and the spacing between neighbouring cavities on the healing efficiency are addressed explicitly and solutions are proposed as a function of the imposed stress.

As introduced in section 1.3, a series of ferritic 12Cr steels with a combination of decent high-temperature mechanical properties and self-healing potential have been designed. **In Chapter 6,** the creep behaviour of two novel experimental alloys with compositions based on the design rules is investigated by performing a series of creep experiments at high temperature (550 °C) with different applied stresses. By carefully examining the microstructures of the creep-failed samples in both the creep-deformed regions and the stress-free regions in the samples, the validity of the self-healing concept in the steels is evaluated. The creep lifetimes of the designed steels are compared with the existing commercial steels under similar creep

conditions. Based on the observations and discussion, suggestions for the design of the next generation of self-healing creep-resistant steels are given.

The main findings in this thesis are compiled in a summary.

REFERENCES

[1] S. van der Zwaag, Self-Healing Materials: An Alternative Approach to 20 Centuries of Materials Science, Springer Series in Materials Science, Dordrecht, 2007.

[2] S. van der Zwaag, N.H. van Dijk, H.M. Jonkers, S.D. Mookhoek, W.G. Sloof, Self-healing behaviour in man-made engineering materials: bioinspired but taking into account their intrinsic character, Philos. Trans. A Math Phys. Eng. Sci. 367(1894) (2009) 1689-704.

[3] M.D. Hager, P. Greil, C. Leyens, S. van der Zwaag, U.S. Schubert, Self-healing materials, Adv. Mater. 22(47) (2010) 5424-30.

[4] S.R. White, N.R. Sottos, P.H. Geubelle, J.S. Moore, M.R. Kessler, S.R. Sriram, E.N. Brown, S. Viswanathan, Autonomic healing of polymer composites, Nature 409(6822) (2001) 794-7.

[5] S. Wang, M.W. Urban, Self-healing polymers, Nature Rev. Mater. 5(8) (2020) 562-583.

[6] H.M. Jonkers, A. Thijssen, G. Muyzer, O. Copuroglu, E. Schlangen, Application of bacteria as self-healing agent for the development of sustainable concrete, Ecol. Eng. 36(2) (2010) 230-235.

[7] J.B. Ferguson, B.F. Schultz, P.K. Rohatgi, Self-Healing Metals and Metal Matrix Composites, Jom 66(6) (2014) 866-871.

[8] Y. Wang, D.T. Pham, C. Ji, E. Harkin-Jones, Self-healing composites: A review, Cogent Eng. 2(1) (2015).

[9] S. Xu, A. Garcia, J.F. Su, Q.T. Liu, A. Tabakovic, E. Schlangen, Self-Healing Asphalt Review: From Idea to Practice, Adv. Mater. Interfaces 5(17) (2018).

[10] A.-S. Farle, C. Kwakernaak, S. van der Zwaag, W.G. Sloof, A conceptual study into the potential of Mn+1AXn-phase ceramics for self-healing of crack damage, J. Eur. Ceram. Soc. 35(1) (2015) 37-45.

[11] N. van Dijk, S. van der Zwaag, Self-Healing Phenomena in Metals, Adv. Mater. Interfaces 5(17) (2018) 1800226.

1

[12] B. Grabowski, C.C. Tasan, Self-Healing Metals, Self-healing Materials 2016, pp. 387-407.

[13] X.G. Zheng, Y.N. Shi, K. Lu, Electro-healing cracks in nickel, Mater. Sci. Eng. A 561 (2013) 52-59.

[14] M.V. Manuel, G.B. Olson, Biomimetic Self-Healing Metals, 2007.

[15] K. Laha, J. Kyono, S. Kishimoto, N. Shinya, Beneficial effect of B segregation on creep cavitation in a type 347 austenitic stainless steel, Scr. Mater. 52(7) (2005) 675-678.

[16] S. Zhang, C. Kwakernaak, W. Sloof, E. Brück, S. van der Zwaag, N. van Dijk, Self Healing of Creep Damage by Gold Precipitation in Iron Alloys, Adv. Eng. Mater. 17(5) (2015) 598-603.

[17] J.N. Greenwood, D.R. Miller, J.W. Suiter, Intergranular Cavitation in Stressed Metals, Acta Metall. Mater. 2(2) (1954) 250-258.

[18] F.R.N. Nabarro, H.L. de Villiers, The Physics of Creep: Creep and Creep-resistant Alloys, 1st ed., CRC Press 1995.

[19] M. Taneike, F. Abe, K. Sawada, Creep-strengthening of steel at high temperatures using nano-sized carbonitride dispersions, Nature 424(6946) (2003) 294-296.

[20] F. Abe, Progress in Creep-Resistant Steels for High Efficiency Coal-Fired Power Plants, J. Press. Vessel Technol. 138(4) (2016) 040804.

[21] K. Laha, J. Kyono, T. Sasaki, S. Kishimoto, N. Shinya, Improved creep strength and creep ductility of type 347 austenitic stainless steel through the self-healing effect of boron for creep cavitation, Metall. Mater. Trans. A 36(2) (2005) 399-409.

[22] R.N. Lumley, A.J. Morton, I.J. Polmear, Enhanced creep performance in an Al-Cu-Mg-Ag alloy through underageing, Acta Mater. 50 (2002) 3597-3608.

[23] R.N. Lumley, I.J. Polmear, Advances in self healing of metals, Proceedings of the First International Conference on Self Healing Materials, Noordwijk aan Zee, Netherlands, 2007.

[24] S.M. He, P.N. Brandhoff, H. Schut, S. van der Zwaag, N.H. van Dijk, Positron annihilation study on repeated deformation/precipitation aging in Fe–Cu–B–N alloys, J. Mater. Sci. 48(18) (2013) 6150-6156.

[25] S.M. He, N.H. van Dijk, M. Paladugu, H. Schut, J. Kohlbrecher, F.D. Tichelaar, S. van der Zwaag, In-situ determination of aging precipitation in deformed Fe-Cu and Fe-Cu-B-N alloys by time-resolved small-angle neutron scattering, Phys. Rev. B 82(17) (2010) 174111.

[26] S.M. He, N.H. van Dijk, H. Schut, E.R. Peekstok, S. van der Zwaag, Thermally activated precipitation at deformation-induced defects in Fe-Cu and Fe-Cu-B-N alloys studied by positron annihilation spectroscopy, Phys. Rev. B 81(9) (2010) 094103.

[27] H. Fang, C.D. Versteylen, S. Zhang, Y. Yang, P. Cloetens, D. Ngan-Tillard, E. Brück, S. van der Zwaag, N.H. van Dijk, Autonomous filling of creep cavities in Fe-Au alloys studied by synchrotron X-ray nano-tomography, Acta Mater. 121 (2016) 352-364.

[28] S. Zhang, J. Kohlbrecher, F.D. Tichelaar, G. Langelaan, E. Brück, S. van der Zwaag, N.H. van Dijk, Defect-induced Au precipitation in Fe–Au and Fe–Au–B–N alloys studied by in situ small-angle neutron scattering, Acta Mater. 61(18) (2013) 7009-7019.

[29] S. Zhang, C. Kwakernaak, F.D. Tichelaar, W.G. Sloof, M. Kuzmina, M. Herbig, D. Raabe, E. Brück, S. van der Zwaag, N.H. van Dijk, Autonomous Repair Mechanism of Creep Damage in Fe-Au and Fe-Au-B-N Alloys, Metall. Mater. Trans. A 46(12) (2015) 5656-5670.

[30] S. Zhang, G. Langelaan, J.C. Brouwer, W.G. Sloof, E. Brück, S. van der Zwaag, N.H. van Dijk, Preferential Au precipitation at deformation-induced defects in Fe–Au and Fe–Au–B–N alloys, J. Alloys Compd. 584 (2014) 425-429.

[31] S. Zhang, H. Fang, M.E. Gramsma, C. Kwakernaak, W.G. Sloof, F.D. Tichelaar, M. Kuzmina, M. Herbig, D. Raabe, E. Brück, S. van der Zwaag, N.H. van Dijk, Autonomous Filling of Grain-Boundary Cavities during Creep Loading in Fe-Mo Alloys, Metall. Mater. Trans. A 47(10) (2016) 4831-4844.

[32] H. Fang, N. Szymanski, C.D. Versteylen, P. Cloetens, C. Kwakernaak, W.G. Sloof, F.D. Tichelaar, S. Balachandran, M. Herbig, E. Brück, S. van der Zwaag, N.H. van Dijk, Self healing of creep damage in iron-based alloys by supersaturated tungsten, Acta Mater. 166 (2019) 531-542.

[33] C.D. Versteylen, M.H.F. Sluiter, N.H. van Dijk, Modelling the formation and self-healing of creep damage in iron-based alloys, J Mater. Sci. 53(20) (2018) 14758-14773.

[34] C.D. Versteylen, N.K. Szymański, M.H.F. Sluiter, N.H. van Dijk, Finite element modelling of creep cavity filling by solute diffusion, Philos. Mag. 98(10) (2018) 864-877.

[35] C.D. Versteylen, N.H. van Dijk, M.H.F. Sluiter, First-principles analysis of solute diffusion in dilute bcc Fe-X alloys, Phys. Rev. B 96(9) (2017) 094105.

[36] H. Yu, W. Xu, S. van der Zwaag, A first step towards computational design of W-containing self-healing ferritic creep resistant steels, Sci .Technol. Adv. Mater. 21(1) (2020) 641-652.

1

[37] COMSOL Multiphysics® v. 5.6. www.comsol.com. COMSOL AB, Stockholm, Sweden.

1

好古敏求 (hào gǔ mǐn qiú)

From *Analects/Shu-Er*, 'I am one who is fond of antiquity, and earnest in seeking it there.'

In memory of our beloved teacher in Shenyang No. 2 high school, who had and symbolised the name Min-qiu.

2

COMPETITIVE HEALING OF CREEP-INDUCED DAMAGE IN A TERNARY FE-3AU-4W ALLOY

'Let's put it this way: imagine the case of the breakdown had taken place after your experiment had been running for 800 hours.'

Zhou Zhou

Autonomous healing of creep-induced grain boundary cavities by Au-rich and W-rich precipitates was studied in a Fe-3Au-4W (wt.%) alloy at a fixed temperature of 823 K (550 °C) with different applied stresses. The ternary alloy, with two supersaturated healing solutes, serves as a model system to study the interplay between two separate healing agents. The creep properties are evaluated and compared with those of the previously studied Fe-Au and Fe-W binary systems. The microstructures of the creep-failed samples are studied by electron microscopy to investigate the cavity filling behavior and the mass transfer of supersaturated solute to the defect sites. Compared to the Fe-Au and Fe-W alloys, the new Fe-Au-W alloy has the lowest steady strain rate and the longest lifetime. The site-selective filling of the creep-induced cavities is attributed to two different categories of precipitates: micron-sized Au-rich precipitates and nano-sized W-rich precipitates. The Au-rich precipitates are found capable to fully heal the cavities, while the W-rich precipitates show only a limited degree of healing. The two types of precipitates show a reluctance to coexistence, and the formation of W-rich precipitates is suppressed strongly. A model is proposed to describe the competitive healing behavior of the Au-rich and W-rich precipitates.

2.1 INTRODUCTION

When metals are exposed to an elevated temperature ($T > 0.4$ T_{melt}), the application of a constant stress generally causes a time-dependent increase in strain. This phenomenon is known as creep. During creep, quasi-spherical micron-sized cavities form preferentially at the grain boundaries oriented perpendicular to the load direction. When these cavities are formed, they grow and coalesce into micro- and subsequently macro-cracks, which ultimately leads to failure. Traditionally, efforts have been made to improve the creep resistance by stabilizing the microstructure of the material and postpone the cavity propagation as long as possible [1-3]. As cavity nucleation is assumed to be inevitable, the concept of self-healing [4-6] is proposed as an alternative strategy, in which the occurrence of the cavities triggers dissolved (non-majority) atoms to move towards the defects and fill them. In this self-healing approach the cavity growth can be interrupted before coalescence takes place.

The idea of self-healing has been applied to various (industrial and model) metallic systems to improve the creep-resistance. Lumley and co-workers [7, 8] demonstrated that underaged Al alloys showed a lower strain rate, and thus a longer lifetime, compared to a fully-aged counterparts. The improvement in the creep performance after an under-ageing heat treatment is achieved by the dynamic precipitation of free solute atoms and the subsequent retardation of dislocation motion during the creep test. Laha and co-workers [9, 10] reported that the combined addition of boron and nitrogen into austenitic stainless steels (with an *fcc* lattice structure) is effective in reducing the cavity growth rate, as well as increasing the creep rupture strength. During creep, BN preferentially precipitates on the free cavity surfaces and thereby partially heals the cavities [9-11]. For ferritic steels (with a *bcc* lattice structure), a series of binary systems [6, 12-20], including Fe-Cu, Fe-Au, Fe-Mo and Fe-W, serving as model alloy systems have been investigated systematically to reveal the mechanism and criteria of self healing. The composition of these alloys was selected such that at the operating temperatures the solute is in a supersaturated state by approximately 1 at.%. The supersaturated solute atoms are expected to segregate at the open volume defect sites and fill them progressively, and thereby the coalescing of the cavities can be prevented or delayed. The Fe-Cu system has been shown to be moderately effective in enhancing the creep resistance [12, 21]. Cu-rich

precipitates were found to fill the cavities formed during creep. However, owing to the similar atomic radius of the precipitating Cu atom and the matrix Fe atom, the Cu atoms were found to show only a weak preference to precipitate in the open-volume cavities, in comparison with precipitation along the intact grain boundaries and dislocations within the matrix [12, 13]. This competing precipitation route leads to a gradual depletion of the available healing atoms (in the form of supersaturated solute Cu) when a cavity is formed and needs to be filled. The Au atom has an atomic radius that is 13% larger than that of the Fe atom, which results in an appreciable strain energy for segregation in the Fe-Au solid solution. It is therefore expected to show an obvious site-selective healing effect, i.e. the Au-rich precipitates will form almost exclusively on the free cavity surface and disc-shaped precipitates connected to the dislocations in the matrix will remain nano-sized as they are restricted in their growth [14, 15, 17, 20]. In a related recent study Zhang and co-workers [22] demonstrated that Au atoms dissolved in bcc iron can also actively heal nuclear radiation damage in a mechanism not unlike that for creep damage healing. Considering the costliness and the limited availability of Au, Fe-Mo [16] and Fe-W [18] systems were investigated as an alternative. In Fe-Mo and Fe-W alloys the precipitating phase responsible for healing is not the solute-rich fcc phase, but the intermetallic Laves phase (Fe$_2$Mo and Fe$_2$W, respectively). Both the Fe-Mo and Fe-W system showed a high self-healing potential and site-selective phenomena similar to the Fe-Au system, except for the slower kinetics due to the lower diffusivity of Mo and W in bcc Fe. Based on the observations from the above-mentioned experiments and complementary computation studies [23], the essential requirements for the self-healing capability can be formulated [6]: (i) a supersaturation to provide the driving force so that the healing agent can precipitate at the defect sites; (ii) a relatively large misfit between the matrix phase and the newly-formed precipitate phase such that the precipitation within the matrix can be restrained by the nucleation barrier; (iii) a larger diffusivity of the healing element compared to the diffusivity of iron, so that the vacancy flux would be reversed away from the cavity due to the Kirkendall effect; and (iv) there should be no chemical reaction between the healing element and iron matrix so that the solute diffusion towards the cavity is not interfered.

So far, the self healing of creep damage in ferritic Fe-based alloys by precipitation triggered by cavities [19] resulting in an extended creep lifetime

[17], has only been demonstrated for binary alloys. To transfer the concept of self healing to systems with a higher complexity closer to that of commercial (multi-component) creep-resistant steels, a ternary Fe-X-Y system with two healing elements can provide insight in the interplay between two separate healing agents in the same system.

In the present study, we explore the damage behavior of a ternary Fe-3Au-4W (wt.%) alloy containing two different healing elements: the fast diffusing Au and the slower diffusing W. The composition of the alloy was selected such that at the pre-defined and set testing temperature of 823K (550 °C) both elements are in a supersaturated state with approximately 1 at.% of supersaturation for both elements. The concentration of each solute element in the Fe-3Au-4W ternary system is comparable to our previously studied Fe-3Au and Fe-4W binary systems. Creep tests at a fixed temperature with different constant applied stresses were performed to evaluate the creep properties of the new ternary alloy. The resulting microstructures of the fractured samples are studied in detail by scanning and transmission electron microscopy to evaluate the cavity filling behavior and the mass transfer of supersaturated solute to the defect sites.

2.2 Experimental

High-purity Fe-Au-W ternary alloy sheets were produced on order by Goodfellow®. The as-received material contains 3.826 wt.% (1.222 at.%) W and 3.073 wt.% (0.916 at.%) Au with balance Fe. Dog-bone shaped creep samples with a gauge length of 12.5 mm and a cross-section of 3 mm² were cut by spark erosion, where the gauge length was chosen to be in the rolling direction. The samples were sealed in an evacuated quartz tube filled with 200 mbar ultra-high purity argon to prevent oxidation during annealing. After annealing for 5 hours at 1141 K (868 °C) in order to solutionize the solute atoms Au and W, the samples were quenched into water. The as-quenched samples were examined using electron microscopy to assure that the samples are properly homogenized and that there is no precipitation before the creep tests (Fig. S2.1). The solutionized as-quenched samples showed an average grain size of 103(37) μm. Creep experiments until rupture were performed under vacuum at a constant temperature of 823 K (550 ℃) and with constant stress levels ranging from 170 to 235 MPa. The experiment conditions are

summarized in Table 2.1, while the experimental details of the test facility can be found in [17].

Both the microstructure in the uniform deformation region and the actual fracture surfaces were characterized via scanning electron microscopy (SEM) using a JEOL JSM 6500F instrument equipped with energy-disperse X-ray spectroscopy (EDS), viz.: ThermoFisher UltraDry detector (30 mm^2) with Noran System Seven software for data acquisition and analysis. To reveal the precipitate crystal structure and composition, transmission electron microscopy (TEM) measurements were performed using a FEI C_s-corrected cubed Titan instrument. Elemental analysis was done with an Oxford Instruments EDX detector X-Max^N 100TLE. Lattice images were collected on a Gatan US1000 camera. ADF (Annular Dark Field) images and EDX spectra for elemental mapping were collected in STEM (Scanning Transmission Electron Microscopy) mode.

2

Table 2.1: Summary of the experiment conditions and the creep results for the present Fe-Au-W alloy and the previous Fe-Au [19,20] and Fe-W [18] alloys. All the experiments are performed at a fixed temperature of 823 K (550 °C).

Alloy	Stress (MPa)	Strain rate (h^{-1})	Lifetime (h)
Fe-Au-W **Grain size: 103 μm**	170	$2.162(3) \times 10^{-5}$	224.5
	180	$2.670(1) \times 10^{-5}$	141.6
	190	$2.625(3) \times 10^{-5}$	134.6
	200	$4.723(6) \times 10^{-5}$	97.4
	210	$7.53(2) \times 10^{-5}$	66.6
	235	$7.29(1) \times 10^{-5}$	50.6
	Stress exponent: $n = 4.0(8)$ (strain rate) $n = 4.6(5)$ (lifetime)		
Fe-Au [19, 20] **Grain size: 57 μm**	60	3.190×10^{-5}	641.7
	80	5.080×10^{-5}	375.7
	100	7.362×10^{-5}	209.9
	117	2.748×10^{-4}	57.2
	Stress exponent: $n = 2.9(9)$ (strain rate) $n = 3.4(8)$ (lifetime)		
Fe-W [18] **Grain size: 127 μm**	100	$2.6(1) \times 10^{-5}$	1113
	140	$8.7(3) \times 10^{-5}$	236.4
	160	$2.0(5) \times 10^{-4}$	104.2
	200	$5.5(1) \times 10^{-4}$	56.8
	Stress exponent: $n = 4.3(4)$ (strain rate) $n = 4.4(4)$ (lifetime)		

2.3 Results

2.3.1 Creep results

The strain versus time results of the Fe-Au-W alloy samples loaded at a fixed temperature of 823 K (550 °C) but for different constant loads are shown in Fig. 2.1a. The derived steady state strain rate (obtained by linear fitting of the strain levels covering 15% to 85% lifetime) and creep lifetime are presented in Fig. 2.1b and 2.1c, respectively. The initial strain of the samples increases with the increase in load. Soon after the loads are fully applied, the steady-state creep begins with a strain rate that remains about constant for most of the lifetime of these small samples. The transition from the steady-state creep to the tertiary creep occurs with a sharp increase in the strain rate, leading to a subsequent failure of the sample. The final strain ranges from 5% to 9%, while the strain attributed by the steady-state creep is below 1%, indicating a brittle nature of the ternary Fe-Au-W alloy. The steady-state strain rate fulfils the Sherby-Dorn equation [24] $\dot{\varepsilon}_S = Ad^m\sigma^n\exp\left(-Q/RT\right)$, where A is a structure dependent constant, d is the grain size, m is the grain size exponent, σ is the applied stress, n is the stress exponent, Q is the activation energy, R is the gas constant and T is the temperature in kelvin. The corresponding stress exponent for the steady-state strain rate n is 4.0(8), while the stress exponent derived from the lifetime corresponds to 4.6(5). The creep results of our previous Fe-Au [19, 20] and Fe-W [18] alloys are also presented in Fig. 2.1b and 2.1c for comparison. The Fe-W alloy has a grain size of 127 μm, which is comparable to the Fe-Au-W grain size of 103 μm, thus the original data are shown. Since the grain size of the Fe-Au alloy was smaller (57 μm), the strain rate and the lifetime of the Fe-Au alloy have been normalized using the grain size exponent (m = -2 [17]). It can be seen that among these three alloys, the Fe-Au-W alloy has the lowest strain rate and the longest lifetime. The stress exponent for the Fe-Au-W and Fe-W alloys are comparable, indicating a similar creep-controlling mechanism. While for the Fe-Au alloy, the creep-controlling mechanism is likely to be different, especially in the low-stress regime. The strain rates and lifetimes for the three alloys with their experimental conditions are summarized in Table 1.
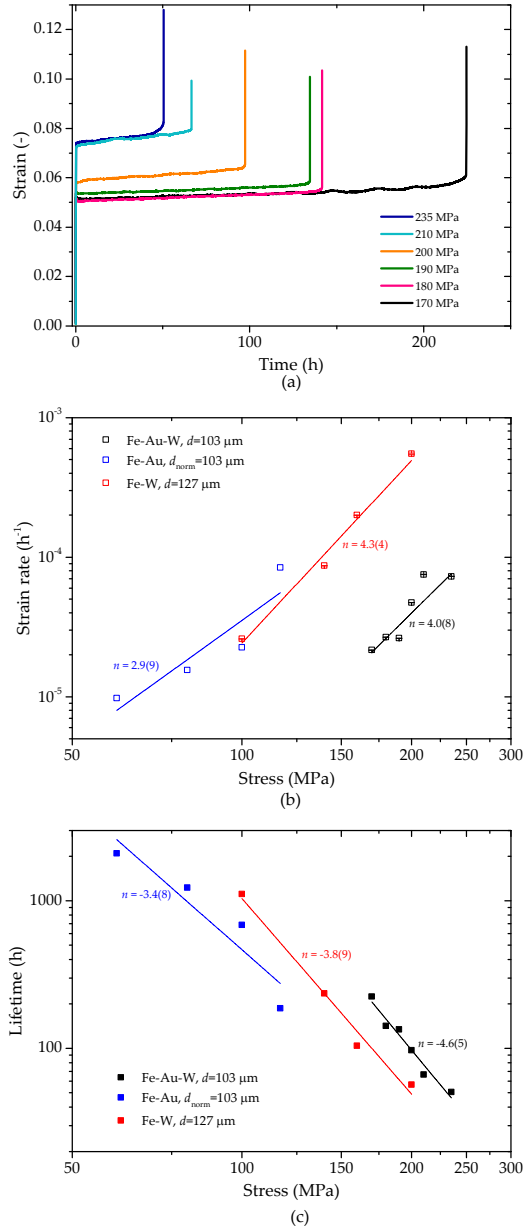
Fig. 2.1: (a): Creep curves for the Fe-Au-W alloy samples with different constant stress levels at a temperature of 823 K (550 °C). (b) Derived steady-stage strain rate and (c) creep lifetime as a function of applied stress. The strain rates and lifetimes of the previous Fe-Au [19, 20] and Fe-W [18] samples are also summarized and compared in (b) and (c).

2.3.2 MICROSTRUCTURE OF THE CREEP-FAILED SAMPLES

The fracture surface of the creep-failed sample after having been exposed to an applied stress of 200 MPa for 97.4 h is shown in Fig. 2.2a. The sample experienced a decohesive rupture at a grain boundary, which is consistent with the sudden transition from the steady-state creep to the tertiary creep, as shown in Fig. 2.1a. Some precipitates can be found on the fracture surface, both on the grain faces and at original grain corners or edges, as indicated by arrows. Some examples of formed cavities and precipitation healing are provided in Fig. 2.2b. The cavities are preferentially formed along the grain boundaries perpendicular to the stress direction (indicated by white arrow). Subsequently, the precipitates nucleate on the free creep cavity surface and then grow to fill the cavity gradually. In Fig. 2.2b, an example of a cavity fully filled by precipitation is indicated by a blue arrow. The precipitate is significantly enriched in Au (17.3 at.% Au and 2.1 at.% W). The precipitate indicated by a yellow arrow inside of the cavity in Fig. 2.2b is enriched in both Au and W (1.7 at.% Au and 3.6 at.% W) with respect to the nominal value. The Au and W concentration profiles along the black line crossing the precipitate in Fig. 2.2b are measured with EDS and are presented in Fig. 2.2c. The precipitate is enriched in Au with a peak concentration of about 17 at.%, while the W concentration remains around the nominal value. The Au concentration is likely to be underestimated, given the limited resolution of the EDS. In agreement with the binary Fe-Au system [20], uniformly dispersed disc-shaped nano-sized Au-rich particles are found within the matrix, as shown in Fig. 2.2b and 2.2d. In contrast to the Fe-Au binary system, no micron-scale Au depletion zone was observed in the current ternary Fe-Au-W alloy. As indicated in Fig. 2.2d, the depletion zone has a maximum width of approximately 0.5 μm. The reduced width of the Au depletion zone suggests a reduction in the effective Au volume diffusivity inside the bulk of the ternary Fe-Au-W alloy due to a suppression of the extensive subgrain formation observed in the binary Fe-Au alloy [17,20].

It is important to note that the precipitates are triggered by the formation of the cavities (instead of triggering the cavities). In the creep-failed samples, many precipitates formed in the cavities show irregular shapes, and their shapes match the geometry of the corresponding cavities, indicating a

cavity-triggered healing behavior. More detailed discussions can be found in [17] and [19].
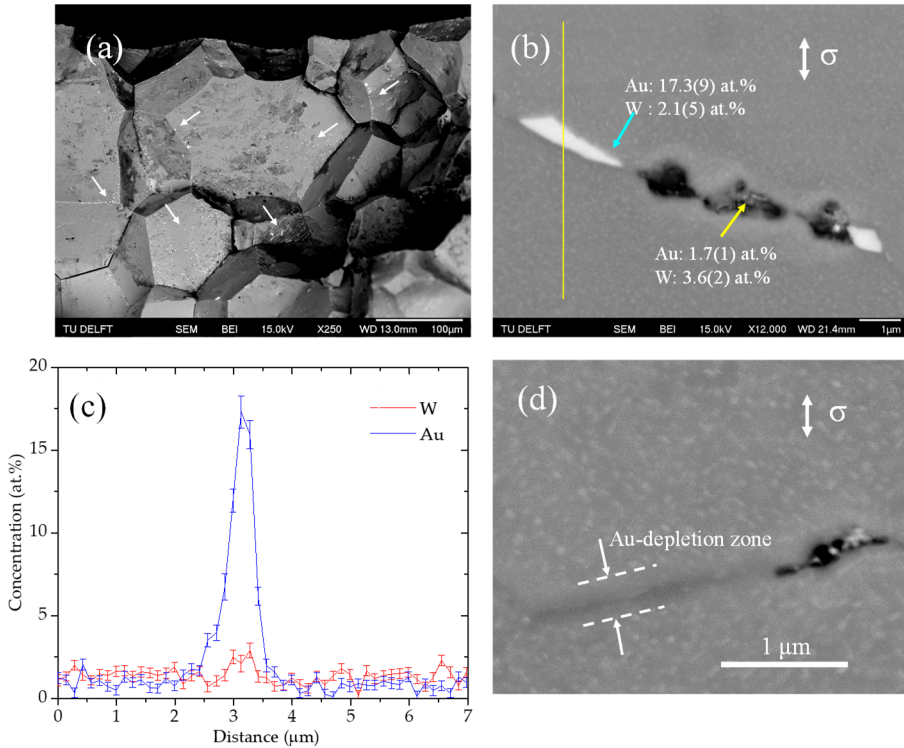
Fig. 2.2: Scanning electron microscopy data for Fe-Au-W alloy sample after creep at a constant stress of 200 MPa at 823 K (550 °C). (a) Fracture surface of the creep-failed sample. The white arrows indicate the precipitates. (b) Micrograph for the same sample. The blue arrow indicated precipitate is significantly enriched in Au while the yellow arrow indicated precipitate is enriched in both Au and W. (c) Composition profile of the line scan in (b). (d) Micrograph of the same sample. Au-rich discs and a Au depletion zone can be observed.

The composition of a collection of precipitates located on samples with varying creep lifetimes is analyzed by EDS and the results are summarized in Fig. 2.3. The vertical dotted line corresponds to the nominal Au concentration and the horizontal dotted line corresponds to the nominal W concentration. The data points located in the blue-shaded region and the yellow-shaded region correspond to the precipitates enriched in W and in Au, respectively. The data points in the non-shaded region represent the precipitates enriched

in both Au and W. It can be observed that the precipitates have a composition that ranges up to 20 at.% Au and 8 at.% W. Independent of the lifetime most of the precipitates are either enriched in Au or enriched in W, and only a few precipitates are enriched in both Au and W. This indicates that the Au-rich and W-rich precipitates are formed independently, and that within the experimental resolution of the EDS, Au-rich and W-rich precipitates rarely occupy the same cavity.

2
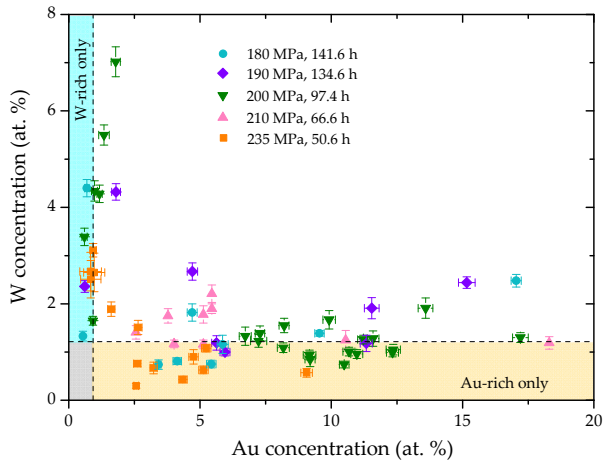
Fig. 2.3: Collected precipitate compositions for precipitates in creep samples with different stress levels and creep lifetimes. The vertical dotted line and the horizontal dotted line indicate the nominal Au concentration and the nominal W concentration, respectively.

In order to characterize the precipitation behavior in more detail, additional TEM experiments were performed. Fig. 2.4 shows the TEM results for the sample that was exposed to a stress of 190 MPa at a temperature of 823 K (550 °C). As shown in Fig. 2.4a, disc-shaped precipitates are found uniformly distributed within the matrix. The discs have a diameter of 40-150 nm and a diameter-to-thickness ratio ranging from 5 to 10. An interface relationship of $(015)_{matrix} \parallel (116)_{precipitate}$ and orientation relationships of $[002]_{matrix} \parallel [002]_{precipitate}$ and $[200]_{matrix} \parallel [110]_{precipitate}$ are found between the matrix and the disc-shaped precipitates. As shown in the elemental map in Fig. 2.4b, the discs are enriched in Au, while the W distribution is about uniform.

A line scan across a precipitate (shown in Fig. S2.2) shows a Au concentration of 56 at.% in the center. The discs have an *fcc* structure, with a lattice parameter of a_0 = 3.95(6) Å, corresponding to a gold concentration of 61(20) at.% for the precipitate. The gold concentration of the surrounding matrix is lower than the nominal value (about 0.6 at%). Au-rich discs are found to be connected to dislocations (Fig. 2.4c). Since no discs were observed in an as-quenched sample, it can be concluded that the disc-shaped precipitates nucleate from the dislocations, which are generated during creep. No W-rich precipitates are found in the matrix of the creep-failed sample. On the grain boundaries with no cavities, many precipitates with a size of 5 – 50 nm are observed (Fig. 2.4d). These precipitates are enriched in either Au or W and the two types of precipitates are usually found in contact with each other (Fig. 2.4e).

2
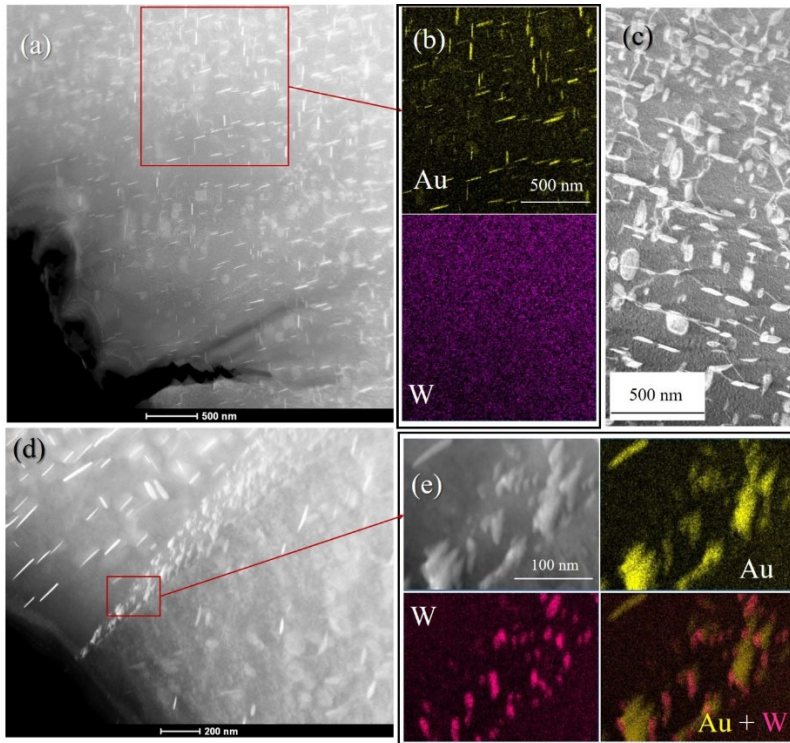
Fig. 2.4: TEM results for the Fe-Au-W alloy sample after creep at a stress of 190 MPa. (a): Disc-shaped precipitates in the matrix. (b): Elemental distribution of Au and W for the selected square area in (a). (c): Disc-shaped precipitates (with 3 perpendicular orientations) connected with dislocations (lines) are observed in the matrix. (d): Precipitates on a grain boundary without cavities. (e): Elemental distribution of Au

and W for the selected square area in (d). By overlapping the distribution of Au and W, one can see that the Au-rich and W-rich precipitates are in contact.

2.3.3 FRACTURE SURFACE

To clarify the formation of creep cavities, precipitation on the creep cavity surface and the interaction between Au-rich and W-rich precipitates, the fracture surfaces after creep were examined. The brittleness of the material and the decohesive rupture enabled a direct observation of the grain boundary fracture, with complementary mirror-like information from both sides of the fracture surface. Fig. 2.5 shows the fracture surface of the creep-failed sample after creep at a stress of 200 MPa. Two kinds of cavities can be observed in Fig. 2.5a and 2.5b: (*i*) large rectangular-shaped cavities (box 1 in Fig. 2.5f) and (*ii*) small ellipsoid-shaped cavities (box 2 in Fig. 2.5f), which are often fully filled with precipitation. In this case, most of the precipitates stick to one side of the broken sample (side A), but generally, the precipitates are found on both surfaces (see the neighbor grain on the right-hand side). By comparing the precipitate shape with the shape of the corresponding dent on the opposite surface, it seems that the ellipsoid cavities are fully filled by the micro-sized precipitates.

As shown in Fig. 2.5c-5f, some nano-sized precipitates (significantly smaller than the ellipsoidal particles) are found inside the rectangular cavities. Unlike the ellipsoidal micro-sized precipitates, the nano-sized precipitates are distributed over the cavity surface, showing only a limited degree of filling. To determine the composition of the two types of the precipitates, the atomic concentrations of Fe, Au and W were mapped using EDS, as shown in Fig. 5c. The ellipsoidal micro-sized particles correspond to Au-rich precipitates (with a highest observed concentration of about 8 at.% Au), while the nano-sized particles in the rectangular cavities are enriched in W (up to about 5 at.% W). A closer observation of the cavities covered with nano-sized particles yields more detailed information. As shown in Fig. 2.5d and 2.5e, spots 1 and 4 are only enriched in W, while spots 2 and 3 are enriched in both Au and W. The nano-sized particles in the rectangular cavities are generally enriched in W, but some of the nano-sized particles are found to be enriched in Au. By comparing this observation with the TEM results in Fig. 2.4d and 2.4e, where nano-sized Au-rich and W-rich precipitates are both found on the grain boundary, it can

be concluded that spots 2 and 3 correspond to a situation where nano-sized Au-rich and W-rich particles both are located inside the rectangular cavity, and that these two types of nano-particles are in direct contact with each other.
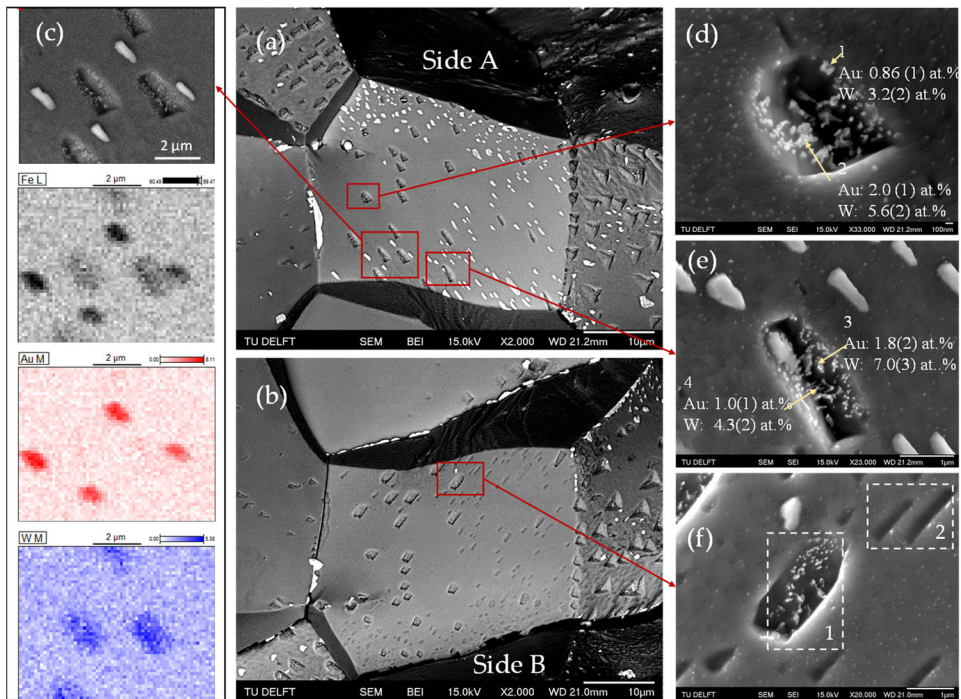
Fig. 2.5: (a) and (b): Both sides of a grain-boundary fracture surface of the Fe-Au-W alloy sample after creep at a stress of 200 MPa. (c): Elemental distribution of Fe, Au and W for the selected square area in (a). (d) to (f): Precipitates of different sizes are found in the cavities: the micro-sized precipitates in (e) are Au-rich, while the nano-sized particles inside of the rectangular cavities are generally W-rich, but some Au-rich nano-sized particles are also found. The micro-sized Au-rich and nano-sized W-rich precipitates rarely coexist, but an occasional example of coexistence is found in (e).

Although it is experimentally found that nano-sized Au-rich and W-rich particles can be formed within the same cavity, in most cases the cavity is filled with either Au-rich or W-rich precipitates. In Fig. 2.5f, boxes 1 and 2 provide some insight in the interaction between Au-rich and W-rich precipitates during healing. In the rectangular cavity in box 1 only nano-sized particles are found. On the contrary, the two cavities in box 2 are filled with Au-rich precipitates, which are attached to the opposite side (side A) of the fracture surface, and the

cavities on side B show a very clean counterpart without nano-sized W-rich particles. In most of the examined cavities, the micro-sized Au-rich and the nano-sized W-rich precipitates demonstrate a persistent reluctance to coexist with each other, within the resolution of the EDS. A rare cavity showing both micro-sized Au-rich precipitates and nano-sized W-rich precipitates is shown in Fig. 2.5e. These fracture surface observations agree well with the result in Fig. 2.3: the precipitates are enriched in either Au or W and only few of the cavities are found to be filled by both types of precipitates.

In addition to the precipitates in the cavities, some uniformly-distributed nano-sized particles are also found in the area around the cavities, as can be seen from Fig. 2.5d to 2.5f. This area of the fracture surface without cavities was intact at the end of the steady-state creep and only formed in the rapidly evolving final (tertiary) creep stage. EDS results show that these particles are enriched in W. No Au-rich particles are found on the fracture surface around the cavities.

The fracture surface of the creep-failed sample at a stress of 235 MPa is presented in Fig. 2.6a to 2.6d. With a shorter lifetime due to a higher stress, the size of both the cavities and precipitates are generally smaller. Two regions can be distinguished from the fracture surface: (*i*) a region with a net-shaped pattern in the vicinity of the grain edges and (*ii*) a flatter interior region. In the flatter region, the precipitate distribution shows a preference towards the grain edges, indicating that the cavities located on the grain edges or corners are preferentially healed. The net-shaped pattern may be induced by subgrain boundaries and dislocation cells that have formed in the initial creep stage [25]. Similar to the creep-failed sample at a stress of 200 MPa presented in Fig. 5, the same two types of precipitates are observed on the fracture surface for a sample with a relatively short lifetime. In Fig. 2.6a to 2.6d the relatively large Au-rich precipitates and the nano-sized W-rich particles, which are scattered over the surface of the rectangular cavities, are indicated by the yellow and blue arrows, respectively. The morphology of the Au-rich precipitates is different from those observed in the samples with a relatively long lifetime. Instead of an ellipsoidal shape, the Au-rich particles have a more irregular shape, especially in the region with the net-shaped pattern. It is worth to note that in Fig. 2.6c and 2.6d, the cavities and the Au-rich precipitates do not have a one-to-one correspondence, as observed in the creep-failed sample at a stress

of 200 MPa. Some of the cavities on side A do not have a corresponding precipitate on side B, indicating that the sample is in an early stage of filling where the Au-rich precipitation has just started to take place, initiated by the formation of the cavity.
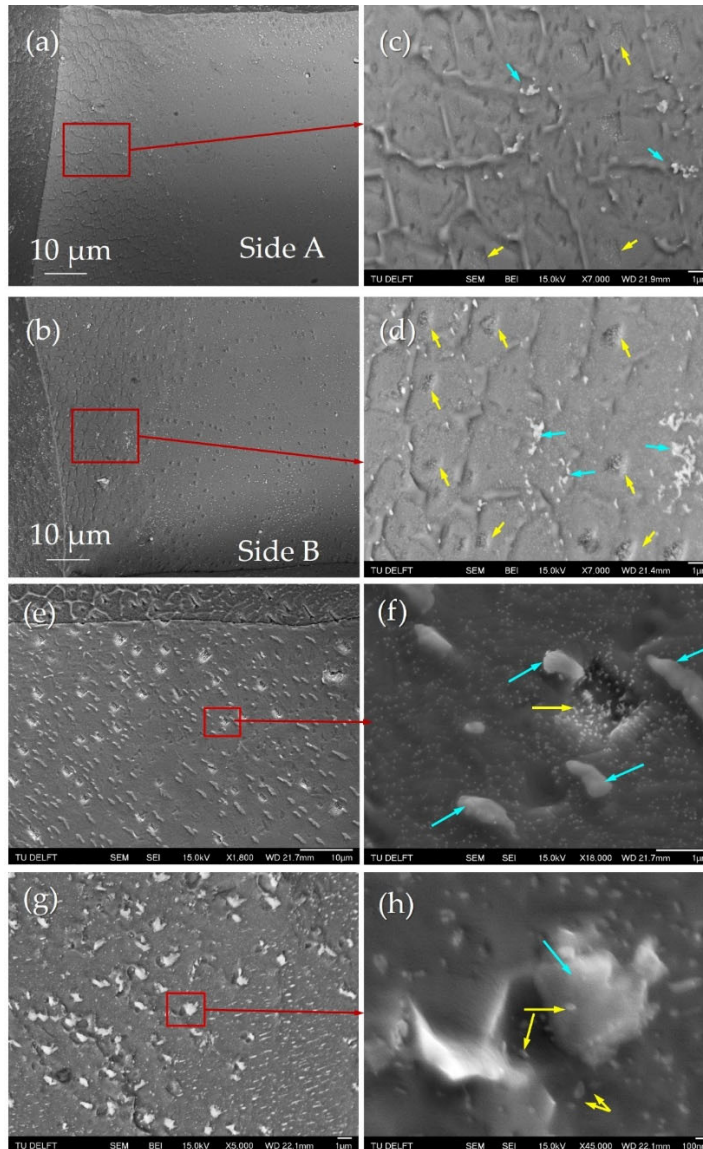
Fig. 2.6: (a) to (d): The fracture surfaces for the Fe-Au-W alloy sample after creep at a stress of 235 MPa. (e) to (h): The fracture surfaces for the Fe-Au-W alloy sample after creep at a stress of 180 MPa. The blue arrows indicate Au-rich precipitates while yellow arrows indicate W-rich particles.

In Fig. 2.6e to 2.6h, the fracture surface of the creep-failed sample at a stress of 180 MPa with a longer lifetime of 141.6 h is presented. The two types of precipitates with micron-sized Au-rich precipitates and W-rich nanoscale precipitates, as well as the reluctance for coexistence of Au-rich and W-rich precipitates in a single cavity, are evident from Fig. 6e and 6f. These observations are consistent with the results for the samples with a stress of 200 MPa (97.4 h) and 235 MPa (50.6 h). However, in Fig. 2.6g and 2.6h, a large number of cavities are half-filled by Au-rich precipitates (indicated by the blue arrow) and are decorated by the nano-sized W-rich particles (indicating by yellow arrows) over the cavity surface. Compared with the observations from samples with shorter lifetimes, it is most probable that these cavities are initially occupied by both W-rich and Au-rich nano-sized precipitates but that during the relatively long lifetime the Au-rich precipitates have overgrown the W-rich precipitates by their faster kinetics.

2.4. DISCUSSION

2.4.1 MECHANISM OF SELECTIVE HEALING

It was experimentally observed that the creep cavities were fully or partially filled by precipitates that segregated from the homogeneous supersaturated matrix. As indicated in Fig. 2.2, both the cavities and the precipitates showed a preference to form at grain boundaries oriented perpendicular to the stress direction or at the grain boundary edges. The observed precipitates are different in composition, size, shape, spatial distribution and degree of filling. As shown in Figs. 2.5 and 2.6, the Au-rich precipitates are usually found to be micron-sized with ellipsoidal shapes, while the W-rich particles are usually roundish and nano-sized. Some nano-sized Au-rich particles are also found in contact with W-rich precipitates. Many micron-sized Au-rich precipitates on the fracture surface show complementary shapes with the cavities they fill on either side of the fracture surface, indicating that the cavities are fully filled. The W-rich precipitates, on the other hand, are scattered over the cavity surfaces, generally showing only a limited degree of filling. For the samples with shorter lifetimes (less than 100 h), the two types of precipitates are in most cases not found to coexist on a micron-scale: the cavities are filled by either micron-sized Au-rich or nano-sized W-rich particles, while coexistence only happens occasionally. However, nano-sized Au-rich and W-rich

precipitates can be found concurrently in the same cavities. This observation from the fracture surfaces is consistent with the precipitates composition distribution shown in Fig. 2.3, where most of the precipitates are enriched in either Au or W. The few precipitates enriched in both Au and W may correspond to (*i*) the occasionally observed coexistence behavior of micron-sized Au-rich precipitate and nano-sized W-rich particles (Fig. 2.5e) or (*ii*) the coexistence of nano-sized Au-rich and W-rich particles (Fig. 2.5d and 2.5e).

It is worth to note that both Au-rich and W-rich precipitates show an obvious site-selectivity, i.e., the precipitates form exclusively on free surfaces. No precipitation takes place within the bulk, except for the nano-sized, disc-shaped Au precipitates (Fig. 2.2d and Fig. 2.4), which were also observed in the binary Fe-Au system [17, 20]. These Au-rich discs were found to be connected to dislocations (Fig. 2.4c), which act as nucleation sites, and can be consumed by the nucleation and growth of the healing precipitates in the nearby grain boundary cavities. After the disc-shaped precipitates are consumed, a depletion zone forms in the vicinity of the grain boundary (Fig. 2.2d). The site selectivity results from the strain energy generated by the misfit between the solute and the matrix atoms.

The healing mechanism of the Fe-Au-W system is illustrated in Fig. 2.7. In stage I (Fig. 2.7a), the as-quenched sample is homogeneous without any matrix precipitates or grain boundary segregation (as confirmed in Fig. S2.1). When the sample is exposed to high temperature and stress (stage II), solute atoms segregate on the grain boundaries in the form of nano-sized Au-rich and W-rich precipitates. Meanwhile, dislocations are generated, which act as nucleation sites for the formation of Au-rich disc-shaped precipitates within the matrix. As indicated in Fig. 2.7b, the Au-rich discs, which are connected to dislocations, form uniformly within the matrix and remain stable until a cavity is formed nearby. When a cavity is generated (stage III), the healing takes place. Since the grain-boundary diffusivity is orders of magnitude larger than the bulk diffusivity, a 1D bulk diffusion towards the grain boundary takes place once a free surface in the form of a creep cavity is generated. The solute Au atoms in the matrix diffuse towards the grain boundary as the grain boundary serves as a fast path in transferring the healing solute towards the cavity. During this process, the nano-sized grain boundary Au-rich precipitates (formed in stage II) are consumed via grain-boundary diffusion. Meanwhile, the nano-sized W-

2

rich precipitates (formed in stage II) are left on the grain boundary, since the diffusivity of W is much slower than that of Au. This phenomenon can be observed in Fig. 2.5d to 2.5f, where W-rich precipitates can be found on the fracture surface around the creep cavities. If the amount of solute and precipitated Au atoms on the grain boundary is not enough to fully fill the cavity, the disc-shaped Au-rich precipitates in the matrix are subsequently consumed. In this situation, a depletion zone for Au is generated in the vicinity of the grain boundary. The width of the depletion zone is either determined by the volume of the cavity (when the cavity is small) or by the bulk solute diffusion length (when the cavity is large). This phenomenon is illustrated in Fig. 2.7c (and supported by the data in Fig. 2.2d). When a cavity forms in the depletion zone for Au (stage IV), it can only be filled by W-rich precipitates, as illustrated in Fig. 2.7d. Unlike the Au-rich precipitates, the W-rich precipitates only provide a limited degree of healing, due to the lower diffusivity of W. Some nano-sized Au-rich particles can also form in these new-formed cavities, but the precipitates are predominantly enriched in W (as observed in Fig. 2.5c).

2.4.2 Filling ratio

Analogous to our previous 3D nano-tomography studies on self-healing of creep damage in Fe-Au [19] and Fe-W [18] alloys, the healing efficiency can be estimated from the filling ratio of the cavities (volume of the precipitate divided by the total volume of the cavity in which it formed). The estimated filling ratios (see supplementary information for details), obtained from the experimental fracture surfaces for the creep-failed samples at different stress levels are shown in Fig. 2.8. As expected, a higher filling ratio is achieved at a lower stress (and correspondingly a longer lifetime). For the lowest stress of 180 MPa (with the longest lifetime) a filling ratio of 71% was achieved. According to our previous research [16, 18, 19], the cavities already start to form at the beginning of the creep. However, the healing only starts after the cavity reaches a certain volume. Therefore, if the sample lifetime is short, the precipitates may not have had enough time to grow and catch up with the growth of the cavities. Owing to the relatively short lifetime, the highest stress of 235 MPa results in the lowest filling ratio.

(a) Stage I

(b) Stage II

(c) Stage III

(d) Stage IV
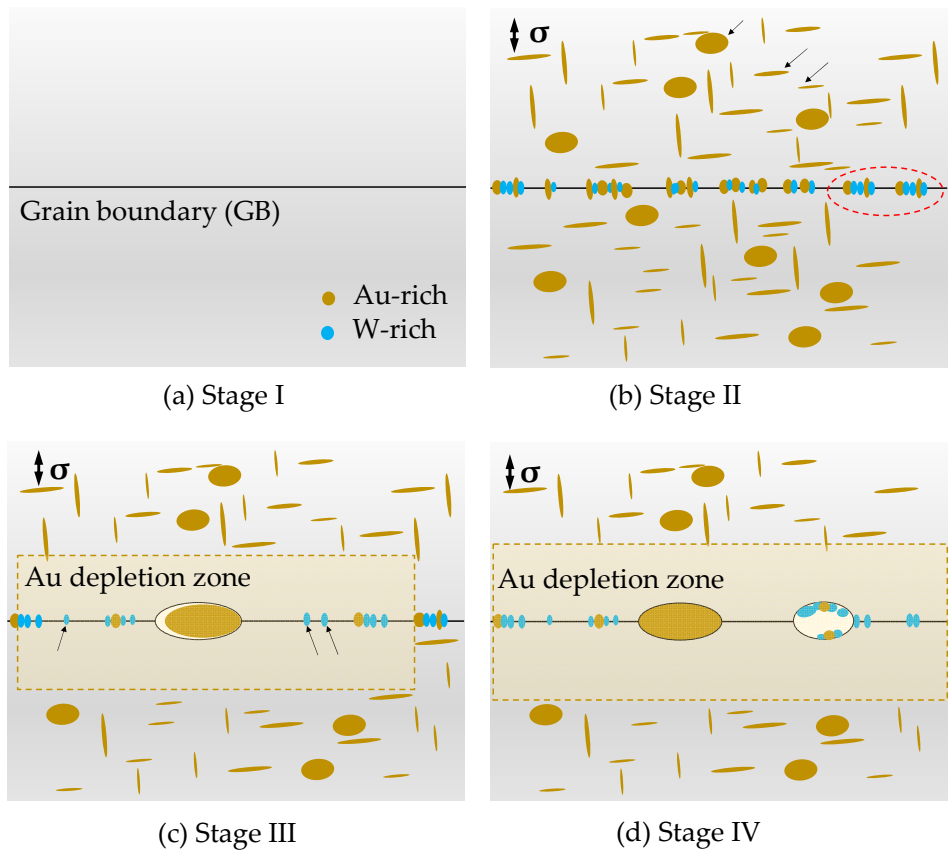
Fig. 2.7: Mechanism of cavity formation and solute healing. (a) The as-quenched sample, showing a homogenized composition without matrix precipitation or grain boundary segregation. (b) When the stress is applied, dislocation-connected Au-discs (indicated by the black arrows) form uniformly in the matrix. Meanwhile, the grain-boundary precipitation (enriched in either Au or W, as indicated by the dashed line) forms. (c) When a cavity is generated, a Au-rich precipitate fills the cavity by 1D diffusion from the bulk to the grain boundary and grain-boundary diffusion towards the cavity. The Au-rich precipitates on the grain boundary is consumed and W-rich particles are left on the grain boundary (indicated by the black arrows). A Au depletion zone is subsequently generated due to the consumption of the Au-discs in the matrix. (d) A cavity forms within the Au depletion zone and is partly filled by nano-sized W-rich precipitates (and some sparse nano-sized Au-rich precipitates).
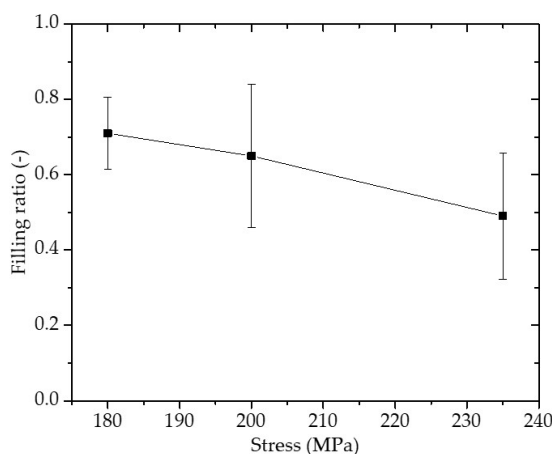
Fig. 2.8: Average filling ratio for the Fe-Au-W alloy samples after creep at a stress of 180, 200 and 235 MPa.

2.4.3 THE SIZE OF THE PRECIPITATES AND THE CREEP CAVITIES

In our previous studies [18, 19], the time evolution of the average volume for a precipitate (or a cavity) was fitted by $V = kt^n$, where V is the average volume of a precipitate a cavity, t is the time, k and n are constants that dependent on the material and the condition whether or not the precipitates (or cavities) are linked to their neighbors. For all the precipitates and isolated cavities, $n = 0.8$. For the linked cavities, the exponent n has a higher value of 1.3.

To compare the results of the current ternary system with the previous binary alloys, the average diameters of the cavities and precipitates as a function of time are shown in Fig. 2.9 (examples of the size distributions are presented in Fig. S2.3). For the present ternary alloy, the average sizes of the cavities and the Au-rich precipitates show an increase with time, although at a stress of 180 MPa (with a lifetime of 141.6 h) both the Au-rich precipitates and the cavities are smaller than their counterparts at a stress of 200 MPa (with a lifetime of 97 h). Although the average cavity size at a stress of 180 MPa is smaller than that at 200 MPa, the size of the top 20% largest cavities in the two samples are comparable. In fact, as shown in Fig. 2.9b, the difference between the top 20% cavity size and the average cavity size increases for a decrease in stress (and correspondingly an increase in lifetime). The top 20% cavities generally correspond to the rectangular cavities (which are partially-filled by W-rich

cavities), while the average cavity sizes are attributed to both the partially-filled and the fully-filled cavities. The partially-filled cavities grow continuously, while the growth of the fully-filled cavities is stopped (or strongly suppressed).
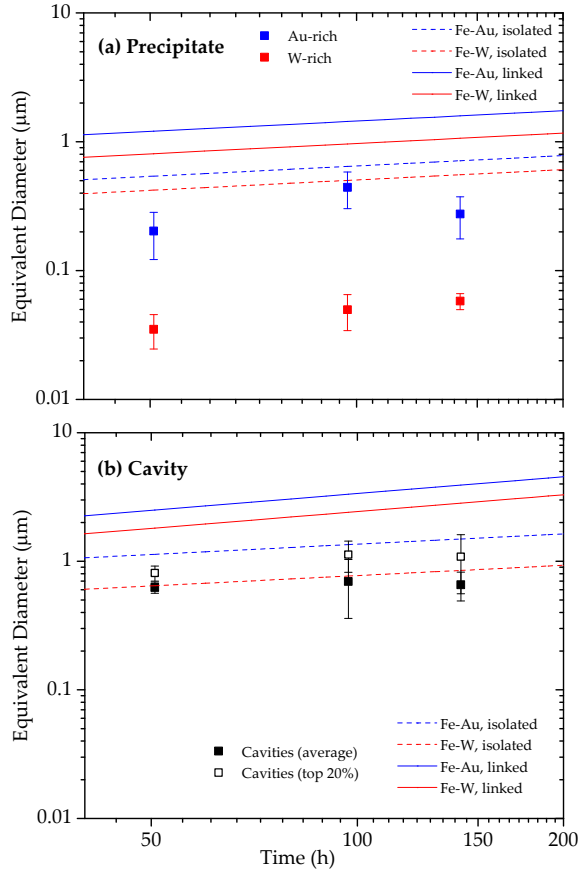
Fig. 2.9: Evolution of the size of (a) the precipitates and (b) the cavities as a function of time. The dotted curves represent the experimental data for the binary Fe-3Au [19] and Fe-4W [18] systems. The equivalent diameter corresponds to $\langle d \rangle = (6/\pi)(kt^n)^{1/3}$, where k and n are the experimentally determined growth constant and growth exponent, respectively.

By comparing the cavity evolution among the three systems, a smaller cavity growth rate is observed for the new ternary alloy. In the Fe-Au-W alloy, Au-rich precipitates are smaller in size than both the Au-rich precipitate in

Fe-Au system and the W-rich Laves precipitates in Fe-W system. The most pronounced difference lies in the size of the W-rich precipitates with only 30-60 nm in diameter in the Fe-Au-W system, which is one order of magnitude smaller than the precipitates in the Fe-W binary system. The formation of W-rich precipitates has apparently been suppressed strongly in the ternary alloy.

2.4.4 NUMBER DENSITY AND VOLUME FRACTION

The number of cavities and of Au-rich precipitates per unit of fracture surface area (2D number density) for the ternary Fe-Au-W alloy is now compared with the data for the binary Fe-Au alloy [19]. Assuming that: (1) all the cavities and precipitates are located on grain boundaries and (2) the decohesive rupture takes place along the grain boundaries whose orientation angles to the stress direction are larger than 45° (about perpendicular to the applied stress). Then the 2D number density can be converted from our current measurement to a 3D volume number density. According to our previous study [20] about 2/3 of the precipitates are located on the grain boundaries with an GB/stress orientation angle larger than 45°. The volume number density is thus estimated to be $n_V = (3/2)n_A/d_G$ for the cavities and $n_V = 3n_A/d_G$ for the Au-rich precipitates, where d_G is the average grain size and n_A is the areal number density of precipitates or cavities (average of the observation on both sides of the fracture surface). Assuming a spherical shape for the cavities (precipitates), the corresponding volume fraction of the cavities (precipitates) can be written as $f_V = (\pi/6)\langle d^3 \rangle n_V$, where $(\pi/6)\langle d^3 \rangle$ corresponds to the average volume of the cavities (precipitates). The results are summarized in Table 2.2. Compared to the binary Fe-Au alloy, the ternary Fe-Au-W alloy has smaller cavities and precipitates, but the number density of the cavities and precipitates is higher. In the binary system a lower stress (and thus a longer lifetime) results in larger cavities, larger precipitates and lower number densities. This phenomenon is related to a precipitate-precipitate coalescence and cavity-cavity linking [19], which can result in an increase in particle size and a decrease in number density. Considering the larger stresses applied to the ternary alloy, as well as its brittle nature, it can be concluded that in the ternary alloy the coalesce of the cavities and precipitates is limited when the stress is higher than 180 MPa.

Table 2.2: Volume number density of the Au-rich precipitates and cavities of the current ternary samples and the previous binary Fe-Au samples [19]. All the experiments are performed at a fixed temperature of 823 K (550 °C).

Sample	Stress (MPa)	Lifetime (h)	$\langle d \rangle$ (μm)		n_V (μm^{-3})		f_V (%)	
			ppt	cavity	ppt	cavity	ppt	cavity
FeAu	60	641.7	0.76(4)	1.5(1)	1.7(1) ×10^{-4}	7.0(5)×10^{-5}	0.098	0.64
	80	375.7	0.63(4)	1.50(6)	1.3(1) ×10^{-4}	7.6(3)×10^{-5}	0.24	0.76
	100	209.9	0.67(3)	0.86(2)	9.3(6) ×10^{-4}	1.94(6)×10^{-4}	0.35	0.24
	117	57.2	0.63(3)	0.85(4)	1.11(7) ×10^{-3}	9.2(5)×10^{-5}	0.14	0.11
FeAuW	180	141.6	0.27(9)	0.7(1)	1.1(4)×10^{-2}	1.4(2) ×10^{-3}	0.032(7)	0.10(2)
	200	97.4	0.44(5)	0.8(2)	3.3(5) ×10^{-3}	1.8(3) ×10^{-3}	0.03(1)	0.09(3)
	235	50.6	0.203(4)	0.6(1)	1.1(3) ×10^{-2}	1.9(1) ×10^{-3}	0.011(6)	0.033(6)

2

2.4.5 HEALING KINETICS

The volume diffusivity of solute Au and W in *bcc*-iron at a temperature of 823 K (550 °C) corresponds to 7.4×10^{-19} m²s^{-1} and 3.3×10^{-21} m²s^{-1} [26], respectively. Given the dilute nature of the ternary alloy it is assumed that these values also apply to the ternary alloy. As no values have been reported for the grain-boundary diffusivity of Au and W in *bcc*-iron, the Fe self-diffusivity along the grain boundary is taken, which amounts to 2.4×10^{-14} m²s^{-1} [27]. The grain-boundary diffusivity is orders of magnitude higher than the volume diffusivity, indicating that volume diffusion is the rate-controlling process. In this situation, the diffusion of the solute atoms towards the creep cavities can thus be simplified by a 1D diffusion [28], i.e., the supersaturated solute atoms diffuse towards the nearest grain boundaries, before they are transferred to the cavities by grain-boundary diffusion. In the diffusion process of the supersaturated solute from the bulk to the creep cavities the volume diffusivity is the rate-controlling factor, while grain boundaries serve as fast diffusion paths. The 1D flux (from one side of the matrix) is estimated by [28]:

$$J_X = \frac{D_X \Delta x}{\Omega} \left(\frac{1}{\sqrt{\pi D_X t}} \right) = \frac{\Delta x}{\Omega} \sqrt{\frac{D_X}{\pi t}} \qquad (2.1)$$

where $\Delta x = x_\infty - x_1$ is the supersaturation of the solute, D_X is the diffusivity of the solute element in the matrix phase, Ω is the atomic volume and t is the time. Assuming that the solute that arrives at the free surface forms a layer with a fixed solute concentration x_p, the layer thickness a follows from the mass

balance $x_p \frac{da}{dt} = \Omega J_X$. Starting from a homogeneous supersaturated matrix with $a(t = 0) = 0$ this results in a parabolic thickening of the precipitate layer:

$$a(t) = \frac{\Omega}{x_p} \int_0^t J_X(a, t')dt' = \frac{2\sqrt{D_X t}}{\sqrt{\pi}} \frac{\Delta x}{x_p} \tag{2.2}$$

When λ is the creep cavity spacing at the grain boundary (oriented perpendicular to the stress) then a surface area $S_0 = \lambda^2$ contributes to the cavity filling by solute transport from the bulk. For a surface area S_0 the total precipitation volume amounts to:

$$V_{diff}(t) = a(t)S_0 = \frac{2S_0\sqrt{D_X t}}{\sqrt{\pi}} \frac{\Delta x}{x_p} \tag{2.3}$$

Experimentally, the total precipitation volume on one single side of the fracture surface with a surface area of S_0 can be estimated as:

$$V_{exp} = \frac{\pi}{6} S_0 \langle d^3 \rangle n_A \tag{2.4}$$

where $(\pi/6)\langle d^3 \rangle$ corresponds to the average volume of the precipitates, n_A is the areal number density.

The calculated and experimental results are shown in Fig. 2.10. It is worth to note that the Au-rich precipitates are more or less uniformly distributed over the whole fracture surface, while the W-rich precipitates are only distributed within the rectangular-shaped cavities. As shown in Fig. 2.5d to 2.5f, the areal number density of W-rich particles is only meaningful when the area of the rectangular-shaped cavity is considered (instead of the whole fracture surface area). Therefore, the values of n_A for the W-rich and Au-rich precipitates in Eq. (4) are studied in different areal units. As shown in Fig. 2.10, the W-rich precipitates volume estimated from the experiments agrees well with the result calculated based on the 1D diffusion, indicating that the precipitation of the W-rich phase is controlled locally by the volume diffusion of W atoms towards the cavity surface. The precipitation of the Au-rich phase, on the other hand, has a faster kinetics compared to the prediction by the 1D diffusion model, suggesting the presence of faster pathways, in comparison to volume diffusion. In our previous study [20], an effective diffusivity, which is two orders of magnitude larger than the volume diffusivity was observed,

owing to the formation of subgrains during creep. Since no evidence of subgrains was observed, the faster healing kinetics might be attributed by other defects, such as dislocations.
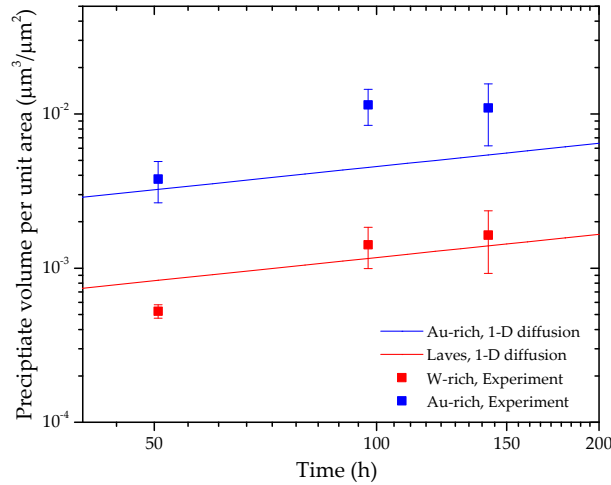
Fig. 2.10: Diffusion controlled precipitation volume as a function of time. The solid curves are calculated by $V_{diff}(t) = (2/\sqrt{\pi})(\Delta x/x_p)\sqrt{D_X t}$ and the scattered data points are calculated by $V_{exp} = (\pi/6)\langle d^3 \rangle n_A$. Note that the W-rich precipitate volume is estimated by assuming that the W-rich precipitates are uniformly distributed over the creep cavity surface.

2.5. CONCLUSIONS

The autonomous healing of creep-induced grain boundary cavities by Au-rich and W-rich precipitates in a Fe-3Au-4W (wt.%) ternary system have been studied. The ternary alloy, with two supersaturated healing solutes inside, serves as a model system to provide insight in the interplay between two separate healing agents. The creep tests were done at a high temperature of 823 K (550 °C) with different applied stresses. The creep properties of the ternary alloy are evaluated and compared with those of the previously studied Fe-Au and Fe-W binary systems. The microstructures of the creep-failed samples are studied in detail by electron microscopy to investigate the cavity filling behavior and the mass transfer of supersaturated solute to the defect sites. The main conclusions are as follows:

(1) Compared with the two binary Fe-Au and Fe-W systems, the ternary Fe-Au-W system shows the lowest steady-state strain rate and the longest creep lifetime. The Fe-Au-W alloy has similar creep rate controlling mechanism as the Fe-W alloy.

(2) During creep at a temperature of 823 K (550 ℃), Au-rich and W-rich precipitates form predominantly on the free surface of the creep-induced cavities and thus heal the cavities. A filling ratio of 71% is achieved for the for the lowest applied stress of 180 MPa.

(3) By investigating the fracture surfaces of the creep-failed samples, two types of precipitates are found: micron-sized Au-rich precipitates and nano-sized W-rich particles. The Au-rich precipitates show the capacity of fully filling the cavities, while the W-rich particles, which are distributed over the cavity surface, show only a limited degree of healing. The two types of precipitates show an apparent reluctance of coexistence when the lifetime is shorter than 100 h.

(4) The healing mechanism of the Fe-Au-W system is as follows: due to the fast Au diffusivity, early-formed creep-induced cavities are filled by the Au-rich precipitates, which results in the formation of a zone that is depleted in Au. The cavities that form at a later stage in this Au-depleted zone can only be partially filled by W-rich precipitates.

(5) Compared to the previous binary Fe-Au and Fe-W systems, the average sizes of the precipitates and the cavities in the ternary Fe-W-Au system are smaller, while their number densities are larger. This indicates that the precipitate-precipitate coalescence and the cavity-cavity linkage is limited.

(6) The Au-rich precipitation is controlled by a combination of volume diffusion and grain boundary diffusion of supersaturated Au solute, which is accelerated by matrix defects, such as dislocations. The W-rich precipitation in the cavities is locally controlled by a 1D diffusion of solute W, while the formation of W-rich Laves phase precipitates is suppressed on microscopic length scales.

2.6 SUPPLEMENTARY MATERIAL

2.6.1. INITIAL MICROSTRUCTURE

The microstructure of the Fe-Au-W sample has been characterised before (as-received sample) and after homogenisation and subsequent quenching (as-quenched sample). In the as-received sample irregular grains can be observed with some Au-rich precipitates along the grain boundary (Fig. S2.1), indicating a strong grain boundary segregation. Besides of the Au-rich precipitates, a limited number of spherical inclusions is present in the grain interior. These inclusions correspond to $FeWO_4$ particles, which remain stable during the homogenisation and the creep experiments. After homogenisation and subsequent quenching, the irregular grains grow into equiaxed grains, the Au-rich precipitates on the grain boundaries are dissolved in the matrix and the stable oxidation particles are unchanged.
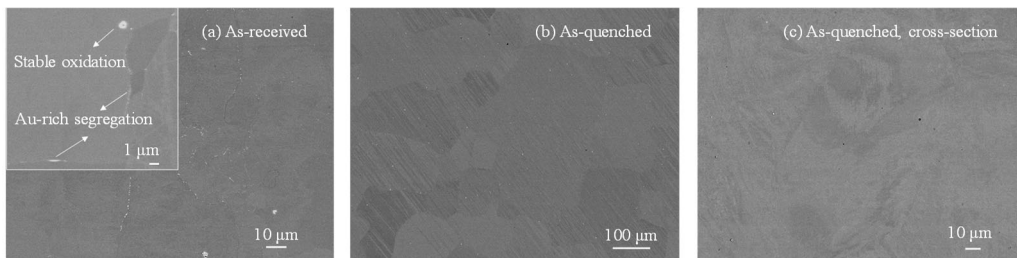
Fig. S2.1: Microstructure of the (a) as-received sample and (b), (c) as-quenched sample. The insert in (a) shows two types of precipitates in the as-received sample, undissolved Au-rich segregation and a stable $FeWO_4$ particle.

2.6.2. ELEMENTAL MAPPING OF AU-RICH PLATE-SHAPED PRECIPITATES IN THE MATRIX
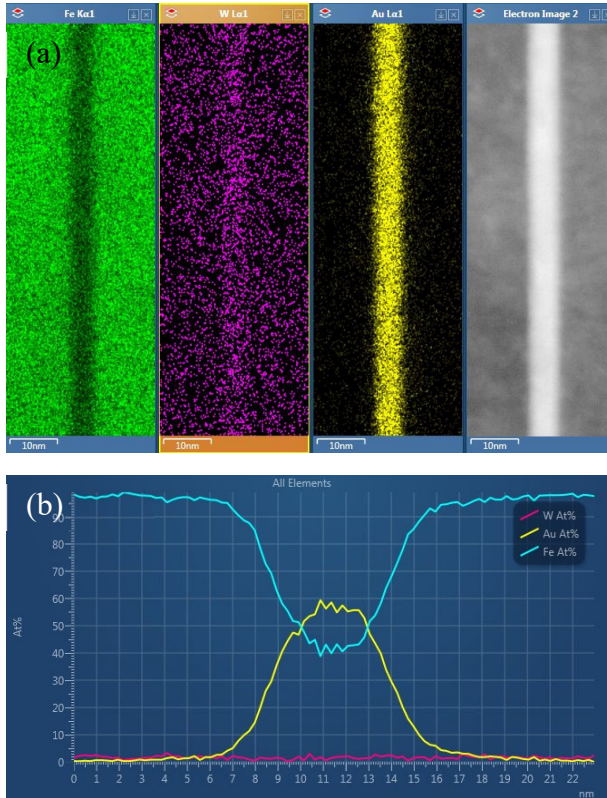
Fig. S2.2: (a) Elemental maps of a disc-shaped precipitate in the matrix in the Fe-Au-W alloy sample after creep at a stress of 190 MPa and (b) the corresponding composition profile obtained from TEM measurements.

2.6.3. DETERMINATION OF THE AVERAGE FILLING RATIO OF THE CREEP CAVITIES ON THE FRACTURE SURFACE

The filling ratios are calculated from the SEM images of the fracture surfaces. For the creep failed samples at a stress of 180, 200 and 235 MPa, at least 5 regions of interest were selected on corresponding sides of the fracture surface (i.e., at least 10 regions of interest for the two sides). Subsequently, the area of each precipitate, each cavity and the whole region of interest was analysed. Given the fact that (1) the Au-rich particles play the main role in cavity filling and (2) some W-rich particles have a size of only several pixels, we focused only on Au-rich precipitates. Any particle with an area less than 0.05 μm^2 (corresponding to an equivalent diameter of about 80 nm) was regarded as noise and was thus ignored in the filling ratio estimation.

For each cavity on the fracture surface the two corresponding sides (A and B) are investigated. When a creep cavity with precipitation inside it is broken up, the total area of the cavity S_{tot} on the fracture surface is equal for side A and side B. The precipitate area covered inside the cavity on side A corresponds to S_A and on side B to S_B. The filling fraction of a cavity is now estimated by $FR = (S_A + S_B)/S_{tot}$. Note that the filling ratio is confined to $0 \leq FR \leq 1$. After determination of the filling fraction for all individual cavities on a selected part of the fracture surface the overall filling ratio is obtained by averaging over the individual values of the probed cavities.

2.6.4. SIZE DISTRIBUTION OF PRECIPITATES AND CAVITIES LOCATED AT THE FRACTURE SURFACE

(a) Sample 200 MPa
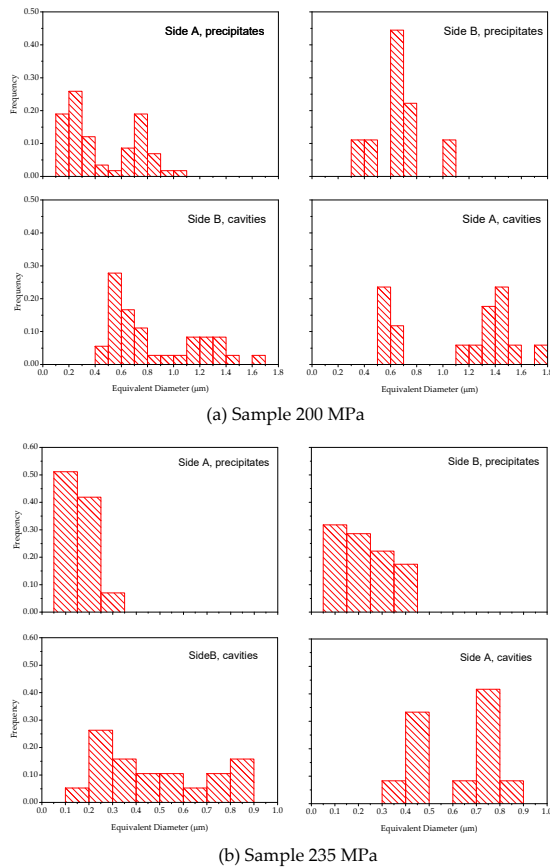
(b) Sample 235 MPa

Fig. S2.3: Size distribution of cavities and precipitates for the Fe-Au-W alloy sample after creep at a stress of (a) 200 MPa and (b) 235 MPa. The precipitates and cavities on each side are analysed separately.

The size distribution of the precipitates and cavities for two regions from the creep-failed samples at a stress of 200 and 235 MPa are presented in Fig. S2.3. The equivalent diameter of a precipitate (or a cavity) is regarded as the diameter of a circle with the equivalent area. At a stress of 200 MPa, the precipitates on one side show a clear corresponding relationship with the cavities on the other side. Especially for the precipitates on side A and the cavities on side B, which demonstrate very similar distributions, indicating that almost each cavity on side B has a corresponding filling precipitate on side A with a smaller size. However, for the larger cavities (with a diameter > 1.4 μm), no corresponding precipitates can be found on either side, indicating that those cavities remain unfilled until the fracture takes place. A different healing behaviour can be observed for an applied stress of 235 MPa, where the cavities have a wider distribution in comparison with the precipitates. Because of the limited lifetime (50.6 h), the precipitates have not fully filled the cavities when failure takes place. Therefore, the sizes of the precipitates and cavities do not match, indicating the presence of many unfilled and partially filled cavities.

References

[1] F.R.N. Nabarro, d. Villiers, Physics Of Creep And Creep-Resistant Alloys, CRC Press 2018.

[2] K. Maruyama, K. Sawada, J.-i. Koike, Strengthening Mechanisms of Creep Resistant Tempered Martensitic Steel, ISIJ Int. 41(6) (2001) 641-653.

[3] M. Taneike, F. Abe, K. Sawada, Creep-strengthening of steel at high temperatures using nano-sized carbonitride dispersions, Nature 424(6946) (2003) 294-296.

[4] M.D. Hager, P. Greil, C. Leyens, S. van der Zwaag, U.S. Schubert, Self-healing materials, Adv. Mater. 22(47) (2010) 5424-30.

[5] B. Grabowski, C.C. Tasan, Self-Healing Metals, Self-healing Materials 2016, pp. 387-407.

[6] N. van Dijk, S. van der Zwaag, Self-Healing Phenomena in Metals, Adv. Mater. Interfaces 5(17) (2018) 1800226.

[7] R.N. Lumley, A.J. Morton, I.J. Polmear, Enhanced creep performance in an Al-Cu-Mg-Ag alloy through underageing, Acta Mater. 50 (2002) 3597-3608.

[8] R.N. Lumley, I.J. Polmear, Advances in self healing of metals, Proceedings of the First International Conference on Self Healing Materials, Noordwijk aan Zee, Netherlands, 2007.

[9] K. Laha, J. Kyono, S. Kishimoto, N. Shinya, Beneficial effect of B segregation on creep cavitation in a type 347 austenitic stainless steel, Scr. Mater. 52(7) (2005) 675-678.

[10] K. Laha, J. Kyono, T. Sasaki, S. Kishimoto, N. Shinya, Improved creep strength and creep ductility of type 347 austenitic stainless steel through the self-healing effect of boron for creep cavitation, Metall. Mater. Trans. A 36A(2) (2005) 399-409.

[11] N. Shinya, J. Kyono, K. Laha, Self-healing Effect of Boron Nitride Precipitation on Creep Cavitation in Austenitic Stainless Steel, J. Intel. Mat. Syst. Str. 17(12) (2016) 1127-1133.

[12] S.M. He, N.H. van Dijk, H. Schut, E.R. Peekstok, S. van der Zwaag, Thermally activated precipitation at deformation-induced defects in Fe-Cu and Fe-Cu-B-N alloys studied by positron annihilation spectroscopy, Phys. Rev. B 81(9) (2010) 094103.

[13] S. van der Zwaag, E. Brinkman, Self Healing Materials: Pioneering Research in the Netherlands, IOS Press 2015.

[14] S. Zhang, J. Kohlbrecher, F.D. Tichelaar, G. Langelaan, E. Brück, S. van der Zwaag, N.H. van Dijk, Defect-induced Au precipitation in Fe–Au and Fe–Au–B–N alloys studied by in situ small-angle neutron scattering, Acta Mater. 61(18) (2013) 7009-7019.

[13] S. Zhang, G. Langelaan, J.C. Brouwer, W.G. Sloof, E. Brück, S. van der Zwaag, N.H. van Dijk, Preferential Au precipitation at deformation-induced defects in Fe–Au and Fe–Au–B–N alloys, J. Alloys Comp. 584 (2014) 425-429.

[16] S. Zhang, H. Fang, M.E. Gramsma, C. Kwakernaak, W.G. Sloof, F.D. Tichelaar, M. Kuzmina, M. Herbig, D. Raabe, E. Brück, S. van der Zwaag, N.H. van Dijk, Autonomous Filling of Grain-Boundary Cavities during Creep Loading in Fe-Mo Alloys, Metall. Mater. Trans. A 47(10) (2016) 4831-4844.

[17] S. Zhang, C. Kwakernaak, W. Sloof, E. Brück, S. van der Zwaag, N. van Dijk, Self Healing of Creep Damage by Gold Precipitation in Iron Alloys, Adv. Eng. Mater. 17(5) (2015) 598-603.

[18] H. Fang, N. Szymanski, C.D. Versteylen, P. Cloetens, C. Kwakernaak, W.G. Sloof, F.D. Tichelaar, S. Balachandran, M. Herbig, E. Brück, S. van der Zwaag, N.H. van Dijk, Self healing of creep damage in iron-based alloys by supersaturated tungsten, Acta Mater. 166 (2019) 531-542.

[19] H. Fang, C.D. Versteylen, S. Zhang, Y. Yang, P. Cloetens, D. Ngan-Tillard, E. Brück, S. van der Zwaag, N.H. van Dijk, Autonomous filling of creep cavities in Fe-Au alloys studied by synchrotron X-ray nano-tomography, Acta Mater. 121 (2016) 352-364.

2

[20] S. Zhang, C. Kwakernaak, F.D. Tichelaar, W.G. Sloof, M. Kuzmina, M. Herbig, D. Raabe, E. Brück, S. van der Zwaag, N.H. van Dijk, Autonomous Repair Mechanism of Creep Damage in Fe-Au and Fe-Au-B-N Alloys, Metall. Mater. Trans. A 46(12) (2015) 5656-5670.

[21] S.M. He, P.N. Brandhoff, H. Schut, S. van der Zwaag, N.H. van Dijk, Positron annihilation study on repeated deformation/precipitation aging in Fe–Cu–B–N alloys, J. Mater. Sci. 48(18) (2013) 6150-6156.

[22] S. Zhang, J. Cizek, Z. Yao, M. Oleksandr, X. Kong, C. Liu, N. van Dijk, S. van der Zwaag, Self healing of radiation-induced damage in Fe–Au and Fe–Cu alloys: Combining positron annihilation spectroscopy with TEM and ab initio calculations, J. Alloys Compd. (2019).

[23] C.D. Versteylen, M.H.F. Sluiter, N.H. van Dijk, Modelling the formation and self-healing of creep damage in iron-based alloys, J. Mater. Sci. 53(20) (2018) 14758-14773.

[24] O.D. Sherby, Factors affecting the high temperature strength of polcyrystalline solids, Acta Metall. Mater. 10(2) (1962) 135-147.

[25] J.S. Zhang, High Temperature Deformation and Fracture of Materials, Elsevier Science2010.

[26] C.D. Versteylen, N.H. van Dijk, M.H.F. Sluiter, First-principles analysis of solute diffusion in dilute bcc Fe-X alloys, Phys. Rev. B 96(9) (2017).

[27] G. Stechauner, E. Kozeschnik, Self-Diffusion in Grain Boundaries and Dislocation Pipes in Al, Fe, and Ni and Application to AlN Precipitation in Steel, J. Mater. Eng. Perform. 23(5) (2014) 1576-1579.

[28] C.D. Versteylen, N.K. Szymański, M.H.F. Sluiter, N.H. van Dijk, Finite element modelling of creep cavity filling by solute diffusion, Philos. Mag. 98(10) (2018) 864-877.

不容易(bù róng yì)

Not easy.

This stamp, together with the two in the following two chapters, makes a set.

3

SURFACE PRECIPITATION OF SUPERSATURATED SOLUTES IN A TERNARY FE-AU-W ALLOY AND ITS BINARY COUNTERPARTS

'If you disagree with your boss, either listen to him, or do it your way, and shove your success in his face.'

A friend from TU Delft

The precipitation of supersaturated solutes at free surfaces in ternary Fe-3Au-4W and binary Fe-3Au and Fe-4W alloys (composition in weight percentage) for different ageing times was investigated at a temperature of 700 °C. The time evolution of the surface precipitation is compared among the three alloys to investigate the interplay between the Au and W solutes in the ternary system. The Au rich grain-interior surface precipitates show a similar size and kinetics in the Fe-Au-W and Fe-Au alloys, while the W rich grain-interior surface precipitates show a smaller size and a higher number density in the Fe Au W alloy compared to the Fe-W alloy. The kinetics of the precipitation on the external free surface for the ternary Fe Au-W alloy is compared to the previously studied precipitation on the internal surfaces of the grain-boundary cavities during creep loading of the same alloy.

3.1 INTRODUCTION

Metals in service degrade due to processes like creep, fatigue, wear, corrosion, and radiation damage. Traditionally, efforts have been made to stabilize the material composition and microstructure so that the occurrence of damage is postponed as long as possible, which corresponds to a damage prevention strategy [1]. Since the initiation of the damage is assumed to be inevitable, the concept of self healing is proposed as an alternative strategy, in which case the occurrence of damage triggers mobile healing agents to move towards the defect and heal the defect site [2,3]. In the self-healing approach, the propagation of damage is interrupted.

The self-healing concept has been applied to improve the creep resistance [4-7], fatigue resistance [8,9] and the radiation damage resistance [10] of various metallic systems. The combined addition of boron and nitrogen into austenitic stainless steels (with an *fcc* lattice structure) is effective in reducing the cavity growth rate, as well as increasing the creep rupture strength [4,11]. The self-healing behavior was studied in underaged Al alloys subjected to creep [5,8] and fatigue [8] conditions. The healing solutes (usually Cu atoms) migrate to the defects and form precipitates via bulk diffusion or pipe diffusion along dislocations. The improvement in creep and fatigue performance is achieved by dynamic precipitation, the subsequent reduction in the dislocation mobility and/or the closure of the incipient cracks. It has been demonstrated that Au atoms dissolved in *bcc* iron can actively heal early-stage radiation damage by solute segregation [10]. In a systematic study on ferritic steels (with a *bcc* lattice structure), a series of binary and ternary alloys [6,7,12-17], including Fe-Cu, Fe-Au, Fe-Mo, Fe-W and Fe-Au-W, were investigated to reveal the mechanism of self healing during creep. The composition of these alloys was selected such that at the operating temperatures the solute is in a supersaturated state by approximately 1 at.%. The supersaturated solute atoms are expected to segregate on the surfaces of the creep-induced grain-boundary cavities and fill them progressively. As a result, the coalescence of neighboring creep cavities can be prevented or delayed.

One of the challenges in studying the healing of the creep-induced defects lies in the observation of both the creep cavities and the precipitation inside these cavities at different stages of the creep life. In previous studies

[7,16], characterisation techniques, such as scanning electron microscopy (SEM), transmission electron microscopy (TEM) and atom probe tomography (APT), provided extensive information on the microstructure including the composition of the precipitates, the orientation relation between the precipitation and the matrix and the local compositional distribution. Recently, synchrotron X-ray nano-tomography was utilized on the Fe-Au and Fe-W systems [12,13], and 3D structures of the cavities and the healing precipitates were reconstructed with a voxel size down to 25 nm. However, these techniques are either limited to 2D information (SEM and TEM) or to small 3D regions with a nanometre length scale (APT). The synchrotron X-ray nano-tomography can probe a wider range of length scales in 3D, but can only provide limited access due to the high demand. Sun and co-workers [18] provided a complimentary solution by linking the precipitation on the free creep-cavity surface during creep to the precipitation behaviour on an external surface during ageing. In contrast to a self-healing system during creep loading, where the precipitation is formed on the internal surface of a cavity, in a surface precipitation experiment [19], the solute diffuses towards the external free surface of the sample and forms surface precipitates there. These precipitates at an external surface are much easier to observe than those at internal surfaces. By comparing the growth kinetics of the precipitates formed on the external surface (from surface precipitation experiments) and on the internal surfaces (from self-healing creep experiments), it was demonstrated that the underlying physics for precipitation on the external surface and on internal surfaces is the same [18].

In the present study, the precipitation of supersaturated solutes in *bcc* iron at free surfaces for ternary Fe-3Au-4W and related binary Fe-3Au and Fe-4W alloys (all in weight percentage) is explored. The time evolution of the Au-rich and W-rich precipitates is investigated for different ageing times. This study aims to provide a complimentary method to understand and predict the precipitation behaviour and the mass transfer of supersaturated solutes. The results for the ternary Fe-Au-W alloy are compared with the binary Fe-Au and Fe-W alloys to investigate the interplay between the two healing agents in the ternary system. The Au-rich and W-rich precipitates found in the ternary Fe-Au-W system are consistent with the ones observed in the binary Fe-Au and Fe-W systems. The Au-rich precipitates formed at 700 °C show an *fcc* structure

with 60 at.% Au and 40 at.% Fe, while the formed W-rich precipitation corresponds to the hexagonal Fe_2W Laves phase.

3.2 EXPERIMENTAL

One ternary Fe-3.07Au-3.80W system and two binary systems, Fe-2.87Au and Fe-3.80W (in weight percentage) were selected for the present surface precipitation study. The Fe-based alloys were produced by Goodfellow®. Small plates with dimensions of about $10 \times 10 \times 0.5$ mm³ were cut from the as-received rolled sheet materials by spark erosion. Subsequently, the samples were sealed separately in evacuated quartz tubes filled with 200 mbar ultra-high purity argon to prevent oxidation during annealing. The annealing (8 h at 868 °C for the Fe-Au-W and Fe-Au alloys and 24 h at 900 °C for the Fe-W alloy) and the subsequent water quenching were performed to dissolve the solute elements into the single phase ferritic (*bcc*) matrix. The samples were then polished to an OPS level, ultrasonically cleaned extensively, and subsequently placed in an alumina crucible that was mounted into a horizontal quartz tube furnace (Carbolite MTF 12/38/850, UK) with an inner tube diameter of 30 mm. The temperature in the furnace tube was measured with a NiCr/NiAl (type K) thermocouple at the sample location. To avoid oxidation of the samples, a gas mixture of argon and 10 vol.% hydrogen was used to flush the furnace for about 1 h at a flow rate of 1 L/min before the samples were heated. Prior to admitting the gas mixture to the furnaces, each gas, i.e. Ar and H_2 (both with a purity better than 5N vol.%, Linde, The Netherlands), was filtered to remove any residual hydrocarbons, moisture and oxygen, with Accosorb (< 10 ppb hydrocarbons), Hydrosorb (<10 ppb H_2O) and Oxysorb (< 5 ppb O_2) filters (Messer Griesheim, Germany), respectively. To further reduce the oxygen level, the argon was passed through an inline quartz tube filter with titanium powder (100 μm, 99.5 wt% purity, TLS Technik GmbH & Co) heated to 800 °C. The flow of each gas was regulated and monitored using mass flow controllers (Bronkhorst, The Netherlands). After flushing the furnace tube, the crucible was heated and kept at 200 °C for 2 h to remove any oxygen and water adsorbed on the surfaces inside the quartz tube. After that, the samples were heated to 700 °C and held isothermally for different times. After the aging, the samples were cooled in the furnace to room temperature. Scanning electron microscopy (SEM, JEOL JSM 6500F, Japan) coupled with energy-disperse X-ray spectroscopy (EDS) was used to characterize the samples after the heat

treatment. In addition, scanning electron microscopy combined with a xenon plasma focused ion beam (Helios G4 PFIB UXe, Thermo Fisher Scientific, USA) was performed to create cross-sections to obtain information on the precipitation underneath the free surface. On small features (cf. Fig. 3g and 3h), the beam energy employed was 5 keV with an effective analysis volume of about 200 nm across.

3.3 RESULTS

The SEM images of the three alloys after ageing for different times are shown in Fig. 3.1. For all three alloys the precipitates are found both on and within the perimeter of the grain boundaries. Based on their surface location with respect to the grain boundaries, the precipitates are referred as the grain-boundary (GB) surface precipitates or grain-interior (GI) surface precipitates, respectively. For the precipitates in the Fe-Au alloy, the EDS results show a gold concentration of 40 – 60 at.%. After ageing for 8 and 32 h (Fig. 3.1d and 3.1e), the GI precipitates vary from grain to grain, in their size, shape and spatial distribution. After 32 h annealing, the GI precipitates are generally larger than their counterparts at 8 h, while after ageing for 100 h, only a limited amount of GI precipitates can be observed for the Fe-Au alloy (Fig. 3.1f), indicating that most of the Au-rich GI precipitates are collected at the grain boundaries. For the Fe-W samples, the precipitates start to form after 32 h of aging (Fig. 3.1g). By EDS it is observed that the W concentration corresponds to 20-32 at.%. The precipitates show some variation in number density for different grains, but their shapes are similar (Fig. 3.1g and 3.1h). From 32 to 100 h, the W-rich precipitates experience an obvious increase in size.

The precipitation in the ternary Fe-Au-W alloy shows more complexity. In the 8 h sample (Fig. 3.1a) only Au-rich precipitates were found. The GI precipitates in different grains show different shapes and distributions, similar to their counterparts in the Fe-Au sample. On the surface of the 32 h sample, precipitates with different compositions can be observed: the GB precipitation is generally enriched in Au, while the GI precipitates can be (1) enriched in W, (2) enriched in Au and (3) enriched in both W and Au. The W-rich precipitates are the small particles scattered within the perimeter of the grain boundaries. Similar to their counterparts in the Fe-W alloy, the W-rich GI precipitates distribute uniformly in the grains, and usually show irregular shapes with

sharp edges. However, for the 32 h samples, the W-rich GI precipitates in the Fe-Au-W ternary alloy are much smaller, compared to those in the Fe-W sample. The Au-rich and (Au/W)-rich precipitates are generally larger and show a roundish shape, which are difficult to differentiate without further compositional analysis. After ageing for 100 h, the W-rich precipitates show a branched surface precipitate structure for some of the grains (Fig. 3.1c). It is clear that there are more W-rich precipitates for some grains (e.g. grain 1) than in others (e.g. grain 2 and 3). Grain 4 in Fig. 3.1c gives an example in which some roundish Au-rich GI precipitates can be observed, while no W-rich precipitates are found.

3
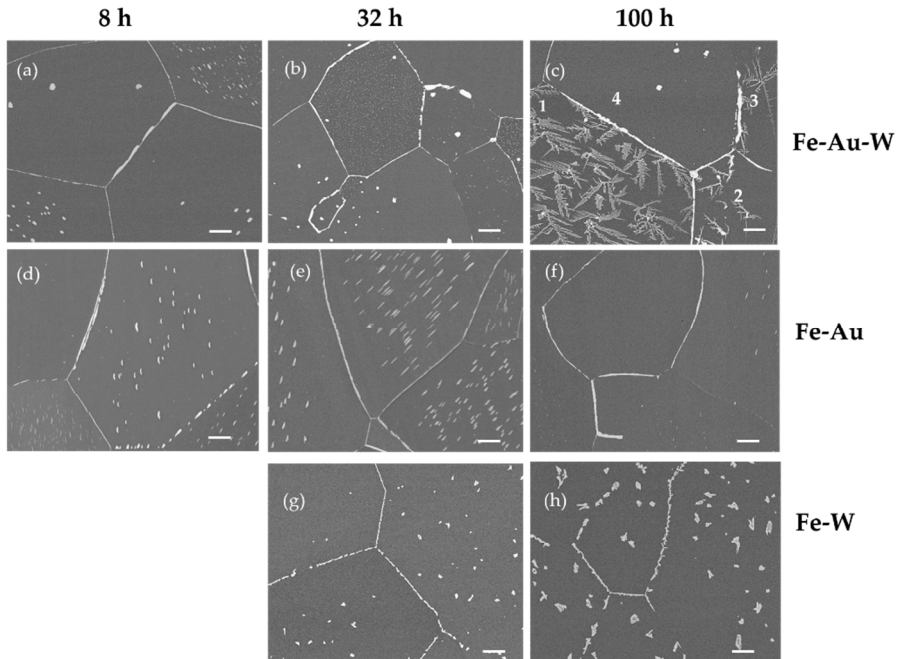
Fig. 3.1: SEM images for the Fe-Au-W, Fe-Au and Fe-W alloys after ageing for different times. (a) to (c): Fe-Au-W sample after ageing for 8, 32 and 100 h, respectively; (d) to (f): Fe-Au sample after ageing for 8, 32 and 100 h, respectively; (g) to (h): Fe-W sample after ageing for 32 and 100 h, respectively. The scale bars correspond to 10 μm.
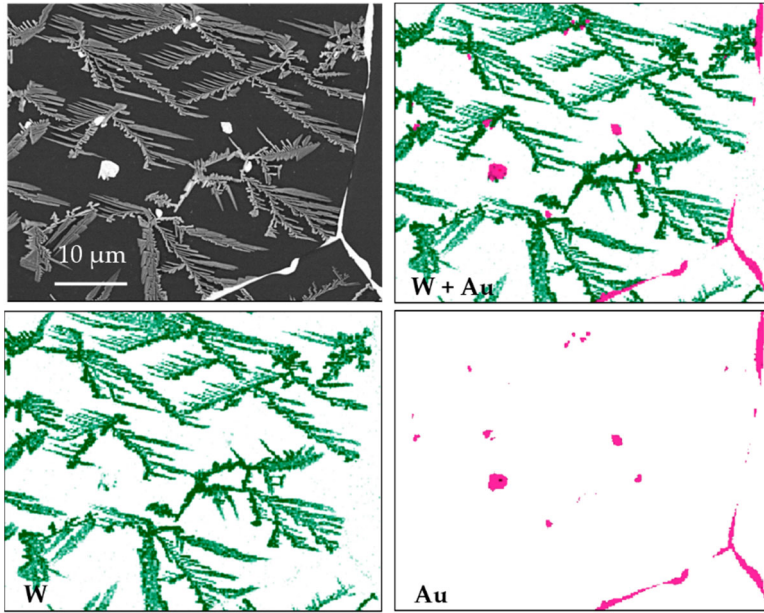
Fig. 3.2: Compositional map of the Fe-Au-W sample after ageing for 100 h.

A compositional map of the Fe-Au-W sample after ageing for 100 h is shown in Fig. 3.2. It can be observed that the grain boundaries are mainly covered by Au-rich precipitates, while the GI branched surface precipitate structures are W-rich. In the interior also Au-rich precipitates can be observed: some are isolated, and some are in contact with the W-rich patterns like snow decorating the branches. From Fig. 3.1 and 3.2, by comparing the 100 h Fe-Au-W ternary sample with its binary counterparts, two major differences can be observed: (1) in the grains covered with the branched surface precipitate structures the area fraction of the W-rich precipitates is much larger for the Fe-Au-W sample than that in the Fe-W sample and (2) in the Fe-Au alloy, the Au-rich precipitates show a strong tendency to dissolve and migrate towards the grain boundaries via the diffusion of Au atoms, leaving only small GI precipitates in the grains (Fig. 3.1f), while in the Fe-Au-W alloy, large Au-rich GI precipitates are found in the majority of the examined grains.

A closer observation of the (Au/W)-rich GI particles yields more detailed information. Fig. 3.3 shows the GI precipitates for the ternary Fe-Au-W alloy after ageing for 32 h. The roundish precipitates in Fig. 3.3a are either enriched in Au or enriched in both Au and W. A SEM image with higher

magnification is provided in Fig. 3.3b. The small precipitate at the top left corner is enriched in both Au and W, while the two larger particles show a core-shell structure. The cores of the particles are enriched in both Au and W, while the shells are enriched in Au only. It is therefore inferred that the W-rich precipitates formed first, while the Au-rich precipitation is added from below, and subsequently wrapped the previously-formed W-rich particles, eventually forming a core-shell structure. There are three types of GI precipitates in Fig. 3.3c and 3.3d: the ones enriched in Au (indicated by yellow arrows), the ones enriched in W (indicated by blue arrows) and the ones with a core-shell structure (indicated by a green arrow). In Fig. 3.3c, it is observed that the majority of the Au-rich GI precipitates are uniformly distributed, but in the vicinity of a core-shell particle, a Au depletion zone is generated. In the depletion zone, only W-rich precipitates can be observed, which indicates that the Au-rich precipitates show a higher mobility on the free surface compared to their W-rich counterparts.

3

Similar to the grain boundaries, the precipitates with a core-shell structure also act as a sink (or assembly site) for the Au-rich precipitates. This explains the difference in size distribution of the Au-rich precipitates between the ternary Fe-Au-W alloy and the binary Fe-Au alloy for long ageing times. In the Fe-Au alloy only the grain boundaries act as a sink for the Au-rich precipitates, and therefore most of the Au-rich GI precipitates are collected by the grain boundaries after 100 h of ageing. In the Fe-Au-W alloy, however, both the grain boundaries and the core-shell particles act as assembly sites for the Au-rich precipitates, and as a result some GI precipitates have survived the long-term aging in the form of core-shell particles. It is worth noting that compared to the uniformly distributed Au-rich precipitates, the precipitates attracted by the assembly sites cover a smaller area fraction. For example, the area fraction of the Au-rich precipitates in regions A_3 and A_4 in Fig. 3c is about twice as high as in regions A_1 and A_2. This strongly suggests that the precipitates thicken during the coarsening. Fig. 3.3e – 3.3h may correspond to the early stage of the core-shell structure formation. In Fig. 3.3g, it is observed that Au-rich precipitates form from both sides of a previously-formed W-rich precipitate, resulting in a sandwich-like structure. This observation of side-by-side formation is consistent with the results from creep-failed samples [17], where Au-rich and W-rich precipitated are found to be present in contact with each other (without forming a compound).
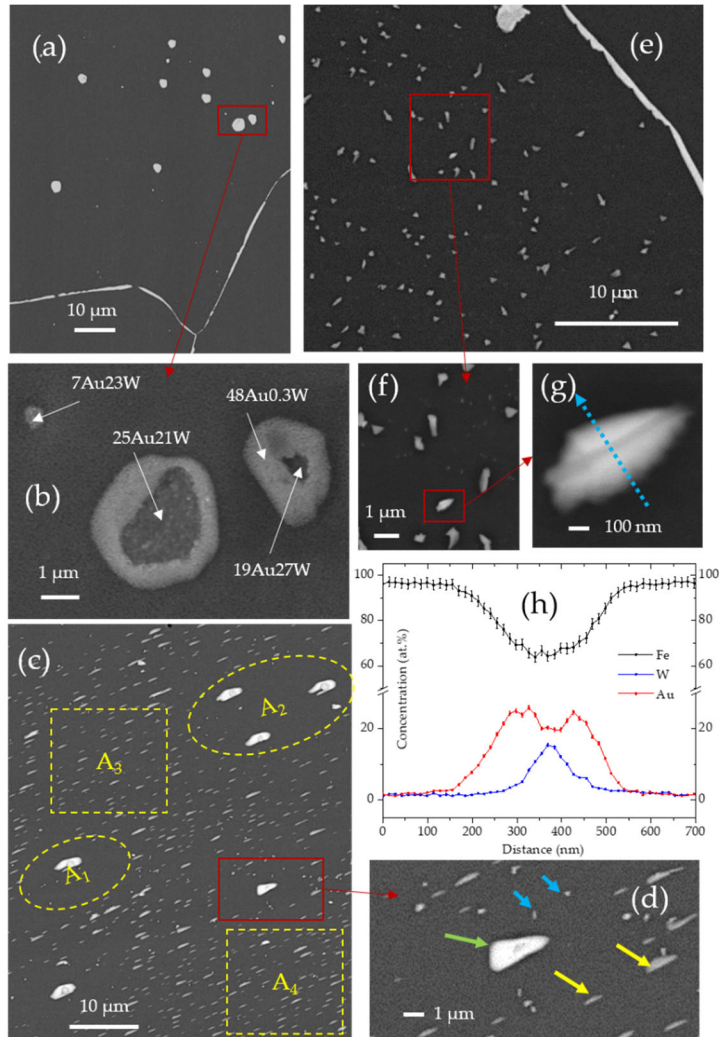
Fig. 3.3: SEM images for the Fe-Au-W sample after ageing for 32 h. (a-b): Morphology and structure of the (Au/W)-rich GI precipitates; (c-d): Effect of the (Au/W)-rich precipitates on the distribution of the Au-rich GI precipitates. (e-g): Au-rich and W-rich GI precipitates form in contact to each other, yielding a sandwich structure; (h) Compositional scan along the line in (g).

It is worth to note that a core-shell structure was also observed in [19], however, different mechanisms account for the structures in the two studies. In reference [19], the core-shell structure was due to the temperature change during cooling and the associated changes in the equilibrium Ge concentration, while in the current study, the core-shell structure results from the Au

diffusion towards the pre-existing W-rich particles, which act as nucleation sites.

To investigate how far the precipitates extend below the surface into the matrix, a plasma focused ion beam (PFIB) was used to further investigate the Fe-Au-W alloy after 100 h of aging, as shown in Fig. 3.4. As indicated in Fig. 3.4a, three cross-sectional slits were generated containing the W-rich precipitates (Fig. 3.4b and 3.4c) and the Au-rich grain boundary (Fig. 3.4d). W-rich precipitates form on the free surface, with an average thickness of about 74 nm (Fig. 3.4b and 3.4c). The matrix precipitates (indicated by the yellow arrows) are Au-rich precipitates. Our previous research [6,7] revealed that these precipitates have a disc-shaped geometry and are generally connected to dislocations. In Fig. 3.4d, a valley filled with Au-rich precipitation along the grain boundary can be observed, with a width of about 1.4 μm and a depth of about 0.9 μm. Au-rich precipitation is also observed on the grain boundary underneath the free surface, suggesting that Au transport primarily proceeds via (1) diffusion along the grain boundaries underneath the surface and (2) surface diffusion. The diffusion paths of the Au atoms are indicated by the green arrows in Fig. 3.4d. It is worth noting that W-rich precipitates are also observed on the Au-covered grain boundary (indicated by a blue arrow in Fig. 3.4d and 3.4e), indicating a segregation tendency of W solutes towards the grain boundaries. However, the solute Au shows a much stronger segregation tendency towards the grain boundaries compared to solute W.

To our knowledge, the Fe-Au-W ternary phase diagram has not yet been measured or calculated. However, given the immiscibility and the positive formation energy for the Au-W system [20, 21], and the fact that the Au-rich and W-rich precipitates form independently instead of forming a compound [17], the phases of the Au-rich and W-rich precipitates were estimated on the basis of the binary phase diagrams for Fe-Au and Fe-W systems, respectively. According to the binary phase diagrams, the Au-rich precipitates should show *fcc* structure with 60 at.% Au and 40 at.% Fe at 700 °C, while the W-rich precipitates should correspond to the Fe_2W Laves phase with a hexagonal structure. The phases of the precipitates were determined by EBSD as shown in Fig. 3.5. The red and blue colours correspond to the *fcc* Au phase and the hexagonal Fe_2W Laves phase, respectively. In the current research, the Au-rich precipitates show a Au concentration of 40 - 60 at.%, while the W-rich

precipitates show a W concentration of 20 - 32 at.%, which is consistent with the expected composition within the accuracy of the EDS. The particles enriched in both Au and W (see Fig. 3.3(b), a particle has 7 at.% Au and 23 at.% W) correspond to a situation where the Au-rich and W-rich precipitates are formed in contact to each other (instead of forming a ternary compound), but due to the spatial resolution limitation of EDS, we cannot separate them.
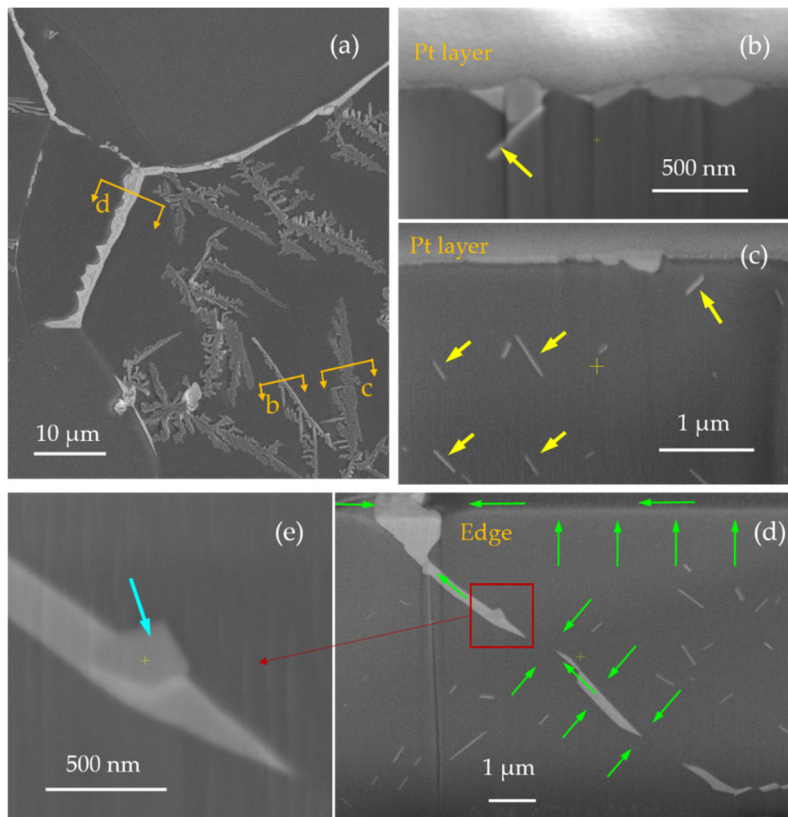
Fig. 3.4: PFIB-SEM results for the Fe-Au-W alloy after ageing for 100 h. (a): The three locations where PFIB was performed; (b) and (c): The cross-section of W-rich precipitates; (d) and (e): the cross-section of an Au-rich grain boundary. The yellow arrows, blue arrow and green arrows indicate the Au-rich matrix precipitates, W-rich precipitate segregated on a grain boundary and the diffusion paths of Au, respectively.
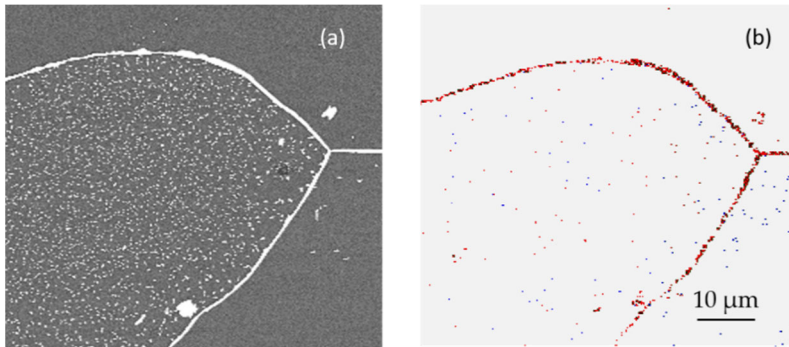
Fig. 3.5: Backscattered electron image (a) and EBSD phase map (b) for a Fe-Au-W sample after 32 h of ageing. The red corresponds to the *fcc* Au phase, while the blue corresponds to the hexagonal Fe_2W Laves phase.

To quantify the precipitation in the three alloys, and thus compare the precipitates in the ternary alloy with its binary counterparts, in Fig. 3.6 the equivalent diameter (for the GI precipitates) and the area fraction (for the sum of the GI and GB precipitates) are presented for the three alloys as a function of the ageing time. For each sample, 7 to 15 grains were analysed, and the average value and the scatter is shown. The Au-rich and W-rich precipitates are presented separately for clarity. The results of Fig. 3.6a indicate that: (1) the equivalent diameter of the GI precipitates increases up to about 32 h for both the Fe-Au-W and Fe-Au alloys. However, from 32 to 100 h, the size of the GI precipitates in the Fe-Au-W alloy remains about constant, while in the Fe-Au alloy the GI precipitates show a significant decrease in size. (2) the area fraction of the GI precipitates for the Fe-Au alloy increases slightly from 8 to 32 h before it decreases significantly from 32 to 100 h, indicating a significant Au diffusion towards the grain boundaries. For the Fe-Au-W alloy the area fraction peaks at 8 h before it decreases gradually from 8 to 100 h. The decrease in area fraction occurs earlier in the Fe-Au-W ternary alloy, because there are more assembly sites (the precipitates with the core-shell structure) for the Au-rich GI precipitates. With the diffusion of Au, some Au-rich precipitates grow at the expense of the others dissolving, resulting in a smaller area fraction. (3) the grain boundaries of the Fe-Au alloy collect more Au-rich GI precipitates compared to the ternary Fe-Au-W counterpart, as can be seen from the area fraction of the GB precipitates. This is consistent with the results in Fig. 1: in the Fe-Au alloy most of the Au-rich GI precipitates are collected by the grain

boundaries after 100 h aging, while in the ternary Fe-Au-W system the particles with a core-shell structure provide extra assembly sites for the Au-rich GI precipitates.
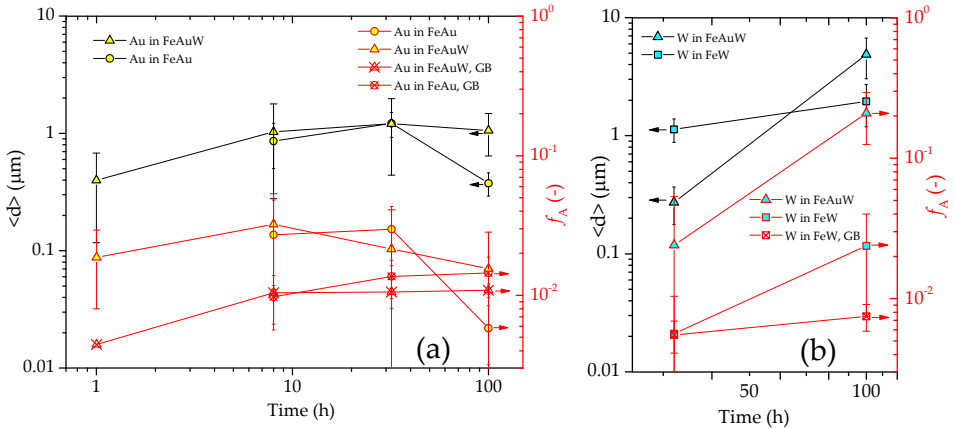
Fig. 3.6: Equivalent diameter of the GI precipitates and area fraction of both the GB and GI precipitates for (a) the Au-rich precipitation in Fe-Au-W and Fe-Au alloys and (b) the W-rich precipitation in Fe-Au-W and Fe-W alloys for different ageing times.

The size and the area fraction of the W-rich precipitates in Fe-Au-W and Fe-W alloys are compared in Fig. 3.6b. Unlike the fast size evolution of the Au-rich GI precipitates that results in a maximum size around 32 h, the W-rich GI precipitates are still growing from 32 to 100 h. The W-rich GI particles are smaller in size in the Fe-Au-W alloy at 32 h, but the smaller particles show a larger area fraction compared to their counterparts in the Fe-W alloy. During the whole ageing process, the area fraction of the W-rich precipitates in the ternary Fe-Au-W alloy is 5-10 times larger than that in the binary Fe-W alloy. It is also worth noting that from 32 to 100 h, the area fraction of the GI precipitates in the Fe-W alloy increased by 5 times, while the area fraction of the GB precipitates remains at a relative constant level. This indicates that the surface diffusion of W is much slower than that of Au, so that the Au-rich GI precipitates on the surface show an obvious tendency to migrate towards the grain boundaries (and to the core-shell structures) via the Au atom diffusion, while the W-rich precipitates tend to be immobile once formed on the surface.

As indicated in Fig. 3.6b, the Au segregation clearly enhances the precipitation kinetics of the W-rich Fe_2W Laves phase on the surface. This is

expected to be caused by the enhanced W diffusion in the matrix and an enhanced nucleation in the ternary Fe-Au-W alloy, as the solute Au depleted diffusion layer below the surface shows a significant shrinkage. From Fig. 3.6b, it is clear that at 100 h the surface fraction for the Fe_2W precipitates in the ternary Fe-Au-W alloy ($f_A \approx 21\%$) is one order of magnitude larger compared to that in the binary Fe-W alloy ($f_A \approx 2\%$). This indicates a much slower kinetics. In fact, the value of the surface fraction f_A observed for the binary Fe-W alloy at 100 h is of the same order as the surface fraction f_A for the ternary Fe-Au-W alloy at 32 h ($f_A \approx 2\%$). As shown in Fig. 3.1, for the ternary Fe-Au-W alloy at 32 h also no branched structure was observed, consistent with the observation for the binary Fe-W alloy at 100 h. It is therefore expected that the branched structure in the binary Fe-W alloy is only formed for a larger surface fraction f_A, which is expected to be reached for significantly longer times (about 400 h). The origin for the transition in morphology from roundish to branched surface precipitates has not been established, but is expected to be related to an anisotropy in growth rate with respect to orientation. As the hexagonal Fe_2W Laves phase has a significantly lower symmetry than the *bcc* Fe-based matrix the most favourable growth conditions are expected for specific orientation relations between the precipitate and the matrix (for which the interfacial strain is minimised). In TEM studies on bulk Fe-Cr-Co-W steels three different orientation relations (OR1: $[10\bar{1}]_\alpha \parallel [\bar{1}2\bar{1}1]_L$, $(111)_\alpha \parallel (\bar{1}10\bar{3})_L$, $(011)_\alpha \parallel (0001)_L$; OR2: $[\bar{1}\bar{1}3]_\alpha \parallel [2\bar{1}\bar{1}0]_L$, $(1\bar{1}0)_\alpha \parallel (01\bar{1}3)_L$, $(4\bar{1}1)_\alpha \parallel (0001)_L$; and OR3: $[011]_\alpha \parallel [2\bar{1}\bar{1}0]_L$, $(100)_\alpha \parallel (02\bar{2}\bar{3})_L$, $(\bar{1}1\bar{1})_\alpha \parallel (0001)_L$) have been identified for the hexagonal Fe_2W Laves phase (L) precipitates and the α-Fe matrix (α) [22]. These orientations relations are expected to also govern the branching growth behaviour of the Fe_2W surface precipitates on the *bcc* Fe matrix.

3.4. DISCUSSION

3.4.1 THE EVOLUTION OF THE SIZE AND SITE DENSITY OF GRAIN-INTERIOR PRECIPITATES
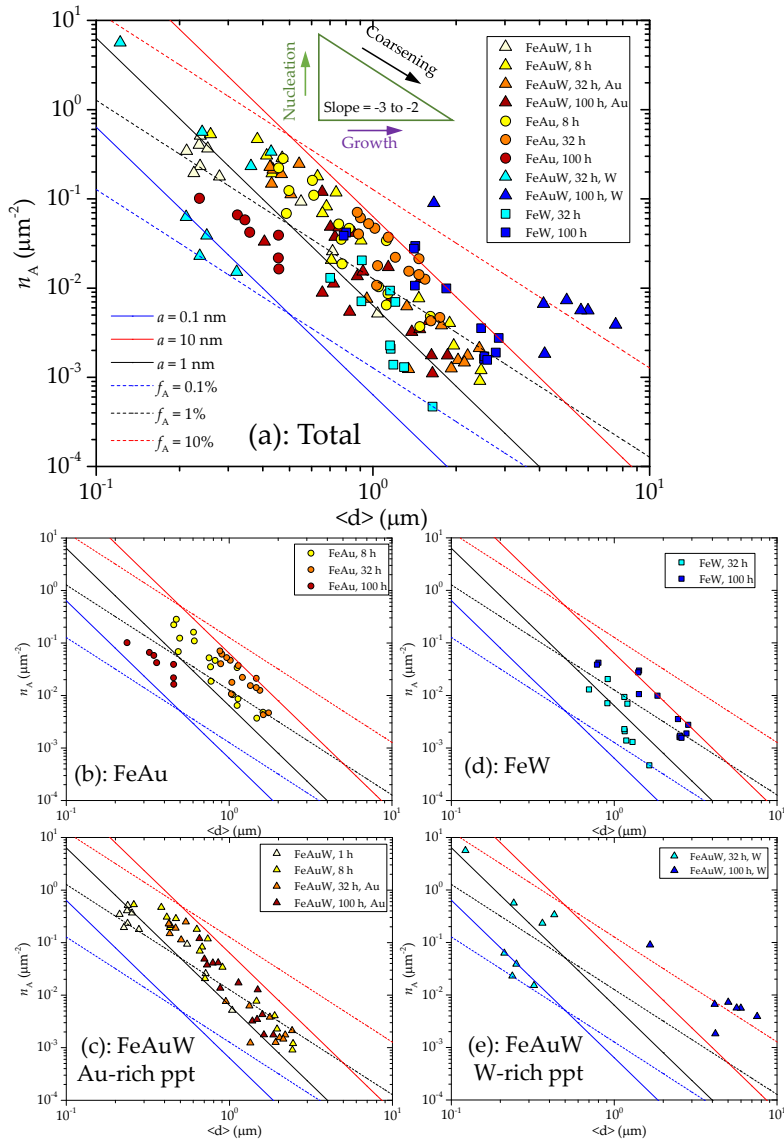
Fig. 3.7: Map of the number density n_A versus the average size $\langle d \rangle$ of the GI precipitates in each grain of the three alloys after different aging times. (a) Summary all the data. (b-e) Individual maps for: (b) Au-rich precipitates in the Fe-Au alloy, (c) Au-rich precipitates in the Fe-Au-W alloy, (d) W-rich precipitates in the Fe-W alloy and (e) W-rich precipitates in the Fe-Au-W alloy, respectively. The dashed straight lines correspond to $n_A \propto \langle d \rangle^{-2}$ scaling behaviour (constant thickness) and the solid lines to $n_A \propto \langle d \rangle^{-3}$ scaling behaviour (shape conservation).

The size and distribution of the GI precipitates in every analysed grain are provided in Fig. 3.7. Each data point corresponds to the information from a

single grain. The Au-rich and W-rich precipitates in the Fe-Au-W alloy are considered separately. Since it is difficult to classify the Au-rich and (Au/W)-rich particles unambiguously just by their shape, the roundish particles with a core-shell structure (Fig. 3.3b) are regarded as Au-rich precipitates. Assuming that the ratio between the GB precipitation and the GI precipitation is constant in each grain after a fixed annealing time, then the total amount of the GI precipitates per unit area is the same for each grain. If all precipitates have a constant thickness, then the area fraction of precipitates shows a scaling relation $n_A \propto \langle d \rangle^m$ with a slope of m = -2. If the precipitates are shape-conserved, then the particles grow in three directions and their thickness is proportional to the corresponding equivalent diameter, resulting a scaling relation $n_A \propto \langle d \rangle^m$ with a slope of m = -3.

For a grain area S_G, a number of precipitates N, and a particle average diameter $\langle d \rangle$, the number density n_A and the area fraction f_A of the GI precipitates correspond to $n_A = N / S_G$ and $f_A = N(\pi/4)\langle d^2 \rangle/S_G \approx n\,(\pi/4)\langle d \rangle^2/S_G = (\pi/4)\langle d \rangle^2 n_A$. The dashed lines in Fig. 3.7 with a slope of m = -2 correspond to 0.1%, 1% and 10% area fraction contours, respectively. Assuming an average GI precipitate height $\langle h \rangle$ that is proportional to its equivalent diameter $\langle d \rangle$ with a scaling factor A, then the total volume V_G of the GI precipitates per unit area S_G (the equivalent thickness of the precipitation layer on the surface if the precipitates spread over the sample surface, covering it uniformly) corresponds to $a = V_G/S_G \approx (NA\langle d \rangle^3)/(N/n_A) = A\langle d \rangle^3 n_A$. The scaling factor A depends on the GI precipitate shape. The solid lines in Fig. 3.7 with a slope of m = -3 correspond to an equivalent thickness of 0.1, 1 and 10 nm, respectively (A = $\pi/20$, for a cylinder-shaped particle with a height of $0.2\langle d \rangle$ [18]).

As indicated in the schematic diagram inserted Fig. 3.7a, it is easy to determine whether the GI precipitates are in the stage of nucleation, growth, coarsening or a combination. For instance, if the precipitates experienced an increase in number density without a change in their size (as indicated by the upward pointing green arrow), then the particles are in the nucleation stage. If the number density keeps constant and the size increases, then the precipitates are growing (indicated by the right pointing purple arrow). A constant area fraction (or equivalent thickness) with an increase in size and a decrease in

number density corresponds to a coarsening process (indicated by the black arrow).

The size and distribution of the GI Au-rich precipitates for the Fe-Au alloy after ageing for 8, 32 and 100 h, respectively, are shown in Fig. 3.7b. By comparing the 8 and 32 h data, it is clear that the collection of the data points shifted towards the right bottom direction, indicating a typical coarsening process. From 32 to 100 h, the number density of the precipitates remains around the same level, yet the average size and the corresponding area fraction and equivalent thickness decreased significantly, resulting from the diffusion of the Au solute towards the grain boundaries. For all the three ageing times, the data points closely follow a $n_A \propto \langle d \rangle^m$ scaling with a slope m of -3.2(3) at 8 h, -3.1(6) at 32 h and -2.3(5) at 100 h. It is therefore indicated that for shorter ageing times ($\leq$ 32 h), the GI precipitates in the Fe-Au system are likely to be shape-conserved, while after ageing for 100 h, the thickness of the precipitates seems to approach a constant value.

The characteristics of the Au-rich GI precipitates in the Fe-Au-W alloy are shown in Fig. 3.7c. At an ageing time of 1 h, most of the precipitates have an equivalent diameter smaller than 0.3 μm, but the equivalent diameter of the largest precipitate already exceeded 1 μm, indicating that growth had occurred in some grains. From 1 to 8 h, the precipitates experience an obvious growth, and the precipitate area fraction and equivalent thickness are similar in all the grains (also similar to the Fe-Au counterpart). The precipitation behaviour in the Fe-Au-W alloy after ageing for 32 and 100 h is very different from the observation in the Fe-Au alloy. Firstly, the precipitate size and number density show a wider distribution. In addition, the decrease in area fraction and equivalent thickness only occurred in limited number of grains. This is consistent with the observation in Fig. 1d, where several large GI particles remained after 100 h of ageing (probably in the form of a core-shell structure). From 1 to 100 h the data points follow a $n_A \propto \langle d \rangle^m$ scaling with a slope m of -2.4(3) at 1 h, -3.0(2) at 8 h, -3.2(2) at 32 h and -2.5(5) at 100 h of aging. This indicates that the precipitation behaviour of the Au-rich is similar for the Fe-Au-W and the Fe-Au alloys.

As shown in Fig. 3.7d, for the W-rich precipitates in the Fe-W alloy, from 32 to 100 h, the GI precipitates increase both in size and number density with aging time, indicating a combined nucleation and growth process. For the Fe-

3

Au-W alloy shown in Fig. 3.7e most of the W-rich precipitates after 32 h ageing have the diameter between 0.2 to 0.4 µm, while their number densities vary by nearly two orders of magnitude. This indicates that the W-rich precipitates are in the nucleation stage. The data points for the Fe-W alloy follow a $n_A \propto \langle d \rangle^m$ scaling with a slope m of -4(1) at 32 h and -2.6(3) at 100 h. Compared to the binary Fe-W alloy, the W-rich precipitates in the ternary Fe-Au-W alloy are much smaller in size (for 32 h of aging), but their area fraction is either similar to or nearly one order of magnitude larger than the precipitate area fraction in the Fe-W system. This is consistent with the W-rich precipitation behaviour in the creep-failed samples [17]: the W-rich particles are smaller in the Fe-Au-W alloy than in the Fe-W alloy, but the total amount of the W-rich precipitates is not suppressed. On the contrary, the W-rich precipitation in the Fe-Au-W alloy seems to be accelerated after long-time ageing: for the 100 h samples, the W-rich precipitates show an average area fraction of about 21% with an average height of about 74 nm (see Fig. 3.4), yielding an equivalent thickness of about 15 nm. Both the area fraction and the equivalent thickness in the Fe-Au-W alloy are much larger than that for the Fe-W alloy. Compared to the Au-rich precipitates, the W-rich precipitates show different growth mechanism: after 100 h of ageing, the W-rich precipitates in the Fe-Au-W sample follow a $n_A \propto \langle d \rangle^m$ scaling with a slope m of -2.1(6), indicating that the W-rich precipitates are plate-shaped with a relatively constant thickness. Two examples are provided in Fig. 3.8, where the W-rich precipitates with different in sizes and number densities in the two grains yield similar area fractions. The lateral growth of the branched surface precipitates stops when the branches are about to make contact. Since the individual branched surface precipitates are sometimes difficult to distinguish (indicated in Fig. 3.8(a)), in the grains where they are formed, the number density of the precipitates may have been underestimated and the equivalent size overestimated.
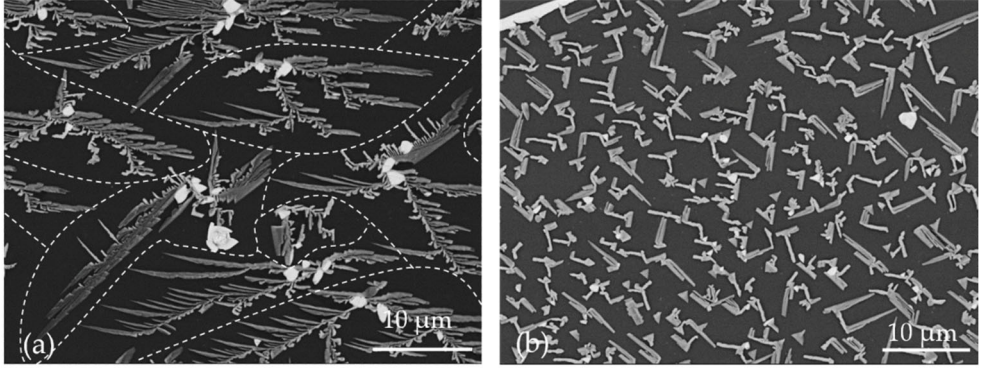
Fig. 3.8: Two examples of W-rich GI precipitates in the Fe-Au-W alloy for an ageing time of 100 h. The equivalent sizes (5.0 and 1.7 µm in (a) and (b), respectively) and number densities of the W-rich precipitates (0.0073 and 0.0900 µm^{-2} in (a) and (b), respectively) are obviously different in the two grains, while the area fractions are similar (22 and 24 % in (a) and (b), respectively). The dashed lines in (a) show the partitions of precipitates.

3.4.2 THE EVOLUTION OF THE EQUIVALENT THICKNESS OF THE GRAIN-INTERIOR PRECIPITATES

The number density n_A and equivalent diameter $<d>$ show for most of the GI precipitates a $n_A \propto \langle d \rangle^m$ scaling with a slope m of about -3, indicating a 3D shape conserving growth and coarsening (see Fig. 3.7). It is therefore easy to obtain the equivalent thickness attributed by the GI precipitates by fitting the data in Fig. 3.7 with a fixed slope of $m = -3$ (assuming $A = \pi/20$).

$$a \approx A\langle d \rangle^3 n_A \qquad (3.1)$$

For the W-rich precipitates in the Fe-Au-W alloy after 100 h of ageing, fitting by Eq. (3.1) yields an equivalent thickness of 102 nm. Since the branched surface precipitates seem to have a constant thickness (as discussed in section 3.4.1), the equivalent layer thickness of the W-rich precipitates is estimated by $a_W \approx hf_A$. After 100 h of ageing the average height of the W-rich precipitates corresponds to $h = 74$ nm.

The surface precipitation of the solutes can be simplified into a 1D diffusion process, where the solute agents diffuse towards the free surface, and after reaching the surface they nucleate to form precipitates. The 1D flux and the equivalent thickness of the precipitation layer are estimated by [23]:

$$J_X = \frac{D_X \Delta x}{\Omega} \left(\frac{1}{\sqrt{\pi D_X t}} \right) = \frac{\Delta x}{\Omega} \sqrt{\frac{D_X}{\pi t}} \tag{3.2}$$

And

$$a(t) = \frac{\Omega}{x_p} \int_0^t J_X(a, t') dt' = \frac{\Delta x}{x_p} \sqrt{\frac{4 D_X t}{\pi}} \tag{3.3}$$

Where $\Delta x = x_\infty - x_1$ is the supersaturation of the solute element X, D_X is the diffusivity of the solute element in the matrix phase, Ω is the atomic volume, t is the time and x_p is the concentration of the solute element in the precipitate phase.

The experimental results estimated by Equation (4.1) and the results calculated by Equations (3.2) and (3.3) are compared in Fig. 3.9. The Au-rich GI precipitates show a similar trend in the ternary Fe-Au-W alloy as in the binary Fe-Au alloy. In the early stage (before 32 h for the Fe-Au sample and 8 h for the Fe-Au-W system), the thickness of the Au-rich GI precipitates shows an increase $a \propto t^\alpha$ with a slope α of approximately 0.5, indicating a diffusion-controlled process. For the W-rich precipitates, the corresponding slope α is much larger than 1/2, indicating that the W-rich precipitates are still in the nucleation stage. Compared to the W-rich GI particles in the binary Fe-W alloy, the precipitates in the ternary Fe-Au-W alloy starts with a smaller size and a higher number density n_A, yielding a lower equivalent thickness. After ageing for 100 h, however, the thickness of the W-rich precipitation in the Fe-Au-W system exceeded that in the Fe-W system by nearly three times, indicating that the W diffusion in the Fe-Au-W system is accelerated for longer ageing times. The acceleration phenomenon may result from the depletion of supersaturated Au solute. At 700 °C, the diffusivity of Au is two orders of magnitude higher than that of W, so that the depletion of Au is much faster. With the diffusion of Au towards the surface, a shrinkage is generated in the Au-depleted matrix, due to the size difference between the Au and Fe atoms. The resulting elastic tensile strain field may cause an enhanced diffusion of W [24].
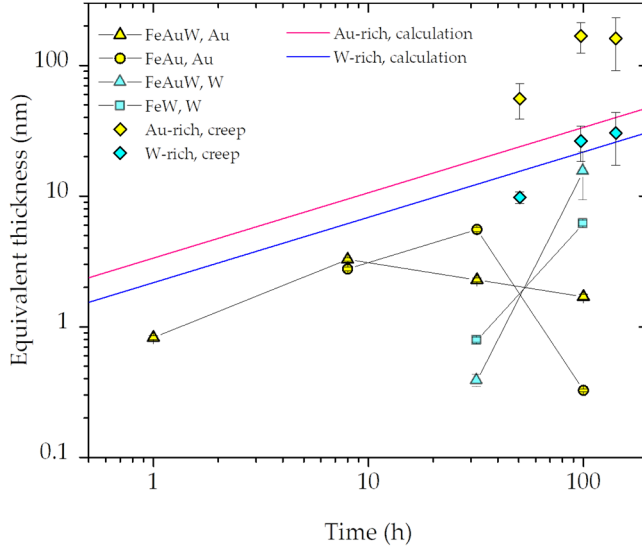
Fig. 3.9: (a): Equivalent thickness of the GI precipitation layer a for the three alloys as a function of ageing time t. The solid lines are calculated by $a(t) = (2/\sqrt{\pi})(\Delta x/x_p)\sqrt{D_X t}$, where Δx is the supersaturated solute fraction, x_p the solute fraction in the precipitate and D_X the solute (volume) diffusivity of element X. The experimental data are obtained from Fig. 3.7 assuming $n_A \propto \langle d \rangle^{-3}$. The scattered data points are creep results from a previous research on Fe-Au-W system [17].

The scattered data on the right top corner corresponds to the equivalent thickness of the particles from the creep experiment [17]. The creep experiments were performed at 550 °C. For comparison the data in Fig. 3.9 were normalised using Equation (3), i.e. by applying a scaling factor $a^{T_1}/a^{T_2} = \left(x_p^{T_2}\Delta x^{T_1}\sqrt{D_X^{T_1}}\right)\Big/\left(x_p^{T_1}\Delta x^{T_2}\sqrt{D_X^{T_2}}\right)$. It is clear that the equivalent thicknesses of both the Au-rich and W-rich precipitates are systematically higher under the creep conditions. Two reasons are expected to be responsible for the difference: (1) During creep a significant amount of excess vacancies and dislocations are generated by the deformation [25,26], which enhances the diffusion of the solutes. (2) for surface precipitation only a fraction of the solutes diffuses towards the grain-interior free surface directly, as the rest of the solutes are attracted by the nearby grain boundaries, through which the solutes can reach the free surface (indirect route with different diffusion rates). Assuming the solutes choose the shortest diffusion path (to either the nearest grain boundary or the nearest free surface), then GI precipitates would no

longer form after the diffusion length reaches half of the grain size. For average grain sizes of 84 μm (Fe-Au sample) and 105 μm (Fe-Au-W sample), the newly-nucleated Au-rich GI precipitates are not expected to form any longer after about 500 h and 800 h ageing, respectively.

3.4.3 LINKING THE SURFACE PRECIPITATION TO THE CREEP CAVITY PRECIPITATION

The external free surface precipitation bears great resemblance to the formation of precipitates on the surface of the internal creep cavities as formed in creep experiments. In a previous study on the Fe-Au system [18], the growth rate of the Au-rich precipitates on the external free surface was found to be comparable to that on the internal free surface of a creep-induced cavity. By comparing the present study with the creep results for the Fe-Au-W alloy [17], similarities are observed in terms of the size and distribution of the precipitates and the interplay between the two solutes. In the Fe-Au-W alloy, the Au-rich and W-rich precipitates are found to form in contact to each other, yielding a sandwich-like structure, for surface conditions (present work) and for creep conditions (ref. [17]). In the Fe-Au-W alloy and the Fe-Au alloy, the evolution of the Au-rich GI precipitates (the ones not connected to grain boundaries) is similar, indicating that the addition of W does not seem to have a strong influence on the kinetics of solute Au. Similar results were obtained under the creep conditions, where the size evolution of the Au-rich precipitates is comparable in the Fe-Au-W alloy [17] and the Fe-Au alloy [13]. The precipitation behavior of the W-rich GI precipitates is however significantly different in the Fe-Au-W alloy compared to the Fe-W alloy. In the present research, it is observed that the W-rich GI precipitates in the Fe-Au-W alloy start with a smaller size and larger number density, but the overall diffusion flux is not reduced for longer ageing times. The creep experiments show similar results: the W-rich precipitates formed in the creep-induced cavities show smaller sizes and a higher number density in the Fe-Au-W alloy [17] compared to the Fe-W alloy [12], indicating that more nucleation sites are available for W-rich precipitation in the Fe-Au-W alloy (both under surface and creep conditions). One explanation may be the increased roughness that is generated with the depletion of the supersaturated Au solute from the underlying matrix. As discussed in section 3.2, the continuous depletion of Au results in a shrinkage of the matrix and strains resulting from local gradients in the solute Au concentration, which further leads to a re-organisation of the surface atoms

into terraces (examples are shown in Fig. 3.10). Therefore, more nucleation sites are available for the W-rich precipitates in the ternary system, which causes a higher nucleation rate together with the enhanced diffusivity. An estimation of the healing kinetics in [17] also indicated that the W diffusion is not suppressed in the relevant creep cavities.

3
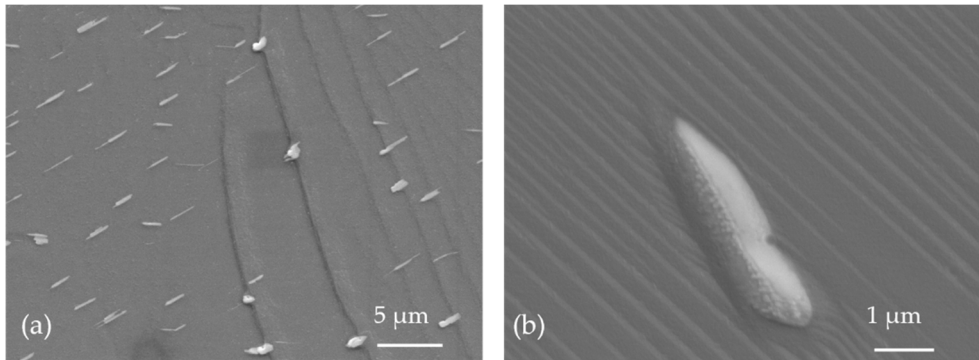
Fig. 3.10: Terraces generated after the nucleation of Au-rich GI precipitates on the surfaces of (a) Fe-Au and (b) Fe-Au-W alloy samples.

One difference between the surface precipitation and the creep-cavity precipitation is the shape of the precipitates. Under surface conditions, the aspect ratio of the Au-rich GI precipitates varies from 1.2 (nearly round) to about 12, while for the Fe-Au-W alloy the W-rich GI precipitates develop into branched surface precipitates after long ageing. However, under creep conditions the shapes of both the Au-rich and W-rich precipitates are constrained by the shape of the creep cavity, so that the Au-rich precipitates with a high aspect ratio and the W-rich branched surface precipitates are not likely to form.

Another difference between the two conditions is the diffusivity of the solutes. As indicated in Fig. 3.9 and discussed in Section 3.4.2, the diffusion of both Au and W solutes are enhanced under the creep condition, due to the deformation-induced excess vacancies and dislocations. The overall deformation-enhanced diffusivity of element X (either solute or host) corresponds to [25,26]:

$$D_X = (1-g)D_X^V + gD_X^P = (1-g)D_X^l\left(1 + x_V^{ex}/x_V^{th}\right) + gD_X^P \qquad (3.5)$$

in which D_X^l is the lattice diffusivity, D_X^V is the solute diffusivity induced by the vacancies, D_X^P is the dislocation-induced pipe diffusivity, x_V^{ex} is the concentration of the excess vacancies, x_V^{th} is the concentration of the vacancies under thermal equilibrium condition, and the factor g corresponds to the fraction of atoms associated with the pipe. Since the production rate of the excess vacancies is proportional to the strain rate, at the strain rates as low as $(2\text{-}7) \times 10^{-5}$ h^{-1} [17], the pipe diffusion is mainly responsible for the diffusion enhancement and Equation (3.5) can be simplified to $D_X = gD_X^P$. At 823 K (550 °C), the Fe self-diffusivity in *bcc* iron is 1.5×10^{-21} m^{2}s^{-1}, while the self-diffusivity along dislocations corresponds to about 10^{-15} m^{2}s^{-1} [27]. For self-diffusion, assuming $g = \pi b^2 \rho$, in which b and ρ are the burger's vector and the dislocation density, and taken as 2.58 Å and 10^{14} m^{-2}, respectively. The enhanced diffusivity is then estimated to be about 28 times larger than the lattice diffusivity, resulting in an equivalent thickness of about 5 times bigger than under surface conditions. For higher strain rates (e.g. for the Fe-Au [13,7] and Fe-W [12] systems) where the diffusion through the excess vacancies can no longer be neglected, a stronger enhancement in diffusivity may be expected.

3.5 CONCLUSIONS

The precipitation of supersaturated solutes at free surfaces was studied in a ternary Fe-3Au-4W alloy and two binary Fe-3Au and Fe-4W counterpart alloys. The surface precipitation can be categorised into GI precipitates (not connected to grain boundaries) or GB precipitates. The Au-rich GI precipitates show a 3D shape-conserving growth before they are collected by the grain boundaries, while the W-rich Laves phase precipitates, which are relatively immobile once nucleated on the surface, are found to grow laterally with a relative constant thickness. The Au-rich GI precipitates are similar in terms of their size and kinetics to those for the ternary Fe-Au-W and binary Fe-Au systems. However, the W-rich GI precipitates in the Fe-Au-W system show a smaller starting size, a higher number density and an overall faster kinetics compared to the binary Fe-W system. While the precipitation on the free surface showed an overall slower diffusivity than during creep conditions, the surface precipitation experiments can qualitatively predict the healing of the creep-induced grain boundary cavities in terms of the interplay between

multiple solutes in the matrix and the resulting solute diffusivities, precipitate nucleation rates and the precipitate size distributions.

REFERENCES

[1] S. van der Zwaag, Self Healing Materials: An Alternative Approach to 20 Centuries of Materials Science, Springer Netherlands 2007.

[2] M.D. Hager, P. Greil, C. Leyens, S. van der Zwaag, U.S. Schubert, Self-healing materials, Adv Mater 22(47) (2010) 5424-30.

[3] N.H. Van Dijk, S. van der Zwaag, Self-Healing Phenomena in Metals, Advanced Materials Interfaces 5(17) (2018) 1800226.

[4] K. Laha, J. Kyono, S. Kishimoto, N. Shinya, Beneficial effect of B segregation on creep cavitation in a type 347 austenitic stainless steel, Scr. Mater. 52(7) (2005) 675-678.

[5] R.N. Lumley, A.J. Morton, I.J. Polmear, Enhanced creep performance in an Al-Cu-Mg-Ag alloy through underageing, Acta Mater. 50 (2002) 3597-3608.

[6] S. Zhang, C. Kwakernaak, W. Sloof, E. Brück, S. van der Zwaag, N. van Dijk, Self Healing of Creep Damage by Gold Precipitation in Iron Alloys, Adv. Eng. Mater. 17(5) (2015) 598-603.

[7] S. Zhang, C. Kwakernaak, F.D. Tichelaar, W.G. Sloof, M. Kuzmina, M. Herbig, D. Raabe, E. Brück, S. van der Zwaag, N.H. van Dijk, Autonomous Repair Mechanism of Creep Damage in Fe-Au and Fe-Au-B-N Alloys, Metall. Mater. Trans. A 46(12) (2015) 5656-5670.

[8] R.N. Lumley, I.J. Polmear, Advances in self healing of metals, Proceedings of the First International Conference on Self Healing Materials, Noordwijk aan Zee, Netherlands, 2007.

[9] N. Shinya, Self-Healing of Metallic Materials: Self-Healing of Creep Cavity and Fatigue Cavity/Crack, in: S.K. Ghosh (Ed.), Self-Healing Materials: Fundamentals, Design Stragegies, and Applications, Wiley - VCH Verlag GmbH & Co. KGaA2008, pp. 219-250.

3

[10] S. Zhang, J. Cizek, Z. Yao, M. Oleksandr, X. Kong, C. Liu, N. van Dijk, S. van der Zwaag, Self healing of radiation-induced damage in Fe–Au and Fe–Cu alloys: Combining positron annihilation spectroscopy with TEM and ab initio calculations, J. Alloys Comp. 817 (2019): 152765.

[11] K. Laha, J. Kyono, T. Sasaki, S. Kishimoto, N. Shinya, Improved creep strength and creep ductility of type 347 austenitic stainless steel through the self-healing effect of boron for creep cavitation, Metall. Mater. Trans. A 36A (2) (2005) 399-409.

[12] H. Fang, N. Szymanski, C.D. Versteylen, P. Cloetens, C. Kwakernaak, W.G. Sloof, F.D. Tichelaar, S. Balachandran, M. Herbig, E. Brück, S. van der Zwaag, N.H. van Dijk, Self healing of creep damage in iron-based alloys by supersaturated tungsten, Acta Mater. 166 (2019) 531-542.

[13] H. Fang, C.D. Versteylen, S. Zhang, Y. Yang, P. Cloetens, D. Ngan-Tillard, E. Brück, S. van der Zwaag, N.H. van Dijk, Autonomous filling of creep cavities in Fe-Au alloys studied by synchrotron X-ray nano-tomography, Acta Mater. 121 (2016) 352-364.

[14] S.M. He, N.H. van Dijk, H. Schut, E.R. Peekstok, S. van der Zwaag, Thermally activated precipitation at deformation-induced defects in Fe-Cu and Fe-Cu-B-N alloys studied by positron annihilation spectroscopy, Phys. Rev. B 81(9) (2010): 094103.

[15] S. van der Zwaag, E. Brinkman, Self Healing Materials: Pioneering Research in the Netherlands, IOS Press 2015.

[16] S. Zhang, H. Fang, M.E. Gramsma, C. Kwakernaak, W.G. Sloof, F.D. Tichelaar, M. Kuzmina, M. Herbig, D. Raabe, E. Brück, S. van der Zwaag, N.H. van Dijk, Autonomous Filling of Grain-Boundary Cavities during Creep Loading in Fe-Mo Alloys, Metall. Mater. Trans. A 47(10) (2016) 4831-4844.

[17] Y. Fu, C. Kwakernaak, W.G. Sloof, F.D. Tichelaar, E. Brück, S. Van der Zwaag, N.H. van Dijk, Competitive healing of creep-induced damage in a ternary Fe-3Au-4W alloy Metall. Mater. Trans. A 51 (2020): 4442-4455.

[18] W.W. Sun, H. Fang, N.H. van Dijk, S. van der Zwaag, C.R. Hutchinson, Linking Surface Precipitation in Fe-Au Alloys to Its Self-healing Potential During Creep Loading, Metall. Mater. Trans. A 48(5) (2017) 2109-2114.

[19] Y. Chen, X.Y. Fang, Y. Brechet, C.R. Hutchinson, Surface precipitation on engineering alloys, Acta Mater. 81 (2014) 291-303.

[20] H. Vijayakumar, A. H. Sriramamurthy, S.V. Nagender Naidu, Calculated phase diagrams of Cu-W, Ag-W and Au-W binary systems. Calphad 12 (1988): 177-184.

[21] R-F. Zhang, Y-X. Shen, L-T. Kong, W-S. Lai, B-X. Liu, Metastable phase selection of an immiscible Au–W System studied by ab initio calculation,

3

molecular dynamics simulation and ion-beam mixing. Jpn. J. Appl. Phys. 43 (2004):7648-7653.

[22] K. Yamamoto, Y. Kimura, Y. Mishima Orientation relationships of icosahedral quasicrystalline phase and Laves phase precipitates in a ferritic alloy. Mater. Trans. 45 (2004): 2598-2601.

[23] C.D. Versteylen, N.K. Szymański, M.H.F. Sluiter, N.H. van Dijk, Finite element modelling of creep cavity filling by solute diffusion, Philos. Mag. 98(10) (2018) 864-877.

[24] J-W. Jang, J. Kwon, B-J. Lee, Effect of stress on self-diffusion in bcc Fe: An atomistic simulation study, Scr. Mater. 63(1) (2010) 39-42.

[25] M. Militzer , W.P. Sun, J.J. Jonas, Modelling the effect of deformation-induced vacancies on segregation and precipitation, Acta Metall. Mater. 42(1) (1994) 133-141.

[26] S.H. Song, X.M. Chen, L.Q. Weng, Solute diffusion during high-temperature plastic deformation in alloys, Mater. Sci. Eng. A 528(24) (2011) 7196-7199.

[27] Y. Shima, Y. Ishikawa, H. Nitta, Y. Yamazaki, K. Mimura, M. Isshiki, Y. Iijima, Self-diffusion along dislocations in ultra high purity iron, Mater. Trans. 43(2) (2002) 173-177

3

守初心(shǒu chū xīn)

To remain true to the original aspiration; never forget why you started.

3

4

SELF HEALING OF CREEP-INDUCED DAMAGE IN FE-3AU-4W BY MULTIPLE HEALING AGENTS STUDIED BY SYNCHROTRON X-RAY NANO-TOMOGRAPHY

'Ze kunnen je wel begrijpen als ze maar naar je willen luisteren.'

Kelly Greene

Constant stress creep experiments at 550 °C were performed on a high-purity Fe-3Au-4W (wt.%) ternary alloy with about 1 at.% supersaturation for Au and W in order to study self healing of grain-boundary cavities by both Au-rich and W-rich precipitates. Using synchrotron X-ray nano-tomography, the development of the creep cavities and the healing precipitates at different stages of creep was visualised using two spatial resolutions (30 and 100 nm voxel size). The healing kinetics was found to strongly depend on the nucleation time of the cavities. Cavities nucleated at an early stage of creep could be fully healed, while the healing of the late-nucleated cavities is much slower due to a decrease in the diffusional flux of the healing supersaturated solutes over time, as a result of (i) a decrease inter-cavity spacing caused by cavity nucleation and (ii) a gradual depletion of the supersaturated solutes near the grain boundaries. The interaction between the competing healing mechanisms for creep cavities by Au-rich and W-rich precipitates is discussed. It was found that Au-rich precipitates are formed much faster than the W-rich precipitates, and thereby effectively provide creep damage healing on different time scales.

4.1 Introduction

When exposed to a combination of a high temperature and constant stress levels even below the quasi-static yield stress, metals experience time-dependent plastic deformation, known as creep, ultimately leading to failure due to accumulated damage. Creep damage often begins with the nucleation of grain boundary cavities, which further grow and coalesce into larger cracks, which ultimately leads to failure [1]. To improve the creep resistance, the traditional mechanism is to tune the microstructure and composition of the metals such that the initiation of the cavities is postponed as long as possible [2-4]. However, since the nucleation of the cavities has been regarded as being unavoidable, the concept of self healing [5-7] has been proposed as an alternative strategy. In self-healing metals, the early-stage cavities can be filled autonomously by the precipitation of the supersaturated solute atoms pre-dissolved in the matrix. Thereby the continuous growth and the more catastrophic coalesce of the cavities can be postponed, if not prevented. In recent years, the concept of self healing has been verified as being effective in prolonging creep lifetimes in multiple metallic systems. For austenitic stainless steels (i.e. steels having an *fcc* lattice structure at the use temperature), Laha and co-workers [8, 9] reported that the combined addition of boron and nitrogen is effective in reducing the cavity growth rate, as well as increasing the creep rupture strength. In a systematic study on ferritic steels (i.e steels or alloys with a *bcc* lattice structure at the use temperature), a series experiments on binary Fe-X and ternary Fe-X-Y alloys, including Fe-Cu [10-12], Fe-Au [13-17], Fe-Mo [18], Fe-W [19] and Fe-Au-W [20], as well as simulation studies [21-23] have been conducted to reveal the healing mechanism during creep. For these model alloys the only creep damage present is the formation and growth of grain boundary cavities and the healing reaction is their autonomous filling due to the formation of solid precipitates in these cavities once formed. Several criteria are fundamental in order to achieve autonomous site-selective healing: (*i*) an extra amount of solute atoms (typically 1 at.% supersaturation at the creep temperature) need to be present into the matrix, providing the driving force for formation of precipitates; (*ii*) the nucleation energy barrier at free surfaces need to be sufficiently lower than the barrier of interior nucleation, assuring the site-selectivity; (*iii*) the solute atoms should have a higher diffusivity compared to the host atoms, so that the cavity can shrink as the

vacancies diffuse outward due to the Kirkendall effect; and (*iv*) the solute atoms should not react with other microstructural components and thereby not have been consumed before reaching the damage sites. Guided by the findings from the model alloys, a series of ferritic chrome steels with a combination of decent high-temperature mechanical properties and self-healing potential have been designed [24]. In these steels other alloying elements than the healing element, W, such as C, Cr, Ni are added to achieve decent mechanical properties, but as in the model alloys, the healing is due to only one solute atom (i.e. the healing agent).

To monitor the damage formation and the subsequent precipitation healing, multiple characterisation techniques have been applied, ranging from the more direct observation-based techniques such as scanning electron microscopy (SEM) and transmission electron microscopy (TEM), to the more indirect small-angle neutron scattering (SANS), which provides information on the evolution of the size distribution. In the past two decades, synchrotron X-ray tomography has been applied as a powerful non-destructive tool to study the cavity evolution during creep [25-27]. The high-flux X-ray beam with a high collimation and monochromaticity allows fast scans with high resolution, and brings insights into early stage cavity nucleation via *in-situ* experiments [25, 28]. The high coherence makes it possible to perform phase contrast imaging and holotomography [29]. Recently, Fang and co-workers [13, 19] utilised synchrotron X-ray nano-tomography on the Fe-Au and Fe-W self-healing systems to monitor the development of both the creep cavities and the healing precipitates with a voxel size down to 30 nm. Recent research by synchrotron X-ray techniques on metals can be found in reviews [30, 31].

In the present study, we explore the damage and healing behaviour in a Fe-3Au-4W (wt.%) ternary system in which not one but two healing agents can act simultaneously. Au and W were selected as the most appropriate elements for such an experiment given the existence of detailed creep damage healing studies on their binary counterparts [13, 19] and the difference in X-ray absorption for W and Au which may make it possible to discriminate between pore filling due to Au-rich or W-rich precipitates.

Creep experiments with a constant stress of 145 MPa at 550 °C were applied and stopped after different times to investigate the microstructure development at different stages of creep. Synchrotron X-ray holotomography

provides a powerful tool to visualise the evolution of both the grain-boundary cavities and the precipitates within the cavities. With two voxel sizes of 100 and 30 nm, Au-rich and W-rich precipitates can be segmented. The segmentation results are compared with the SEM results from a previous research on the same ternary system [20]. The growth of cavities and the mass transfer of solute towards the damage sites are also compared with the previously studied two binary counterparts [13, 19].

4.2 EXPERIMENTAL

4.2.1 SAMPLE PREPARATION AND CREEP TESTS

High-purity Fe-Au-W alloy sheets were ordered from GoodFellow. The composition of the samples is Fe-3.8W-3.1Au (in wt.%). Dog-bone shaped creep samples with a gauge length of 12.5 mm and a cross-section of 3 mm² (6 mm width and 0.5 mm thickness) were cut by spark erosion. The samples were then sealed in quartz tubes filled with 200 mbar ultra-high purity argon to prevent oxidation during annealing. After the homogenising process (at 868 °C for 5 h), the samples were quenched in water. The as-quenched samples were examined with scanning electron microscopy to assure a uniform homogenised matrix in which no precipitates can be observed before creep tests. The solutionised as-quenched samples showed an average grain size of 77 μm. A limited amount of $FeWO_4$ particles could be detected in the grain interior both for the as-received and creep-loaded samples. These particles are expected to remain stable during creep and they do not show an obvious effect on the grain boundary cavity formation or the healing, not did the lead to internal cavity formation.

The creep experiments were performed in vacuum at a fixed temperature of 550 °C with a constant stress of 145 MPa. The creep lifetime is estimated to be inversely proportional to the steady strain rate, which fulfils the Sherby-Dorn equation [32] $\dot{\varepsilon}_S = Ad^m\sigma^n\exp\left(-Q/RT\right)$, where A is a structure dependent constant, d is the grain size, m is the grain size exponent, σ is the applied stress, n is the stress exponent, Q is the activation energy, R is the gas constant and T is the temperature in kelvin. Taking the stress exponent n = 4.6 [20] and assuming the grain size exponent m the same as that of the Fe-Au alloy (m = -2 [16]), the estimated lifetime of the ternary Fe-Au-W alloy with the grain size of 77 μm yields 240 h. In order to study the microstructure

development at different stages of creep, the creep experiments were interrupted after 10, 50, 100, 150 and 223 hours. The microstructure in the uniform deformation region was characterised via scanning electron microscopy (SEM) using a JEOL JSM 6500F instrument equipped with energy-disperse X-ray spectroscopy (EDS). To reveal the precipitate crystal structure and composition, transmission electron microscopy (TEM) measurements were performed using a FEI C_s-corrected cubed Titan instrument. Elemental analysis was done with the Thermo Fisher Scientific super-X detector in the ChemiSTEM™ configuration. Lattice images were collected on a Gatan camera. ADF (Annular Dark Field) images and EDX spectra for elemental mapping were collected in STEM (Scanning Transmission Electron Microscopy) mode.

4.2.2 Synchrotron X-ray nano-tomography

The interrupted creep samples were further machined for the tomography experiments. Rectangular samples with a cross section of 300×300 μm² and a length of approximately 6 mm were cut from the uniform deformation region by spark erosion, with their long axis aligned with the loading direction during creep. Tomography measurements were performed at the ID16A-NI nano-imaging beamline of the European Synchrotron Radiation Facility (ESRF) in Grenoble, France [33]. The beamline provides a high-brilliance beam focused down to nano size (13 nm), allowing the observation of 3D microstructure for the creep-induced cavities and the precipitates formed in the cavities. The rectangular samples were mounted on a rotation stage and illuminated by the X-ray beam. A series of 2D X-ray projections (in total 1800 projections for each scan) were recorded as the sample rotated around an axis over 180 degrees at 4 focus-to-sample distances for the phase retrieval [29]. Combining the information at the 4 distances, the phase map for each angle was obtained running inhouse developed GNU Octave scripts. With the ESRF PyHST software package [34], the obtained phase maps were reconstructed to 3D digital images. For each sample, two resolutions were used with the corresponding voxel sizes of 100 nm and 30 nm. The volume of view (VoV) of the 30 nm scan is selected within the VOV of the 100 nm scan, allowing one to compare the microstructure of a same region with different resolutions. The 100 nm and 30 nm scans yield reconstructed volumes of $321.6\times321.6\times321.6$ μm³ and $96.48\times96.48\times96.48$ μm³, respectively. The VoVs to be analysed were selected

by on-line prior inspection of the X-ray images. The VoV should contain at least one grain boundary perpendicular to the loading direction, to show some form of creep damage and to be fully contained in the sample, preferably as close to the central axis as possible.

4.2.3 PHASE SEGMENTATION AND QUANTITATIVE ANALYSIS

The subsequent tomographic rendering and phase segmentation are performed with the FEI Avizo software. From the microstructure characterisation and in line with previous electron microscopy studies [20], 4 phases are detected in the creep-failed Fe-Au-W samples, namely the *bcc* matrix, the *fcc* Au-rich precipitates (with an Au concentration of about 60 at.%), the W-rich Fe_2W Laves precipitates, and the cavities. The $FeWO_4$ particles are not taken into consideration since they do not affect the damage formation and self-healing behaviour. The electron densities of the precipitates can be estimated based on their composition and crystal structure. Since the electron densities of the precipitates (3.71 $e/Å^3$ for $Au_{60}Fe_{40}$ and 3.38 $e/Å^3$ for Fe_2W, respectively) are higher than that of the matrix (2.21 $e/Å^3$ for Fe) and even more so for the cavities (vacuum), the precipitates (including the Au-rich and W-rich ones) and the cavities can be separated from the matrix by applying carefully selected threshold values to the grey value in the reconstructed slices. In the current work, the features with a higher electron density have a lower grey scale value, while a lower electron density results in a higher grey scale value. This means that in the reconstructed slices the precipitates are darker than the matrix, while the cavities are brighter.

In addition to the thresholds $I_{ppt/m}$ and $I_{cav/m}$ to separate the precipitates, cavities and the matrix ($I_{ppt/m}$ is the threshold between the precipitates and the matrix and $I_{cav/m}$ the threshold between the cavity and the matrix), another threshold $I_{Au/W}$ ($I_{Au/W} < I_{ppt/m}$) is required to further segment the Au-rich and W-rich precipitates. Based on the microstructures of the precipitates (further discussed in section 4.3.2) and previous results [20], the two types of precipitates are found to form separately for most of the cases. Therefore, it is safe to label a precipitate either Au-rich or W-rich. For each labelled precipitate, if the majority of its voxels have a grey scale between $I_{Au/W}$ and $I_{ppt/m}$, this precipitate is categorised as W-rich. Due to the small size of the W-rich precipitates, the segmentation of the Au-rich/W-rich precipitates is

only applied to the scans with a voxel size of 30 nm (and not for the scans with a voxel size of 100 nm). For both resolutions, objects (precipitates and/or cavities) with a volume smaller than 8 voxels (i.e. with a volume smaller than 8×10^{-3} and 2.16×10^{-4} μm^3 for the scans with a voxel size of 100 nm and 30 nm, respectively) were regarded as noise, and therefore ignored.

After the phase identification, the binary images were used for further analysis in MATLAB using the DIPimage toolbox [35]. For each object (cavity or precipitate), its shape was determined by the shape complexity, its elongation and flatness [13, 19]. The elongation and flatness are calculated from the three semi-axes of an equivalent ellipsoid with the same moments of inertia as the object itself. It is assumed that the volume occupied by a precipitate was previously occupied by an open cavity. By checking the contact between the precipitates and the open volume for each cavity, we determine how many precipitates are contributing to fill the cavity, how much volume has been filled, and how much volume remains open. The total volume of a cavity is therefore $V_{cav} + V_{prec}$, where V_{prec} is the volume of the precipitates in contact with the open volume V_{cav}. The filling ratio of an individual cavity is therefore $FR = V_{prec}/(V_{cav} + V_{prec})$. More detailed on the applied methodology for the shape classification and the filling ratio calculation can be found in reference [13]. A quantitative analysis is applied based on the scans with a 100 nm resolution, which provide a larger illuminated volume and therefore a better statistical significance. A volume rendering for the same region of interest (ROI) with both the 100 nm and 30 nm voxel sizes is shown in Fig. S4.1 (supplementary Information). As expected, the two resolutions provide similar results for objects with a relatively large size, while some difference can be observed for the smaller objects and more detailed features can be distinguished for the smallest voxel size.

4.3. RESULTS

4.3.1 CREEP RESULTS

The strain-time curves of the creep experiments at a stress of 145 MPa and a temperature of 550 °C are shown Fig. 4.1. The steady-state creep begins with a relatively constant strain rate soon after the load is fully applied. Given the reproducibility of these creep curves interrupted at different times, the general characteristics of the creep-induced cavities and the corresponding healing

precipitates can be monitored as a function of time. It is clear that the samples interrupted at 10, 50, and 100 h are in the steady-state creep regime, while the two samples with longer times (150 and 223 h, respectively) show an onset towards tertiary creep, where the strain rate increases rapidly compared to the steady-state creep. It is found that the strain contribution from the steady-state creep is less than 1%, which is consistent with previous results on the same alloy [20]. The strain rate for the 5 samples lies between $1.85(9)\times10^{-5}$ h^{-1} and $2.359(2)\times10^{-5}$ h^{-1}, with an average strain rate of $2.09(4)\times10^{-5}$ h^{-1}. Taking the steady-state creep rate for the ternary alloy with different grain sizes (77 μm in the present study and 103 μm in the previous study [20]), a grain size exponent of m = -2.2 is deduced.
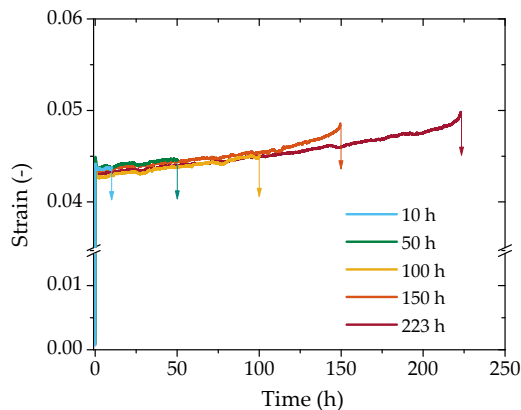
Fig. 4.1: Creep curves for the Fe-Au-W alloy samples with a constant applied stress of 145 MPa at a temperature of 550 °C. The creep experiments were interrupted after the indicated creep times.

4.3.2 MICROSTRUCTURE OF THE CREEP SAMPLES

Fig. 4.2(a) shows a SEM image of a grain boundary with grain-boundary cavities and healing precipitates for the Fe-Au-W alloy sample with a creep time of 223 h (at 145 MPa and 550 °C). Several grain-boundary cavities are fully filled by relatively large precipitates (indicated by yellow arrows), while others show a very limited degree of filling, and only nano-sized precipitates can be observed inside the cavities (indicated by blue arrows). EDS results demonstrate that the larger precipitates in the cavities with a high filling ratio are significantly enriched in Au (about 18 at.% Au), while the nano-sized

precipitates in the cavities with a limited filling ratio are generally enriched in W (1.8 - 4.8 at.% W). Apart from the precipitates formed exclusively at the free surface of the cavities, nano-sized Au-rich precipitates can also be observed in the matrix, as indicated by the triangular region. As shown in Fig. 4.2(b), these precipitates are found to be disc-shaped and are generally connected with dislocations formed during creep. These disk-shaped Au-rich precipitates are restrained from growing, due to the strain energy resulting from the mismatch between the precipitate lattice and the matrix lattice. Examples for dislocations and the strain contrast are indicated by the red arrows and circles in Fig. 4.2(b). It is worth to note that the disc-shaped Au-rich precipitates can be consumed by the nucleation and growth of the healing precipitates in the nearby cavities [16]. In fact, on the upper side of the grain boundary in Fig 4.2(a), a depletion zone is formed, where fewer Au-rich nano-sized precipitates can be observed. It is deduced that during the creep, the disc-shaped precipitates in the depletion zone are dissolved into the matrix and diffused towards the grain boundary in the form of Au atoms, through which they are further transported to the cavities and nucleate as Au-rich healing precipitates [16].

The TEM bright field (BF) and high angle annular dark field (HAADF) images with the EDX maps reveal the morphology and the composition of the nano-sized precipitates in the partially-filled cavities, as shown in Fig. 4.2(c). Consistent with the SEM-EDS result, most of the precipitates located at the cavity surface with a low filling ratio are enriched in W; for example, the particle indicated by the dashed blue circle has 29 at.% W and 4 at.% Au. The composition of the precipitates is in line with the expected composition of Fe_2W Laves phase. Due to the limited size of the W-rich precipitates, it was difficult to uniquely establish the lattice structure. The co-existence of Au-rich and W-rich precipitates is found both at cavity surfaces (e.g. Fig. 4.2(c)) and at grain boundaries. An example of this co-existence is given in Fig. 4.2(d): the Au-rich and W-rich precipitates form in contact to each other, showing a sandwich structure, instead of isolated particles. The Au-rich precipitates were confirmed to show an *fcc* structure with a composition of about 60 at.% Au.

4
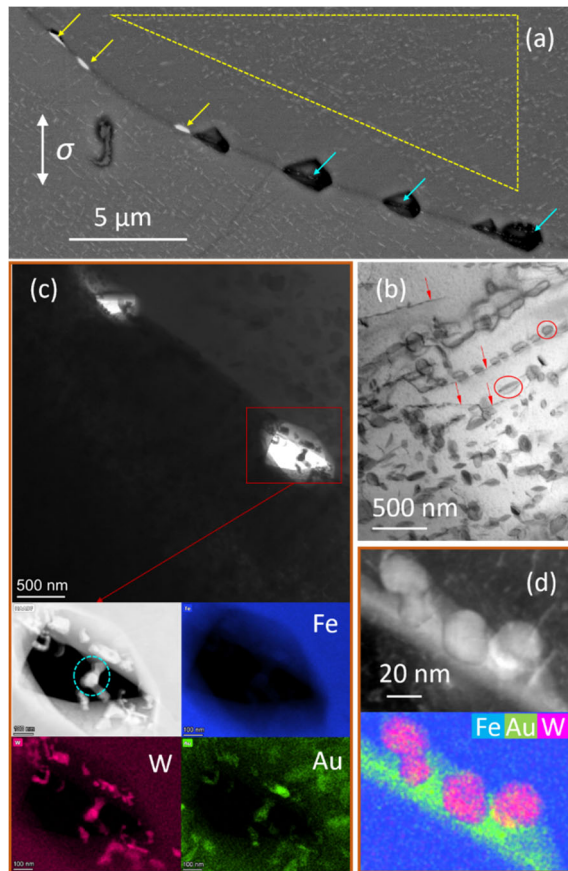
Fig. 4.2: SEM and TEM data for the Fe-Au-W alloy sample after 223 h creep with a constant applied stress of 145 MPa at 550 °C. (a) SEM image of a grain boundary and its vicinity. The yellow arrows indicate cavities that are filled by Au-rich precipitates, while the blue arrows indicate the nano-sized W-rich precipitates that show a limited degree of filling. Nano-sized Au-rich precipitates in the matrix are indicated by the dashed triangle. In between of the grain boundary and the triangular region with nano-sized Au-rich matrix precipitates, a precipitate-free depletion zone is observed. (b) TEM bright field (BF) image for the nano-sized Au-rich precipitates. The red arrows and circles indicate the dislocations and strain contrast, respectively. (c) TEM BF and high angle annular dark field (HAADF) images with EDX maps for grain-boundary cavities. The encircled particle is mainly enriched in W (29 at.%) while its Au concentration is slightly higher (4 at.%) than nominal. (d) Example for co-existence of the Au-rich and W-rich precipitates at a grain boundary. The Au-rich and W-rich precipitates have formed in contact to each other, rather than in the form of isolated particles.

4.3.3 TOMOGRAPHIC RENDERING

Fig. 4.3 shows a 3D overview of the creep cavity and healing precipitate distribution in the samples with creep times ranging from 10 to 223 h for a voxel size of 100 nm. The TEM results in Fig. 4.2 indicate that the W-rich precipitates generally have a size of about 100 nm (consistent with previous results [20]), which is comparable to the resolution of this scan. Therefore, all the precipitates will be combined in the analysis of the 100 nm resolution data, without classification in either Au-rich or W-rich precipitates. The cavities and precipitates are represented by red and green volumes, respectively. It is clear that with the increase in creep time: (1) more features can be observed and (2) the features, including the cavities and the precipitates, are growing in size. In the sample after 10 h of creep, some cavities and sporadic precipitates are observed, with an average equivalent diameter of 0.54 μm for the cavities and 0.41 μm for the precipitates. Most of the cavities are empty, indicating that the cavities are in their initial growth state just after nucleation. In the sample after 50 h of creep, more features (especially more precipitates) are observed in comparison to the sample after 10 h of creep. In addition, the cavities and precipitates start to show interaction: one or more precipitates are usually found in the vicinity of a cavity, indicating that the precipitates have multiple nucleation sites at the cavity surface. From 50 to 100 h of creep, both the cavities and the precipitates experienced obvious growth. Most of the cavities and the precipitates are located at the grain boundaries, especially at the transverse grain boundaries oriented perpendicular to the load direction. Cavities on some grain boundaries are significantly elongated, indicating a fast propagation of the cavities. In the binary Fe-Au [13] and Fe-W [19] samples, a significant amount of cavities were found to show a linkage of neighbouring cavities in the later stages of creep, in some cases resulting in cavities covering the whole grain boundary with the volume larger than 1000 μm^3. The cavity linkage is also observed in the current ternary Fe-Au-W system for the longest creep times (150 and 223 h). However, due to the limited creep strain in the ternary system, the linkage phenomenon is not as obvious as in the binary counterparts. The largest open volume found in the 223 h sample was less than 200 μm^3.

4

4
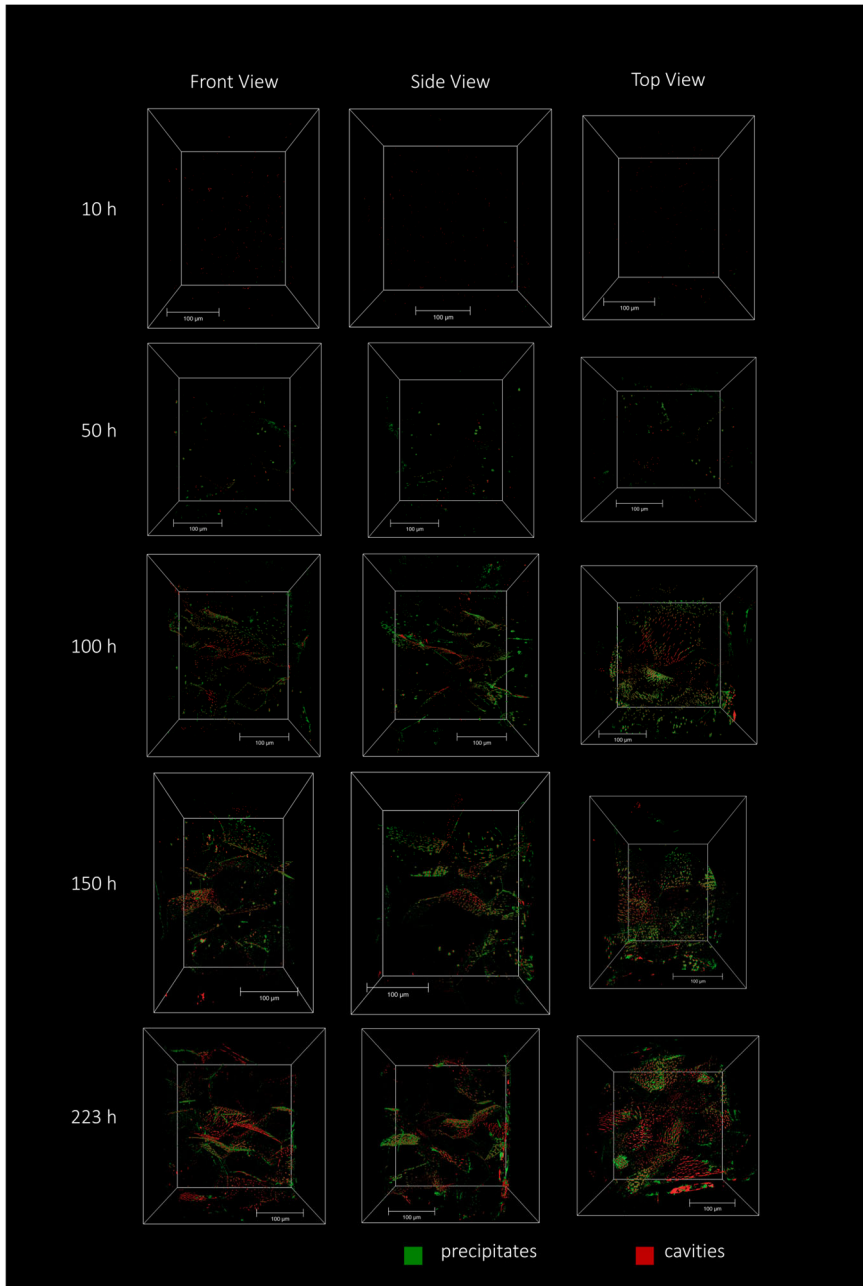
Fig. 4.3: Tomographic images of the Fe-Au-W alloy after creep at 550 °C with a constant applied stress of 145 MPa for different times. The images are obtained with a voxel size of 100 nm. The applied stress is normal to the top view.

Fig. 4.4 and Fig. 4.5 show examples of the cavities and precipitates from samples with different creep times. As illustrated in Fig. 4.4, in the sample after 10 h of creep most of the cavities have an elliptical or spherical shape: three cavities with a size of about 1 μm are aligned along the grain boundary direction. After 50 h of creep, the average equivalent diameter of the cavities increased from 0.54 μm (10 h) to 0.74 μm (50 h), and one or more precipitates are found to nucleate at the surface of the cavities. It is also worth to note that for the cavities, more complex shapes have developed, even though the increase in size is limited compared to the sample with 10 h of creep. Where the cavities after 10 h of creep usually have an ellipsoidal shape with smooth surfaces, after 50 h the cavities show more detailed features with tails and edges. As indicated by the white arrows (Fig.4.4(b), top view), the cavities appear to grow only in specific directions (as indicated by the white arrows), as for other directions the growth is restricted by precipitation. This anisotropic growth results in cavities with more complex shapes compared to the ones observed in the 10 h sample (which had limited to time to grow after nucleation). The completion between cavity growth and precipitate healing is more obvious in the first example for the sample after 150 h of creep (Fig. 4.5(a)): the precipitates form around the cavity surface until the cavity is eventually wrapped by the precipitates. For the longer creep times a linkage of cavities is observed for part of the cavities. Fig. 4.5(b) provides a clear example showing the early stage of linkage between two neighbouring cavities (indicated by the yellow boxes). A late stage of linkage can be observed in Fig. 4.5(c) and 4.5(d), where the linkage of cavities results in a cleavage of the grain boundaries. In Fig. 4.5(b), the precipitates are observed at the notch of the cavity (indicated by the solid white circles) and the linking point between the two cavities (indicated by the dashed white circles). The morphology of the cavities and precipitates provides indirect evidence that the precipitates are formed after the occurrence of the cavities.

4
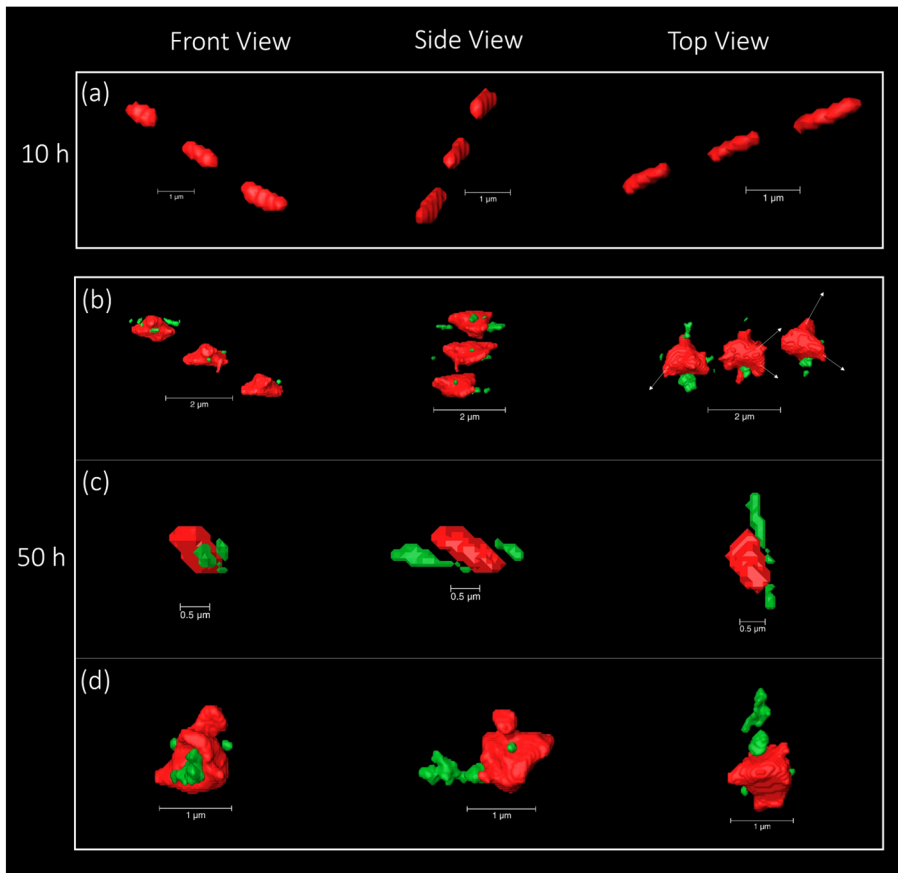
Fig. 4.4: Examples of early-stage creep cavities and healing precipitates after (a) 10 h and (b) – (d) 50 h creep. The red and green volumes indicates cavities and precipitates, respectively. The white arrows in (b) indicate the growth direction of the cavities (the cavity growth in other directions seem to be blocked by the precipitates).
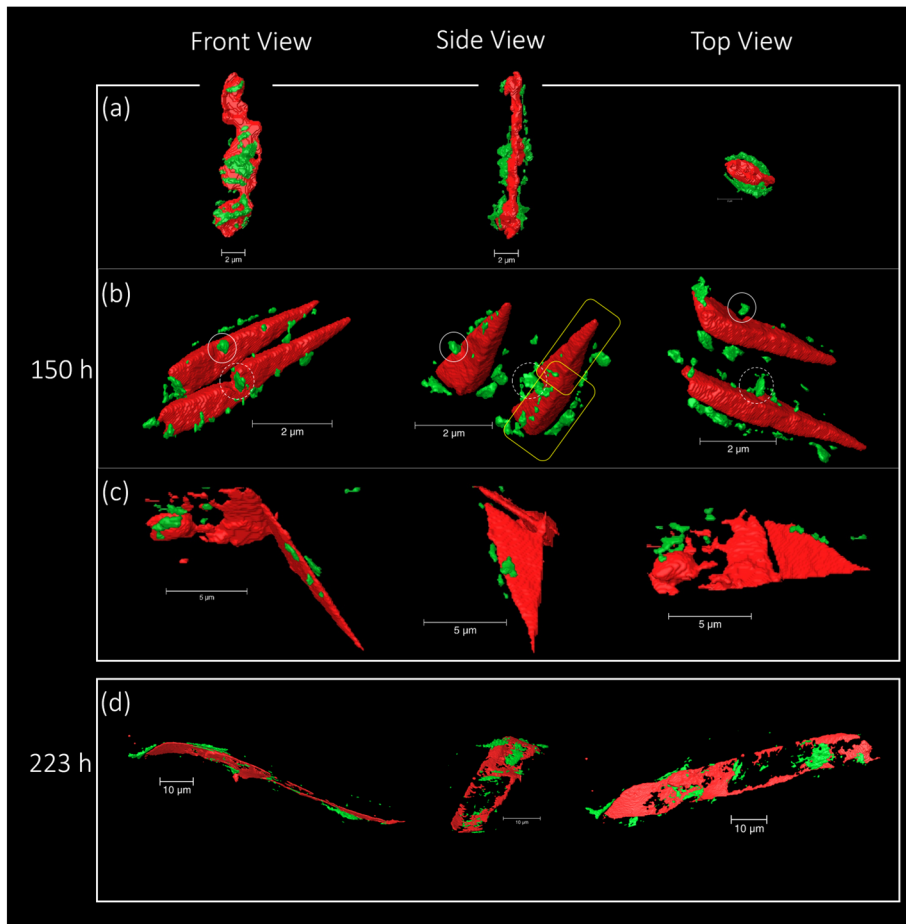
Fig. 4.5: Examples of late-stage creep cavities and healing precipitates after (a) – (c) 150 h and (d) 223 h creep. The red and green volumes indicates cavities and precipitates, respectively. Yellow boxes indicate the linkage of two originally isolated cavities. Precipitates were found at the notch and at the linking point of the cavities, as indicated by the solid and dashed circles, respectively.

4
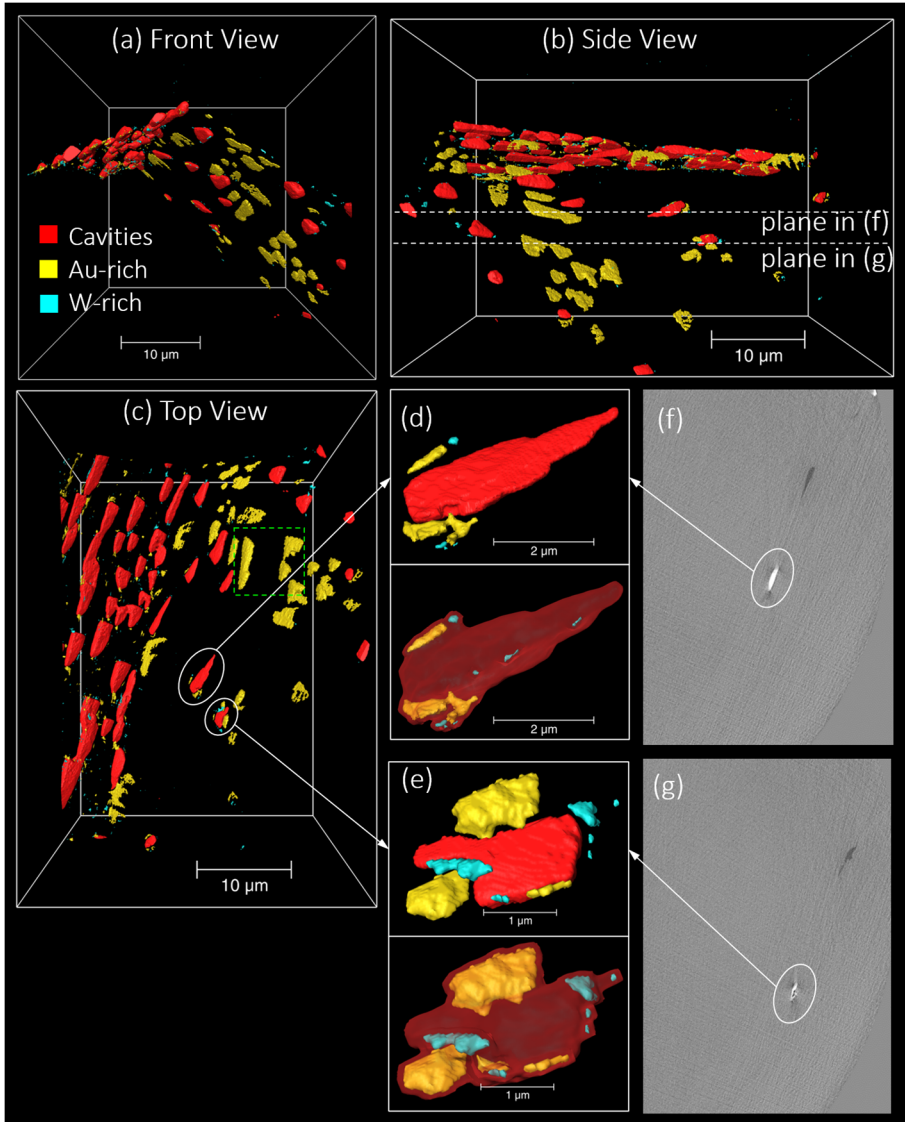
Fig. 4.6: Example of the further segmentation of Au-rich and W-rich precipitates in the 223 h sample. (a) - (c) Front view, side view and top view for a region of interest (ROI) with a volume of 30 × 30 × 40 μm³. (d) - (e) Two examples of cavities partly filled by both Au-rich and W-rich precipitates. The precipitates and open volumes are shown separately on the left, while for better visualisation, larger transparent contours are presented on the right to indicate the original cavity in the absence of healing. (f) - (g) Two tomography slices normal to the stress direction. The circles in (f) and (g) correspond to the partially-filled cavities in (d) and (e), respectively. The green box in (c) shows examples of fully filled cavities, some after linkage with their neighbours. The dashed lines in (b) indicate the position of the slices in (f) and (g).

In Fig. 4.6, an example of the further segmentation of Au-rich and W-rich precipitates at the enhanced resolution of 30 nm for the sample with the longest creep time of 223 h. Fig. 4.6(a) to 4.6(c) show a region of interest (ROI) with a volume of $30\times30\times40$ μm^3 from different directions. The red, yellow and blue volumes represent the cavities, the Au-rich precipitates and the W-rich precipitates, respectively. It is clear that about half of the cavities are fully filled by Au-rich precipitates, while the other cavities show very limited degree of filling. Small W-rich precipitates are frequently found in the partly filled cavities, showing a limited filling capacity due to its low diffusivity. The green dashed box in Fig. 4.6(c) shows cavities that are fully filled with Au-rich precipitates, and even shows a clear linkage of neighbouring cavities. Fig. 4.6(d) and 6(e) show two cavities partly filled by both Au-rich and W-rich precipitates. On the left, the precipitates and cavities are shown separately, while on the right, a larger transparent red contour is presented to indicate the original cavity with no healing for better visualisation. The contour is generated by dilating the sum of all the three phases (cavity, Au-rich precipitate and W-rich precipitate) by two voxels.

These observations are consistent with the previous SEM results at the fracture surface of creep failed samples of the same Fe-Au-W alloy [20]. Fig. S4.2(a) (Supplementary Information) shows details of features on a grain boundary located at the fracture surface after creep. The white precipitates (4 examples are indicated by yellow arrows) are mainly enriched in Au, and the corresponding cavities are fully filled by these Au-rich precipitates. Meanwhile, other cavities are still open (4 examples are indicated by red arrows), and only small precipitates with equivalent diameters of about 100 nm are observed at the surface of the open cavities. Most of the nano-sized precipitates are found to be enriched in W, as indicated by blue arrows in Fig. S4.2(c) and S4.2(d). Examples of cavities that are fully filled by Au-rich precipitates with linkage between neighbouring cavities as observed in Fig. 6(c) can also be observed in the SEM image at the fracture surface of the creep failed sample, as indicated by green boxes in Fig. S4.2(b). The examples shown in Fig. S4.2(b) and S4.2(d) indicated by the dashed red curves show two cavities partly filled by both Au-rich (yellow arrows) and W-rich (blue arrows) precipitates similar to the examples of Fig. 4.6(d) and 4.6(e).

4

4.3.4 Shape and linkage of cavities

In previous studies on the creep damage healing of cavities in the two binary counter systems [13, 19], the cavities were categorised into either isolated or linked cavities. The majority of the cavities was found to correspond to isolated ones. The number density of linked cavities was one order of magnitude lower than that for the isolated cavities. However, although the linked cavities were less frequently observed, they contributed more to the volume fraction, as they were generally much larger in size. In the present work, we use the shape classification and the linkage criteria introduced in references [13, 19]. Based on their elongation, flatness and complexity values the cavities are grouped into: (*i*) sphere, (*ii*) equiaxed, (*iii*) rod, (*iv*) sheet and (*v*) complex. The sphere and equiaxed shaped cavities are expected to be isolated, while the rod, sheet and complex shaped cavities are further identified as linked if their major axis exceeds the average inter-cavity spacing.

In Fig. S4.3 the number density and volume fraction for different shapes and types (isolated or linked) are shown as a function of the creep time. Unlike the results for the binary Fe-Au and Fe-W systems [13, 19], the linked cavities in the ternary Fe-Au-W system do not contribute significantly to the number density and volume fraction. Due to the limited strain in the creep experiments of the Fe-Au-W system, it is not likely that the isolated cavities link with multiple neighbours and develop into large-scale cavities. In the ternary system, the linked cavities are generally only twice as large as the isolated cavities. The average equivalent cavity diameter after a creep time of 100 h, 150 h and 223 h corresponds to 0.92(1), 1.09(1) and 1.17(1) μm for the isolated cavities and 1.89(7), 1.93(6) and 2.09(6) μm for the linked cavities, respectively. Therefore, unless specified otherwise, in the present study we treat all the cavities and precipitates together without categorising them in isolated or linked cavities.

4.3.5 Filling ratio

To quantify the creep damage as well as the degree of healing it is crucial to measure both the (remaining) cavity volume as well as the precipitate volume formed inside that cavity. For an individual cavity, the ratio between the precipitate volume formed inside the cavity and the sum of the precipitate volume and the open volume of the cavity is defined as the filling ratio *FR*. For an empty cavity *FR* = 0 and for a fully filled cavity *FR* = 1. In Fig. 4.7 the filling

ratio of each cavity is plotted as a function of its cavity volume (precipitates and open volume) at different creep times. With increasing creep time the volume of the unfilled, partly-filled and fully-filled cavities spans over a wider range of volumes, indicating a continuous cavity growth and a continuous precipitate healing. The lower limit of the unfilled cavities is determined by the resolution of the tomography, which indicates that cavity nucleation keeps taking place during the whole creep process. The upper limit of the unfilled cavities increases with time, indicating that some of the cavities remain unfilled through the creep process without any sign of precipitation (within the resolution limit). The maximum volume of the fully healed cavity also increases with time, which again indicates that the healing takes place continuously and that larger cavities can start to become filled after a longer time of existence. In the binary Fe-W system [13, 19], the maximum volume of the unfilled cavities is orders of magnitude larger than the fully-filled ones. In the current ternary Fe-Au-W system, however the maximum volume of the unfilled and fully filled cavities are comparable for a fixed creep time. This difference may originate from the limited cavity linkage in the ternary system (as shown in Fig. 4.3 and described in sections 4.3.3 – 4.3.4).

For a creep time of 10 h, the filling ratio is generally either 0 or 1 (see Fig. 4.7(a)), since the cavities and precipitates are small and partial filling can not be detected reliably, and few interactions between them are observed (see Fig. 4.3(a)). For a creep time of 50 h precipitates are found to nucleate at the surface of the cavities (see Fig. 4.3(b)), resulting in a filling ratio ranging from 0 to 1 (Fig. 4.7(b)). For a longer creep time (Fig. 4.7(c) to 4.7(e)), the filling ratio continues to cover the whole range from 0 to 1. The observed distribution of filling ratios results from the continuous nucleation and growth of the cavities and the continuous filling of the open volume by the precipitates. In Fig. 4.7(f), the average filling ratio *<FR>* as a function of the average cavity size *<V>* is presented for the partly-filled cavities. With an increase in creep time, the average cavity volume increases while the average filling ratio decreases. This indicates that for longer creep times the cavity filling progressively lags behind the cavity growth (especially for the large ones).

4
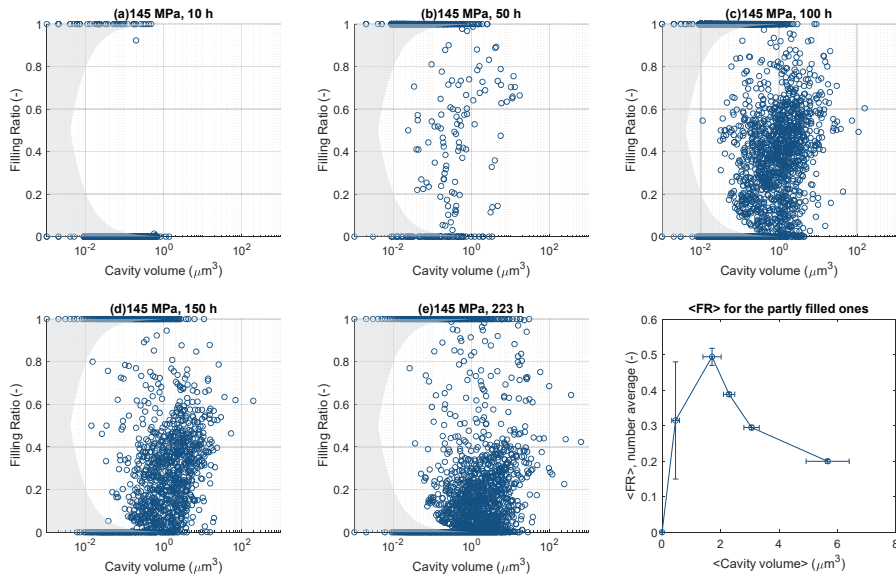
Fig. 4.7: (a) – (e) Filling ratio FR of individual cavities as a function of the cavity volume (sum of the open volume and the precipitation volume at the cavity surface) for the Fe-Au-W alloy after different creep times. (f) Average filling ratio <FR> as a function of the average cavity volume for the partly filled cavities. The grey shaded area indicates the resolution limit for the determination of the filling ration FR of the partially filled cavities.

4.4. Discussion

4.4.1 Time evolution of the cavities and precipitates

To monitor the time evolution of the cavities and the precipitates during creep, we have categorised the cavities into three groups: (*i*) empty, (*ii*) partially-filled and (*iii*) fully-filled. The number density and volume fraction as a function of creep time are summarised in Fig. 4.8 for these three categories. Several results can be observed from Fig. 8: (1) For the empty cavities both the number density and volume fraction show an increase with creep time, confirming a continuous cavity nucleation (as described in section 4.3.5). (2) For the fully-filled cavities an obvious increase in both the number density and volume fraction with creep time is observed during the whole creep process. This is in line with the results in Fig. 4.7 and proves that the healing of the cavities takes place continuously. (3) For the partially-filled cavities both the number density

and the volume fraction initially show an increase before they stabilise at a roughly constant level after 100 h. A stabilisation of the number of partially filled creep cavities is expected for a continuous process of concurrent creep cavity nucleation, cavity growth and cavity filling. When the cavity nucleation rate, cavity growth rate and the cavity filling rates are more or less stable in time then the number density of partially filled cavities will also stabilise as after an initial stage the rate at which new cavities are formed and existing cavities are fully filled will equalise in a steady-state creep process. It is worth to note that the number density of the precipitates in the partially-filled cavities is higher than that of the corresponding cavities. This indicates that multiple precipitates are formed in a single cavity during the healing process (on average about 3 to 4 precipitates per cavity). This is in agreement with the examples shown in Figs. 4.5 and 4.6. (4) The partially-filled cavities and the precipitates therein both experience an increase in volume fraction, but the volume fraction of cavities increases faster, resulting in a decrease in the filling ratio (as illustrated in Fig. 4.7(f)).
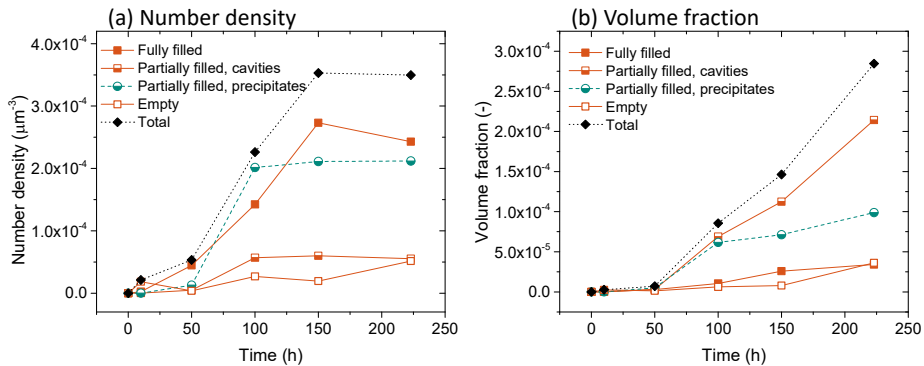
Fig. 4.8: Time evolution of (a) the number density and (b) the volume fraction of the cavities. Three groups of cavities (empty, partially-filled and fully-filled) are categorised based on their degree of filling. The data for the precipitates in the partially filled cavities are also presented for comparison.

Fig. 4.9 summarises the distribution in orientation of the cavities and the precipitates as a function of the angle between the long axis of the cavity/precipitate and the stress direction. For the shortest creep time (10 h) the freshly nucleated cavities show no preferred orientation. With an increase in creep time to 50 h and beyond, most cavities are found to form with an angle

close to 90°, indicating that the creep cavities prefer to nucleate at the grain boundaries oriented perpendicular to the stress direction (load-bearing grain boundaries) and that they tend to propagate in the grain boundary surface. The precipitates also show a preference for a 90° angle for a creep time of 100 h and beyond. The time lag in the formation of the preferred orientation for the precipitates (at $t \approx 100$ h) after the preferred orientation is observed for the cavities (at $t \approx 50$ h) provides strong evidence that the creep cavities initiate the formation of precipitates. Cavity nucleation has already started at the earliest creep time of 10 h, while the preferred orientation of the cavities only develops between 10 and 50 h. The precipitates nucleate after the occurrence of the cavities, and they subsequently grow in accordance with the shape of the cavities. This behaviour is consistent with the results from the previous study on the binary Fe-Au system [16].
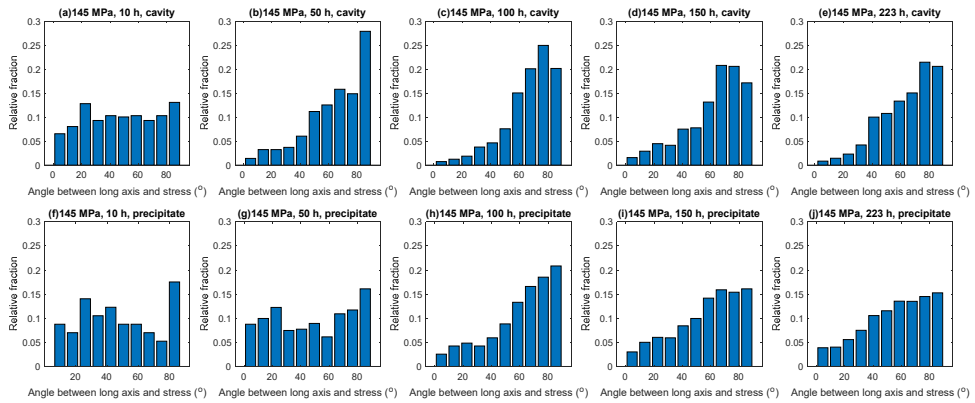
Fig. 4.9: Distribution of the angle between the long axis of the cavities ((a) - (e)) / precipitates ((f) - (j)) and the loading direction for different creep times. An angle of 90° indicates that the corresponding cavity / precipitate is oriented perpendicular to the load direction.

To compare the cavity and precipitates sizes in the ternary Fe-Au-W alloy with the two binary Fe-Au and Fe-W counterparts, the number distribution of the cavities and the precipitates are fitted to a log-normal distribution:

$$D_N(d) = \frac{N_0}{d\omega\sqrt{2\pi}} \exp\left(-\frac{\left(ln\, d - ln\, \bar{d}\right)^2}{2\omega^2}\right) \tag{4.1}$$

where N_0 is the number density, d the equivalent diameter, $\bar{d}$ the mean equivalent diameter and ω the relative width of the distribution. The fitting parameters for the ternary Fe-Au-W alloy are summarised in Table S4.1. The previously obtained fitting parameters of the Fe-Au [13] and Fe-W [19] binary alloys are also shown for comparison. Generally, the size of the cavities and precipitates in the Fe-Au-W ternary system is comparable with those of the Fe-Au binary system, but the number density and volume fraction for the two systems shows obvious differences, which are mainly caused by: (1) the difference in their experimental conditions (interrupted experiments for Fe-Au-W versus creep-failed experiments for Fe-Au) and (2) the limited linkage of the cavities observed for the Fe-Au-W alloy.

4.4.2 NUCLEATION OF CAVITIES AND PRECIPITATES
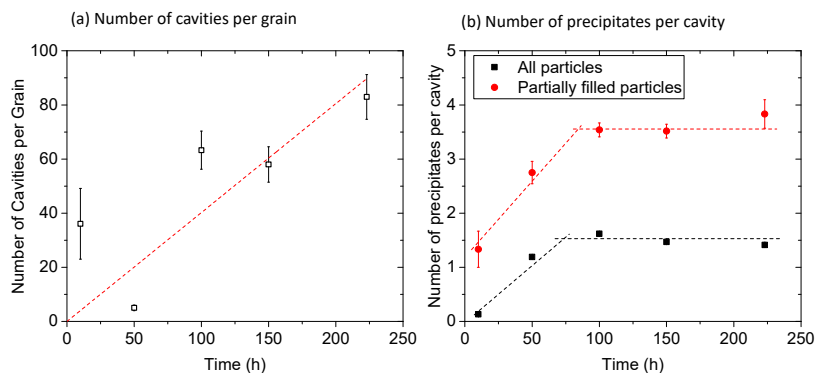
Fig. 4.10: (a) Number of cavities per grain as a function of the creep time. The data are fitted linearly with a straight line through the origin. (b) Number of precipitates per cavity as a function of time. The black data points are the average number of precipitate per cavity, while the red data points correspond to the average number of precipitates in partially-filled cavities. The dashed lines are a guide to the eye.

During creep, the cavities preferentially nucleate at the grain boundaries, before they are being filled by the precipitates. The nucleation rate of the grain boundary cavities can be estimated by plotting the number of cavities per grain as a function of time, as shown in Fig. 4.10(a). Assuming that the volume illuminated by the synchrotron is made up of repetitive units with the size of d_g^3 (d_g being the grain size), and that each unit contains one transverse grain boundary that collects all the cavities and precipitates, then the number of cavities per grain can be estimated by $N_0 d_g^3$, where N_0 is the number density of

cavities (listed in Table S4.1). In Fig. 4.10(a), it is clear that the number of cavities per grain generally increases linearly with the creep time, indicating a continuous nucleation. This is consistent with the findings in [36], where based on the data from literature, Wu and co-workers summarised that the number of cavities per unit area in low-alloy steels is proportional with the strain. A linear fit yields a nucleation rate of 0.40(7) cavities/grain/h for the Fe-Au-W alloy (at 145 MPa and 550 °C). This value is lower than the result from the Fe-W alloy, which is 1.35(5) cavities/grain/h (at 140 MPa and 550 °C) [19]. However, given the difference in the grain size for the two systems with d_g = 77 μm for Fe-Au-W and d_g = 127 μm for Fe-W, the nucleation rate per unit grain-boundary area is comparable for the two alloys. For a grain-boundary area of 100×100 μm² (oriented perpendicular to the stress) the estimated cavity nucleation rate is 0.67(12) cavity/h for the Fe-Au-W alloy and 0.84(3) cavity/h for the Fe-W alloy.

The average number of precipitates per cavity is shown in Fig. 4.10(b). Unlike the number of cavities per grain boundary, which keeps increasing with the creep time, the number of precipitates stabilises around 100 h to an average value of 1.5 precipitates per cavity. As this number is 0 for the empty cavities and 1 for the fully-filled cavities, this means that for the partially-filled cavities the number of precipitates per cavity needs to be larger than 1. As shown in Fig. 4.10(b), the number of precipitates per cavity for the partially-filled cavities is found to increase up to a creep time of 100 h and then stabilises at 3 to 4 precipitates per cavity, indicating a continuous nucleation of new precipitates at the cavity surface. This is consistent with the results shown Fig. 4.8(a).

It is worth to note that the average number of precipitates per cavity in the ternary Fe-Au-W alloy is approximately 3 times the value observed in the Fe-W binary alloy at a comparable stress level (145 MPa for Fe-Au-W and 140 MPa for Fe-W). Two reasons may be responsible for this. (1) Due to the limited diffusivity of W, the formation and growth of healing Laves phase in the Fe-W system is slower than the Au-rich precipitates in the Fe-Au-W system. Therefore, more empty cavities exist in the Fe-W system, which results in a lower average number of precipitates per cavity. (2) Another reason is related to the limited size of the W-rich precipitates in the ternary system. From the 3D rendering shown in Fig. 4.6, the W-rich precipitates in the ternary alloy have

a size of about 100 nm, and multiple W-rich precipitates are often found to contribute to the healing of a single cavity. In the Fe-W system [19], on the other hand, the W-rich precipitates range up to larger sizes, indicating that several precipitates can grow into a 'cluster' and thereby be analysed as a single healing precipitate within a cavity.

4.4.3 GROWTH OF CAVITIES AND PRECIPITATES

In previous studies [13, 19], the time evolution of cavity and precipitate was found to follow a power-law $V = kt^n$, where V is the average volume of the cavities (or precipitates) and t the creep time. The time exponent is 0.8 for the precipitates and the isolated cavities, while the linked cavities show a higher time exponent of 1.3 [13, 19]. In Fig. 4.11(a) and 4.11(b) the average volume of the cavities and the precipitates in the ternary alloy are plotted as a function of creep time. For comparison, the time evolution for the volume of the cavities and precipitates in the binary systems is also presented. The blue and yellow regions correspond to the fitting results from the Fe-W system and Fe-Au system, respectively. The green areas represent the overlap of the two binary systems. The upper and lower limits represent the linked and isolated features, respectively. The average volume of the cavities in the ternary Fe-Au-W system lies in between that of the isolated cavities in the two binary systems, which is consistent with the observation that most cavities in the ternary Fe-Au-W system are isolated. The average volume for the precipitates in the ternary Fe-Au-W system show a comparable behaviour as the precipitates in the binary Fe-Au alloy. The growth of both the cavities and the precipitates follows a power law $V = kt^n$. For the cavities, the time exponent n is 0.87(7), indicating a similar growth mechanism as the binary counterparts. The time exponent n for the precipitates yields 0.4(1) for the average volume of the individual precipitates. Considering the fact that potentially multiple precipitates are located in one cavity (as discussed in section 4.4.2), the average value for the total precipitate volume within one cavity can also be calculated (red data points in Fig. 4.11(b)), which gives a fitted time exponent n of 0.6(1). These results indicate that the growth behaviour of the precipitates in the ternary system is similar to the binary systems when the precipitates within one cavity are treated as a whole.
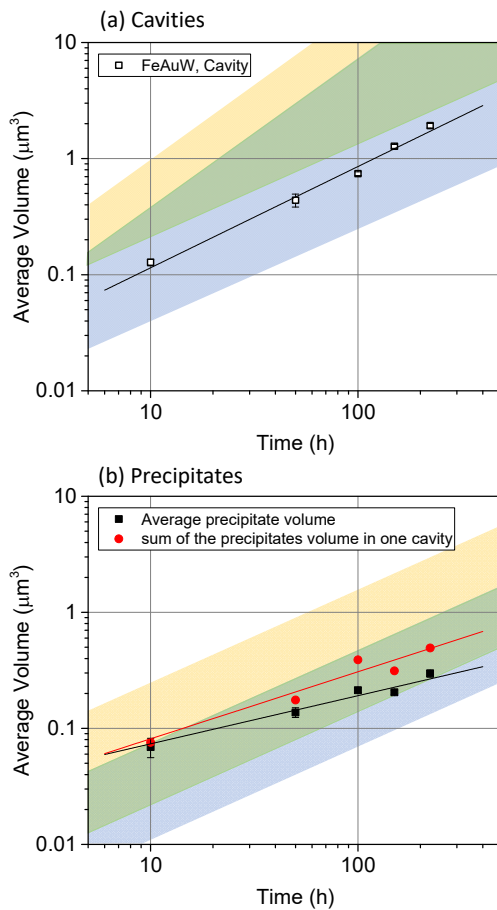
Fig. 4.11: Average volume $\langle V \rangle$ of (a) the cavities and (b) the precipitates as a function of time. The lines are fits to $\langle V \rangle = kt^n$. The blue and yellow shaded areas show the range of Fe-W and Fe-Au alloys, respectively and the green areas for the overlap. The upper and lower limits represent the linked and isolated features, respectively. In (b), the black data points are the average volumes of all the precipitates, while the red ones show the average value for the summed volume of the precipitates in each cavity. The fitting parameters are listed in Table S4.2 (supplementary information).

Multiple dominating mechanisms have been proposed to describe the growth of creep cavities, including diffusion, plasticity, grain boundary sliding, or a combination of them [37]. In a coupled model [38-41], it is suggested that the creep cavities, being controlled by grain-boundary diffusion, are embedded in the power-law controlled deforming matrix. Generally, diffusional growth is dominant for smaller cavities, lower stress levels and lower temperatures,

while plasticity dominates otherwise. A diffusion length $\Lambda = \left(\frac{D_{gb}\Omega\delta\sigma_0}{k_B T \dot{\varepsilon}}\right)^{1/3}$ [42] has been introduced, where D_{gb} is the diffusivity of vacancies at the grain boundary, δ the grain boundary thickness, Ω the atomic volume, σ_0 the applied stress, $\dot{\varepsilon}$ the strain rate, k_B the Boltzmann constant and T the temperature. The ratio between the cavity radius a and the diffusion length Λ can be used to estimate whether diffusional growth is dominant. As (a/Λ) increases, the creep flow becomes more important, and the power-law limit is reached when $(a/\Lambda) \to \infty$. In the ternary system, the diffusion length at a stress of 145 MPa and a temperature of 550 °C corresponds to $\Lambda \approx 30$ μm, which is larger than the average inter-cavity spacing (ranging from 4 to 7 μm for different creep times). It can therefore be assumed that the cavity growth in the Fe-Au-W ternary system is controlled by the vacancy diffusion through the grain boundaries, with an inward flux of $J_v = -\frac{1}{\Omega}\frac{D_{gb}x_v}{k_B T}\nabla\mu$, where x_v is the vacancy concentration at the grain boundary and $\nabla\mu$ the gradient in chemical potential, which is related to the stress gradient. Assuming that the stress distribution around one cavity does not change over time, the inward vacancy flux is then constant in time and the cavity volume increases linearly with time. This is consistent with the fitted time exponent n of 0.87(7) in Fig. 4.11(a).

4

Once a cavity is formed at the grain boundary, the autonomous healing starts to take place by depleting the supersaturated solute agents dissolved in the matrix. The solute in the vicinity of the grain boundary cavities depletes first, and the depletion zone then expands over time. Depending on (1) the ratio of the solute diffusivity in the grain boundary and in the bulk, and (2) the ratio between the inter-cavity spacing and the cavity diameter, the amount of solute atoms transported to a cavity scales as $V \propto t^n$, where the time exponent n ranges from 0.5 to 1 [22]. A time exponent of 0.6, as shown in Fig. 4.11(b), indicates a cross-over from 2D to 1D diffusion (see the fitting parameters listed in Table S4.2).

In the Fe-Au-W alloy, the solute diffusivity in the grain boundary is much higher (about a factor 10⁶) than that in the bulk. For a ratio between the inter-cavity spacing λ and the cavity diameter a of $\lambda/a < 20$, a 1D diffusion profile is expected to develop over time [22]. In this situation, the total amount of the solute agents transported to the grain-boundary creep cavities scales with the 1D matrix diffusion length towards the grain boundary $2\sqrt{D_m t}$, where

D_m is the solute diffusivity in the matrix and t the creep time. To monitor the total amount of solute involved in the cavity filling, we calculated the equivalent precipitates layer thickness (i.e., the equivalent thickness of the precipitation layer on the surface if the precipitates are spread out over the grain boundary, covering it uniformly). The experimentally derived equivalent precipitates layer thickness for the ternary Fe-Au-W alloy is shown in Fig. 4.12. The values for the binary Fe-Au and Fe-W alloys are also presented for comparison. In addition to the experimental data points the predictions for 1D diffusion of supersaturated Au and W are indicated by solid lines.

The experimental data points for Fe-Au-W alloy clearly demonstrate the development of the 1D diffusion after a creep time of about 100 h, as the time evolution of the equivalent layer thickness closely follows the $t^{1/2}$ power law predicted for 1D diffusion (for shorter times a faster growth rate is found). The experimental equivalent thickness for the ternary alloy is less than the calculated thickness for Au-rich precipitates. This indicates that the 1D solute diffusion is constrained by the availability of free cavity surface in partially filled cavities. The calculated layer thickness can therefore only act as an upper bound. The solute diffusion in the binary Fe-Au and Fe-W alloys, however, seems to be enhanced to a certain extent. In Fe-Au system [16] a higher effective diffusivity (two orders magnitude higher than the bulk diffusivity) was observed, resulting from an enhanced sub-grain formation during creep. For the Fe-W system, the enhancement in solute diffusivity may have resulted from the relatively large creep strain and the higher strain rate, compared to the Au-containing alloys. A higher creep rate is accompanied with the generation of excess vacancies [43, 44], which accelerate the diffusivity of both the solute and the host atoms. Militzer and coworkers [43] have proposed that during high-temperature deformation, the excess vacancy concentration first increases with time, then it drops and approaches the steady-state value due to the vacancy annihilation at grain boundaries and dislocations. The strain rate in the Fe-W alloy (about 10^{-4} h^{-1} at 550 °C) yields an excess vacancy concentration that is about 30 times higher than the thermal equilibrium value, which can result in an enhanced diffusivity.
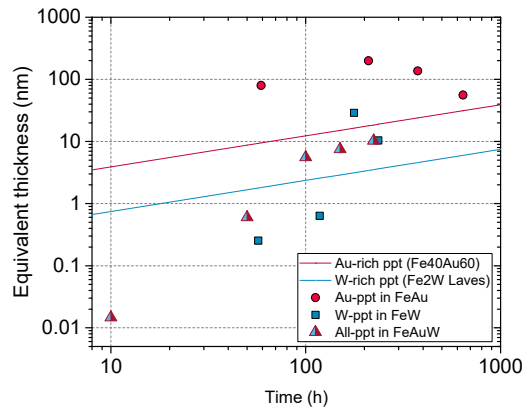
Fig. 4.12: Equivalent thickness *l* of the precipitation layer if all the precipitates were spread over the surface uniformly. The solid lines are calculated assuming 1D diffusion by $l(t) = (4/\sqrt{\pi})(\Delta x/x_p)\sqrt{D_X t}$, where Δx is the supersaturated solute fraction, x_p the solute fraction in the precipitate and D_X the solute (volume) diffusivity of element *X*. The experimental data are calculated by $f_V d_g$, where f_V and d_g are the volume fraction of the precipitates and the grain size, respectively.

It is interesting to note that W-rich precipitates seem to have a very limited contribution in the cavity healing in the Fe-Au-W alloy. In fact, in the ROI as shown in Fig. 4.6, W-rich precipitates have taken only about 5% of the total volume of all the precipitates. While in Fig. 4.12, it is indicated that at the same creep time, the W-rich precipitation is expected to be at a level of 20% compared to the Au-rich precipitation. It is, however, not yet determined that tungsten diffusion is constrained in the Fe-Au-W alloy. In a previous study on free surface precipitation for the Fe-Au-W, Fe-Au and Fe-W alloys [45], the nucleation of W-rich precipitates in the Fe-Au-W ternary alloy also showed some delay. At a temperature of 700 °C a large amount of W-rich precipitates was formed at the outer free surface of the Fe-Au-W alloy sample. The overall surface precipitation kinetics at the outer sample surface of the Fe-Au-W alloy was not significantly suppressed compared to that of the Fe-W alloy. Since the creep experiments in the present study were performed at a lower temperature, longer creep times may be necessary for a more complete investigation on the effectiveness of the W-rich precipitation kinetics to achieve self healing of creep damage.

4.4.4 HEALING MECHANISM

In previous synchrotron X-ray tomography studies [13, 19], it was found that the isolated and linked cavities show a different healing behaviour. The isolated cavities can be healed continuously until a fully filling is achieved, while a linkage of the cavities can cause a sharp drop in filling ratio. In the present work, linkage of the cavities is rare due to the limited creep strain, as discussed in section 4.3.4. Nevertheless, as shown in Fig. 4.7, the average filling ratio of the partly filled cavities decreases with time, and the majority of the data points shifts towards the right bottom, indicating an increasing cavity volume and a decreasing average filling ratio. As shown in Fig. 4.12, the solute diffusion generally follows a 1D character after a creep time of 100 h, which results in a decreasing solute flux towards the grain boundary. This indicates that if a cavity is formed at a later creep stage, when the solute flux from the matrix to the creep cavity is reduced by the development of the 1D diffusion profile, more time will be needed to fully fill the cavity. Another reason for the decreasing filling ratio is the continuous nucleation of cavities, and therefore the decrease in the average inter-cavity spacing. In the work by Versteylen and co-workers [22], it is demonstrated that within the 1D diffusion regime, the time to full filling scales with $(\lambda/d_{cav})^4$, where λ is the inter-cavity spacing and d_{cav} is the diameter of the cavity. For a grain boundary with a constant nucleation rate per unit of surface area $\dot{N}$, the inter-cavity spacing corresponds to $\lambda = (\dot{N}t)^{-1/2}$, where t is the creep time. The time evolution of the cavity diameter scales as $d \propto V^{1/3} \propto t^{0.3}$, where cavity volume scales as $V \propto t^{0.87}$, as discussed in section 4.4.3. The ratio between the inter-cavity spacing and the cavity diameter then scales as $(\lambda/d_{cav}) \propto t^{-0.8}$, which agrees well with the experimental observation of $(\lambda/d_{cav}) \propto t^{-0.6(1)}$, in Fig. S4.4 (Supplementary Information). Therefore, the time required to fully fill cavity of a fixed size increases significantly for longer nucleation times. Assuming a cavity nucleated at the grain boundary, and it starts to be healed at $t = t_0$ (t_0 is after the nucleation time). The cavity volume yields

$$V_{cav} = V_0 + k(t - t_0)^n \tag{4.2}$$

where k and n are fitting parameters for cavity growth, and V_0 the volume of the cavity when its healing starts.

The precipitates form due to solute atoms diffusing towards the cavity surface from both sides of the grain boundary, and this process can be simplified to a 1D diffusion problem. The solute atoms first diffuse towards the nearest grain boundaries from both sides, and then migrate through the grain boundary (acting as a fast diffusion path), before being transferred to the cavity surface. From t_0 to t, the sum volume of the healing agent (and therefore the precipitate volume) corresponds to

$$V_{ppt} = 2\lambda^2 \frac{\Delta x}{x_p} \frac{1}{\sqrt{\pi}} \left(2\sqrt{D_X t} - 2\sqrt{D_X t_0}\right) \tag{4.3}$$

where $\Delta x = x_\infty - x_e$ is the supersaturation of the solute, x_p the concentration of the solute element in the precipitate phase, D_X the diffusivity of solute X, λ the inter-cavity spacing. $2\sqrt{D_X t}$ and $2\sqrt{D_X t_0}$ correspond to the solute diffusion length at t and t_0, respectively. A schematic representation is given in Fig. S4.5(a) (supplementary information). When healing starts at time t_0, the inter-cavity spacing is

$$\lambda = \frac{d_g}{\sqrt{\dot{N}_g t_0}} \tag{4.4}$$

where d_g is the grain size, $\dot{N}_g$ the nucleation rate (per grain per unit of time). Therefore, Eq.(4.3) can be written as

$$V_{ppt} = 4 \frac{d_g^2}{\dot{N}_g t_0} \frac{\Delta x}{x_p} \frac{\sqrt{D_X}}{\sqrt{\pi}} \left(\sqrt{t} - \sqrt{t_0}\right) \tag{4.5}$$

The filling ratio of the cavity can then be calculated by V_{ppt}/V_{cav}. Taking $\dot{N}_g$ = 0.4/grain/h (as discussed in section 4.4.2), D_{Au} = 7.4×10⁻¹⁹ ms⁻² at 550 °C [23] (since Au is the dominating healing agent), x_p = 0.6, Δx = 0.01 and d_g = 77 μm, For cavities with different starting volumes and different start-healing times, the filling ratios versus cavity volume are shown in Fig. 4.13. It is clear that for a cavity that nucleated later (and therefore its healing also starts later), more time is required to achieve a fully filling. For the cavities nucleated at late stage of creep, their filling ratios eventually show an upper limit, after which the filling ratio decreases with time. This behaviour qualitatively agrees with the time evolution of the filling ratios presented in Fig. 4.7. For each V_0, a critical time can be derived, and if a cavity starts to be filled after this time, it is less likely to be fully filled. It is worth to note that a

higher cavity nucleation rate (which can be resulted from a higher stress level) leads to a faster decrease in the inter-cavity spacing, and therefore a lower overall filling ratio, as shown in Fig. S4.5(b) (Supplementary information).
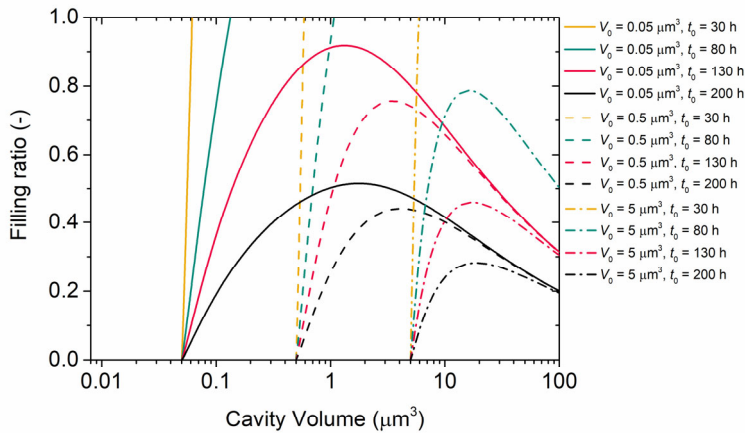
Fig. 4.13: Prediction of the filling ratio of the cavities with a different time t_0 (indicated by different colours) and a different volume V_0 (indicated by different line types), where V_0 is the volume of the cavity when its healing starts, and t_0 the time when healing starts. The nucleation rate of the cavities is fixed at 0.4/grain/h.

4.5. Conclusions

Creep experiments with a constant applied stress of 145 MPa at a temperature of 550 °C were performed on a high-purity ternary Fe-Au-W alloy with 1 at.% supersaturation for both Au and W at the creep temperature to study the autonomous healing of grain-boundary cavities by Au-rich and W-rich precipitates. The development of the creep cavities and the healing precipitates at different creep stages was investigated by synchrotron X-ray nano-tomography. The main conclusions are:

(1) During creep, the grain-boundary cavities are continuously formed and subsequently healed by precipitation on the cavity surface. The sequential order is proven by: (a) the similarity in morphology of cavities and precipitates, (b) the development of the angle between the long-axis and the load direction for cavities and precipitates and (c) the time evolution of the distribution of the empty, partially-filled and fully-filled cavities.

(2) Compared to the binary Fe-Au and Fe-W counterparts, the linkage of the cavities in the ternary Fe-Au-W system is rare, due to the limited creep strain and the low strain rate. The cavities in the ternary system show similar nucleation and growth behaviour as the cavities in the Fe-W alloy. In the Fe-Au-W alloy the solute diffusion is not significantly enhanced by a relatively high sub-grain formation (Fe-Au alloy) or a relatively high strain rate (Fe-W alloy).

(3) Cavities nucleated at an early creep stage can be fully healed, while due to a decrease in the diffusional solute flux and the inter-cavity spacing over time, a longer time is required to fully fill the late formed cavities. This results in an overall decrease in filling ratio of the partially filled but still growing cavities with time.

(4) High-resolution tomography with a resolution of 30 nm allows for a 3D segmentation of the Au-rich and the relatively small W-rich precipitates (about 100 nm in size). The results is in accordance with the 2D observation from SEM and TEM images. However, for the situation where Au-rich and W-rich precipitates form in contact to each other, an even higher resolution is sometimes required for proper segmentation due to the small size of W-rich precipitates and the limited contrast between both precipitates.

(5) The supersaturated Au solute diffuses significantly faster than the supersaturated W. This results in a fast filling of creep cavities by Au-rich precipitates and a relatively slow filling by W-rich precipitates. This difference in healing kinetics indicates that supersaturated Au and W provide two healing agents that operate on different time scales. Combining both can significantly extend the time scale over which self healing of creep damage can potentially be achieved.

4

4.6 SUPPLEMENTARY MATERIAL
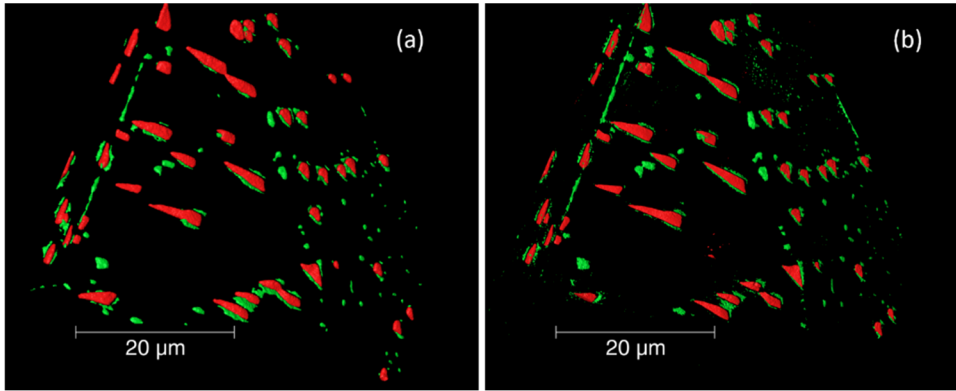
Fig. S4.1: 3D volume rendering for a same region of interest with a voxel size of (a) 100 nm and (b) 30 nm. The red and green refer to cavities and precipitates, respectively.

4
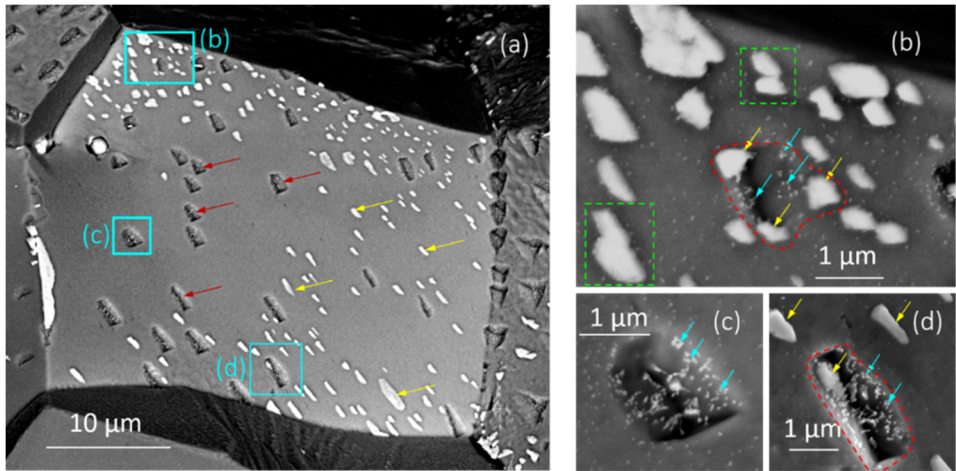
Fig. S4.2: SEM results for a creep-failed sample of the same Fe-Au-W alloy [20]. Fracture surface for a sample exposed to 200 MPa at 550 °C with a lifetime of 97 h. The red, yellow and blue arrows indicate the cavities, Au-rich and W-rich precipitates, respectively. The green boxes in (b) shows examples of fully filled cavities, which resembles the situation in Fig. 4.6(c). The irregular red dashed circles in (b) and (d) show two examples where both Au-rich and W-rich precipitates are contributing in filling one cavity, which highly resembles the situation in Fig. 4.6(d) and 6(e).
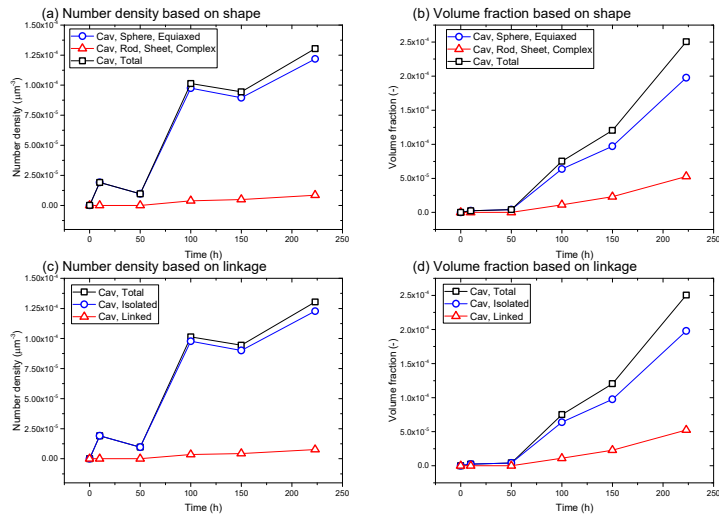
Fig. S4.3: Number density and volume fraction of the cavities as a function of time. In (a) and (b) the cavities are categorised based on shape, while in (c) and (d) the cavities are categorised based on whether they are linked.

4
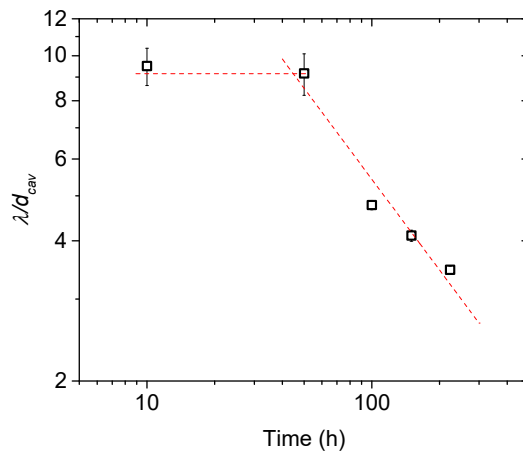
Fig. S4.4: Ratio between the inter-cavity spacing λ and equivalent diameter d_{cav} of cavity as a function of time. An exponential fit $\lambda/d_{cav} \propto t^{\,n}$ from 50 – 223 h yields an exponent n = -0.6(1). The line connecting 10 and 50 h is a guide to the eye.
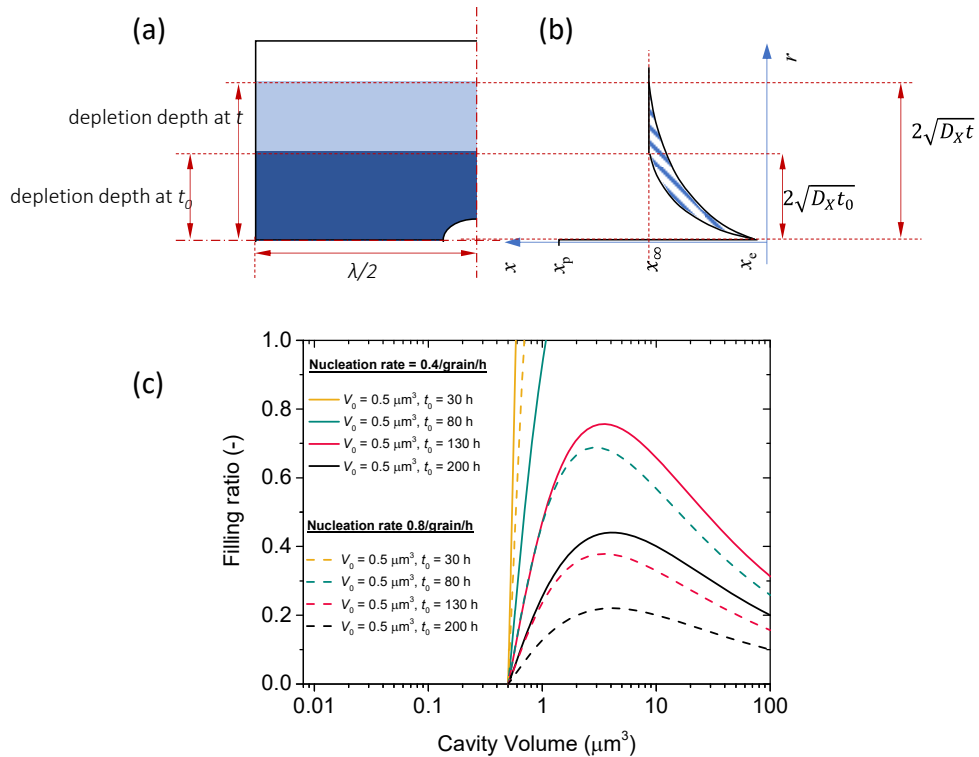
Fig. S4.5: Schematic picture of the cavity filling mechanism showing (a) the depletion of solute with time and (b) the concentration profile of the solute for different times. By the time healing starts at time t_0 the cavity has an equivalent diameter of d_{cav}. The dashed area in (b) indicates the amount of healing solute transported to the cavity from time t_0 to time t. (c) Prediction of the filling ratio for cavities with a different healing-start time t_0 (indicated by colours) and nucleation rate $\dot{N}_g$ (indicated by dashed and solid lines). The volume of the cavity V_0 at time t_0 is fixed at 0.5 µm³.

Table S4.1: Fitted parameters N_0, d and ω for a log-normal size distribution of cavities (cav) and precipitates (prec). The number density N_p and volume fraction f_v are from the 3D tomographic data. The data of Fe-W [19] and Fe-Au [13] systems are presented for comparison.

Phase		Experiment conditions		Fitting results			Experiment result	
		σ MPa	Time h	N_0 ×10⁻⁵µm⁻³	$\bar{d}$ µm	ω -	N_p ×10⁻⁵µm⁻³	f_v %
FeAuW	Cav	145	10	8(2)	1.1(5)	1.0(3)	1.92	0.00025
			50	1.1(2)	0.82(9)	0.47(9)	0.97	0.00043
			100	14(1)	1.16(6)	0.50(4)	10.13	0.00751
			150	13(1)	1.60(7)	0.45(4)	9.44	0.01204
			223	18(2)	1.48(9)	0.68(5)	13.04	0.02504
	Prec	145	10	0.3(1)	0.44(9)	0.7(1)	0.27	0.00002
			50	7.8(6)	0.52(1)	0.41(2)	5.68	0.00078
			100	50(2)	0.68(1)	0.55(1)	33.90	0.00721
			150	69(3)	0.66(1)	0.52(2)	47.51	0.00971
			223	66(2)	0.683(9)	0.55(1)	44.72	0.01331
FeW	Cav	140	59	2.5(1)	0.32(1)	0.77(2)	1.90	0.0122
			118	3.9(1)	0.51(1)	0.64(1)	3.41	0.0235
			177	14(1)	0.55(1)	0.74(2)	14.10	0.0322
			236	19(1)	0.62(1)	0.61(1)	18.30	0.1623
		160	52	6.2(3)	0.66(2)	0.69(3)	6.04	0.0063
			104	8.3(1)	0.48(1)	0.65(1)	8.15	0.019
	Prec	140	59	0.84(3)	0.44(1)	0.56(3)	0.81	0.0002
			118	0.62(2)	0.45(2)	0.70(1)	0.48	0.0005
			177	17(1)	0.43(1)	0.57(1)	17.20	0.0228
			236	9.9(1)	0.52(1)	0.59(1)	9.62	0.0082
		160	52	3.6(2)	0.62(2)	0.55(2)	3.82	0.0009
			104	6.2(1)	0.45(1)	0.66(1)	6.00	0.0017
FeAu	Cav	117	57	9.2(5)	0.85(4)	0.62(4)		0.11
		100	210	19.4(6)	0.86(2)	0.57(2)		0.24
		80	376	7.6(3)	1.50(6)	0.80(3)		0.76
		60	642	7.0(5)	1.5(1)	0.92(8)		0.64
	Prec	117	57	111(7)	0.63(3)	0.50(4)		0.14
		100	210	93(6)	0.67(3)	0.55(4)		0.35
		80	376	130(10)	0.63(4)	0.54(6)		0.24
		60	642	17(1)	0.76(4)	0.60(5)		0.098

Table S4.2: Fit parameters of the average volume V as a function of creep time t to a power law dependence $V = kt^n$. The data of Fe-W [19] and Fe-Au [13] systems are presented for comparison.

Sample	Particle type	Cavities		Precipitates	
		k	n	k	n
		($\mu m^3 h^{-n}$)		($\mu m^3 h^{-n}$)	
FeAuW	All	0.0154(1)	0.87(7)	0.028(4)	0.4(1)
	Sum volume in a cavity			0.0224(4)	0.6(1)
FeW	Isolated	0.0061(2)	0.8	0.0017(1)	0.8
	Linked	0.019(2)	1.3	0.012(2)	0.8
FeAu	Isolated	0.033(6)	0.8	0.0036(5)	0.8
	Linked	0.05(1)	1.3	0.04(1)	0.8

Movie

Movie S4.1: 3D visualization with a voxel size of 100 nm indicating the segmentation and spatial distribution of cavities and precipitates in the Fe-Au-W sample after creep at 550 °C and 145 MPa for 150 h.

Filename: MovieS1_FeAuW_550C_145MPa_150h_100nm.mpg

4

File description:

This movie shows the correspondence between the original 3D volume image (grey value) and segmented 3D volume image (colour) by clipping slices from the loading direction (vertical). In the grey valued 3D volume image the bright and dark features are cavities and precipitates, respectively (see main text of the manuscript for details). After segmentation the cavities and precipitates are denoted in red and green colours, respectively.

REFERENCES

[1] J.N. Greenwood, D.R. Miller, J.W. Suiter, Intergranular Cavitation in Stressed Metals, Acta Metall. Mater. 2(2) (1954) 250-258.

[2] F.R.N. Nabarro, H.L. de Villiers, The Physics of Creep: Creep and Creep-resistant Alloys, 1st ed., CRC Press1995.

[3] M. Taneike, F. Abe, K. Sawada, Creep-strengthening of steel at high temperatures using nano-sized carbonitride dispersions, Nature 424(6946) (2003) 294-296.

[4] F. Abe, Progress in Creep-Resistant Steels for High Efficiency Coal-Fired Power Plants, J. Press. Vessel Technol. 138(4) (2016) 040804.

[5] M.D. Hager, P. Greil, C. Leyens, S. van der Zwaag, U.S. Schubert, Self-healing materials, Adv. Mater. 22(47) (2010) 5424-30.

[6] N. van Dijk, S. van der Zwaag, Self-Healing Phenomena in Metals, Adv. Mater. Interfaces 5(17) (2018) 1800226.

[7] B. Grabowski, C.C. Tasan, Self-Healing Metals, in: M.D. Hager, S. van der Zwaag, U. S. Schubert (Eds.), Self-healing Materials, Springer International Publishing, Cham, Switzerland, 2016, pp. 387-407.

[8] K. Laha, J. Kyono, S. Kishimoto, N. Shinya, Beneficial effect of B segregation on creep cavitation in a type 347 austenitic stainless steel, Scr. Mater. 52(7) (2005) 675-678.

[9] K. Laha, J. Kyono, T. Sasaki, S. Kishimoto, N. Shinya, Improved creep strength and creep ductility of type 347 austenitic stainless steel through the self-healing effect of boron for creep cavitation, Metall. Mater. Trans. A 36(2) (2005) 399-409.

[10] S.M. He, P.N. Brandhoff, H. Schut, S. van der Zwaag, N.H. van Dijk, Positron annihilation study on repeated deformation/precipitation aging in Fe–Cu–B–N alloys, J. Mater. Sci. 48(18) (2013) 6150-6156.

[11] S.M. He, N.H. van Dijk, M. Paladugu, H. Schut, J. Kohlbrecher, F.D. Tichelaar, S. van der Zwaag, In-situ determination of aging precipitation in deformed Fe-Cu and Fe-Cu-B-N alloys by time-resolved small-angle neutron scattering, Phys. Rev. B 82(17) (2010) 174111.

[12] S.M. He, N.H. van Dijk, H. Schut, E.R. Peekstok, S. van der Zwaag, Thermally activated precipitation at deformation-induced defects in Fe-Cu and Fe-Cu-B-N alloys studied by positron annihilation spectroscopy, Phys. Rev. B 81(9) (2010) 094103.

[13] H. Fang, C.D. Versteylen, S. Zhang, Y. Yang, P. Cloetens, D. Ngan-Tillard, E. Brück, S. van der Zwaag, N.H. van Dijk, Autonomous filling of creep cavities in Fe-Au alloys studied by synchrotron X-ray nano-tomography, Acta Mater. 121 (2016) 352-364.

[14] S. Zhang, J. Kohlbrecher, F.D. Tichelaar, G. Langelaan, E. Brück, S. van der Zwaag, N.H. van Dijk, Defect-induced Au precipitation in Fe–Au and Fe–Au–B–N alloys studied by in situ small-angle neutron scattering, Acta Mater. 61(18) (2013) 7009-7019.

4

[15] S. Zhang, C. Kwakernaak, W. Sloof, E. Brück, S. van der Zwaag, N. van Dijk, Self Healing of Creep Damage by Gold Precipitation in Iron Alloys, Adv. Eng. Mater. 17(5) (2015) 598-603.

[16] S. Zhang, C. Kwakernaak, F.D. Tichelaar, W.G. Sloof, M. Kuzmina, M. Herbig, D. Raabe, E. Brück, S. van der Zwaag, N.H. van Dijk, Autonomous Repair Mechanism of Creep Damage in Fe-Au and Fe-Au-B-N Alloys, Metall. Mater. Trans. A 46(12) (2015) 5656-5670.

[17] S. Zhang, G. Langelaan, J.C. Brouwer, W.G. Sloof, E. Brück, S. van der Zwaag, N.H. van Dijk, Preferential Au precipitation at deformation-induced defects in Fe–Au and Fe–Au–B–N alloys, J. Alloys Compd. 584 (2014) 425-429.

[18] S. Zhang, H. Fang, M.E. Gramsma, C. Kwakernaak, W.G. Sloof, F.D. Tichelaar, M. Kuzmina, M. Herbig, D. Raabe, E. Brück, S. van der Zwaag, N.H. van Dijk, Autonomous Filling of Grain-Boundary Cavities during Creep Loading in Fe-Mo Alloys, Metall. Mater. Trans. A 47(10) (2016) 4831-4844.

[19] H. Fang, N. Szymanski, C.D. Versteylen, P. Cloetens, C. Kwakernaak, W.G. Sloof, F.D. Tichelaar, S. Balachandran, M. Herbig, E. Brück, S. van der Zwaag, N.H. van Dijk, Self healing of creep damage in iron-based alloys by supersaturated tungsten, Acta Mater. 166 (2019) 531-542.

[20] Y. Fu, C. Kwakernaak, W.G. Sloof, F.D. Tichelaar, E. Brück, S. van der Zwaag, N.H. van Dijk, Competitive Healing of Creep-Induced Damage in a Ternary Fe-3Au-4W Alloy, Metall. Mater. Trans. A 51(9) (2020) 4442-4455.

[21] C.D. Versteylen, M.H.F. Sluiter, N.H. van Dijk, Modelling the formation and self-healing of creep damage in iron-based alloys, J Mater. Sci. 53(20) (2018) 14758-14773.

[22] C.D. Versteylen, N.K. Szymański, M.H.F. Sluiter, N.H. van Dijk, Finite element modelling of creep cavity filling by solute diffusion, Philos. Mag. 98(10) (2018) 864-877.

[23] C.D. Versteylen, N.H. van Dijk, M.H.F. Sluiter, First-principles analysis of solute diffusion in dilute bcc Fe-X alloys, Phys. Rev. B 96(9) (2017) 094105.

[24] H. Yu, W. Xu, S. van der Zwaag, A first step towards computational design of W-containing self-healing ferritic creep resistant steels, Sci. Technol. Adv. Mater. 21(1) (2020) 641-652.

[25] A. Isaac, F. Sket, W. Reimers, B. Camin, G. Sauthoff, A.R. Pyzalla, In situ 3D quantification of the evolution of creep cavity size, shape, and spatial orientation using synchrotron X-ray tomography, Mater. Sci. Eng. A 478(1-2) (2008) 108-118.

4

[26] A. Pyzalla, B. Camin, T. Buslaps, M. Di Michiel, H. Kaminski, A. Kottar, A. Pernack, W. Reimers, Simultaneous tomography and diffraction analysis of creep damage, Science 308(5718) (2005) 92-5.

[27] R. Kumar, J. Villanova, P. Lhuissier, L. Salvo, In situ nanotomography study of creep cavities in Al-3.6-Cu alloy, Acta Mater. 166 (2019) 18-27.

[28] M. Huppmann, B. Camin, A.R. Pyzalla, W. Reimers, In-situ observation of creep damage evolution in Al-Al2O3 MMCs by synchrotron X-ray microtomography, Int J. Mater. Res. 101(3) (2010) 372-379.

[29] P. Cloetens, W. Ludwig, J. Baruchel, D. Van Dyck, J. Van Landuyt, J.P. Guigay, M. Schlenker, Holotomography: Quantitative phase tomography with micrometer resolution using hard synchrotron radiation x rays, Appl. Phys. Lett. 75(19) (1999) 2912-2914.

[30] N.H. van Dijk, Synchrotron X-ray Radiation Studies on Metals and Alloys, in: Encyclopedia of Materials: Metals and Alloys, Elsevier, 2022, pp. 682-694.

[31] P. Sedigh Rahimabadi, M. Khodaei, K.R. Koswattage, Review on applications of synchrotron‐based X‐ray techniques in materials characterization, Xray Spectrum. 49(3) (2020) 348-373.

[32] O.D. Sherby, Factors affecting the high temperature strength of polcyrystalline solids, Acta Metall. Mater. 10(2) (1962) 135-147.

[33] A. Somogyi, B. Lai, P. Cloetens, S. Bohic, M. Salome, L. Bloch, M. Hubert, F. Fus, Y. Yang, A. Pacureanu, J.C. da Silva, High-energy cryo x-ray nano-imaging at the ID16A beamline of ESRF, X-Ray Nanoimaging: Instruments and Methods III, 2017.

[34] A. Mirone, E. Brun, E. Gouillart, P. Tafforeau, J. Kieffer, The PyHST2 hybrid distributed code for high speed tomographic reconstruction with iterative reconstruction and a priori knowledge capabilities, Nucl. Instrum. Meth. B 324 (2014) 41-48.

[35] https://diplib.org/.

[36] R. Wu, R. Sandström, Strain dependence of creep cavity nucleation in low alloy and 12%Cr steels, Mater. Sci. Technol. 12(5) (1996) 405-415.

[37] M.E. Kassner, T.A. Hayes, Creep cavitation in metals, Int. J. Plast. 19(10) (2003) 1715-1748.

[38] W. Beere, M.V. Speight, Creep cavitation by vacancy diffusion in plastically deforming solid, Met. Sci. J. 12(4) (1978) 172-176.

[39] G.H. Edward, M.F. Ashby, Intergranular Fracture during Power-Law Creep, Acta Metall. Mater. 27(9) (1979) 1505-1518.

4

[40] A. Needleman, J.R. Rice, Plastic Creep Flow Effects in the Diffusive Cavitation of Grain-Boundaries, Acta Metall. Mater. 28(10) (1980) 1315-1332.

[41] E. Van Der Giessen, M.W.D. Van Der Burg, A. Needleman, V. Tvergaard, Void growth due to creep and grain boundary diffusion at high triaxialities, J. Mech. Phys. Solids. 43(1) (1995) 123-165.

[42] I.W. Chen, A.S. Argon, Diffusive growth of grain-boundary cavities, Acta Metall. Mater. 29(10) (1981) 1759-1768.

[43] M. Militzer , W.P. Sun, J.J. Jonas, Modelling the effect of deformation-induced vacancies on segregation and precipitation, Acta Metall. Mater. 42(1) (1994) 133-141.

[44] S.H. Song, X.M. Chen, L.Q. Weng, Solute diffusion during high-temperature plastic deformation in alloys, Mater. Sci. Eng. A 528(24) (2011) 7196-7199.

[45] Y. Fu, C. Kwakernaak, J.C. Brouwer, W.G. Sloof, E. Brück, S. van der Zwaag, N.H. van Dijk, Surface precipitation of supersaturated solutes in a ternary Fe–Au–W alloy and its binary counterparts, J. Mater. Sci. 56(8) (2020) 5173-5189.

4

但拨云(dàn bō yún): enjoy collecting clouds

Based on a Chinese idiom 拨云见日 (bō yún jiàn rì): to dispel the coulds and see the sun.

It describes the situation where one has finally conquered all the obstacles and reached the destination. In the first beginning of a PhD, one may expect a process of 'dispelling the clouds and seeing the sun', but it is more likely that for many people, there is no 'sun' after years of dispelling clouds. Maybe they should learn to enjoy clouds collecting and roll the boulder as Sisyphus did. Control the controllable and let time do the rest.

5

MODELLING THE GROWTH AND FILLING OF CREEP-INDUCED GRAIN-BOUNDARY CAVITIES IN SELF-HEALING ALLOYS

'I know a lot of people from the northeast. They are so attached to their homeland that they hate to leave it. That's why, girl from the northeast, you impress me.'

A taxi driver in Beijing

A set of numerical and analytical models is presented to predict the growth and contraction of grain-boundary creep cavities in binary self-healing alloys. In such alloys the healing is realised by preferential precipitation of supersaturated solutes at the free surface of the cavity. The cavity grows due to the diffusional flux of vacancies towards the cavity, which is driven by the stress gradient along the grain boundary. Upon deposition of healing solute atoms on the cavity wall, effectively vacancies are removed from the cavity due to the inverse Kirkendall effect. The competition between the inward and outward vacancy fluxes results in the growth or shrinkage of the open volume of the creep cavity. The model also shows the conditions in which the solute transport is to be regarded as a 1D, 2D or a 3D case. It is found that for low stress levels the filling ratio of the creep cavity (i.e. the precipitate volume divided by the sum of that volume and the remaining unfilled cavity volume) can proceed to unity, i.e. to complete filling and annihilation of the pore. For high applied stresses complete filling is not achieved and the open volume of the creep cavity will continue to grow once a maximum filling ratio is reached. The critical stress leading to complete filling of the creep cavity by solute precipitation can be calculated for different values of the model parameters such as relative diffusion rates, the degree of supersaturation and the inter-cavity spacing.

5.1 Introduction

Creep takes place when metals are exposed to a combination of a constant mechanical stress below the yield stress and a relatively high temperature (higher than $0.4T_m$, where T_m is the melting temperature). During creep loading of polycrystalline metals, quasi-spherical micron-sized cavities form preferentially at those grain boundaries oriented perpendicular to the load direction. Upon prolonged loading such pores grow and coalesce into micro and subsequent macro cracks, which leads to complete fracture of the sample or even the installation [1]. Traditionally, the strategy to improve the creep resistance and the high-temperature properties, has been to create a microstructure which retards the cavity formation and minimises the growth as long as possible [2-5], but irrespective of the metallurgical strategy used, cavities once formed will continue to grow, coalesce and the largest ones will finally induce catastrophic failure. Some years ago the concept of self healing has been proposed as an alternative strategy [6-8] In this approach the occurrence of creep cavities triggers dedicated solute atoms (so called self-healing solutes) to move towards these cavities, to fill them and make them harmless before they grow to catastrophic dimensions. Provided that the diffusivity of the selected solute atoms is faster than the diffusivity of the host atoms, then due to the Kirkendall effect, the diffusion of the healing agent towards the cavity surface results in a net diffusion of vacancies in the opposite direction, i.e. the vacancies are removed from the creep-induced cavity [9] and the empty volume of the cavity becomes smaller. Furthermore, once the cavity is completely filled the driving force for directed vacancy flux is removed and the damage can be considered to have been healed. As a result, the coalescence of neighbouring creep cavities is prevented. In case the growth of the cavities is faster than the rate of filling then only partial cavity filling will take place and cavities will continue to grow but at a lower rate than in non-self-healing system. This is expected to have a much smaller effect on the desired life time extension.

The self-healing concept based on selective precipitation has been tested and verified for multiple binary and more complex metallic systems. Laha and co-workers [10-13] reported the unexpected experimental finding that the addition of boron and nitrogen is effective in suppressing the cavity growth rate of austenitic stainless steels (with an *fcc* lattice structure) leading

5

to an increased creep rupture strength. In order to demonstrate intentional filling of creep damage by tailored precipitation on the cavity wall, Van Dijk and Van der Zwaag initiated a number of creep damage studies using selected binary Fe-X and ternary Fe-X-Y alloys, including Fe-Cu [14-16], Fe-Au [17-21], Fe-Mo [22], Fe-W [23] and Fe-Au-W [24]. These systems were selected on the basis of the following considerations: i) they can be brought into a supersaturated state (typically 1 at.%) at a creep relevant temperature at which the alloy is in a ferritic state (here 550 °C) by prior homogenisation and rapid quenching, ii) the energy barrier for precipitation on a free surface is considerably lower than that in the grain interior, iii) the diffusion coefficient of the solute is higher than that of the iron atoms and finally iv) the solute atoms are not consumed in other reactions while migrating to the cavity [8, 20]. These alloys serve as model alloys for future self-healing multicomponent ferritic creep steels as they have the advantage that no other metallurgical reactions than the intended healing reaction can take place.

In order to predict the pore filling behaviour of the creep cavities in such binary alloys, a semi-quantitative model has been proposed by Versteylen and co-workers [9]. In this model, the vacancy flux towards the cavity is controlled by the stress-induced gradient in the chemical potential on the grain boundary surrounding the creep cavity, while the opposite vacancy flux (i.e., the Kirkendall flux) results from the transport of the supersaturated solute. The competition between the two vacancy fluxes leads to a desirable reduced strain rate. Their model also delivers a critical stress below which complete pore filling is possible. However, in the model by Versteylen and co-workers the normal stress at the grain boundary was not calculated explicitly and the solute diffusion was simplified as a stationary time-independent flux. In reality, however, with the evolution of the solute diffusion profile in the matrix, the solute flux decreases with time [20].

In the present work, a model is proposed to predict the evolution of the open volume of a grain-boundary cavity as a function of time. The inward vacancy flux is driven by the stress distribution along the grain boundary, while the time-dependent outward vacancy flux results from the solute segregation on the cavity surface. Both the stress distribution and the solute flux are calculated with a multi-physics finite element package (COMSOL® [25]). The time evolution of the filling ratio, and the resulting critical stress, are calculated

5

based on the accumulated inward and outward vacancy fluxes. The influences of the grain-boundary to bulk diffusivity ratio, the level of solute supersaturation, and the spacing between neighbouring cavities on the healing efficiency are addressed explicitly and solutions are proposed as a function of the imposed stress. The model does not address the initial nucleation of the precipitate on the cavity wall nor does it take into account the kinetics of the internal atomic transport within the precipitate formed. The paper ends with a simple analytical model for the pore filling process taking the results from the numerical model to justify the assumptions made in the analytical model.

5.2 MODEL DESCRIPTION

5.2.1 MODEL GEOMETRY

As shown in Fig. 5.1(a), the rotationally symmetric simulation box is a cylinder with radius λ and height H. The radius λ reflects half the distance between the centres of neighbouring creep cavities on the same creep affected grain boundary and the height H reflects half of the grain size. The vertical axis (z) and the radial axis (r) are indicated by the red dashed- lines. It is assumed that a pre-existing cavity is located at the centre. According to Raj and Ashby [26], creep cavities are lens-shaped with a cavity radius a, an equilibrium opening angle of $\psi \approx 75°$ and a cavity height h that scales with the cavity radius as $h/a = (1 - \cos(\psi))/\sin(\psi) \approx 0.77$ [27]. In the present model, the cavity is assumed to have an ellipsoidal shape to simplify the calculation of the stress distribution (see 5.2.2 for details). The cavity radius is taken as a = 0.5 μm, with a corresponding cavity height of $h \approx 0.77a$ and an ellipsoidal cavity volume of $V = \frac{4}{3}\pi h a^2 = \left(\frac{h}{a}\right)\left(\frac{4}{3}\pi a^3\right) \approx 0.77\left(\frac{4}{3}\pi a^3\right)$. Note that for a lens-shaped cavity the cavity volume is slightly smaller: $V = \left[1 - \frac{3}{2}\cos(\psi) + \frac{1}{2}\cos^3(\psi)\right]\left(\frac{4}{3}\pi a^3\right) \approx 0.62\left(\frac{4}{3}\pi a^3\right)$. In all simulations the grain-boundary width is assumed to be δ = 2 nm and the height of the simulation box is fixed at H = 10 μm. The radius of the simulation box λ varies from 2.5 to 25 μm. This combination of pore and matrix dimensions ensures that the reservoir of solute atoms (i.e. the number of supersaturated solute atoms in the total matrix volume considered) is not depleted during the healing process.
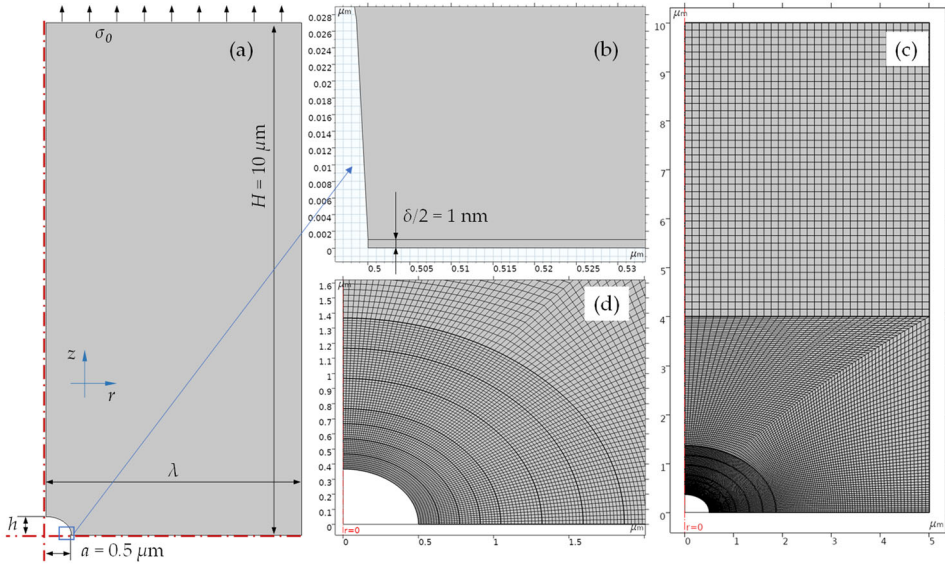
Fig. 5.1: (a) and (b): Dimensions of the cylindrical model. The creep cavities have a fixed radius of a = 0.5 μm with an inter-cavity spacing of λ. Constant stress σ_0 is applied to the upper edge of the cell. The elliptical cavity has a height given by the ratio h/a = $(1-\cos(\psi))/\sin(\psi)$, where ψ = 75°. The half width of the grain boundary is $\delta/2$ = 1 nm. (c) and (d): Mesh for the model (for the case with λ = 5 μm). 4 layers of boundary mesh are applied to the grain boundary.

5.2.2 CAVITY GROWTH BY STRESS-DRIVEN VACANCY DIFFUSION

Multiple theoretical models have been proposed to describe the growth of creep cavities. Depending on the applied stress, temperature, and the creep stage, the dominant cavity growth mechanism can be diffusion, plasticity, grain-boundary sliding, or a combination thereof [28]. A coupled model was proposed [29-32], which proposed that the creep cavities, their growth being controlled by grain-boundary diffusion of vacancies, are embedded in a matrix controlled by power-law deformation. Generally, diffusive growth dominates cavity behaviour in case of a small cavity, a low stress level σ_0 and a low temperature T, while plasticity effects dominate otherwise. A diffusion length $\Lambda = \left(\frac{D_{gb}\Omega\delta\sigma_0}{kT\dot{\varepsilon}}\right)^{1/3}$ [33] has been introduced to estimate the conditions in which diffusive growth dominates, where $\dot{\varepsilon}$ is the strain rate, k is Boltzmann's constant, D_{gb} the grain-boundary diffusivity and Ω the atom volume. As (a/Λ) increases, the creep flow becomes more important, and the power-law limit is

reached when $(a/\Lambda) \to \infty$. In the present study the dimension of the model box was taken to be comparable or larger than the diffusions lengths calculated for the tested model alloys [17, 20, 23, 24], to make sure that the growth of the cavity is controlled by the vacancy diffusion through the grain boundary.

In the model it is assumed that the cavity growth at elevated temperatures results from vacancy diffusion and that the vacancy diffusion is driven by the stress gradient. The vacancy flux through the grain boundary in contact with the cavity can be written as [34-36]

$$J_v = -\frac{1}{\Omega} \frac{D_{gb}^v x_v}{kT} \nabla \mu \tag{5.1}$$

in which D_{gb}^v is the vacancy diffusivity at the grain boundary, x_v is the vacancy concentration, and μ is the chemical potential. Assuming that the vacancy concentration is at equilibrium, the stress dependent contribution to the chemical potential is $\Delta\mu(\sigma_n) = -\sigma_n\Omega$, in which σ_n is the local normal stress on the grain boundary [36]. The stress distribution along the grain boundary with an ellipsoidal creep cavity is calculated by the finite element method using COMSOL® [25]. The *Linear Elastic Material* module with nodal serendipity (quadratic) elements is used, in which a constant stress σ_0 is applied uniformly to the top edge of the simulation volume (Fig. 5.1(a)). At a temperature of $T = 550$ °C (823 K) the Young's modulus E is taken to be 165 GPa [37] and the Poisson's ratio v is set to 0.33 [37].

Fig. 5.2 shows the normal stress σ_n (normalised by the applied stress σ_0) distribution for different (λ/a) ratios, in which r is the distance from the centre of the (empty) cavity with radius a. A stress concentration occurs at the edge of the cavity $(a/r) \to 1$ while σ_n approaches the applied stress σ_0 at the far end of the grain boundary with $(a/r) \to (a/\lambda)$. The stress distribution shows similar profiles along the grain boundary for the cases where $(\lambda/a) \geq 5$. The stress distribution can be fitted with a simple phenomenological expression:

$$\frac{\sigma_n}{\sigma_0} = 1 + A\left[\exp\left(B\frac{a}{r}\right) - 1\right] \tag{5.2}$$

where $A = 1.65(2) \times 10^{-3}$ and $B = 6.82(3)$ are dimensionless constants. The inward vacancy flux in equation (1) can now be estimated using equation (2), and is proportional to the applied stress σ_0.
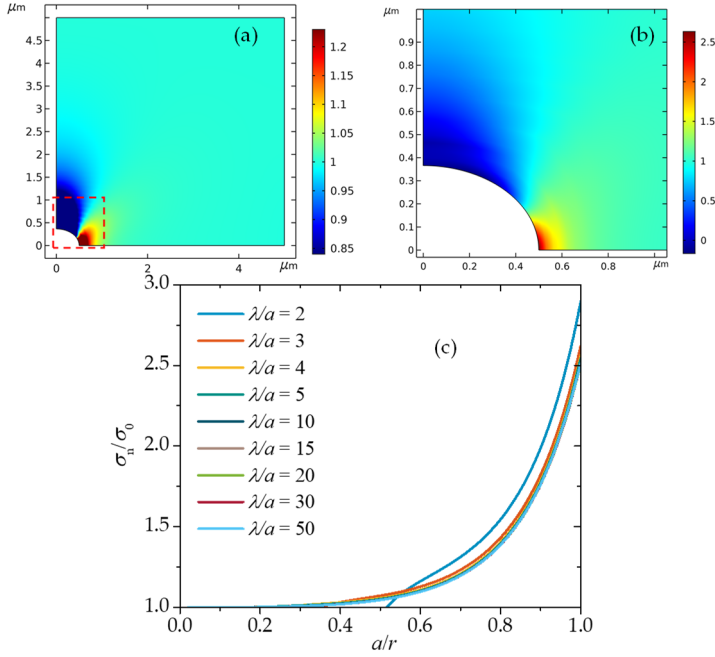
Fig. 5.2: (a): Distribution of the normal stress σ_n (normalised by the applied stress σ_0). (b): The circled region in (a). (c): Distribution of the normal stress σ_n along the grain boundary for various λ/a ratios. σ_0 and a correspond to the applied stress and the void radius, respectively. Note that the scale is different in (a) and (b).

The equilibrium vacancy concentration at the grain boundary corresponds to [38]:

$$x_v = x_v^{eq} = \exp\left(-\frac{Q(1 + \alpha s^2)}{k_B T}\right) \tag{5.3}$$

where Q is the vacancy formation energy at the grain boundary, α is a dimensionless proportionality constant, and s is the relative magnetic order parameter in the ferromagnetic state (scaled to its vale at $T = 0$ K). The vacancy formation energy at the grain boundary $Q = Q_{gb} \approx Q_m/2$ is taken as half of that in the bulk with $Q_m = 0.58$ eV [39]. The vacancy diffusivity at the grain boundary is taken as the Fe grain boundary diffusivity of the Fe host atoms [39], i.e., $D_{gb}^v = D_{gb}^h = D_{gb}^{Fe} = 1.74 \times 10^{-12}$ m^{2}s^{-1} at a temperature of 550 °C. The equilibrium vacancy concentration at the grain boundary of *bcc* Fe then corresponds to $x_v^{eq} \approx 7.4 \times 10^{-4}$ at 550 °C.

5.2.3 SOLUTE DIFFUSION AND CAVITY CLOSING

When a grain-boundary cavity, and hence an open volume, is present then healing solute atoms start to diffuse towards the cavity in order to precipitate at the cavity surface leading to a reduction in the level of supersaturation. The diffusion of solute atoms is driven by the solute concentration gradient, which can be described by

$$J_s = -\frac{1}{\Omega}\frac{D_s x_s}{kT}\nabla\mu = -\frac{1}{\Omega}D_s\nabla x_s \tag{5.4}$$

where D_s and x_s are the diffusivity and the concentration of the solute, respectively.

In a binary alloy system containing also vacancies the mass balance gives $x_s + x_h + x_v = 1$, where x_h is the concentration of host atoms. Assuming that the vacancy concentration is low everywhere in the system and at equilibrium, the flux of the host atoms can be written as $J_h = -\frac{1}{\Omega}D_h\nabla x_h \approx \frac{1}{\Omega}D_h\nabla x_s$. The difference in diffusivity between the host and the solute atoms results in a net vacancy flux, i.e., the Kirkendall flux:

$$J_v^K = -(J_s + J_h) \approx \frac{1}{\Omega}(D_s - D_h)\nabla x_s \tag{5.5}$$

The vacancy flux is oriented opposite to the direction of the fastest diffusing component. In a self-healing system, the solute atoms need to show a higher diffusivity than the host atoms in order to generate a vacancy flux oriented outwards of the cavity. 'Vacancies" making up the open volume of the pre-existing cavity can be removed from the cavity when the Kirkendall vacancy flux $|J_v^K|$ (oriented outwards) is higher than the stress-driven vacancy flux $|J_v^\sigma|$ (oriented inwards).

The *Transport of Diluted Species* module with linear Lagrange elements in COMSOL® [25] is used to simulate the solute transport to the cavity. The solute concentration at the cavity edge is maintained at 1 mol/m³ (0.07 at.%), while the initial solute concentration in the bulk and the grain boundary is set at 350, 700, 1400, 2800, 4200, and 5600 mol/m³, corresponding to a supersaturation of 0.25, 0.5, 1, 2, 3, and 4 at.%, respectively. The Au diffusivity in *bcc* Fe at 550 °C (7.39×10^{-19} m²/s) [40] is used as the solute diffusivity in the bulk, while the self-diffusivity for *bcc* Fe at 550 °C (1.50×10^{-21} m²/s) [40] is set as the host diffusivity in the bulk. In order to estimate the effect of (1) the

5

grain boundary diffusivity and (2) the interspacing between two neighbouring cavities on the solute transport efficiency, the grain boundary diffusivity is set to be 10^n times the diffusivity in the bulk, in which $n = 1 – 9$, while the length of the simulation box is set to 2.5, 5, 10, and 25 μm, corresponding to the relative inter-cavity spacing (λ/a) of 5, 10, 20 and 50. The simulation time is 1000 hours for all cases. In total 8319, 14527, 21601 and 26113 elements with 7395, 13456, 20398 and 24800 vertices are used for the simulation box with the length of 2.5, 5, 10, and 25 μm, respectively.

5.3. RESULTS AND DISCUSSION

5.3.1 SOLUTE TRANSFER PROFILE

Fig. 5.3(a) to (c) show the solute concentration profile for different D_{gb}/D_m ratios after 1000 hours, for a condition where the supersaturation is 1 at.% and the relative inter-cavity spacing is $\lambda/a = 20$. The white arrows indicate the transport direction of the solute. In Fig. 5.3(a) it can be seen that for a relatively low grain-boundary diffusivity ($D_{gb}/D_m = 10$) the solute transport has a 3D nature: the solute concentration contour reflects the geometry of the cavity, indicating a more or less uniform solute transport in both the matrix and in the grain boundary. As shown in Fig 3(c), for a relatively high value for the grain boundary diffusivity ($D_{gb}/D_m = 10^8$) the concentration profile reflects primarily the grain-boundary geometry (instead of the cavity geometry), indicating the 1D nature of the solute transport towards the grain boundary. In this case the grain boundary provides a fast diffusion path. As a result the solute in the matrix tends to diffuse vertically towards the grain boundary with a vertical diffusion length $L_\perp = 2\sqrt{D_m^s t}$ (D_m^s is the solute diffusivity in the matrix). The 1D nature of the diffusion pattern can also be induced from the direction of the diffusion indicated by the white arrows: in Fig. 5.3(c), the solute diffusion is approximately perpendicular to the grain boundary, while in (a), the diffusion direction is perpendicular to the cavity edge. As shown in Fig. 5.3(b), an intermediate value for the relative grain boundary diffusivity ($D_{gb}/D_m = 10^4$) provides a diffusion pattern that reflects a crossover between 1D and 3D solute diffusion. The present findings are in line with previous results by Versteylen and co-workers [27].

5
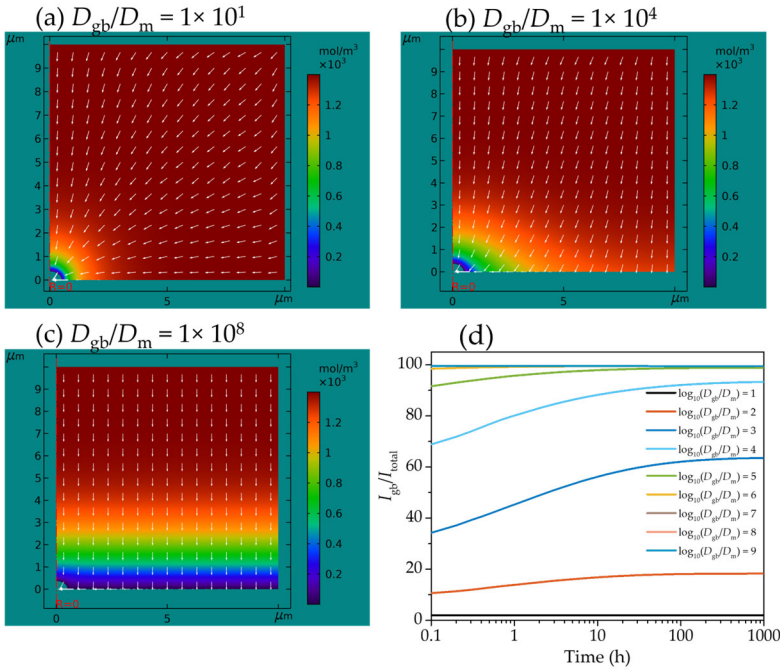
Fig. 5.3: (a) – (c): Solute concentration pattern after 1000 h. The supersaturation is set to Δx = 1 at.%, and the relative inter-cavity spacing is λ/a = 20. The grain-boundary/matrix diffusivity ratios are 10, 10⁴ and 10⁸, respectively. The white arrows indicate the local direction of the solute flux. (d): Fraction of I_{gb} in I_{total}, where I_{total} is the total surface integrated vacancy flux removed from the cavity and I_{gb} the is vacancy flux removed through the grain-boundary/cavity interface.

5

5.3.2 VACANCY FLUXES

As a result of the Kirkendall effect the solute diffusion generates a vacancy flux in the opposite direction. Thereby the vacancies present in the cavity can be removed through either the cavity/matrix interface, or the cavity/grain boundary interface. Fig. 5.3(d) shows the percentage of the vacancy flux through the cavity/grain boundary interface. It is clear that the higher the grain-boundary diffusivity, the larger fraction of vacancies that is removed via the grain boundary. In previous work [20], the ratio for Au diffusivity in the grain boundary (D_{gb}^{Au}) and in the *bcc* Fe matrix (D_m^{Au}) was estimated to be $D_{gb}^{Au}/D_m^{Au} = 10^5 - 10^6$, meaning that the grain boundary carries approximately 99% of the transport capacity for (λ/a) ≥ 20 (Fig. 5.3(d)), 91% for (λ/a) = 5, and 97% for (λ/a) = 10.

Fig. 5.4 shows the evolution of the inward stress-driven vacancy flux (dashed lines) and the outward Kirkendall vacancy flux (solid lines) as a function of time. The inward vacancy flux is constant in time and proportional to the applied stress, while the outward Kirkendall flux decreases with time and is affected by the grain-boundary diffusivity D_{gb}, the supersaturation Δx and the half inter-cavity spacing λ. The Kirkendall flux, which is proportional to the solute flux transported to the cavity, shows a power-law relationship with time $J_v^K \propto t^n$, with an time exponent n ranging from $n = -1/2$ to $n = 0$, depending on (D_{gb}/D_m) and (λ/a). From the value of the time exponent n, one can estimate whether the solute-driven vacancy diffusion has a 1D, 2D or 3D character [27]. For instance, in Fig. 5.4(a), for a low diffusivity ratio value $(D_{gb}/D_m = 10)$, the comparable diffusivity in the bulk and in the grain boundary leads to a solute diffusion field that is almost uniform in the bulk and in the grain boundary (as shown in Fig. 5.3(a)), indicating the 3D character of the diffusion. This is consistent with the time exponent n, which shows an increase from an initial value of about -1/2 and approaches 0 for longer times. It is worth to note that for an ideal 3D diffusion, the solute flux is constant for longer time scales, but even for a low diffusivity ratio, the 3D diffusion character will eventually breakdown once the depletion zone reaches the edge of the simulation box. After that, the depletion of the solute is no longer uniform throughout the matrix and the grain boundary, and the solute flux (as well as the Kirkendall vacancy flux) can no longer remain constant. For a high grain-boundary diffusivity $(D_{gb}/D_m = 10^6 – 10^9)$, the solute in the grain boundary depletes first, and during the this stage, the outward vacancy flux is determined by the grain boundary diffusivity D_{gb} and the width of the grain boundary δ. This process can be simplified as a 2D diffusion, where the solute atoms are mainly transported from the grain boundary (instead of the matrix) to the cavity surface and the time exponent for J_v^K corresponds to $n = 0$. After that, the grain boundary acts as a fast diffusion path, through which the solute in the bulk can be transported towards the cavity, and the diffusion pattern experiences a transition from 2D to 1D. Once the 1D diffusion pattern is developed, the bulk solute diffusivity becomes the limiting parameter for the solute transport, while the grain boundary diffusivity no longer limits the diffusion. Therefore, for high D_{gb}/D_m ratios (at fixed values of λ/a and supersaturation Δx) on longer time scales the flux into the cavity approaches to the same level and the time exponent stabilises at $n = -1/2$.

5
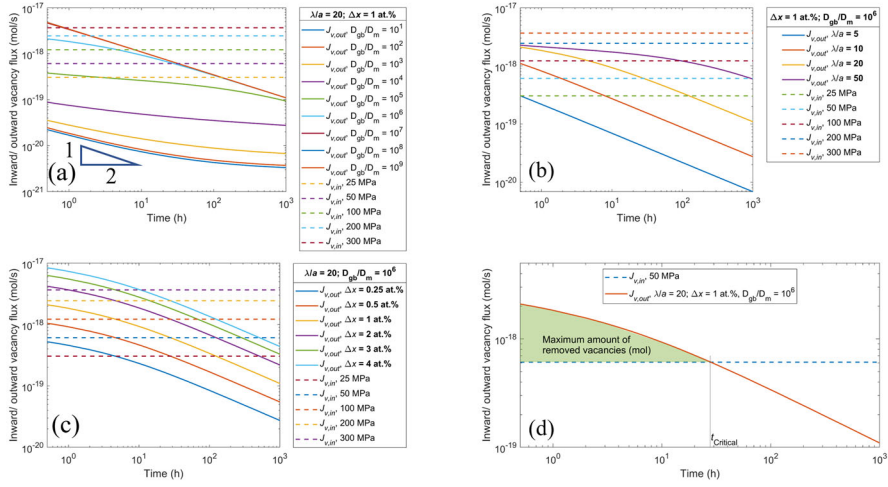
Fig. 5.4: (a) – (c): Stress-driven vacancy flux $|J_v^\sigma|$ (inward vacancy flux) and Kirkendall vacancy flux $|J_v^K|$ (outward vacancy flux) through the cavity surface. The effect of (a) the ratio of a variable grain-boundary diffusivity D_{gb} with respect to the matrix diffusivity D_m, (b) relative inter-cavity spacing λ/a, and (c) supersaturation Δx on the Kirkendall flux. The open volume of the cavity shrinks if the Kirkendall vacancy flux $|J_v^K|$ is larger than the stress-driven vacancy flux $|J_v^\sigma|$ and grows otherwise. The cross-over of the inward and outward fluxes corresponds to the critical time, at which the possible maximum filling is achieved and the open volume of the cavity starts to grow if not fully healed. The integrated area between the two fluxes corresponds to the net amount of vacancies removed by the Kirkendall flux at the corresponding time (in mol unit). An example is shown in (d).

The 2D to 1D transition can be seen clearly in Fig. 5.4(b): for a relatively large value of λ/a (see e.g. λ/a = 50), the time exponent n decreases gradually from 0 to -1/2. For a fixed grain-boundary diffusivity D_{gb}, the transition time for the crossover from 2D to 1D behaviour is determined by the time required for the depletion of the solute in the grain boundary. This cross-over time from 2D to 1D behaviour $t_{2D\text{-}1D}$ can be estimated by comparing the diffusion length $2\sqrt{D_{gb}t}$ with the distance between the cavity and the edge of the simulation box λ - a, resulting in $t_{2D\rightarrow1D} \approx 4(\lambda - a)^2/D_{gb} \approx 4\lambda^2/D_{gb}$. For relatively small values of λ/a (see λ/a = 5 and 10), the 1D diffusion pattern is developed within relatively short time scales, so that the time exponent starts from -1/2 in our simulations. During the 2D diffusion stage, the outward vacancy flux, which is limited by the grain-boundary diffusivity D_{gb}, is the same for different λ/a ratios as the diffusion profile has not reached the edge of the diffusion box.

While during the 1D diffusion stage, where the matrix diffusivity D_m is the limiting parameter, the outward vacancy flux is proportional to the $(\lambda/a)^2$. It is observed from Fig. 5.4(c) that the supersaturation Δx does not change the nature of the diffusion, but a higher supersaturation leads to a higher concentration gradient, and therefore a larger solute flux into the cavity.

As explained in section 5.2, the open volume of the cavity shrinks when the Kirkendall vacancy flux is larger than the stress-driven vacancy flux and grows otherwise. The time integrated difference between the two vacancy fluxes equals to the amount of vacancies removed from the pre-existed cavity at the corresponding time (in mol). Since the stress-driven vacancy flux is assumed to be constant, while the outward vacancy flux decreases with time, a cross-over takes place at a certain time t_{cr}, at which the possible maximum filling is achieved and the cavity, if not fully healed, starts to grow although solutes remain to be transported to the cavity, as illustrated in Fig. 5.4(d).

5.3.3 FILLING RATIO

Starting from a pre-existing cavity with an initial volume V_0, hypothetical 'vacancies' making up the cavity are being removed by the Kirkendall flux ($J_v^K > 0$) and real vacancies coming from the solid matrix are added by the stress-driven vacancy flux ($J_v^\sigma > 0$). In the current model we do not actually calculate the displacement of the original pore-matrix boundary, but keep it constant and only calculate the total volume of solute atoms entering the cavity and forming the precipitate. We make no assumptions on the shape of the precipitate, nor do we describe the precipitate/remaining empty pore interface. In this sense the model is a degenerate moving boundary or Stephan problem [41].

The filling ratio is can now simply be defined as the ratio between the net amount of the removed vacancies and the amount vacancies in the original cavity (V/Ω):

$$FR = \left(\frac{\Omega}{V}\right) \int_0^t \left[\oint_S (J_v^K + J_v^\sigma)dS\right] dt' \qquad (5.6)$$

where S is the cavity surface and t the time (note that the positive direction for the flux through the closed surface S is pointing outwards). It is assumed that the stress-driven vacancy flux only enters the cavity through the grain boundary/cavity interface, while the Kirkendall flux can enter the cavity from

5

both the grain boundary and from the matrix. The filling ratio thus defined effectively equals the filling ratio as defined in experimental high-resolution tomographic studies on creep damage healing (the volume of the precipitate divided by the sum of that volume and the remaining empty cavity) [17, 23].
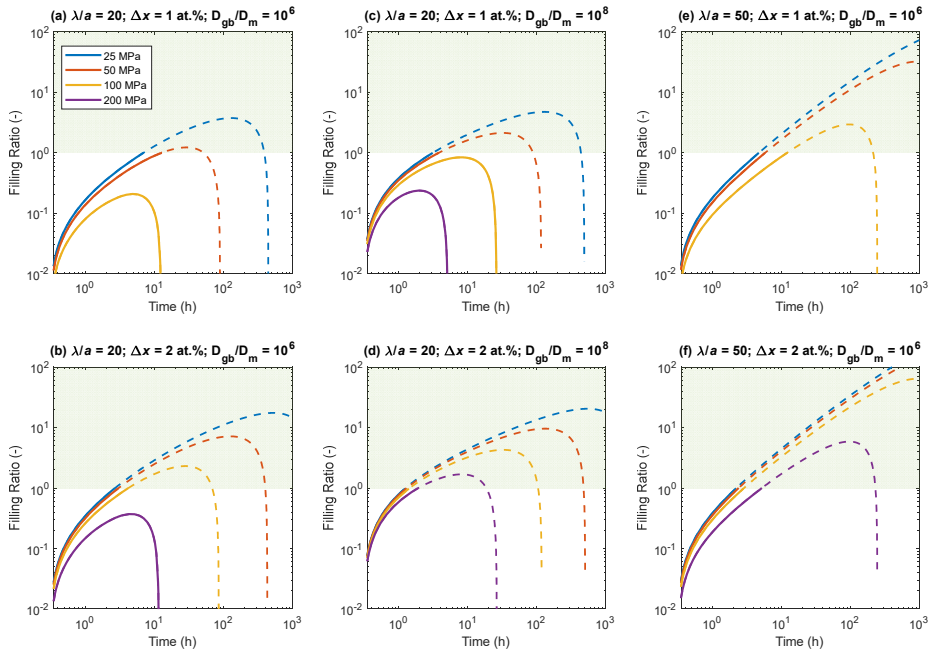
Fig. 5.5: Time evolution of the filling ratio as a function of applied stress σ_0 for different values of the supersaturation Δx, the grain-boundary diffusivity to matrix diffusivity ratio D_{gb}/D_m and the relative inert-cavity spacing λ/a. A cavity with a filling ratio equal to or higher than 1 (highlighted green) is regarded as fully-filled. The transport of the vacancies and solute stops after the cavity is fully filled. The data in (a) for 200 MPa is below the lower limit.

Fig. 5.5 compares the time evolution of the filling ratio for different values of the supersaturation Δx, the grain boundary/matrix diffusivity ratio D_{gb}/D_m, the relative inter-cavity spacing λ/a and the applied stress σ_0. We can clearly distinguish two sorts of overall behaviour: for the first one, the cavity can become fully filled (i.e. proceeds to a FR of 1.0) at the healing time t_h and the reaction stops.. For the second type, the filling ratio initially increases and then peaks at a critical time t_{cr} at a level below $FR = 1$, which corresponds to the maximum filling ratio that can be achieved. For $t > t_{cr}$ the filling ratio again

decreases, indicating that the open volume of the cavity starts to grow faster than can be made up by the solute transport.. When the filling ratio eventually reaches a negative value (*FR* < 0), the open volume of the partially filled cavity is larger than its original size. For the sake of completeness the dashed line segments in the figures 5 for conditions at which the condition *FR* = 1 is reached show the hypothetical behaviour assuming that achieving the completely filled state does not lead to a change in transport rate. The filling ratio demonstrates the competition between the outward Kirkendall vacancy flux and the inward stress-driven vacancy flux. Generally, at a given time, a higher filling ratio can be achieved with a higher supersaturation, a higher grain-boundary diffusivity and a larger relative inter-cavity spacing, while a higher stress level results in a lower filling ratio.
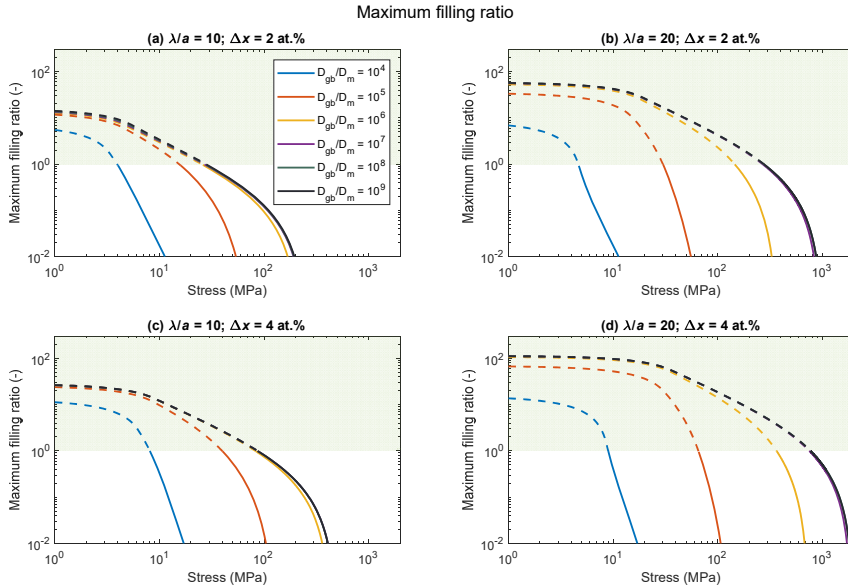
Fig. 5.6: Maximum filling ratio as a function of applied stress σ_0 for different values of the supersaturation Δx, the grain-boundary diffusivity to matrix diffusivity ratio D_{gb}/D_m and the relative inert-cavity spacing λ/a. For a maximum filling ratio equal to or higher than 1, the cavity can be fully filled under the corresponding combination of parameters. Note that the curves overlap for $D_{gb}/D_m > 10^6$.

Fig. 5.6 shows the maximum filling ratio for various combinations of parameters. In Fig. 5.7, the time of healing t_h (solid line, for the case where the cavity can be fully filled) and the critical time t_{cr} (dotted line, for the case where the cavity cannot be fully filled) are presented. Since the stress-driven inward

vacancy flux eventually will exceed the outward Kirkendall vacancy flux, for proper healing it is crucial that the cavity becomes free of any remaining 'empty' volume before t_{cr} is reached.
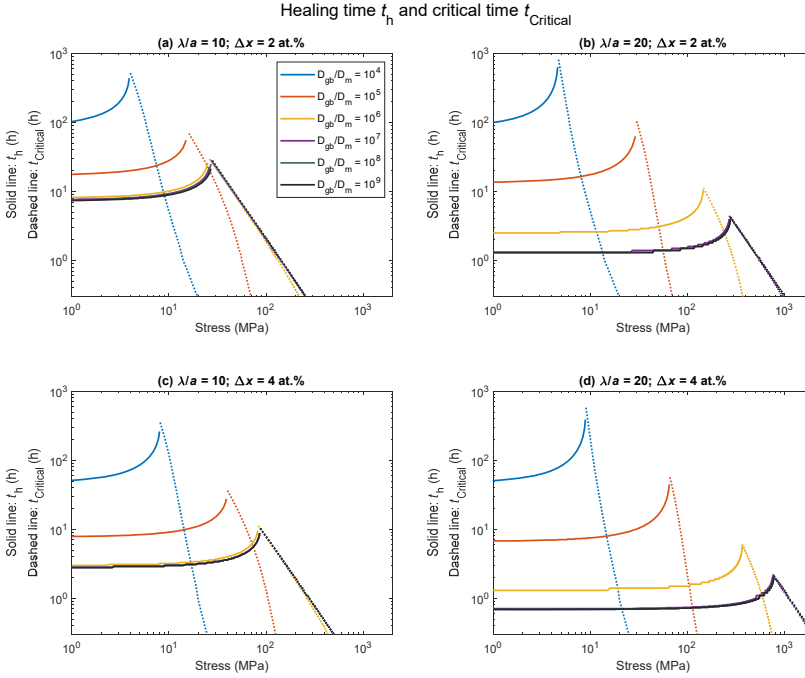
Fig. 5.7: Time of healing t_h at which the cavity is fully filled (solid lines, for the situations where the cavity can be fully filled) and critical time t_{cr} at which the maximum filling is achieved (dotted lines, for the situations where fully filling cannot be achieved) as a function of applied stress σ_0 for different values of the supersaturation Δx, the grain-boundary diffusivity to matrix diffusivity ratio D_{gb}/D_m and the relative inert-cavity spacing λ/a. For $t < t_{cr}$, the net vacancy flux is oriented away from the cavity and therefore the cavity is shrinking as the vacancies are removed from the open volume of the cavity by the Kirkendall flux. For $t > t_{cr}$, the net vacancy flux is oriented towards the cavity, leading to a growth of the open volume of the cavity. Note that the curves overlap for $D_{gb}/D_m > 10^6$.

5.3.4 CRITICAL STRESS

From Figs. 6 and 7 it is clear that there is an upper threshold for the applied stress, above which the cavity cannot be fully filled. In Fig. 5.8 the calculated critical stress as a function of the grain-boundary/bulk diffusivity ratio D_{gb}/D_m is shown for different values of the relative inter-cavity spacing λ/a and the

supersaturation Δx. It can be seen that both the grain boundary diffusivity and the inter-cavity spacing play a significant role in the critical stress. The critical stress increases with the grain boundary diffusivity D_{gb}, until it reaches a level where a quasi 1D diffusion pattern exists and the bulk diffusivity becomes the limiting diffusion rate. When D_{gb} is high enough so that D_m becomes the limiting diffusion rate, a larger inter-cavity spacing λ results in a higher critical stress, since the solute atoms are collected and transported towards the cavity over a larger grain-boundary surface area $\pi(\lambda^2 - a^2)$.

With a small relative inter-cavity spacing (e.g. $\lambda/a = 5$), the critical stress level is expected to be low even if the grain boundary diffusivity is sufficiently high. This is the situation for the late creep stages : more cavities are located at the grain boundary, resulting in a decrease in the cavity interspacing. This further leads to a fast growth of the open volume of the cavity and the subsequent coalesce of neighbouring cavities, which causes the catastrophic failure of the material. In the initial creep stage, where the grain boundary cavities have a small size and the inter-cavity interspacing is large, the cavities can still be filled relatively easy. In the fully-filled cavities the open volume disappears and the open volume will need to nucleate somewhere else at the grain boundary, in which case the vacancy and solute diffusion start over again.

From Fig. 5.8 it can be deduced that the critical stress can be raised by increasing (a) the supersaturation level, and (b) the diffusivity difference between the healing solute and the host. In practice, the intended supersaturation level should not be higher than a certain limit dictated by the criteria that the healing atoms are fully soluble in the matrix at the homogenising temperature, and that the strain penalty between the matrix and the precipitate is large enough to suppress solute consuming precipitation in the bulk. Furthermore, the diffusivity for the solute should always be higher than the diffusivity of the host, while a higher solute ratio is beneficial.

For the situation of 3D diffusion the grain boundary diffusivity and the bulk diffusivity should be comparable, the solute atoms can be transported to the cavity if their distance to the cavity surface is less than the diffusion length $L = 2\sqrt{D_s t}$ (D_s being the diffusivity of the solute atoms), resulting in a depletion zone of the healing atoms resembling the shape of the cavity, and the critical stress is independent of the interspacing distance λ. For the situation of

5

1D diffusion, as explained in sections 5.3.1 and 5.3.2, all the solute atoms within a volume $\pi(\lambda^2 - a^2)L_\perp$ on both sides of the grain boundary can be transported to the cavity (where $L_\perp$ is the vertical diffusion length determined by the solute diffusivity in the bulk D_m^s), and therefore a large λ significantly increase the healing capacity. In practice, a quasi-1D diffusion pattern is observed [20] since the grain boundary diffusivity is usually orders of magnitude higher than the bulk diffusivity.
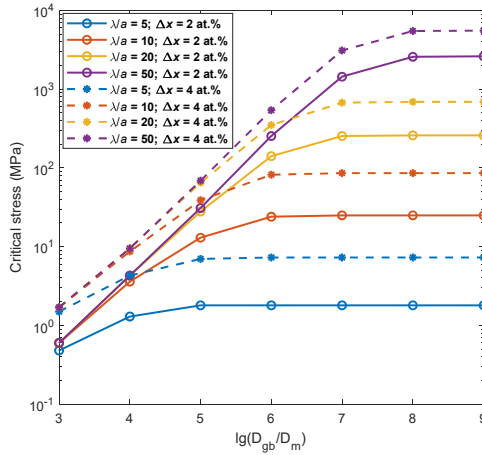
Fig 5.8: Critical stress as a function of the grain-boundary/bulk diffusivity ratio D_{gb}/D_m for different values of the relative inter-cavity spacing λ/a (colours) and the supersaturation Δx (markers and line types). Full filling can only be achieved when the applied stress is below the critical value.

The effect of the supersaturation on the critical stress is shown in Fig. 5.9. A scaling relation $\sigma_{Critical} \propto (\Delta x)^m$ applies, with $m \approx 1$ for a lower D_{gb}/D_m ratio (indicating a 3D diffusion), and $m \approx 2$ for a higher D_{gb}/D_m ratio (indicating a 1D diffusion), respectively. The 3D to 1D transition is especially obvious with a lower interspacing/pore radius ratio $\lambda/a = 10$, since less time is required to develop the 1D diffusion pattern for a lower interspacing-radius ratio. In fact, when $\lambda/a = 10$, the bulk diffusivity becomes the limiting parameter when $D_{gb}/D_m \geq 10^6$, while for a higher interspacing-radius ratio $\lambda/a = 50$, the grain boundary diffusivity D_{gb} still plays a role on the critical stress when $D_{gb}/D_m = 10^8$.
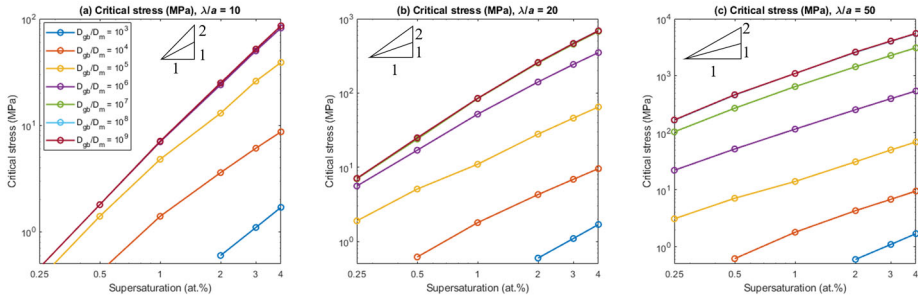
Fig. 5.9: Critical stress as a function of supersaturation Δx. Different colours correspond to grain boundary/bulk diffusivity ratio D_{gb}/D_m. From (a) to (c), the inter-cavity spacing λ/a ratio is equal to 10, 20 and 50, respectively.
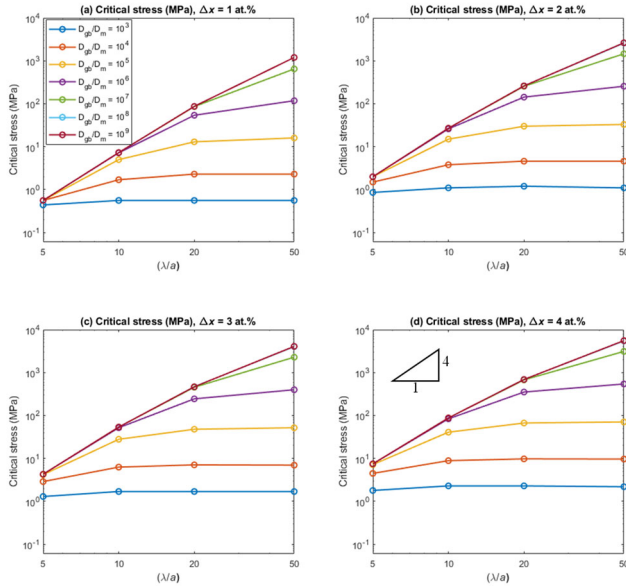
Fig. 5.10: Critical stress σ_{cr} as a function of the relative inter-cavity spacing λ/a for different levels of supersaturation Δx and different values of the grain boundary/bulk diffusivity ratio D_{gb}/D_m. From (a) to (d), supersaturation Δx is equal to 1, 2, 3, and 4 at.%, respectively.

The interspacing-radius ratio λ/a has a crucial influence on the critical stress, as demonstrated in Fig. 5.10. A scaling relationship $\sigma_{Critical} \propto (\lambda/a)^k$ is obtained with $k = 0 - 4$. For a lower D_{gb}/D_m ratio, which corresponds to a 3D

diffusion regime, the critical stress is almost independent of λ/a. In this situation, the healing atoms are transported through the bulk, and whether a solute atom can be transported towards the cavity is determined by its distance to the cavity surface. Therefore, the interspacing distance λ does not significantly affect the healing kinetics. However, a higher D_{gb}/D_m ratio results in a 1D diffusion, where a solute atom can be transported towards the cavity through the grain boundary (instead of through the bulk) as long as its vertical distance to the grain boundary is within the diffusion length $L_\perp = 2\sqrt{D_x^m t}$. As a result, a larger λ means that more solute atoms can be used to heal the cavity, leading to a higher critical stress.

5.3.5 ANALYTICAL MODEL

From the finite element model simulations we can identify the dominant mechanism for the self healing of creep cavities by supersaturated solute corresponds to 1D matrix diffusion of the solute towards the grain boundary and subsequently transport of this solute though the grain boundary towards the free cavity surface connected to the grain boundary. This 1D solute diffusion is observed for the following conditions: (1) $D_{gb} \gg D_m^s > D_m^h$ and (2) $2\sqrt{D_{gb}t} \gg (\lambda - a)$. The first condition indicates the grain boundary acts as a much faster transport route for solute than the matrix. In order to reverse the vacancy flux by the Kirkendall effect, the diffusivity of the solute atoms needs to be higher than that of the host atoms in the matrix. The second condition requires that the grain boundary is largely depleted from supersaturated solutes as the diffusion length exceeds the distance between the creep cavity surface and the edge of the simulation box (half of the inter-cavity spacing). This condition can only be met for a finite inter-cavity spacing, which is generally the case for practical situations. The second condition can also be translated in a time requirement: $t \gg t_{2D \rightarrow 1D} \approx 4(\lambda - a)^2 / D_{gb}$. For $\lambda = 20$ μm and $D_{gb} = 2.4 \times 10^{-14}$ m²s⁻¹ (at 550 ℃) [20] this characteristic time for the onset of 1D diffusion amounts to $t_{2D\text{-}1D} \approx 400$ s. Under these conditions an approximate analytical model will be constructed, for which the results can than subsequently be compared to those of the full finite element model.

The time evolution of the cavity depends on the competition between the stress-driven vacancy flux and the Kirkendall vacancy flux. Combining Eqs.

(1) and (2) the stress-driven vacancy flux at the interface between the cavity surface and the grain boundary ($r = a$) can be written as:

$$J_v^\sigma(a) = \left(\frac{D_{gb}^v x_v}{kT}\right)\nabla\sigma|_{r=a} = -\left(\frac{D_{gb}^v x_v}{kT}\right)AB\exp(B)\left(\frac{\sigma_0}{a}\right) \qquad (5.7)$$

where A and B are the fitting parameters for the stress distribution along the grain boundary.

This inward stress-driven vacancy flux is constant in time given a stable stress distribution. The integrated stress-driven flux provides the time evolution of the open volume of the cavity:

$$V(t) = V(0) + V_\sigma(t) = V_0 - (2\pi a\delta)J_v^\sigma(a)\Omega t = V_0 + \alpha\sigma_0 t \qquad (5.8)$$

where $V_0 \propto a^3$ is the initial cavity volume and $\alpha = \left(\frac{D_{gb}^v x_v}{kT}\right)(2\pi\delta)\Omega AB\exp(B)$ is a temperature dependent constant.

For 1D solute diffusion in the matrix towards the grain boundary the difference in diffusivity between the solute and the host atoms results in a 1D Kirkendall vacancy flux at the interface between the matrix and the grain boundary. When the solute transport is much faster in the grain-boundary than in the matrix the solute concentration in the grain boundary is nearly constant and close to its equilibrium value. In that case the 1D Kirkendall vacancy flux at the interface between the matrix and the grain boundary can be estimated by [27]:

$$J_v^K\left(|z| = \frac{\delta}{2}, t\right) \approx -\frac{(D_m^s - D_m^h)\Delta x}{\Omega}\frac{1}{\sqrt{\pi(D_m^s - D_m^h)t}} \qquad (5.9)$$

where D_m^s and D_m^h are the matrix diffusivities for the solute and the host atoms, respectively. This Kirkendall vacancy flux is time dependent and for $D_m^s > D_m^h$ oriented from the grain boundary towards the matrix. The integrated vacancy flux provides the time evolution of the open volume of the cavity:

$$V_K^{1D}(t) \approx 2[\pi(\lambda^2 - a^2)]\Omega\int_0^t J_v^K\left(|z| = \frac{\delta}{2}, t'\right)dt' = -\beta t^{1/2} \qquad (5.10)$$

where the factor arises from the vacancy transport at the top and bottom interfaces of the grain boundary and $\beta = 4(\lambda^2 - a^2)\Delta x \sqrt{\pi(D_m^s - D_m^h)}$ is a temperature dependent constant.

Combining all contributions to the time evolution of the open volume of the cavity gives:

$$V(t) = V(0) + V_\sigma(t) + V_K^{1D}(t) = V_0 + \alpha\sigma_0 t - \beta t^{-1/2} \qquad (5.11)$$

Healing of a creep cavity is achieved when the open volume of the cavity vanishes as a result of the solute transport at $V = 0$. The lowest time solution is given by $t^{1/2} = \left[\beta - \sqrt{\beta^2 - 4\alpha\sigma_0 V}\right]/2\alpha\sigma_0$. The critical maximum stress for which a solution can be obtained is:

$$\sigma_{cr} = \frac{\beta^2}{4\alpha V_0} \propto \left(\frac{\lambda^2 - a^2}{a^2}\right)^2 \left(\frac{D_m^s - D_m^h}{D_{gb}^v}\right)(\Delta x)^2 \approx \left(\frac{\lambda}{a}\right)^4 \left(\frac{D_m^s}{D_{gb}^v}\right)(\Delta x)^2 \qquad (5.12)$$

The corresponding critical time is related to the critical stress by $\alpha t_{cr}\sigma_{cr} = V_0$. As shown in Fig. 5.11, the value of $\alpha t_{cr}\sigma_{cr} / V_0$ is approximately constant for a low inter-spacing ratio λ/a. For an inter-spacing ratio $\lambda/a = 5$ and a diffusivity ratio D_{gb}/D_m higher than 10^5, a value of $\alpha t_{cr}\sigma_{cr}/V_0 = 2.3$ is found, which indicates that the simplified analytical model is a reasonable approximation. Assuming that the region where the processes are dominated by 1D diffusion is marked by a value of $\alpha t_{cr}\sigma_{cr}/V_0 < 10$, then it can be seen that for diffusivity ratio D_{gb}/D_m higher than 10^7, the 1D diffusion behaviour is found for $\lambda/a < 30$. For lower values of the diffusivity ratio ($D_{gb}/D_m < 10^7$) the critical λ/a value for 1D diffusion behaviour continuously decreases and reaches a value of $\lambda/a \approx 10$ for $D_{gb}/D_m = 10^4$. This behaviour is qualitatively in line with the 1D diffusion results in the absence of stress [27]. The critical time is the maximum time for which a solution can be obtained and this scales as:

$$t_{cr} = \frac{4V_0}{\beta^2} \propto \left(\frac{\lambda^2 - a^2}{a^2}\right)^{-2} \left(D_m^2 - D_m^h\right)^{-1}(\Delta x)^{-2} \approx \left(\frac{\lambda}{a}\right)^{-4} (D_m^s)^{-1}(\Delta x)^{-2} \quad (5.13)$$

For a stress below the critical stress ($\sigma_0 < \sigma_{cr}$) the time to complete filling t_h can be expressed in terms of the critical time t_{cr} and the critical stress σ_{cr} :

$$\frac{t_h}{t_{cr}} = \left(\frac{\sigma_{cr}}{\sigma_0}\right)^2 \left[1 - \sqrt{1 - \frac{\sigma_0}{\sigma_{cr}}}\right]^2 \qquad (5.14)$$

The healing time grows continuously to $t_h = t_{cr}$ for $\sigma_0 = \sigma_{cr}$. These results of the simplified analytical model for the case of 1D solute diffusion are qualitatively in line with the results of the finite element model calculations. It is worth to recall that these time scales need to be large compared to the characteristic time scale $t_{2D\rightarrow 1D} \approx \lambda^2 / (4D_{gb})$, which is required to deplete the solute in the grain boundary and establish the 1D diffusion pattern.
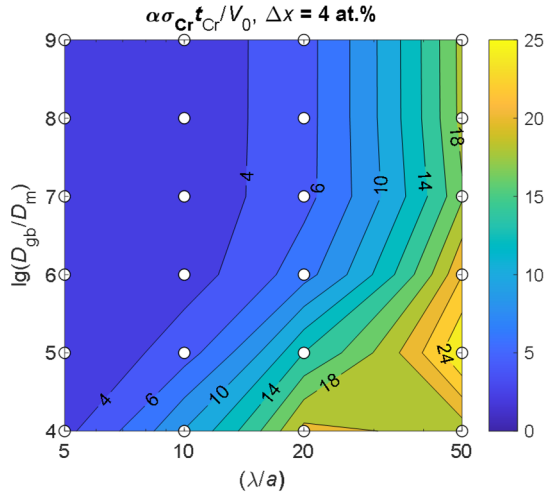
Fig. 5.11:. The value of $\alpha t_{cr}\sigma_{cr}/V_0$ for as a function of the relative inter-cavity spacing λ/a and the grain boundary/bulk diffusivity ratio D_{gb}/D_m for a supersaturation Δx of 4 at.% . A value close to 1 represents a 1D diffusion pattern. The contour where $\alpha t_{cr}\sigma_{cr}/V_0 = 10$ is plotted to indicate the boundary for the 1D diffusion regime.

5.4. CONCLUSIONS

We have developed a set of models which predicts the growth and filling of grain boundary creep cavities in self-healing binary alloys as a function of time, stress, level of supersaturation and inter-cavity spacing and diffusion ratio's. The competition between the inward and outward vacancy fluxes results in the growth or shrinkage of the open volume of the creep cavity. It is found that the filling ratio shows a maximum value at a critical time t_{cr}, which corresponds to the time when the inward vacancy flux exceeds the outward vacancy flux (integrated over the surface area). Two conditions can be distinguished: one

where the cavity becomes fully filled before this critical time is reached (and the process stops) and one where the only partial filling will take place and the growth of the cavity will continue, For each combination of parameters, the critical applied stress σ_{cr} is calculated, below which the cavity can be fully filled.

The analytical model, fed by insights from the numerical model, shows that for conditions leading to quasi 1D solute transport, the critical stress approximately scales as $\sigma_{cr} \propto (\lambda/a)^4 \left(D_m^s/D_{gb}^v\right)(\Delta x)^2$, where λ/a is the relative inter-cavity spacing, D_m^s/D_{gb}^v the ratio of the solute diffusivity in the matrix and the vacancy diffusion in the grain boundary and Δx is the supersaturation of the solute. The critical healing time obtained at the critical stress scales as $t_{cr} \propto 1 / \sigma_{cr}$, while for lower stresses the pore filling time t_h can be expressed in terms of t_{cr} and σ_{cr}.

ACKNOWLEDGMENTS

REFERENCES

[1] J.N. Greenwood, D.R. Miller, J.W. Suiter, Intergranular Cavitation in Stressed Metals, Acta Metall. Mater. 2(2) (1954) 250-258.

[2] F. Abe, Progress in Creep-Resistant Steels for High Efficiency Coal-Fired Power Plants, J. Press. Vessel Technol. 138(4) (2016) 040804.

[3] K. Maruyama, K. Sawada, J.-i. Koike, Strengthening Mechanisms of Creep Resistant Tempered Martensitic Steel, ISIJ Inter. 41(6) (2001) 641-653.

[4] F.R.N. Nabarro, H.L. de Villiers, The Physics of Creep: Creep and Creep-resistant Alloys, 1st ed., CRC Press1995.

[5] M. Taneike, F. Abe, K. Sawada, Creep-strengthening of steel at high temperatures using nano-sized carbonitride dispersions, Nature 424(6946) (2003) 294-296.

[6] B. Grabowski, C.C. Tasan, Self-Healing Metals, Self-healing Materials2016, pp. 387-407.

[7] M.D. Hager, P. Greil, C. Leyens, S. van der Zwaag, U.S. Schubert, Self-healing materials, Adv. Mater. 22(47) (2010) 5424-30.

5

[8] N. van Dijk, S. van der Zwaag, Self-Healing Phenomena in Metals, Adv. Mater. Interfaces 5(17) (2018) 1800226.

[9] K. Laha, J. Kyono, S. Kishimoto, N. Shinya, Beneficial effect of B segregation on creep cavitation in a type 347 austenitic stainless steel, Scr. Mater. 52(7) (2005) 675-678.

[10] K. Laha, J. Kyono, T. Sasaki, S. Kishimoto, N. Shinya, Improved creep strength and creep ductility of type 347 austenitic stainless steel through the self-healing effect of boron for creep cavitation, Metall. Mater. Trans. A 36(2) (2005) 399-409.

[11] N. Shinya, J. Kyono, K. Laha, Self-healing Effect of Boron Nitride Precipitation on Creep Cavitation in Austenitic Stainless Steel, J. Intell. Mater. Syst. Struct. 17(12) (2016) 1127-1133.

[12] N. Shinya, J. Kyono, K. Laha, C. Masuda, Self healing of creep damage through autonomous boron segregation and boron nitride precipitation during high temperature use of austenitic stainless steels, Proceedings of the First International Conference on Self Healing Materials, Noordwijk aan Zee, The Netherlands, 2007.

[13] R.N. Lumley, A.J. Morton, I.J. Polmear, Enhanced creep performance in an Al-Cu-Mg-Ag alloy through underageing, Acta Mater. 50(14) (2002) 3597-3608.

[14] R.N. Lumley, I.J. Polmear, Advances in self healing of metals, Proceedings of the First International Conference on Self Healing Materials, Noordwijk aan Zee, The Netherlands, 2007.

[15] S.M. He, P.N. Brandhoff, H. Schut, S. van der Zwaag, N.H. van Dijk, Positron annihilation study on repeated deformation/precipitation aging in Fe–Cu–B–N alloys, J. Mater. Sci. 48(18) (2013) 6150-6156.

[16] S.M. He, N.H. van Dijk, M. Paladugu, H. Schut, J. Kohlbrecher, F.D. Tichelaar, S. van der Zwaag, In-situ determination of aging precipitation in deformed Fe-Cu and Fe-Cu-B-N alloys by time-resolved small-angle neutron scattering, Phys. Rev. B 82(17) (2010) 174111.

[17] S.M. He, N.H. van Dijk, H. Schut, E.R. Peekstok, S. van der Zwaag, Thermally activated precipitation at deformation-induced defects in Fe-Cu and Fe-Cu-B-N alloys studied by positron annihilation spectroscopy, Phys. Rev. B 81(9) (2010) 094103.

[18] H. Fang, C.D. Versteylen, S. Zhang, Y. Yang, P. Cloetens, D. Ngan-Tillard, E. Brück, S. van der Zwaag, N.H. van Dijk, Autonomous filling of creep cavities in Fe-Au alloys studied by synchrotron X-ray nano-tomography, Acta Mater. 121 (2016) 352-364.

5

[19] S. Zhang, J. Kohlbrecher, F.D. Tichelaar, G. Langelaan, E. Brück, S. van der Zwaag, N.H. van Dijk, Defect-induced Au precipitation in Fe–Au and Fe–Au–B–N alloys studied by in situ small-angle neutron scattering, Acta Mater. 61(18) (2013) 7009-7019.

[20] S. Zhang, C. Kwakernaak, W. Sloof, E. Brück, S. van der Zwaag, N. van Dijk, Self Healing of Creep Damage by Gold Precipitation in Iron Alloys, Adv. Eng. Mater. 17(5) (2015) 598-603.

[21] S. Zhang, C. Kwakernaak, F.D. Tichelaar, W.G. Sloof, M. Kuzmina, M. Herbig, D. Raabe, E. Brück, S. van der Zwaag, N.H. van Dijk, Autonomous Repair Mechanism of Creep Damage in Fe-Au and Fe-Au-B-N Alloys, Metall. Mater. Trans. A 46(12) (2015) 5656-5670.

[22] S. Zhang, G. Langelaan, J.C. Brouwer, W.G. Sloof, E. Brück, S. van der Zwaag, N.H. van Dijk, Preferential Au precipitation at deformation-induced defects in Fe–Au and Fe–Au–B–N alloys, J. of Alloys Compd. 584 (2014) 425-429.

[23] S. Zhang, H. Fang, M.E. Gramsma, C. Kwakernaak, W.G. Sloof, F.D. Tichelaar, M. Kuzmina, M. Herbig, D. Raabe, E. Brück, S. van der Zwaag, N.H. van Dijk, Autonomous Filling of Grain-Boundary Cavities during Creep Loading in Fe-Mo Alloys, Metall. Mater. Trans. A 47(10) (2016) 4831-4844.

[24] H. Fang, N. Szymanski, C.D. Versteylen, P. Cloetens, C. Kwakernaak, W.G. Sloof, F.D. Tichelaar, S. Balachandran, M. Herbig, E. Brück, S. van der Zwaag, N.H. van Dijk, Self healing of creep damage in iron-based alloys by supersaturated tungsten, Acta Mater. 166 (2019) 531-542.

[25] Y. Fu, C. Kwakernaak, W.G. Sloof, F.D. Tichelaar, E. Brück, S. van der Zwaag, N.H. van Dijk, Competitive Healing of Creep-Induced Damage in a Ternary Fe-3Au-4W Alloy, Metall. Mater. Trans. A 51(9) (2020) 4442-4455.

[26] C.D. Versteylen, M.H.F. Sluiter, N.H. van Dijk, Modelling the formation and self-healing of creep damage in iron-based alloys, J. Mater. Sci. 53(20) (2018) 14758-14773.

[27] COMSOL Multiphysics® v. 5.6. www.comsol.com. COMSOL AB, Stockholm, Sweden.).

[28] R. Raj, M.F. Ashby, Intergranular fracture at elevated temperature, Acta Metall. Mater. 23(6) (1975) 653-666.

[29] C.D. Versteylen, N.K. Szymański, M.H.F. Sluiter, N.H. van Dijk, Finite element modelling of creep cavity filling by solute diffusion, Philos. Mag. 98(10) (2018) 864-877.

[30] M.E. Kassner, T.A. Hayes, Creep cavitation in metals, Int. J. Plast. 19(10) (2003) 1715-1748.

5

[31] W. Beere, M.V. Speight, Creep cavitation by vacancy diffusion in plastically deforming solid, Met. Sci. 12(4) (1978) 172-176.

[32] G.H. Edward, M.F. Ashby, Intergranular Fracture during Power-Law Creep, Acta Metall. Mater. 27(9) (1979) 1505-1518.

[33] A. Needleman, J.R. Rice, Plastic Creep Flow Effects in the Diffusive Cavitation of Grain-Boundaries, Acta Metall. Mater. 28(10) (1980) 1315-1332.

[34] E. Van Der Giessen, M.W.D. Van Der Burg, A. Needleman, V. Tvergaard, Void growth due to creep and grain boundary diffusion at high triaxialities, J. Mech. Phys. Solids. 43(1) (1995) 123-165.

[35] I.W. Chen, A.S. Argon, Diffusive growth of grain-boundary cavities, Acta Metall. Mater. 29(10) (1981) 1759-1768.

[36] A. Inoue, H. Nitta, Y. Iijima, Grain boundary self-diffusion in high purity iron, Acta Mater. 55(17) (2007) 5910-5916.

[37] C. Herring, Diffusional Viscosity of a Polycrystalline Solid, Int. J. Appl. Phys. 21(5) (1950) 437-445.

[38] N. Eliaz, L. Banks-Sills, Chemical Potential, Diffusion and Stress – Common Confusions in Nomenclature and Units, Corros. 26(2-3) (2008).

[39] D. Hull, D.E. Rimmer, The growth of grain-boundary voids under stress, Philos. Mag. 4(42) (1959) 673-687.

[40] ASM Handbook, Volume 1, ASM International, Materials Park, OH, 1990.

[41] L. Ruch, D.R. Sain, H.L. Yeh, L.A. Girifalco, Analysis of Diffusion in Ferromagnets, J. Phys. Chem. Solids. 37(7) (1976) 649-653.

[42] C.D. Versteylen, N.H. van Dijk, M.H.F. Sluiter, First-principles analysis of solute diffusion in dilute bcc Fe-X alloys, Phys. Rev. B 96(9) (2017) 094105.

[43] E. Javierre, C. Vuik, F.J. Vermolen, S. van der Zwaag, A comparison of numerical models for one-dimensional Stefan problems, J. Comput. Appl. Math 192(2) (2006) 445-459.

5

岁月·文明(suì yuè, wén míng): civilisation, age.

Based on '给岁月以文明，而不是给文明以岁月 (give civilisation to ages, not let civilisation age)'.

From *The Dark Forest*, the second book in the *Three-body* trilogy by Cixin Liu

5

6

EXPERIMENTAL STUDY OF CREEP-RESISTANT PROPERTIES AND SELF-HEALING POTENTIAL IN COMPUTATIONALLY DESIGNED 12CR STEELS

'Mediocre researchers are ususally excellent cooks.'

Hao Yu

A series of creep experiments at high temperature (550 °C) with different applied stresses have been performed on two matching experimental self-healing creep-resistant 12Cr alloys. The alloys are computationally designed to have an optimal combination of a decent creep resistance and a good self-healing potential. These alloys serve as the first step from the binary Fe-X and ternary Fe-X-Y self-healing model alloys towards multi-component industrial steels. Compared to the present commercial creep-resistant steels, the designed steels show a good creep resistance and lifetime. The validity of the self-healing behaviour in these steels is evaluated based on the observed damage and Laves phase precipitation of the creep-failed samples in both stress-affected and stress-free regions. Based on the findings suggestions for follow-up experiments and the design of the next generation of self-healing creep-resistant steels are given.

6.1 INTRODUCTION

CO_2 emission reduction has become increasingly important to protect the global environment. In response to the restrictions on emission, the power industry is driven to maximise the thermal efficiency by increasing the steam parameters, i.e. the materials need to withstand high temperature and high pressure, where their lifetimes can be strongly restricted by the occurrence of fatigue and creep damage [1, 2]. 9 – 12% Cr ferrite/ martensite steels have been developed to meet the demand, due to their high resistance to temperature and oxidation, and lower thermal expansion compared to austenite steels [2-5]. The outstanding creep resistance is associated with the microstructure of the high Cr steels: they generally consist of a ferrite matrix strengthened by finely distributed precipitates, a high density of dislocations and a strong solid-solutioning.

Traditionally, extensive efforts have been made to stabilise the microstructures such that the occurrence of creep-induced damage and microstructure degradation are delayed as much as possible. However, since the initiation of damage (e.g. in the form of grain-boundary cavities) is inevitable, the concept of self healing [6-8] has been proposed as an alternative strategy. In self-healing creep-resistant alloys, the creep-induced grain-boundary cavities can autonomously be filled by the precipitation of supersaturated solute atoms that were pre-dissolved in the matrix. Therefore, the growth and coalesce of creep cavities, which are considered as a main cause for creep failure, can be postponed. Self healing has been verified as being effective in prolonging the creep lifetime in multiple metallic systems, including austenitic stainless steels [9, 10], Al alloys [11, 12] and ferritic alloys [13-23]. As described in the previous chapters, the healing mechanism and its criteria have been studied in detail based on a series of studies on binary and ternary Fe-based model alloys. Recently, Yu and co-workers [24] have applied the mechanism of self healing to design a series of ferritic high-Cr creep-resistant steels with multiple components. In these steels, the element W is added to provide not only the solid solutioning effect, but also as the healing agent to form Fe_2W Laves phase precipitates at the creep damage sites. Other alloying elements, such as C, Cr, Ni are present to achieve decent high-temperature mechanical properties by providing precipitate and solid-

6

solution strengthening effects. The designed steels serve as the first step from the self-healing model alloys towards multi-component industrial steels.

In this work, the previously presented design of the 12Cr self-healing creep-resistant steels is summarised in section 6.2. Following that, the creep behaviour of the two novel experimental alloys with compositions based on the design rules is investigated by performing a series of creep experiments at high temperature (550 °C) with different applied stresses. By carefully examining the microstructures of the creep-failed samples in both the creep-deformed regions and the stress-free regions in the samples, we evaluate the validity of the self-healing concept in the steels. The creep lifetimes of the designed steels are compared with the existing commercial steels under similar creep conditions. Based on the observations and discussion, suggestions for the design of the next generation of self-healing creep-resistant steels are given.

6.2 DESIGN DESCRIPTION

The design aims to find a set of alloys with decent mechanical properties in combination with self-healing capacity. The design philosophy and resulting design rules already presented in more detail in previous publications [25-27], follows a goal-means strategy [28]: the required properties are firstly translated into microstructure, and based on metallurgical models, the desired microstructure can further be linked to a combination of elementary composition and heat-treatment parameters. In the present work, the design process can generally be summarised as follows: firstly, alloy candidates (in the form of combinations of elementary composition and heat-treatment temperatures) are generated based on a genetic algorithm (GA). Secondly, the aforementioned parameters of the generated alloy candidates are used as input for the thermodynamic calculations, which are performed with the commercial software Thermo-Calc. The thermodynamic calculations yield the equilibrium phase composition for each alloy candidate, which can then be linked to the corresponding microstructures. Finally, the alloying candidates are screened based on certain criteria, and for the candidates fulfilling all the screening criteria (so-called 'go/no go' criteria), their mechanical properties and self-healing potential are quantitatively evaluated based on metallurgical models. In general, the candidates with better properties have a higher opportunity to pass their genes in the next iteration in the GA.

6

The composition and homogenisation temperature of each alloy candidate generated by the GA are selected within a range, as shown in Table 6.1. For both the mechanical properties and the self-healing property, a certain amount of 'go/no go' criteria need to be fulfilled and certain parameters are formulated to predict the performance of the alloy. The mechanical properties are evaluated by the precipitation hardening factor (PH factor) and the solid-solution strengthening factor (SSS factor), which describe the precipitation-hardening effect and the solid-solution effect of the alloy candidate (after a certain exposure time at the set service temperature), respectively. The self-healing potential is evaluated by the healing reservoir, and the balance between the creep damage rate and the healing rate. In the present study, the alloying elements in the ferritic matrix contribute to the solid-solution strengthening effect (see section 6.2.1), while the $M_{23}C_6$ phase serves as the precipitation hardening phase (see section 6.2.1) and the Laves phase as the self-healing agent (see section 6.2.2).

Table 6.1: Search range for the concentration (in wt.%) of each alloying element and the homogenisation temperature (in °C).

	C	Cr	Mn	Si	W	Fe	T_{homo}
Minimum	0	12	0	0	0	Balance	800
Maximum	0.1	20	5	5	3		1200

A relative recent addition to the design strategy was the inclusion of a kinetic criterion which aimed to tailor the kinetics of the healing reaction (i.e. the formation of Laves phase precipitates in the grain boundary cavities) to the intended life time [24].

6.2.1 DESIGN FOR MECHANICAL PROPERTIES AFTER LONG-TIME CREEP

The steels are designed to show a fully ferritic matrix strengthened by both precipitation and solid solution. The design process follows a two-step equilibrium calculation, which resembles a typical heat treatment for the production of ferritic steels. The first heat treatment (corresponding to the first equilibrium calculation) is performed at the homogenisation temperature and aims for a homogenised solid-solution ferritic structure with limited primary carbide, while the second heat treatment (corresponding to the second equilibrium calculation) is performed at the service temperature (550 °C in the

present study), where the equilibrium phase composition should be in line with the desired creep-resistant microstructure, i.e. a ferritic matrix with decent precipitation strengthening and solid-solution strengthening effects.

The go/no go criteria for creep-resistant properties include:

(1) At the homogenising temperature, the volume fraction of the ferrite matrix should be higher than 99%.

(2) At the homogenising temperature, the volume fraction of the primary carbide should be lower than 0.5%.

(3) At the service temperature, the sum volume fraction of the ferrite matrix, precipitation strengthening phase ($M_{23}C_6$) and healing phase (Laves phase) should be higher than 99%.

(4) At the service temperature, the Cr concentration in the ferritic matrix should be higher than 12 wt.% for corrosion and oxidation resistance.

If all the go/no go criteria are fulfilled, the PH factor and SSS factor are calculated for each alloy candidate and stored in a database for further use. Taking the coarsening of precipitates into consideration, the contribution of the precipitation hardening effect to the yield strength can be described by $\sigma_p = \alpha G b / L$, where α is a proportionality factor, G the shear modulus, b the Burgers vector, and L the average inter-particle spacing. The PH factor, taken as the reciprocal of the average spacing, is written as [25, 26]:

$$PH \ factor = 1/L = \sqrt{f_p}/r = \sqrt{f_p}\Big/\sqrt[3]{r_0^3 + Kt} \tag{6.1}$$

where

$$r_0 = \frac{2\gamma}{G_V} \tag{6.2}$$

and

$$K = 8\gamma V_m^p \Big/ \sum_1^n \frac{9(x_i^p - x_i^m)^2}{x_i^m D_i / RT} \tag{6.3}$$

where f_p is the volume fraction of the precipitates, r the radius of the precipitate after a duration t, r_0 the critical radius of the precipitate, K the coarsening rate of the precipitate, G_V the thermodynamic driving force for precipitation (per unit of volume), γ the interfacial energy between the matrix

and the precipitate, V_m^p the molar volume of the precipitate, x_i^m and x_i^p the fractions of the precipitate forming elements on both the matrix (m) side and the precipitate (p) side, respectively. D_i is the diffusion coefficient of element i, R the gas constant and T the service temperature (in K). In the current study, the time is set to 10^5 hours.

The solid-solution strengthening effect is estimated by the weighted sum of atomic concentration of solutes in the matrix. The SSS factor is expressed as [27]

$$\text{SSS factor} = \sum_i k_i x_i \tag{6.4}$$

where k_i is the strengthening coefficient for each 1 at.% of alloying element i and x_i the atomic percent of alloying element i in the solid solution. The values of k_i for various elements are listed in Table 6.2.

Table 6.2: Solid-solution strengthening coefficient [27].

Element	C	Cr	Mn	Si	W
k	1103.5	2.6	16.9	25.8	31.8

6.2.2 DESIGN FOR SELF HEALING

Healing of the grain-boundary cavities is achieved by the formation of the Laves phase at the cavity surface. Two considerations are taken into account regarding to the self-healing capacity: (*i*) the matrix should provide a sufficient healing reservoir and (*ii*) the healing kinetics should be tailored to the intended lifetime of the installation. Implicitly, the kinetics of the healing reaction is tailored to the kinetics of pore formation.

For (*i*), a go/no go criterion is set as:

(5) At the service temperature, the volume fraction of the Laves phase should be higher than 1%.

The volume fraction is chosen based on the tomography results in [16]. It is demonstrated that the volume fraction of the creep cavities in a creep-failed sample is below 0.76%.

For (*ii*), it is crucial to estimate the formation time for both the cavities and healing precipitates. The formation time of cavities is related to the stress

level, while the nucleation time of Laves phase is estimated by its chemical driving force (which is relatively easy to calculate with Thermo-Calc), based on a linear relationship between the driving force and the logarithm of the incubation time summarised from reported data. The relationship between the calculate thermodynamic driving force and the experimentally observed incubation time for Laves phase in commercial ferritic creep steels, extracted by Yu and co-workers [24] from reported literature [29-32], is shown in Fig. 6.1.
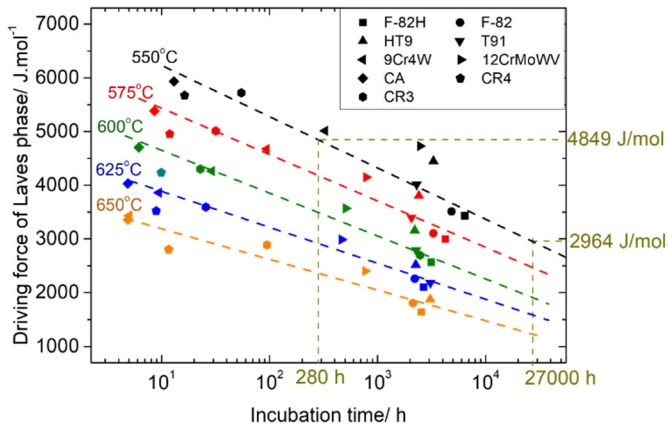
Fig. 6.1: Experimentally observed incubation times for Laves phase precipitation at different creep temperatures. The data are from [29-32] and were collected by [24]. The driving force and the incubation time for the Laves phase in the two example alloys selected for the experiments in the current study are indicated by the yellow dash lines.

6.2.3 SELECTED ALLOYS

Eventually, two alloys were selected as the first batch of self-healing steels to examine the feasibility of the design model. The composition, homogenisation temperature, the PH factor, the SSS factor, the chemical driving force and the corresponding incubation time for Laves phase precipitation are summarised in Table 6.3. The two steels meet the following requirements: (*i*) they fulfil all the go/no go criteria; (*ii*) they have comparable PH and SSS factors, i.e. they are expected to show similar mechanical properties at a temperature of 550 °C; and (*iii*) the chemical driving forces of Laves phase in the two steels widely differ, so that the formation times of the healing agent are also expected to be different (approximately 300 h and 30000 h, respectively). To simplify, we

name the steels as fast self-healing (F-SH) steel and slow self-healing (S-SH)steel. Generally, the S-SH is expected to heal the damage that occurs on a time scale of about 1000 days, while in the F-SH, the healing can take place after 10 days of service. It is straightforward that the S-SH is more suitable for low-stress conditions, where damage is likely to accumulate after long service times. For a higher stress level, where creep damage is expected to occur earlier, on the contrary, the F-SH is expected to show a better healing potential. Given the large differences in predicted onset times for the healing reaction, the F-SH alloy is expected to show a healing reaction during some of the creep experiments with a maximum testing time of 2500 hours, while the S-SH system should not show such a healing reaction in the same time period.

Table 6.3: Designed composition, homogenising temperature of the two selected alloys, and their corresponding PH factor, SSS factor, driving force DF and estimated healing time t_{init} at 550 °C.

	C	Cr	Mn	Si	W	T_{homo}	PH	SSS	DF	t_{init}
	wt.%	wt.%	wt.%	wt.%	wt.%	°C	$\times 10^6$	-	J/mol	h
S-SH	0.026	12	0.81	0.32	1.45	1200	8.65	69	2964	30000
F-SH	0.023	13.03	0.01	0.97	3.00	1200	8.71	80	4849	300

6.3 EXPERIMENTAL

6.3.1 SAMPLE PREPARATION

The samples were produced by Benxi Steel Group, China. The compositions of the alloys slightly deviate from the designed values, as shown in Table 6.4. The phase components of the two alloys as a function of temperature are calculated with Thermo-Calc and the result is shown in Fig. 6.2. It is clear that both the F-SH and S-SH have two *bcc* temperature regions, which are listed in Table 6.4.

The sample ingots were homogenised at 1200 °C for 5 h, and subsequently, their thickness was reduced from 15 mm to 5 mm by a two-path hot rolling with a final temperature of 850 °C, before they were quenched in water. The oxidation layer was removed by acid pickling with a 10% hydrochloric acid solution. After that, the samples were cold-rolled to 1.5 mm-thick sheets. The thickness of the sheets were further reduced to 0.5 mm by milling, from which dog-bone shaped creep samples with a gauge length of 12.5 mm and a cross-section of 3 mm^2 (thickness of 0.5 mm and width of 6 mm)

were machined by spark erosion, with the gauge length along the rolling direction.

Table 6.4: Composition (in wt.%) and temperature ranges (in °C) to achieve a *bcc* matrix for the S-SH and the F-SH alloys.

	C	Cr	Mn	Si	W	Al	Fe	*bcc* region 1	*bcc* region 2
S-SH	0.023	12	0.81	0.20	1.1	0.05	Bal.	650 – 820	Above 1180
F-SH	0.022	12.6	0.023	0.81	2.2	0.02		770 – 920	Above 1030
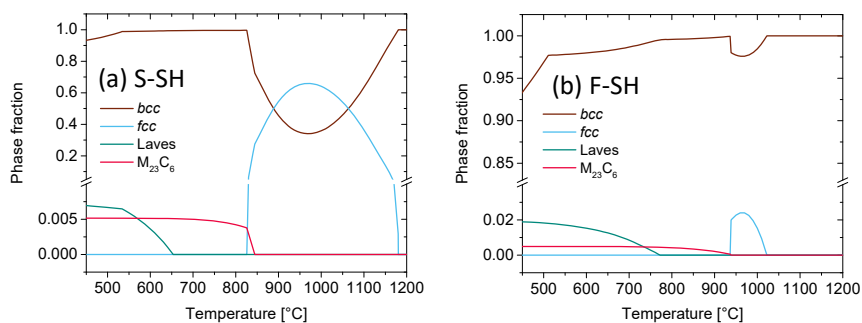
Fig. 6.2: Equilibrium phase components of the S-SH and F-SH alloys as a function of temperature.

6.3.2 RECRYSTALLISATION HEAT TREATMENT

During the cold-rolling pre-treatment, a large amount of deformed grains and dislocations are generated which control the resulting grain size upon the recrystallisation treatment. A set of recrystallisation heat treatment experiments were performed with various combinations of temperature and time. Several considerations were taken into account when choosing the recrystallisation heat treatment parameters: (*i*) the alloys should show a homogenised *bcc* single phase with equiaxed grains after the treatment; (*ii*) the grain sizes in the S-SH and the F-SH should be comparable so that the effect of grain sizes on the creep behaviour can be neglected; and (*iii*) the grain size of the alloys should preferably be small (< 1/10 of the sample thickness, i.e. < 50 μm) to avoid the situation where only a few grains exist in the cross section of the sample, in which case the creep behaviour is highly dependent on the local microstructure. Furthermore, the final grain size should be comparable to that of commercial ferritic creep steels to allow comparison of the properties of the experimental alloys with those of commercial 12 Cr steels. Eventually, the S-SH

and the F-SH samples were recrystallised for 4 hours at 750 °C and 810 °C, respectively. The grain size after annealing corresponds to 20(2) and 22(5) μm for the S-SH and the F-SH samples, respectively. The processing parameters for the other heat treatment experiments are listed in Table 6.5. Prior to annealing, the samples were sealed in quartz tubes filled with 200 mbar ultra-high purity argon to prevent oxidation. The samples were quenched in water after annealing. The as-quenched samples were examined with scanning electron microscopy to assure a uniform homogenised matrix. A limited amount of $M_{23}C_6$ particles were detected in the grain interior of the as-received samples. These particles are expected to remain stable during creep.

Table 6.5: Parameters and result of recrystallisation heat treatment experiments on S-SH and F-SH. The numbers in bracket correspond to standard deviation. The eventually chosen parameters are highlighted bold.

	Parameter		Result	
	Temperature (°C)	Time (min)	Single phase (Y/N)	Grain size (μm)
	780	10	N	
	780	30	Y	22(6)
	780	60	Y	27(5)
	790	15	Y	9(1)
	790	60	Y	23(9)
S-SH	**790**	**240**	**Y**	**20(2)**
	790	960	Y	32(6)
	1100	1	N	15(3)
	1150	1	N	29(6)
	1200	1	N	243(80)
	780	10	Y	15(4)
	780	30	Y	17(4)
	780	60	Y	20(4)
	810	15	Y	20(4)
	810	60	Y	24(7)
F-SH	**810**	**240**	**Y**	**22(5)**
	810	960	Y	21(4)
	1100	1	N	36(9)
	1150	1	Y	187(38)
	1200	1	Y	255(66)

6.3.3 CREEP EXPERIMENT AND CHARACTERISATION

Creep experiments until rupture were performed under vacuum at a constant temperature of 550 °C and with constant stress levels ranging from 100 to 260

MPa. The experimental details of the test facility can be found in [21] and in Chapters 2 and 4. The microstructures in the uniform deformation region (stress-affected region) and the stress-free region were characterised via scanning electron microscopy (SEM) using a JEOL JSM 6500F instrument equipped with energy-disperse X-ray spectroscopy (EDS). To reveal the precipitate crystal structure and composition, transmission electron microscopy (TEM) measurements were performed using a FEI C_s-corrected cubed Titan instrument. Elemental analysis was done with the Thermo Fisher Scientific super-X detector in the ChemiSTEM™ configuration. Lattice images were collected on a Gatan camera. Annular Dark Field (ADF) images and energy-disperse X-ray spectroscopy (EDX) spectra for elemental mapping were collected in Scanning Transmission Electron Microscopy (STEM) mode.

6.4 RESULTS

6.4.1 MICROSTRUCTURE AFTER RECRYSTALLISATION
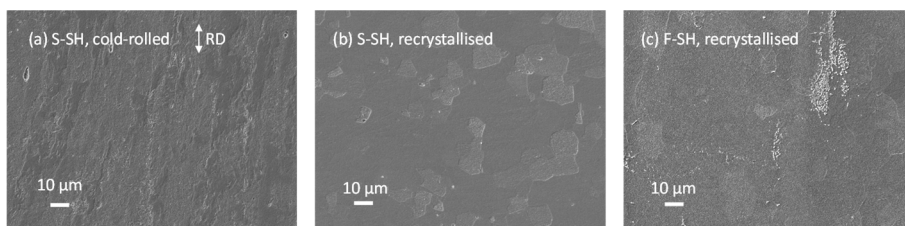
Fig. 6.3: SEM images for (a) S-SH, after cold rolling; (b) and (c) S-SH and F-SH, after recrystallisation for 4 h at 790 °C and 810 °C, respectively. The white particles in (c) are indissoluble $M_{23}C_6$ precipitates. The rolling direction (RD) is indicated by the arrow in (a).

As introduced in section 6.3.2, lower recrystallisation temperatures (810 °C and 790 °C for the F-SH and the S-SH, respectively, instead of the designed 1200 °C) were used for the two alloys. As shown in Fig. 6.3, after annealing for 4 h, the elongated grains from cold rolling in both the F-SH and the S-SH have recrystallised into equiaxed grains with comparable grain sizes (22(5) and 20(2) μm for F-SH and S-SH, respectively). However, a limited amount indissoluble particles are observed in both the two alloys, as indicated in Fig. 6.3(c). These particles have a size of approximately 1 μm, and their sizes do not show an obvious change for annealing times up to 16 h at 790 or 810 °C. With EDS, the particles are found to be enriched in Cr, while TEM examination on creep-failed samples confirmed that the particles show a $M_{23}C_6$ structure with

a composition of 11C55Cr4W (in at.%). It is worth to mention that the particles can be dissolved after 1 min annealing at 1200 °C. However, lower recrystallisation temperatures of 790 and 810 °C were selected to control the grain growth.

6.4.2 CREEP RESULTS

The creep results for the F-SH and the S-SH alloys with different constant stresses at a fixed temperature of 550 °C are presented in Figs. 6.4 and 6.5, respectively. The final strain of both the F-SH and S-SH alloys are generally higher than 50%, indicating a ductile nature. For the F-SH alloy, as shown in Fig. 6.4(b), the strain rate shows a continuous increase when the applied stress levels are relatively high (> 180 MPa), while for lower stress levels (< 180 MPa), a more obvious steady-state creep takes place, where the strain rate remains relatively constant. For the lowest stress level (130 MPa), the strain rate shows a decrease before the tertiary creep takes place after strain exceeds 40%. For the S-SH alloy, as shown in Fig. 6.5(b), the initial primary creep is followed by a steady-state creep and tertiary creep. The steady-state strain rate fulfils the Sherby-Dorn equation [33] $\dot{\varepsilon}_S = A d^m \sigma^n \exp(-Q/RT)$, where A is a structure-dependent constant, d the grain size, m the grain size exponent, σ the applied stress, n the stress exponent, Q the activation energy, R the gas constant and T the temperature (in K). In Figs. 6.4(c), 6.5(c), 6.4(d) and 6.5(d), the minimum strain rate and the creep lifetime as a function of the applied stress are presented, respectively. The corresponding stress exponent for the strain rate n yields 7.8(6) and 9.4(6) for the F-SH and the S-SH alloys, respectively. The stress exponent derived from the lifetime corresponds to 10.2(5) and 9.3(6) for the F-SH and the S-SH alloys, respectively. The high values for the stress exponents indicate substantial dislocation climb.

6
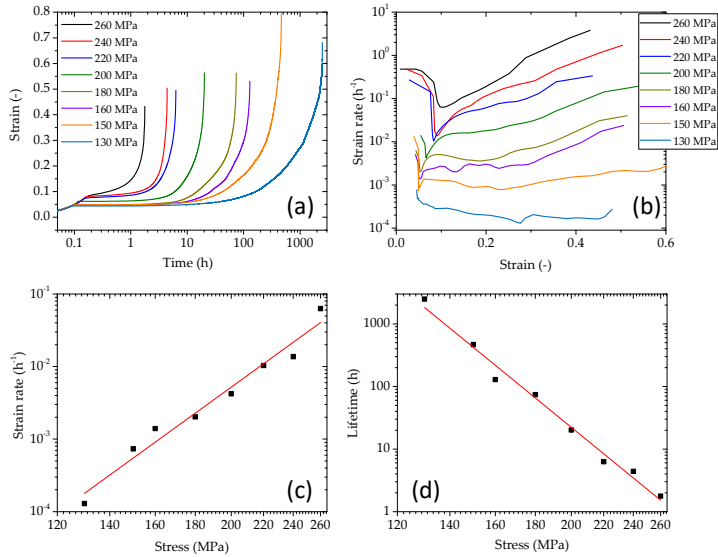
Fig. 6.4: Creep results for the F-SH alloy with different constant loads at a fixed temperature of 550 °C. (a) Creep curves; (b) derived strain rate versus strain; (c) derived steady-state strain rate and (d) creep lifetime as a function of applied stress.

6
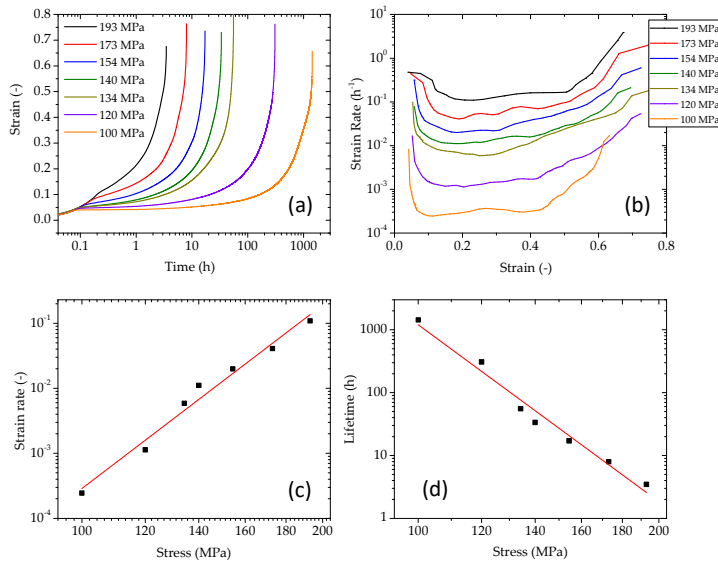
Fig. 6.5: Creep results for the SSSH alloy with different constant loads at a fixed temperature of 550 °C. (a) Creep curves; (b) derived strain rate versus strain; (c) derived steady-state strain rate and (d) creep lifetime as a function of applied stress.

6.4.3 MICROSTRUCTURE AFTER CREEP

A representative fracture surface of the creep-failed F-SH sample having been exposed to an applied stress of 130 MPa at 550 °C for 2487 h is shown in Fig. 6.6(a). Consistent with the results from the creep curves, the fracture surface demonstrates typical ductile characteristics with a significant reduction in thickness and obvious dimples. The selected square in Fig. 6.6(a) is shown in (b) with a higher magnification. The white spots scattered on the fracture surface corresponds to W-rich precipitates. An overview of the microstructure in both the stress-affected uniform deformation area and the stress-free area is presented in Fig. 6.6(c) and Fig. 6.6(d), respectively. The grains in the stress-affected region are substantially elongated along the loading direction after creep, with an average aspect ratio of 2.4(2). The grains in the stress-free region, on the contrary, do not show an obvious change before and after creep. Assuming that the grains before creep are cubic with the volume of d^3, while the elongated grains after creep have the dimensions of a^2c, with c/a the aspect ratio. Assuming that the volume of the grain does not change during creep, a final strain of 0.7 (i.e. c/d = 1.7 and a/d = $(1.7)^{-1/2}$ = 0.77) yields an aspect ratio of c/a = 2.2. This indicates a uniform flow in the stress-affected region, which can resulted from both dislocation creep and diffusion creep [34].
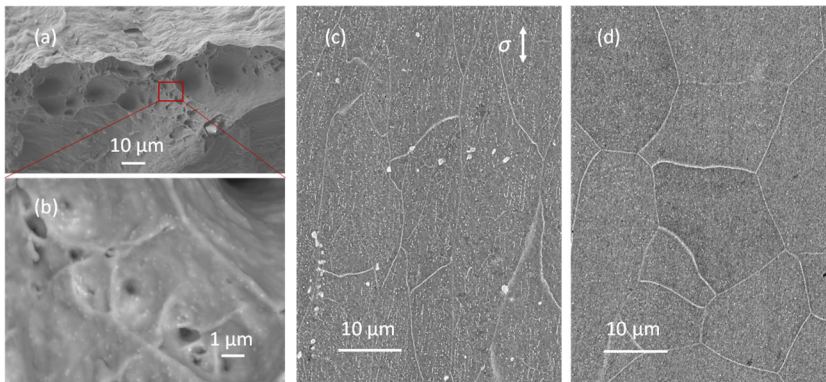
Fig. 6.6: Microstructure of the creep-failed F-SH sample after 2487 h with a constant stress of 130 MPa at 550 °C. SEM images of (a) and (b) fracture surface, (c) stress-affected uniform deformation region (loading direction indicated by the arrow) and (d) stress-free region.

The detailed microstructure of the creep-failed F-SH sample with a lifetime of 2487 h is presented in Fig. 6.7. SEM images of the uniform deformation region and the stress-free region are compared in (a) and (b), respectively. It is clear that the grain boundaries are decorated by precipitates, while in grain interior, nano-sized precipitates (white spots) and pores (black spots, indicated by red arrows) are observed. The precipitates in the stress-affected region (Fig. 6.7(a)) are generally aligned along the loading direction, while the ones in the stress-free region (Fig. 6.7(b)) are randomly distributed, showing no obvious pattern. The pores are generally round-shaped and are found in the grain interior, instead of showing a preference to the grain boundary. Since the pores can be observed in both the stress-affected and stress-free regions, it is logical to assume that at least some of the pores already exist in the as-quenched samples and are not formed during creep. Features at subgrain boundaries can also be observed in the uniform deformation region. The formation of subgrains, frequently observed in both metals [35] and ceramics [36] during creep with a stress exponent close to 5, takes place through the climb of dislocations during plastic deformation, and the size of the subgrains is usually found to be inversely proportional to the applied stress. Some large $M_{23}C_6$ particles (approximately 1 µm in size) are observed in Fig 6.7(a), as indicated by blue arrows. These particles are present in the matrix and do not show an obvious change in size or morphology during creep.

The scanning TEM image with the EDX maps reveals the morphology and the composition of precipitates in the uniform deformation region, both at the grain boundary and in the matrix, as demonstrated in Fig. 6.7(c). The average composition of the grain boundary and grain interior precipitates corresponds to 18W20Cr7Si (in at.%), which is richer in Si compared to the equilibrium composition calculated by Thermo-Calc (which gives 33W17Cr0.5Si). The composition of the precipitates is generally in line with that of the Laves phase. It is worth to note that a nano-sized $M_{23}C_6$ particle is also detected with TEM, as shown in Fig. 6.7(d). Unlike the unwanted large $M_{23}C_6$ particles with the size of about 1 µm formed before creep, the nano-sized $M_{23}C_6$ was designed to be present and to serve as the precipitation hardening phase during long time creep.

6
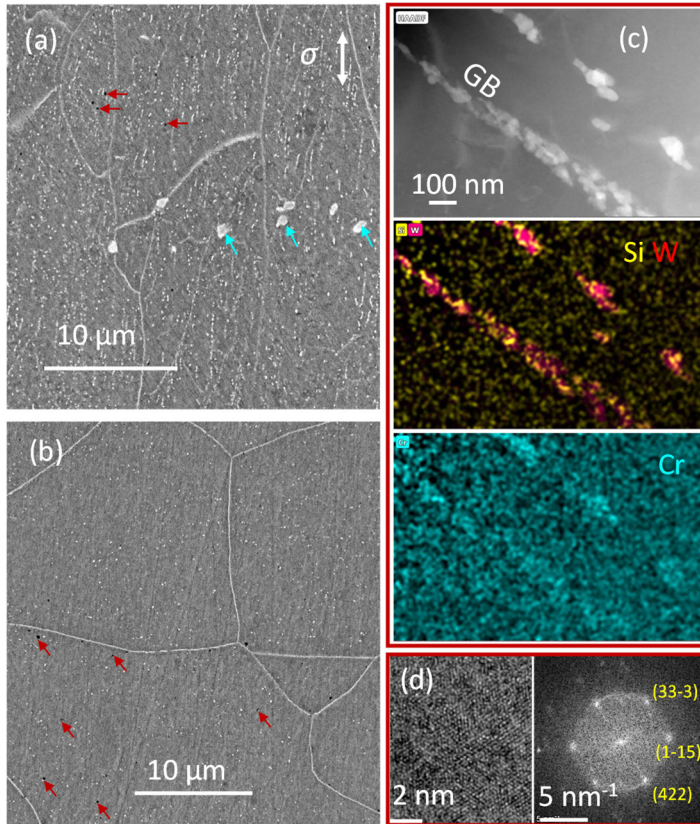
Fig. 6.7: SEM and TEM data for the F-SH sample after 2487 h creep with a constant stress of 130 MPa at 550 °C. (a) SEM image of the uniform deformation region. The black spots correspond to the pores, as indicated by the red arrows. The blue arrows indicate insoluble $M_{23}C_6$ inclusions. (b) SEM image of the stress-free region. The red arrows indicate the pores. (c) Scanning mode (STEM) image and EDX composition for both grain boundary (GB) and grain-interior precipitates. (d) HREM of a nano-sized $M_{23}C_6$ precipitate in the matrix and the associated Fourier transform (FFT).
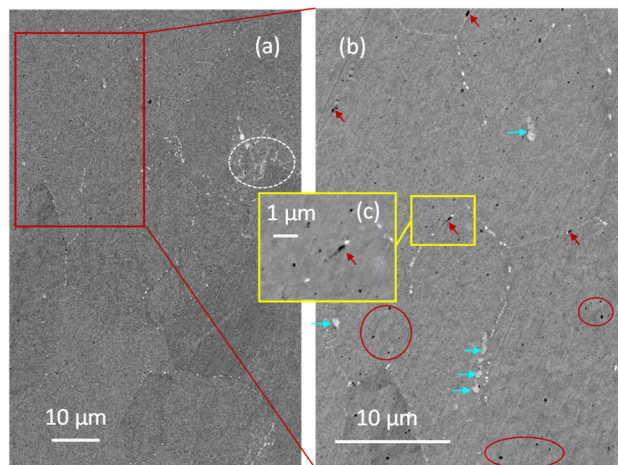
Fig. 6.8: SEM data for the stress-affected region in a creep-failed S-SH sample after 1434 h creep with a constant stress of 100 MPa at 550 °C. (b) and (c) correspond to higher magnifications. The white dashed circle in (a) indicates the existence of subgrains. The red arrows and red circles in (b) and (c) indicate grain-boundary cavities and grain-interior pores, respectively. The insoluble $M_{23}C_6$ inclusions are indicated by blue arrows.

The microstructure of the uniform deformation region for the creep-failed S-SH sample with a constant load of 100 MPa at 550 °C (resulting in a lifetime of 1434 h) is shown in Fig. 6.8. Similar to the results for the F-SH alloy, elongated grains are also observed in the S-SH sample, with an aspect ratio of 2.5(1). The precipitates show an obvious preference for grain boundaries, while no grain interior precipitates are observed in this sample. Compared to the F-SH counterpart, more grain interior pores can be observed in the S-SH sample, as indicated by the red circles in Fig. 6.8(b). As indicated by red arrows, grain-boundary cavities are also frequently observed in addition to the grain interior pores, and some of the cavities show an elongated shape (instead of the round-shaped grain-interior pores in both the F-SH and S-SH alloys), indicating a growth behaviour during creep. An example of an elongated grain boundary cavity is given in Fig. 6.8(c). Round pores are also observed in the stress-free regions (not shown here), but they do not indicate a preference to the grain boundaries, and show no tendency of deformation. The fine structures in the white dashed circle in Fig. 6.8(a) may indicate the existence of subgrains, although the subgrains are not decorated by the precipitates, as the ones in the F-SH sample. Insoluble $M_{23}C_6$ particles are also observed in the S-SH sample, as indicated by blue arrows in Fig. 6.7(b).

Table 6.6: Equivalent diameter $\langle d \rangle$, number density n_A and area fraction f_A of the precipitates (Prec) and pores (Pore) in both the stress-affected and stress-free regions in the F-SH and S-SH alloys. The equilibrium phase fraction of the Laves phase f_{eq}^{Laves} is also given. The numbers in brackets correspond to the error. The dash (–) indicates that no precipitation is observed.

Sample	Stress (MPa)	Lifetime (h)	Phase	Region	$\langle d \rangle$ μm	n_A μm^{-2}	f_A %
F-SH (f_{eq}^{Laves} = 1.70 %)	130	2487	Prec	σ-affected	0.080(1)	2.500	1.529
				σ-free	0.074(3)	0.912	0.460
			Pore	σ-affected	0.056(1)	0.121	0.034
				σ-free	0.054(1)	0.142	0.036
	150	465	Prec	σ-affected	0.049(5)	0.334	0.068
				σ-free	–		
			Pore	σ-affected	0.056(2)	0.112	0.033
				σ-free	0.073(2)	0.121	0.059
S-SH (f_{eq}^{Laves} = 0.59%)	100	1434	Prec	σ-affected	0.111(2)	0.215	0.259
				σ-free	0.134(4)	0.158	0.282
			Pore	σ-affected	0.086(1)	0.299	0.209
				σ-free	0.068(1)	0.140	0.054
	120	308	Prec	σ-affected	0.101(2)	0.188	0.175
				σ-free	–		
			Pore	σ-affected	0.078(2)	0.105	0.060
				σ-free	0.062(2)	0.093	0.034

The equivalent diameter, number density and area fraction of the precipitates (excluding the large $M_{23}C_6$ inclusions) and pores (including the grain boundary cavities and grain interior pores) in both the stress-affected (σ-affected) and stress-free (σ-free) regions in the F-SH and S-SH alloys are compared in Table 6.6. Several observations can be made from the table: (1) the number density of precipitates in the stress-affected region is significantly higher than that in the stress-free region, indicating an enhancement of precipitation nucleation by the deformation. However, the deformation does not show an obvious effect on the growth of precipitates. (2) The precipitates need time to nucleate and grow to a detectable size. In the stress-free regions, no precipitates are detected in the samples with relatively short creep times (approximately 500 h for the F-SH alloy and 300 h for the S-SH alloy, respectively). (3) For the F-SH alloy, the size and number density of the pores

do not show an obvious difference for the stress-affected and stress-free regions, indicating that most of the pores are imperfections already present in the as-quenched sample, instead of generated during creep. In fact, the number densities of the pores after different creep times (in both the stress-affected and stress-free regions) are comparable, which indicates that most of the pores already existed before creep and did not show an obvious change with time. However, for the S-SH alloy, the number density of the pores in the stress-affected region exceeds that in the stress-free region, indicating the nucleation of new cavities during creep.

6.5 DISCUSSION

6.5.1 CREEP PROPERTIES

The alloys are designed to show decent creep properties combined with a self-healing potential, where the creep resistance is provided by (1) the precipitation strengthening effect from the $M_{23}C_6$ precipitates that form during creep and (2) the solid-solution strengthening effect of the dissolved elements in the matrix. In Fig. 6.9, the lifetimes of the F-SH and S-SH alloys with different constant loads at a temperature of 550 °C are compared with those of a collection of commercial 9 – 12Cr creep steels alloys. The grain size of the commercial alloys generally lies between 6.0 and 9.0, corresponding to a grain size range of 53.4 – 13.3 μm, which is comparable to the grain sizes of the F-SH and S-SH alloys in the present study. The dashed lines correspond to the conditions where self healing is not expected to happen ($t < t_{init}$, where t_{init} is the incubation time for the Laves phase as shown in Table 6.3), while the solid lines correspond to the conditions where self healing is expected according to the design ($t > t_{init}$). For the F-SH alloy, the dashed line and the solid line are generated by piecewise fitting the experimental data with a relatively short lifetime ($t_R < 100$ h) and long lifetime ($t_R > 100$ h), respectively. It can be seen that the lifetimes of the F-SH and S-SH alloys are generally in the same regime as the commercial alloys with no Nb or V, i.e. the commercial steels that are not strengthened by MX precipitates. Compared to the S-SH alloy, the F-SH alloy shows a better creep-resistance potential, and promising lifetimes can be expected in the low stress (and therefore the long lifetime) regime. In fact, at the designed time for precipitate nucleation, a transition of the stress exponent can be observed, indicating a better creep resistance for long-time creep. While

6

this transition is in line with the concept behind the design, more extensive testing would be required to get statistical confirmation of this slope change.

As introduced in section 6.2, the two alloys were designed to have comparable mechanical properties and a similar creep resistance by controlling their precipitation hardening factor (PH factor) and solid-solution strengthening factor (SSS factor). In practice, apart from the precipitation hardening and solid-solution hardening, due to the substantial deformation and the existence of sub-microstructures, both the F-SH and S-SH alloys are also strengthened by dislocations and subgrains. The creep experiments clearly demonstrate that the F-SH alloy shows longer lifetimes and a higher resistance for nucleation and growth of cavities, and therefore shows better overall creep resistant potential. One obvious reason is the precipitation strengthening effect provided by the nano-sized Laves phase precipitates in the matrix of the F-SH alloy after long-time creep (approximately when $t > t_{init}$). After 2487 hours of creep, Laves precipitates with an equivalent diameter of 80 nm and a number density of 2.5 μm^{-2} are formed more or less uniformly in the uniform deformation region of the F-SH alloy, yielding an average inter-particle spacing of approximately 600 nm. This is consistent with a typical Laves particle spacing in high-Cr alloys [37], and can provide approximately 70 MPa Orowan stress. According to the design, the nucleation of the Laves precipitates in the matrix is expected after approximately 300 h. This calculated time is comparable with the experimental results in Table 6.6: the bulk precipitates were observed after approximately 500 h of creep. In the S-SH alloy, however, the Laves phase precipitates are expected to form in the matrix only after approximately 30000 h of creep. Therefore, the Laves precipitates are mainly observed at the grain boundaries, and as a result, the matrix is not strengthened by the Laves phase particles. It is worth to note that the Laves phase is designed for the self-healing property, while $M_{23}C_6$ precipitates are expected to serve as the precipitation hardening phase. However, nano-sized $M_{23}C_6$ precipitates were only sparsely detected with TEM, instead of uniformly distributed. One possible reason for the absence of $M_{23}C_6$ nano-particles is the existence of the large insoluble $M_{23}C_6$ inclusions, which may have immobilised C and therefore no $M_{23}C_6$ can be formed during creep. The $M_{23}C_6$ inclusions are not uniformly distributed, but they generally show an area fraction of 0.03 – 0.1%, which corresponds to 0.03 – 0.1 at.% of C given the carbon concentration in $M_{23}C_6$ inclusion (11 at.% as discussed in section

6.4.1). The total carbon concentration in the F-SH and S-SH alloys is approximately 0.10 at.%, and therefore it is possible that the samples are depleted in C, in which case the nucleation of nano-sized $M_{23}C_6$ precipitates is strongly supressed during creep.
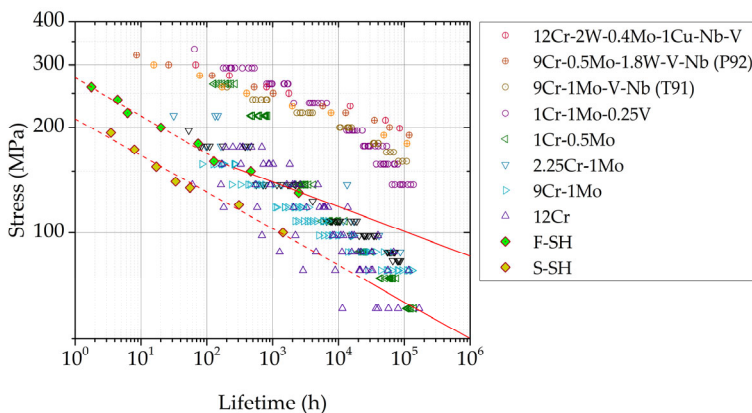
Fig. 6.9: Lifetimes of the F-SH and S-SH alloys with different constant loads at a temperature of 550 °C compared to a collection of commercial alloys. The data for commercial alloys are from [38-45]. The dashed lines and solid lines correspond to the situations where $t < t_{init}$ and $t > t_{init}$, respectively.

The solid-solution strengthening effect for the two alloys during creep is difficult to quantify. The two alloys are designed to have similar SSS factors, however, the SSS factors are calculated based on the solid strengthening elements in the matrix at equilibrium. During creep, however, the samples start with an as-quenched state, and therefore all the alloying elements dissolved in the matrix during recrystallisation serve as solid-solutioning elements before the equilibrium is reached. For the F-SH alloy, the area fraction of Laves phase in the deformed region approaches to the equilibrium level after 2487 h of creep at 550 °C, while for the S-SH alloy, the area fraction of Laves phase in the stress-affected region is still much lower than equilibrium phase fraction after 1434 h of creep at 550 °C.

6.5.2 SELF-HEALING POTENTIAL

The self healing of creep-induced cavities is designed to take place by selective precipitation of the Fe_2W Laves phase at the free surface of the cavities. In the present study, Laves phase precipitates have been observed in both the F-SH and S-SH creep-failed samples. However, the nucleation sites of the

precipitates (or self-healing selectivity) differ from the designed ones. One reason is the absence of grain-boundary cavities, which may result from a different creep mechanism compared to the binary and ternary model alloys. In the model alloys [16, 19, 21-23], most of the cavities were found to nucleate at the grain boundaries, especially the grain boundaries oriented perpendicular to the load direction. These cavities provide preferred nucleation sites for the healing precipitates. In the present study on the F-SH and S-SH alloys, the high stress exponents indicates that the deformation is controlled by dislocation climbing, instead of vacancy diffusion. As a result, almost no cavities are observed at the grain boundaries, except for a few cases in the S-SH alloy after 1434 h of creep. As a result, the interaction between the cavities and precipitates is also limited.

Another reason for the weak site selectivity for the Laves phase precipitation is that the limited strain energy failed to restrain the nucleation of precipitates in the matrix. In the F-SH alloy, a large amount of precipitates were formed in the stress-affected region after approximately 500 h creep, both at the grain boundaries and the grain interior. The grain-interior precipitation shows clear patterns aligned along the loading direction, indicating that the sub-microstructures formed during creep, such as subgrains and dislocations, provide preferred nucleation sites for precipitation. In the stress-free regions, the precipitates takes longer time to nucleate, and were observed more or less uniformly distributed after 2487 h. The existence of precipitates in the stress-free region indicates that the chemical driving force for the Laves phase is too high, so that the strain energy is not enough to prevent nucleation in the bulk. In the S-SH alloy, which has a lower chemical driving force, the precipitates are generally located at the grain boundaries, while nucleation in the grain interior is suppressed by the strain energy as intended in the design model.

The strain energy resulting from the mismatch between the precipitation and the matrix can be described as [46]

$$\Delta G_S = \frac{v_p \varepsilon_V^2 E_p E_m}{3\left[2\left(1 - 2v_p\right)E_m + \left(1 + v_m\right)E_p\right]} \tag{6.5}$$

where E_p and E_m are the Young's moduli of the precipitation and the matrix, v_p and v_m the Poisson's ratios of the precipitation and matrix, $\varepsilon_V = v_p/v_m - 1$

the volume misfit between the precipitation and the matrix. v_p and v_m are the molar volumes of the precipitation and matrix phase, respectively. Taking E_m = 205 GPa, v_m = 0.29 [47], E_p = 337 GPa, v_p = 0.29 [48], the molar strain energies for the formation of the Laves phase in the *bcc* matrix under equilibrium conditions at 550 °C correspond to 2461 J/mol and 2690 J/mol for the S-SH and F-SH alloys, respectively. The molar volumes of the precipitation and matrix phases are calculated by Thermo-Calc. With the compositions listed in Table 6.4. The chemical driving forces of the S-SH and F-SH alloys slightly deviate from the designed values in Table 6.3, yielding 2208 J/mol and 4362 J/mol, respectively. It is clear that the chemical driving force for nucleation of the Laves phase in the F-SH alloy is much higher than the corresponding strain energy. Therefore, a large amount of precipitates was observed even in the stress-free region.

6.5.3 Suggestions for the design of the next generation of self-healing creep-resistant alloys

The present study is based on the computational design of the first generation of multi-component creep-resistant steels that include self-healing capacities. From the creep results and the corresponding microstructure of the creep-failed samples, several comments and suggestions can be summarised that can be used as input for the design of a next generation of self-healing creep-resistant alloys.

(1) In the design, the nucleation kinetics of the healing Laves phase is innovatively linked to its chemical driving force. As discussed in section 6.5.2, the chemical driving force of Laves phase in the F-SH alloy is 4362 J/mol, which corresponds to an experimental nucleation time of approximately 900 h. This time is consistent with the time when the Laves phase was observed in the stress-free region at 550 °C (approximately 500 h). For the S-SH alloy, the relatively low chemical driving force indicates a very long nucleation time of 30000 h, and such time is not reached in the present study. However, in the S-SH alloy with the longest creep time (approximately 1500 h), no bulk precipitation was observed in the stress-free region. The empirical relationship between the chemical driving force and the bulk nucleation time therefore provides a reasonable estimate for the nucleation kinetics. The selectivity of the healing precipitation, however, is not fulfilled by the current design. In order to assure that the healing takes place exclusively at the creep

6

cavity sites, an extra criteria needs to be added, i.e. the strain energy resulting from the misfit between the precipitation and the matrix should exceed the corresponding chemical driving force. Otherwise the healing phase may nucleate in the bulk and be depleted before the damage healing is needed, as is the situation for the F-SH alloy. Given the fact that the grain boundaries of both the F-SH and S-SH alloys are decorated by Laves precipitation, it may also be worth to consider the addition of alloying elements that can suspend the nucleation of the Laves phase at grain boundaries.

(2) Formation of grain-boundary cavities is crucial for selective self healing to take place. Therefore, the design suits better for the situation where the creep is controlled by vacancy diffusion, rather than dislocation climb. The initial design is indeed aimed for lower stress levels and longer time scales (where diffusion creep is likely to take place). However, in order to finish the experiments within a shorter and more practical time scale, a combination of a higher creep temperature and lower stress levels, where the creep is likely to be controlled by diffusion, is more suitable to verify the effectiveness of the design.

(3) As discussed in section 6.5.1, the $M_{23}C_6$ precipitates did not nucleate as nano-sized strengthening precipitates as designed, but were already present in the form of micro-sized inclusions even before creep experiments. This can be modified by optimising the casting, homogenisation, hot rolling and recrystallisation parameters, such that a fine grain size and a homogenised matrix with no $M_{23}C_6$ inclusions are both fulfilled. As described in section 6.3, the casted sample ingots were first hot-rolled to a thickness of 5 mm with a finishing temperature of approximately 850 °C before they were quenched in water. From the homogenisation temperature of 1200 °C to the finishing temperature (which is difficult to control in practice), some $M_{23}C_6$ particles may have formed (see Fig. 6.1 for the temperature range of $M_{23}C_6$) and remained thereafter. The designed recrystallisation temperature, 1200 °C is able to re-dissolve the $M_{23}C_6$ particles. However, different recrystallisation temperatures were chosen to restrain the grain growth. A possible solution could be multiple paths of cold rolling with a recrystallisation at 1200 °C in between. The high temperature recrystallisation aims to homogenise the microstructure and dissolve the $M_{23}C_6$ (and Laves phase) into the matrix, while

6

the grain size can be controlled by the high dislocation density generated during multiple paths of cold rolling.

6.6 CONCLUSIONS

In this work, a series of creep experiments with different applied stresses but at a fixed high temperature (550 °C) are described and analysed for two custom-designed self-healing creep-resistant 12Cr alloys. The alloys, which were computationally designed to combine a decent creep resistance with self-healing potential but for different intended lifetimes, serve as the first step from the self-healing binary and ternary model alloys towards multi-component industrial steels. Compared to the present commercial creep-resistant steels, the newly designed steels, especially the F-SH alloy (i.e. the one designed with a fast self-healing kinetics starting after only 300 hours) shows a good creep resistance and lifetimes comparable to those of existing creep steels, due to a combination of precipitation strengthening, solid-solution strengthening and subgrain strengthening effects. Regarding the self healing aspect, the F-SH steel shows an increase in lifetime beyond the onset time for Laves phase (i.e. the healing agent) precipitation. The S-SH steel, designed not to show any self-healing reaction unless exposed to creep conditions for 30000 hours, indeed shows no self-healing behaviour during the maximal testing time in this research (1500 hours). Based on all observations we conclude that the cavity formation is not properly quantified by the design rules due to the absence of kinetic information on grain-boundary cavities formed during creep, which would result from a dislocation climb dominated creep mechanism. For future alloy design calculations, the formation time of the healing phase in the bulk can be estimated following the same principle in the current design, i.e.based on the chemical driving force of this phase. In order to achieve site selective self healing, the balance between the chemical driving force and the strain energy between the precipitate and the matrix should be taken into consideration. This will require setting a new value for the critical energy for Laves phase formation.

ACKNOWLEDGEMENTS

6

References

[1] G. Golański, C. Kolan, J. Jasak, Degradation of the Microstructure and Mechanical Properties of High-Chromium Steels Used in the Power Industry, Creep 2018.

[2] F. Abe, Progress in Creep-Resistant Steels for High Efficiency Coal-Fired Power Plants, , J. Press. Vessel Technol. 138(4) (2016) 040804.

[3] A. Aghajani, C. Somsen, G. Eggeler, On the effect of long-term creep on the microstructure of a 12% chromium tempered martensite ferritic steel, Acta Mater. 57(17) (2009) 5093-5106.

[4] M.I. Isik, A. Kostka, G. Eggeler, On the nucleation of Laves phase particles during high-temperature exposure and creep of tempered martensite ferritic steels, Acta Mater. 81 (2014) 230-240.

[5] W. Yan, W. Wang, Y.-Y. Shan, K. Yang, Microstructural stability of 9–12%Cr ferrite/martensite heat-resistant steels, Front. Mater. 7(1) (2013) 1-27.

[6] M.D. Hager, P. Greil, C. Leyens, S. van der Zwaag, U.S. Schubert, Self-healing materials, Adv. Mater. 22(47) (2010) 5424-30.

[7] N. van Dijk, S. van der Zwaag, Self-Healing Phenomena in Metals, Adv. Mater. Interfaces 5(17) (2018) 1800226.

[8] B. Grabowski, C.C. Tasan, Self-Healing Metals, Self-healing Materials 2016, pp. 387-407.

[9] K. Laha, J. Kyono, S. Kishimoto, N. Shinya, Beneficial effect of B segregation on creep cavitation in a type 347 austenitic stainless steel, Scr. Mater. 52(7) (2005) 675-678.

[10] K. Laha, J. Kyono, T. Sasaki, S. Kishimoto, N. Shinya, Improved creep strength and creep ductility of type 347 austenitic stainless steel through the self-healing effect of boron for creep cavitation, Metall. Mater. Trans. A 36(2) (2005) 399-409.

[11] R.N. Lumley, A.J. Morton, I.J. Polmear, Enhanced creep performance in an Al-Cu-Mg-Ag alloy through underageing, Acta Mater. 50 (2002) 3597-3608.

6

[12] R.N. Lumley, I.J. Polmear, Advances in self healing of metals, Proceedings of the First International Conference on Self Healing Materials, Noordwijk aan Zee, Netherlands, 2007.

[13] S.M. He, P.N. Brandhoff, H. Schut, S. van der Zwaag, N.H. van Dijk, Positron annihilation study on repeated deformation/precipitation aging in Fe–Cu–B–N alloys, J. Mater. Sci. 48(18) (2013) 6150-6156.

[14] S.M. He, N.H. van Dijk, M. Paladugu, H. Schut, J. Kohlbrecher, F.D. Tichelaar, S. van der Zwaag, In-situ determination of aging precipitation in deformed Fe-Cu and Fe-Cu-B-N alloys by time-resolved small-angle neutron scattering, Phys. Rev. B 82(17) (2010) 174111.

[15] S.M. He, N.H. van Dijk, H. Schut, E.R. Peekstok, S. van der Zwaag, Thermally activated precipitation at deformation-induced defects in Fe-Cu and Fe-Cu-B-N alloys studied by positron annihilation spectroscopy, Phys. Rev. B 81(9) (2010) 094103.

[16] H. Fang, C.D. Versteylen, S. Zhang, Y. Yang, P. Cloetens, D. Ngan-Tillard, E. Brück, S. van der Zwaag, N.H. van Dijk, Autonomous filling of creep cavities in Fe-Au alloys studied by synchrotron X-ray nano-tomography, Acta Mater. 121 (2016) 352-364.

[17] S. Zhang, J. Kohlbrecher, F.D. Tichelaar, G. Langelaan, E. Brück, S. van der Zwaag, N.H. van Dijk, Defect-induced Au precipitation in Fe–Au and Fe–Au–B–N alloys studied by in situ small-angle neutron scattering, Acta Mater. 61(18) (2013) 7009-7019.

[18] S. Zhang, C. Kwakernaak, W. Sloof, E. Brück, S. van der Zwaag, N. van Dijk, Self Healing of Creep Damage by Gold Precipitation in Iron Alloys, Adv. Eng. Mater. 17(5) (2015) 598-603.

[19] S. Zhang, C. Kwakernaak, F.D. Tichelaar, W.G. Sloof, M. Kuzmina, M. Herbig, D. Raabe, E. Brück, S. van der Zwaag, N.H. van Dijk, Autonomous Repair Mechanism of Creep Damage in Fe-Au and Fe-Au-B-N Alloys, Metall. Mater. Trans. A 46(12) (2015) 5656-5670.

[20] S. Zhang, G. Langelaan, J.C. Brouwer, W.G. Sloof, E. Brück, S. van der Zwaag, N.H. van Dijk, Preferential Au precipitation at deformation-induced defects in Fe–Au and Fe–Au–B–N alloys, J. Alloys Compd. 584 (2014) 425-429.

[21] S. Zhang, H. Fang, M.E. Gramsma, C. Kwakernaak, W.G. Sloof, F.D. Tichelaar, M. Kuzmina, M. Herbig, D. Raabe, E. Brück, S. van der Zwaag, N.H. van Dijk, Autonomous Filling of Grain-Boundary Cavities during Creep Loading in Fe-Mo Alloys, Metall. Mater. Trans. A 47(10) (2016) 4831-4844.

[22] H. Fang, N. Szymanski, C.D. Versteylen, P. Cloetens, C. Kwakernaak, W.G. Sloof, F.D. Tichelaar, S. Balachandran, M. Herbig, E. Brück, S. van der Zwaag,

6

N.H. van Dijk, Self healing of creep damage in iron-based alloys by supersaturated tungsten, Acta Mater. 166 (2019) 531-542.

[23] Y. Fu, C. Kwakernaak, W.G. Sloof, F.D. Tichelaar, E. Brück, S. van der Zwaag, N.H. van Dijk, Competitive Healing of Creep-Induced Damage in a Ternary Fe-3Au-4W Alloy, Metall. Mater. Trans. A 51(9) (2020) 4442-4455.

[24] H. Yu, W. Xu, S. van der Zwaag, A first step towards computational design of W-containing self-healing ferritic creep resistant steels, Sci. Technol. Adv. Mater. 21(1) (2020) 641-652.

[25] Q. Lu, W. Xu, S. van der Zwaag, A strain-based computational design of creep-resistant steels, Acta Mater. 64 (2014) 133-143.

[26] Q. Lu, W. Xu, S. van der Zwaag, The design of a compositionally robust martensitic creep-resistant steel with an optimized combination of precipitation hardening and solid-solution strengthening for high-temperature use, Acta Mater. 77 (2014) 310-323.

[27] Q. Lu, W. Xu, S.v.d. Zwaag, Designing new corrosion resistant ferritic heat resistant steel based on optimal solid solution strengthening and minimisation of undesirable microstructural components, Comput. Mater. Sci. 84 (2014) 198-205.

[28] G.B. Olson, Computational design of hierarchically structured materials, Science 277(5330) (1997) 1237-1242.

[29] F. Abe, H. Araki, T. Noda, The Effect of Tungsten on Dislocation Recovery and Precipitation Behavior of Low-Activation Martensitic 9cr Steels, Metall. Trans. A 22(10) (1991) 2225-2235.

[30] Y. Hosoi, N. Wade, S. Kunimitsu, T. Urita, Precipitation Behavior of Laves Phase and Its Effect on Toughness of 9cr-2mo Ferritic Martensitic Steel, J. Nucl. Mater. 141 (1986) 461-467.

[31] M. Nakahashi, S. Komatsu, S. Nakamura, M. Yamada, On the Precipitation of Laves Phase in 12cr-Mo-V-W Steel Heated for a Long-Time, J. Jpn. I. Met. 47(5) (1983) 426-431.

[32] M. Tamura, H. Hayakawa, M. Tanimura, A. Hishinuma, T. Kondo, Development of Potential Low Activation Ferritic and Austenitic Steels, J. Nucl. Mater. 141 (1986) 1067-1073.

[33] O.D. Sherby, Factors affecting the high temperature strength of polcyrystalline solids, Acta Metall. Mater. 10(2) (1962) 135-147.

[34] 10 - Superplasticity, in: J.-S. Zhang (Ed.), High Temperature Deformation and Fracture of Materials, Woodhead Publishing 2010, pp. 154-171.

[35] M.E. Kassner, Five-Power-Law Creep, Fundamentals of Creep in Metals and Alloys 2015, pp. 7-102.

6

[36] T.G. Langdon, Creep, in: R.J. Brook (Ed.), Concise Encyclopedia of Advanced Ceramic Materials, Pergamon, Oxford, 1991, pp. 92-96.

[37] F. Abe, 9 - Development of creep-resistant steels and alloys for use in power plants, in: A. Shirzadi, S. Jackson (Eds.), Structural Alloys for Power Plants, Woodhead Publishing 2014, pp. 250-293.

[38] NIMS creep data Sheet, National Institute for Materials Science, Tokyo, Tsukuba, 2013.

[39] NIMS creep data Sheet, National Institute for Materials Science, Tokyo, Tsukuba, 2018.

[40] NIMS creep data Sheet, National Institute for Materials Science, Tokyo, Tsukuba, 2014.

[41] NIMS creep data Sheet, National Institute for Materials Science, Tokyo, Tsukuba, 1990.

[42] NIMS creep data Sheet, National Institute for Materials Science, Tokyo, Tsukuba, 1996.

[43] NIMS creep data Sheet, National Institute for Materials Science, Tokyo, Tsukuba, 1986.

[44] NIMS creep data Sheet, National Institute for Materials Science, Tokyo, Tsukuba, 1997.

[45] NIMS creep data Sheet, National Institute for Materials Science, Tokyo, Tsukuba, 1994.

[46] D. Kashchiev, Chapter 20 - Strain energy, in: D. Kashchiev (Ed.), Nucleation, Butterworth-Heinemann, Oxford, 2000, pp. 309-314.

[47] ASM Handbook, Volume 1, ASM International, Materials Park, OH, 1990.

[48] S. Yamasaki, M. Tanaka, T. Morikawa, Y. Watanabe, M. Yamashita, S. Izumi, Evaluation of cleavage fracture behavior of C14 Fe2W Laves phase by first principle calculation and crystal orientation analysis, Tetsu-To-Hagane/J. Iron Steel Inst. 107(11) (2021) 977-985.

6

名利双收(míng lì shuāng shōu)

To gain both fame and fortune; To be famous and rich.

6

SUMMARY

When high-temperature steels are loaded under under industrially relevant conditions not only creep (i.e. a time dependent strain increase even under nominally constant loading conditions) occurs, but also local damage is formed. At relatively short exposure times quasi-spherical micron-sized cavities form preferentially at the grain boundaries oriented perpendicular to the principal loading direction. These cavities subsequently grow and coalesce into micro and macro cracks, which ultimately lead to failure of the structure. The concept of self healing, in which such damage is healed in-situ and under the applied loading conditions rather than is being prevented by a special microstructure, provides a new principle to extend the creep lifetime. Well-selected supersaturated solute atoms can selectively segregate at the free internal surface of the grain boundary cavities and fill them, thereby preventing the coalescence of cavities. This reduction in coalescence rate leads to an extended lifetime. The potential of the concept has been demonstrated in previous studies for binary Fe-based model alloys in which only one healing reaction can take place. The current work aims to take the validation one step further and to demonstrate it for a Fe-3Au-4W (in weight percent) model system in which two healing reactions can take place simultaneously, but without any intention to achieve decent mechanical properties. This work also aims to apply the self-healing concept for two multi-component steels designed to have both decent mechanical properties and to demonstrate self-healing behaviour when exposed to the right conditions.

In **Chapter 1,** the routes towards self healing in metals exposed to high temperatures and suffering from creep damage is explained and the specific goals for the work as described in this thesis are presented.

In **Chapter 2**, autonomous healing of creep-induced grain boundary cavities by Au-rich and W-rich precipitates is studied in a Fe-3Au-4W (wt.%) alloy at a fixed temperature of 823 K (550 °C) with different applied stresses. The ternary alloy, with two supersaturated healing solutes, serves as a model system to study the interplay between two separate healing agents. The creep

properties are evaluated and compared with those of the previously studied Fe-Au and Fe-W binary systems. The microstructures of the creep-failed samples are studied by electron microscopy to investigate the cavity filling behaviour and the mass transfer of supersaturated solute to the defect sites. Compared to the Fe-Au and Fe-W alloys, the new Fe-Au-W alloy has the lowest steady strain rate and the longest lifetime. The site-selective filling of the creep-induced cavities is attributed to two different categories of precipitates: micron-sized Au-rich precipitates and nano-sized W-rich precipitates. The Au-rich precipitates are found to be capable to fully fill, i.e. heal the cavities, while the W-rich precipitates only lead to a limited degree of pore filling, i.e. healing. The two types of precipitates show an apparent reluctance of coexistence when the lifetime is shorter than 100 h.

In **Chapter 3**, the precipitation of supersaturated solutes at free external sample surfaces in ternary Fe-3Au-4W and binary Fe-3Au and Fe-4W alloys (composition in weight percentage) for different ageing times is investigated at a temperature of 700 °C. The time evolution of the surface precipitation is compared among the three alloys to investigate the interplay between the Au and W solutes in the ternary system. The kinetics of the precipitation on the external free surface for the ternary Fe-Au-W alloy is compared to the previously studied precipitation on the internal surfaces of the grain-boundary cavities during creep loading of the same alloy. The Au-rich grain-interior surface precipitates show a similar size and kinetics in the Fe-Au-W and Fe-Au alloys, while the W-rich grain-interior surface precipitates show a smaller size and a higher number density in the Fe-Au-W alloy compared to the Fe-W alloy. While the stress-free precipitation kinetics on the free surface indicated an overall slower diffusivity than during precipitation on internal surfaces during creep conditions, the surface precipitation experiments can qualitatively predict the healing of the creep-induced grain boundary cavities in terms of the interplay between multiple solutes in the matrix, precipitate nucleation rates and the precipitate size distributions.

In **Chapter 4**, constant stress creep experiments at 550 °C are described and analysed for a high-purity Fe-3Au-4W (wt.%) ternary alloy with about 1 at.% supersaturation for Au and W at the loading temperature in order to study self healing of grain-boundary cavities by both Au-rich and W-rich precipitates. Using synchrotron X-ray nano-tomography, the development of

the creep cavities and the healing precipitates at different stages of creep is visualised using two spatial resolutions (30 and 100 nm voxel size). The healing kinetics is found to strongly depend on the nucleation time of the cavities. Cavities nucleated at an early stage of creep could be fully healed, while the healing of the late-nucleated cavities is much slower due to a decrease in the diffusional flux of the healing supersaturated solutes over time, as a result of (i) a decrease inter-cavity spacing caused by cavity nucleation and (ii) a gradual depletion of the supersaturated solutes near the grain boundaries. The interaction between the competing healing mechanisms for creep cavities by Au-rich and W-rich precipitates is discussed. It is found that Au-rich precipitates are formed much faster than the W-rich precipitates, and thereby effectively provide creep damage healing on different time scales.

In **Chapter 5**, a set of numerical and analytical models is presented to predict the growth and filling of grain boundary creep cavities in self-healing binary alloys as a function of time, stress, level of supersaturation and inter-cavity spacing and diffusion ratio's. The cavity grows due to the diffusional flux of vacancies towards the cavity, which is driven by the stress gradient along the grain boundary. Upon deposition of healing solute atoms on the cavity wall, effectively vacancies are removed from the cavity due to the inverse Kirkendall effect. The competition between the inward and outward vacancy fluxes results in the growth or shrinkage of the open volume of the creep cavity. It is found that the filling ratio shows a maximum value at a critical time t_{cr}, which corresponds to the time when the inward vacancy flux exceeds the outward vacancy flux (integrated over the surface area). Two conditions can be distinguished: one where the cavity becomes fully filled before this critical time is reached (and the process stops) and one where the only partial filling will take place and the growth of the cavity will continue. For each combination of parameters, the critical applied stress σ_{cr}, below which the cavity can be fully filled, is calculated. The analytical model shows that for conditions leading to quasi 1D solute transport, the critical stress approximately scales as $\sigma_{cr} \propto (\lambda/a)^4 (D_m^s/D_{gb})(\Delta x)^2$, where λ/a is the relative inter-cavity spacing, D_m^s/D_{gb} the ratio of the solute diffusivity in the matrix and the vacancy diffusion in the grain boundary and Δx the supersaturation of the solute.

In **Chapter 6**, a series of creep experiments with different applied stresses but at a fixed high temperature (550 °C) are described and analysed

for two custom-designed self-healing creep-resistant 12Cr alloys. The alloys, which were computationally designed to combine a decent creep resistance with self-healing potential but for different intended lifetimes, serve as the first step from the self-healing binary and ternary model alloys towards multi-component industrial steels. Compared to the present commercial creep-resistant steels, the newly designed steels, especially the F-SH alloy (i.e. the one designed with a fast self-healing kinetics starting after only 300 hours) shows a good creep resistance and lifetimes comparable to those of existing creep steels, due to a combination of precipitation strengthening, solid-solution strengthening and subgrain strengthening effects. Regarding the self healing aspect, the F-SH steel shows an increase in lifetime beyond the onset time for Laves phase (i.e. the healing agent) precipitation. The S-SH steel, designed not to show any self-healing reaction unless exposed to creep conditions for 30000 hours, indeed shows no self-healing behaviour during the maximal testing time in this research (1500 hours). Based on all observations we conclude that the cavity formation is not properly quantified by the design rules due to the absence of kinetic information on grain-boundary cavities formed during creep, which would result from a dislocation climb dominated creep mechanism. For future alloy design calculations, the formation time of the healing phase in the bulk can be estimated following the same principle in the current design, i.e. based on the chemical driving force of this phase. In order to achieve site selective self healing, the balance between the chemical driving force and the strain energy between the precipitate and the matrix should be taken into consideration. This will require setting a new value for the critical energy for Laves phase formation on free internal surfaces.

SAMENVATTING

Wanneer hoge-temperatuur stalen mechanisch belast worden onder industrieel relevante condities dan treedt niet alleen kruip (een tijd afhankelijke toename in de lengteverandering die zelfs optreedt bij een constante aangelegde belasting) op, maar wordt er ook lokale schade gevormd. Bij relatief korte meettijden worden er micrometer grote holtes gevormd die zich bij voorkeur bevinden op de korrelgrenzen die loodrecht georiënteerd zijn ten opzichte van de voornaamste spanningsrichting. Deze holtes gaan vervolgens groeien en samensmelten tot micro- en macro-scheuren, die uiteindelijk toe leidt dat de structuur het begeeft. Het concept van zelf-herstellen, waarin deze schade in-situ wordt hersteld onder de belastingscondities, in plaats van het voorkomen van schade middels een speciale microstructuur, geeft een nieuwe methode om de levensduur tijdens kruip te verlengen. Goed geselecteerde atomen die in oplossing zijn kunnen selectief uitscheiden op de vrije interne oppervlakken van de holtes die zich op de korrelgrenzen bevinden, deze holtes vullen en daarmee het samensmelten van holtes voorkomen. De afname in het tempo waarin de holtes samensmelten leidt tot een velenging van de levensduur. De potentie van dit concept is aangetoond in voorgaande studies voor binaire op Fe gebaseerde modellegeringen, waarin slecht één herstel reactie plaats kan vinden. Het huidige onderzoek heeft als doel om het demonstreren van de methode één stap verder te brengen door de effectiviteit aan te tonen voor een ternaire Fe-3Au-4W (in gewichtsprocent) modelsysteem, waarin twee herstel-reacties tegelijkertijd plaats kunnen vinden maar zonder de intentie om voor toepassingen bruikbare mechanische eigenschappen te bereiken. Dit onderzoek is er ook op gericht om het concept van zelf-herstellen toe te passen in twee multi-component stalen die beiden ontworpen zijn om voor toepassingen redelijke mechanische eigenschappen te geven en om tegelijkertijd zelf-herstellend gedrag te vertonen wanneer ze aan geschikte condities worden blootgesteld.

In **Hoofdstuk 1**, de routes naar zelf-herstellend gedrag in metalen die blootgesteld zijn aan hoge temperatuur en lijden aan kruipschade zijn toegelicht en de specifieke doelen voor het onderzoek dat beschreven is in dit proefschrift zijn gepresenteerd.

In **Hoofdstuk 2**, het autonome herstel van kruipholtes op korrelgrenzen door Au-rijke en W-rijke precipitaten is onderzocht in een Fe-3Au-4W (gewicht %) legering op een temperatuur 823 K (550 °C) en bij verschillende aan gelegde spanningen. De ternaire legering, met twee herstellende opgeloste elementen in oververzadiging, dient als model systeem om de wisselwerking tussen twee verschillende herstellende middelen te onderzoeken. De kruipeigenschappen zijn geëvalueerd en vergeleken met die van de eerder onderzochte binaire Fe-Au en Fe-W systemen. De microstructuren van de door kruip gebroken samples zijn bestudeerd met elektronenmicroscopie om het vulgedrag van de kruipholtes en het massatransport van de oververzadigde oplossing naar de schadelocaties te onderzoeken. In vergelijking met de Fe-Au en Fe-W legeringen, de nieuwe Fe-Au-W legering vertoont het laagste tempo van lengteverandering en de langste levensduur. De ruimtelijke voorkeur voor precipitatie ter plaatse van de kruip-geïnduceerde holtes is toegeschreven aan twee verschillende soorten precipitaten: microscopische Au-rijke precipitaten en nanoschaal W-rijke precipitaten. Het is gevonden dat de Au-rijke precipitaten in staat zijn de holtes volledig te vullen, en daarmee de kruipholtes te herstellen, terwijl de W-rijke precipitaten slechts tot een geringe mate van vulling (herstel) van de kruipholtes leidt. De twee soorten precipitaten lijken elkaar te vermijden wanneer de levensduur korter dan 100 h is.

In **Hoofdstuk 3**, is de precipitatie van oververzadigde oploste elementen aan vrije externe oppervlakken onderzocht in ternaire Fe-3Au-4W en binaire Fe-3Au and Fe-4W legeringen (samenstelling in gewicht procent) voor verschillinde tijden op een temperatuur van 700 °C. De tijdevolutie van de oppervlakteprecipitatie van de drie legeringen is met elkaar vergeleken om de wisselwerking tussen het opgeloste Au en W in het ternaire systeem te onderzoeken. De kinetiek van de precipitatie op het externe oppervlak voor de ternaire Fe-Au-W legering is vergeleken met de eerder onderzochte precipitatie op de interne oppervlakken van de kruipholtes aan de korrelgrenzen gedurende kruip in dezelfde legering.

De Au-rijke oppervlakte-precipitaten in het midden van de korrels vertonen een vergelijkbare afmeting en kinetiek in de Fe-Au-W en Fe-Au legeringen, terwijl de W-rijke oppervlakte-precipitaten in het midden van de korrel een kleinere afmeting en een hogere deeltjesdichtheid voor de Fe-Au-W legering vertonen dan voor de Fe-W legering. De spanningsvrije precipitatie-kinetiek aan het oppervlak vertoont een langzamere diffusie dan gedurende precipitatie aan interne oppervlakken tijdens kruip-condities. De experimenten naar oppervlakte-precipitatie kunnen een kwalitatieve voorspelling geven van het herstel van de kruip-geïnduceerde holtes aan de korrelgrenzen in termen van de wisselwerking tussen de verschillende oplossingselementen in de matrix, de precipitatie-kiemsnelheid en de grootte-distributie van de precipitaten.

In **Hoofdstuk 4**, worden kruip experiment beschreven die bij constante spanning en een temperatuur van 550 ^{o}C zijn uitgevoerd en geanalyseerd voor een ternaire Fe-3Au-4W (gewicht %) met hoge zuiverheid met ongeveer 1 atoom % oververzadiging voor Au en W bij de temperatuur waarbij de spanning is aangelegd om het zelf-herstellend gedrag van kruipholtes aan korrelgrenzen door Au-rijke en W-rijke precipitaten te bestuderen. Door gebruik te maken van synchrotron Röntgen nano-tomografie, is de ontwikkeling van de kruipholtes en de herstellende precipitaten gevisualiseerd bij verschillende kruipstadia met behulp van twee resoluties (met een voxel grootte van 30 en 100 nm). De herstel-kinetiek bleek sterk af te hangen van de tijd waarop de holtes gekiemd waren. Holtes die waren gekiemd in een vroeg stadium van de kruip konden volledig worden hersteld, terwijl het herstel van de laat-gekiemde holtes aanzienlijk langzamer is door een afname van de diffusieflux van de herstellende oververzadigde oplossingselementen in de tijd, als een gevolg van (i) een afname van de afstand tussen de holtes door het kiemen van nieuwe holtes en (ii) een geleidelijke afname van de oververzadiging van de oplossingselementen in de buurt van de korrelgrenzen. De interactie tussen de concurrerende herstel-mechanismen voor kruipholtes door Au-rijke en W-rijke precipitaten is bediscussieerd. Er is gevonden dat de Au-rijke precipitaten veel sneller worden gevormd dan de W-rijke precipitaten, waardoor beiden effectief een herstel van de kruipschade bewerkstelligen op verschillende tijdschalen.

In **Hoofdstuk 5**, een set van numerieke en analytische modellen is gepresenteerd om de groei en het vullen van kruipholtes op korrelgrenzen in zelf-herstellende binaire legeringen te voorspellen als functie van tijd, spanning, de mate van oververzadiging, de afstand tussen naburige holtes en de verhouding tussen de diffusie-constanten. De holte groeit vanwege de diffusieflux van vacatures gericht naar de kruipholte, welke wordt gedreven door de gradiënt in de spanning langs de korrelgrens. Bij het afzetten van herstellende atomen van de oplossingselementen op de wand van de kruipholte worden effectief vacatures verwijderd uit de holte als gevolg van het inverse Kirkendall effect. De competitie tussen de naar binnen gerichte en de naar buiten gerichte vacature-fluxen resulteert in een groei of krimp van het open volume van de kruipholte. Er is gevonden dat de vulfractie een maximale waarde vertoont voor een kritische tijd t_{cr}, welke correspondeert met de tijd waarop de naar binnen gerichte vacature-flux de naar buiten gerichte vacature-flux overstijgt (geïntegreerd over het oppervlak). Er kunnen twee gevallen worden onderscheiden: één waarin de holte volledig wordt gevuld voordat de kritische tijd wordt bereikt (en het vulproces stopt) en één waarin alleen de holte slechts gedeeltelijk kan worden gevuld en de groei van de holte uiteindelijk weer toeneemt. Voor elke combinatie van parameters is de kritische aangelegde spanning σ_{cr}, waar beneden de holte volledig kan worden gevuld, berekend. Het analytische model toont aan dat voor de situatie waarin een quasi 1D transport van oplossingselementen plaats vindt de kritische spanning ongeveer schaalt als $\sigma_{cr} \propto (\lambda/a)^4 (D_m^s/D_{gb})(\Delta x)^2$ waarin λ/a de ratio is van de afstand tussen de holtes en de afmeting van de holte, D_m^s/D_{gb} is de ratio van de diffusieconstante van het oplossingselement in de matrix en de diffusieconstante van de vacatures in de korrelgrenzen en Δx de oververzadiging van het oplossingselement.

In **Hoofdstuk 6**, een reeks kruipexperimenten met verschillende spanningen maar bij een vaste hoge tempratuur (550 ᵒC) zijn beschreven en geanalyseerd voor twee speciaal ontworpen zelf-herstellende 12Cr kruipstalen. De legeringen, welke waren ontworpen om een redelijke resistentie tegen kruip te combineren met een zelf-herstellende potentie dienen als een eerste stap van de zelf-herstellende binaire en ternaire modellegeringen naar multi-component industriële staalsoorten. Vergeleken met de huidige commerciële kruip-stalen de nieuw ontworpen stalen, in bijzonder de F-SH legering (degene die ontworpen is met een snelle zelf-

herstellende kinetiek die start na slechts 300 uur), vertonen een goede kruip-resistentie en een levensduur die vergelijkbaar is met bestaande kruipstalen door een combinatie van versteviging door precpitaten, door oplossings-elementen en door sub-korrels. Met betrekking tot de zelf-herstellende aspecten, de F-SH staal vertoont een toename in levensduur na de starttijd voor de precipitatie van de Laves fase (het herstel-middel). De S-SH legering, welke was ontworpen om geen zelf-herstellende reactie te vertonen tenzij blootgesteld aan kruip-condities voor tenminste 30000 uur, vertoont inderdaad geen zelf-herstellend gedrag gedurende de maximale testtijd van dit onderzoek (1500 uur). Gebaseerd op alle observaties concluderen we dat de vorming van holtes niet nauwkeurig gekwantificeerd is in de ontwerpregels door het ontbreken van kinetische informatie over holtes die vormen gedurende kruip op korrelgrenzen, welke zouden leiden tot een *dislocation climb* gedomineerd kruip-mechanisme. Voor toekomstige berekeningen voor het ontwerpen van legeringen de karakteristieke tijd voor het vormen van de herstel-fase in de matrix kan worden afgeschat middels dezelfde principes van het huidige ontwerp, dus gebaseerd op de chemische drijvende kracht van deze fase. Om zelf-herstellend gedrag te plaatse van de kruipschade te bewerkstelligen moet de balans tussen de chemische drijvende kracht en de vervormingsenergie tussen het precipitaat en de matrix in beschouwing worden genomen. Dit vereist het opstellen van een nieuwe waarde voor de kritische energie voor de formatie van de Laves fase op vrije interne oppervlakken.

总结

在工业条件下对高温钢施加载荷，钢内会发生蠕变（金属材料在高温下施加载荷时，产生的与时间相关的塑性变形现象）和局部损伤。在较短的时间内，微米级孔洞优先在垂直于主应力方向的晶界上形成，随后，这些孔洞长大、合并成微观和宏观裂纹，最终导致材料失效。自修复这一概念为延长材料的蠕变寿命提供了新的思路：其不利用某种特定的微观组织或组分来预防上述损伤，而是在不去除载荷的条件下，对损伤进行原位修复。在自修复材料中，特定的过饱和溶质原子可以选择性地在晶界上孔洞内表面析出，并对孔洞进行填充，从而阻止孔洞的合并。通过合并率的降低，蠕变寿命得以延长。通过前期对二元铁基模型合金（即模型合金中只存在一种修复元素）的研究，自修复的可行性已经得到了证明。本文旨在在另外两种体系中进一步验证自修复的可行性。其一是另一种三元模型合金 Fe-3Au-4W（重量百分比），该模型合金中存在两种修复元素，但不存在旨在提高机械性能的设计。其二是两种多组分钢，这两种钢通过前期的成分设计，应当同时具备良好的机械性能和自修复能力。

在第一章中，阐述了在高温蠕变环境下自修复行为的产生机理，并介绍了本文的具体研究内容。

在第二章中，通过对 Fe-3Au-4W（重量百分比）合金在固定温度 823K（550℃）不同应力下的蠕变实验，研究了富金（Au）和富钨（W）的析出物对合金中晶界上孔洞的修复行为。该三元模型合金中存在两种过饱和的修复元素，因此可以用来研究两种独立的修复元素之间的相互作用。本章研究了该三元合金的蠕变性能，并将其与 Fe-Au、Fe-W 二元合金的蠕变性能进行对比。此外，通过电子显微镜对蠕变失效样品微观组织进行表征，讨论了过饱和溶质向缺陷的转移及蠕变孔洞的填充行为。与 Fe-Au 和 Fe-W 合金相比，Fe-Au-W 三元合金在蠕变中应变速率最低，蠕变寿命最长。微米级的富 Au 析出相和纳米级的富 W 的析出相对蠕变中形成的孔洞均具有填充效果。富 Au 相可以完全填充孔洞，亦即使孔洞愈合；而富 W 相只能部分填充孔洞。当蠕变寿命低于 100 小时时，两种析出相之间存在明显的不共存现象。

在第三章中，对三元 Fe-3Au-4W 和二元 Fe-3Au、Fe-4W 合金（重量百分比）在 700 ℃进行了不同时长的时效处理，以此研究过饱和溶质在样品外表面的析出行为。通过对比三种合金表面析出相随时间的变化，研究了三元体系中 Au 和 W 两种溶质之间的相互作用。通过本实验与 Fe-Au-W 蠕变实验的比较，对比研究了析出相在样品外表面和孔洞内表面（孔洞在蠕变条件下于晶界上形成）的动力学行为。富 Au 的 GI（grain-interior，晶界范围内）表面析出相在 Fe-Au-W 和 Fe-Au 合金中具有相似的尺寸和动力学表现，而对比 Fe-Au-W 和 Fe-W 合金中的结果，可以发现富 W 的 GI 表面析出相在 Fe-Au-W 合金中尺寸更小，数密度更高。由于外表面无应力作用，溶质元素向外表面的扩散速率整体上低于在蠕变条件下向孔洞内表面的扩散速率。表面析出实验可以从基体中多种溶质的相互作用、析出相的形核速率、析出相的尺寸及分布等方面定性地预测蠕变过程中晶界孔洞的自修复行为。

在第四章中，通过对高纯度的 Fe-3Au-4W（重量百分比）合金在 550 ℃进行恒定应力的蠕变实验，研究富 Au 和富 W 析出相对晶界上孔洞的修复行为。在该温度下，Au 和 W 的过饱和度约为 1 at.%。通过同步辐射 X 射线纳米层析成像技术，利用两种空间分辨率（30 和 100 nm 体素）对蠕变不同阶段的孔洞和修复析出相进行了可视化。孔洞形核时间对修复动力学影响很大：蠕变早期形成的孔洞可以完全修复，而后期形成的孔洞修复速率则大大降低。这是因为用于修复的过饱和溶质的扩散通量随时间降低，而导致扩散通量降低的原因包括：（i）晶界上孔洞之间的距离随着孔洞形核而缩短；（ii）晶界附近的过饱和溶质被逐渐消耗。本章讨论了富 Au 和富 W 相对蠕变孔洞的修复机制，研究表明富 Au 相的析出远快于富 W 相，这可以使蠕变孔洞的修复在不同的时间尺度上得以进行。

在第五章中，提出了一组数值模型和解析模型，用以预测二元合金中晶界上蠕变孔洞的长大的修复受时间、应力、过饱和度、孔洞间距、晶内/晶界扩散速率比的影响。在该模型中，晶界上的应力梯度导致空位向孔洞的扩散，进而导致孔洞的长大。随着用于修复的溶质原子在孔洞内表面沉积，由于反向 Kirkendall 效应，空位从孔洞中移除。上述两个空位通量的大小关系决定了蠕变孔洞的继续长大或者收缩。研究发现，填充率在临界时间 t_{cr} 达到极大值，在该时间点，内向空位通量超过外向空位通量（空位通量对孔洞表面积进行积分）。模型预测了两种不同的情况：一种情况是孔洞在临界时间 t_{cr} 之前被完全填充，另一种情况是在到达在临界时间 t_{cr} 时孔洞只被部分

填充。在第一种情况下，修复过程在孔洞被完全填充之后停止；在第二种情况下，孔洞将在t_{cr}之后继续长大。本章计算了各种参数下的临界应力σ_{cr}，当施加应力低于该临界应力时，孔洞可以被完全修复。解析模型给出了对于准 1D 扩散条件下的临界应力近似比例关系，$\sigma_{cr} \propto (\lambda/a)^4 \left(D_m^s/D_{gb}\right)(\Delta x)^2$，其中$(\lambda/a)$为孔洞间距与孔洞直径的比值，$\left(D_m^s/D_{gb}\right)$为溶质在基体中的扩散速率与晶界中空位扩散速率的比值，Δx为溶质过饱和度。

在第六章中，在固定高温（550 ℃）不同应力下对两种 12Cr 抗蠕变钢进行了蠕变实验。两种合金的成分经过计算设计，应同时具备良好的抗蠕变性能和自修复能力，但二者的预期使用寿命不同。这些合金的设计是将自修复概念从二元和三元模型合金转向多组分工业钢的第一步尝试。本章将设计钢的蠕变性能与现有的商业蠕变钢进行比较，结果表明设计钢，尤其是 F-SH 钢（该合金中修复动力学较快，设计的起始修复时间为 300 小时）表现出良好的抗蠕变性，其蠕变寿命与现有的抗蠕变钢相当。这种抗蠕变性来自于析出强化、固溶强化和亚晶粒强化。在自修复方面，在修复相 Laves 相的析出起始时间之后，F-SH 合金的蠕变寿命有所增长。S-SH 合金中修复动力学较慢，设计的起始修复时间为 30000 小时。该合金在本章的最长测试时间（1500 小时）内的确未表现出自修复行为。在实验中，两种合金表现出位错攀移控制的蠕变机制，该机制对晶界上孔洞形成的影响并未在合金设计中纳入考量，因此该设计未能全面量化蠕变过程中晶界孔洞的形成动力学。对于未来的合金设计，应考虑以下内容：第一，可以沿用本章中的方法，即利用化学驱动力评估基体中修复相的析出时间。第二，为实现位点选择性的自修复（即修复相只在损伤位置形成），应同时考虑修复相的析出驱动力和修复相与基体间的应变能，这需要对 Laves 相在孔洞内表面的形成能设置一个新的临界值。

有意思(yǒu yì si)

Interesting. Can have both positive and negative connotations.

ACKNOWLEDGEMENTS

As I type this sentence, I have just finished my second-to-last meeting with my supervisors. Our next meeting is scheduled for September 6, which is more than two months away, but only nine days before my defence. It's hitting me that the next meeting is my last meeting as a PhD candidate and that, although it feels so unreal, my graduation *is* very much for real. After finishing my thesis, I have been avoiding writing my acknowledgement. I have been preparing for this moment for the past four years. This acknowledgement should be easy to write, I have thought. Not until now have I realised the reason for my procrastination. I am not only concerned about my limited English, but also, more importantly, I don't want to go, and I'm definitely not ready or willing to leave. It feels like yesterday when Sybrand and I had our first Skype meeting, during which he asked me if I liked gold. Who doesn't? The first time I met Niels, which is also like yesterday, he explained the letter *ij* in Dutch, and *dijk* became my second Dutch word. The first was *fiets*. The same day I met Niels, I also met Ekkes, who was the first "foreigner" who pronounced my name perfectly correctly, including the tones. But now, after more than one thousand yesterdays, here I am, having only one last meeting remaining, ready to start my acknowledgement.

First and foremost, I would like to thank my corresponding promotor, Sybrand van der Zwaag. Sybrand, thank you for offering me the position and for being supportive and encouraging throughout the adventure. I have enjoyed it every single day. I can always rely on you to steer me in the right direction while granting me sufficient freedom. I deeply admire you for being full of fantastic ideas, brilliant insights, wide-ranging curiosity, and infinite energy. It surprises me that you can host a meeting directly after an overnight flight, and that you can still keep your door open despite your full agenda. I may have mentioned this before, but if we were in a Hollywood movie, you would be the superhero always ready to save or change the world. I cannot overemphasise my appreciation for all the effort and time you have spent to extend my contract, not even to mention the comforting words when I was terrified by the residency problem. Thank you for being my promotor and guide accompanying me on my paths of academic research and daily life.

My sincere appreciation goes to my promoter, Niels van Dijk. Niels, I hope to have developed some thinking patterns of a physicist after four years, although I am proud enough to be a material scientist. I have benefited so much from the way you see things by extracting the essence from the misty facts and simplifying it into a physics-based model. On top of being an excellent supervisor, you are also someone I can share my feelings with. I cannot imagine I would have made it without your patience, calmness, tolerance and encouragement, especially when facing the haunting oxidation problem and the endless delay caused by Covid-19. I have enjoyed our discussions not only of the research, but also of the "irrelevant" movies, stories and anecdotes. Several times, however, I felt guilty for taking your time for half an hour while asking only for five minutes. You have mentioned once that I may have been unlucky, but I truly believe that it is only because I have used up all the luck in the world by being your student. Nothing exceeds this honour.

A special thanks goes to my other promotor, Ekkes Brück, for all the fruitful discussions in our progress meetings, and for providing a community as warming as FAME. I have never felt isolated although my topic is different from all the other PhDs. Thank you for driving us to Alkmaar. I miss the Christmas lunches and dinners ever since the pandemic started.

I had amazing predecessors who guided me towards the splendid world of self healing. Haixing, thank you for showing me how to operate the creep tester, the polishing machine, the furnace, and for the countless discussions. I have always seen you as someone who is born to be a scientist. Hao, it was your experience with Fortran and GA that encouraged me to toddle towards coding. Don't take me wrong, you are more than an excellent cook. Casper Versteylen, you had just finished your thesis when I first met you at 3mE, and I hope you are proud to know that after four years of reading, your thesis is falling apart in my hands. Shasha, we have never met, but reading your notes in our experiment log makes me feel connected and bonded to you.

My research would not have been finished without having had the privilege to collaborate with so many excellent researchers. Kees Kwakernaak, thank you for the training of SEM and EBSD. In your SEM lab, sometimes it felt as if I were observing the whole universe through a micron square region. More importantly, it meant everything to me when you told me that you had faith in me before my go/no go evaluation, when I didn't have faith in myself. Wim Sloof, I owe you many thanks for allowing me to use the well-designed and well-cared for equipment and instruments. I truly admire your passion and love for work. My thanks goes to Dr. Frans Tichelaar for his expertise and deep

insights in TEM and for the fruitful discussions. Dr. Hussein Farahani, I deeply appreciate our discussions, not only about Dictra, but also about our feelings at different stages during the PhD. I would like to express my gratefulness to the collaborators, Dr. Peter Cloetens, Dr. Federico Monaco and the staff on beamline ID16A-NI at ESRF. Although I could only attend the measurement remotely, I was fortunate to be involved, for nano-tomography has been my dream even before I came to Delft. Thanks to Dr. Dominique Ngan-Tillard and Joost van Meel, for providing the access to the workstation and for helping during my usage of Avizo. Thanks to Dr. Lambert van Eijck for allowing me to take so much time on the desktop of NPM2. I would like to acknowledge Dr. Joachim Kohlbrecher at PSI for his support with the SANS measurements. I truly cherished the chance of being involved in on-site experiments with Covid lurking in the background. I am also thankful to the people who participated in the surface precipitation experiments at different stages. Hans Brouwer, I have seldom known someone who is as good at and as proud of their jobs as you are (as you should be). The experiments would never have worked without you. Paula Martin Rojo, thank you for the countless failures we went through before the experiments finally succeeded. Thank you to Dr. Meng Zhao for generously sharing his experience and code of surface segregation. Thanks to Sander van Asperen for the support in sample preparation. Thank you Drs. Daniel Scheiber and Lorenz Romaner from Materials Center Leoben for the discussion on grain boundary segregation. Thank you Dr. Ivan Batashev for calculating the formation energy of Au/W structures. I appreciate all the support and discussions from many people on the simulation project. Thanks to Drs. Fred Vermolen, Marcel Sluiter, and Abdelrahman Hussein for the fruitful discussions. Dimosthenis Giannopoulos, thank you for your help when I started using COMSOL and for sharing the information of the webinars. Xiaohui Wang, thank you for sharing so much information, so many tips, experiences, and even warnings and complaints. I have just noticed that you may be the only person who is in the acknowledgement of both my master's thesis at DUT and my doctoral thesis at TUD for technical reasons. Most of the preliminary experiments on the designed steels were performed in China in the first half of 2020, when the pandemic made it ten times harder to organise and perform any sort of activities. Therefore, I treasure and appreciate the extensive help from many people. Thank you Prof. Wei Xu for offering me access to the lab at such a crucial moment. Thank you Dr. Xincheng Yan for the days of experiments. Thank you Dr. Chunxia Yao for the access to the microscopy. A special thanks goes to Dr. Xiaolei Shi for improvising many treatments for metals in a composite lab, and for taking me to the workshop in the intense heat of

summer. Thank you Yang Su for the large amount of assistance in the subsequent creep tests and the microstructure characterisation.

I feel lucky to have known such fascinating officemates, groupmates, and faculty mates. Zhou Zhou, doubtlessly you are brilliant, kind, and always calm. Thank you for cheering me up when I lost 300 hours of data by reminding me of an imaginary world where the power outage took place after 800 hours. You are also an excellent teacher, who can explain things in a simple and clear way. Wenqin, thank you for sharing the photo of your old book. The small incident that you may have forgotten helped a lot in dragging me out of my nadir of darkness. Huanhuan, you are the most optimistic, energetic, and fearless person I know. You have so many qualities that I admire, and I truly believe that there is literally nothing in the world that you cannot achieve. Xinmin, you are a warm-hearted and thoughtful host, who always takes care of your friends and guests. I have benefited so much from your experience, good or bad, and I feel reassured just knowing you are there. Bei, there must be a bug in the universe such that *we* have so much in common. I hope the universe never debugs and that after fifty years we can look back on our tears and smile, or on our laughter and cry. Yueer and Ziying, you make me feel so young, and thanks to you, the number of my acquaintances has increased exponentially. Fengqi, Chao Ma, Hamutu and Hanggai, thank you for helping me with moving, and/or for repairing my bike. Bowei, it was from you that I heard "Happy Chinese New Year" for the first time since I had arrived in the Netherlands. My gratitude also goes to other PhD and postdoc fellows whom have enriched my days at RID, LR and 3mE: Abdulkadir Biffo, Alexandros Vasileiadis, Angie Rangel Cardenas, Anika Kiecana, Anton Tuluk, Bing Xu, Carlo Belloni, Chaofan Chen, Chenglong Zhao, Diego Pineda Quijano, Elif Kaymazlar, Eveline van der Maas, Evgenii Velichko, Gawel Kus, Guus Verhaar, Hanan Al-Kutubi, Hugo Veldhuizen, Jianing Zhu, Jiawei Lai, Jingjing Zhao, Jun Liu, Katja Garina, Luke van Koppen, Mariana Cruz, Marlon Mopon, Maxim Ariëns, Michael Maschek, Miisa Tavaststjerna, Ming Liu, Paul Denissen, Pierfrancesco Ombrini, Qi Jia, Qi Shen, Qidi Wang, Remco van der Jagt, Rui Guo, Runze Wang, Satya Ammu, Shengnan Zhang, Tadhg Mahon, Tammo Schwietert, Theo Famprikis, Tinashe Darikwa, Victor Landgraf, Vincent Stuber, Vincenzo Montano, Violetta Arszelewska, Viviam Marques Pereira, Zhaolong Li, Zhu Cheng, and the names of the earlier generations.

I acknowledge the support and kindness of the colleagues at the RID and LR. I would like to give my thanks to Clemens Dransfeld, Bilim Atli Veltin, and Lars Bannenberg for your kind suggestions and information on job hunting. Anton Lefering, thank you for helping me with the furnace, the SQUID, the

diamond cutting machine, and many other instruments. I'm especially grateful to you for shipping me 10 kg samples during the first wave of Covid. I have enjoyed chatting with you, and needless to say, you are a unique you, one of a kind. Jouke Heringa, you have always been my first solution whenever I have encountered computer-related problems that cannot be solved by restarting. Thank you for giving me the access to the clusters and for saving my life twice by saving the data on my hard disc. Wim Bouwman, thank you for explaining to me the multi-scattering in SANS. Bert Zwart, thank you for making countless quartz tubes, and I felt so lucky to have the 4000th one. Thanks to Martijn de Boer for continuously taking care of my creep tester and for cutting the board, which eventually became my cooking platform. Thanks to Kees de Vroege for solving the LabView problem caused by the Windows update. Thank you Henk Schut for allowing me to use the spot welder. Sorry for all the scratches on your desk, for the set-up was too heavy and I could only slide it on the desk instead of lifting it up. Thanks to Piet van der Ende for helping me several times to plug in the connecting pin of the creep tester before I found a way to do that by myself. Thank Kees Goubitz and Michel Steenvoorden for organising the coffee. Thanks to Robert Dankelman for talking to me in Dutch. Thanks to Marlies Nijemeisland for the DSC test. I enjoyed our talk on the train back to the Netherlands from Aachen. Thank you Durga Mainali Sharma for the SEM training at LR. A special thanks goes to Shanta Visser, Ilse van der Kraaij and Nicole Banga, for taking care of millions of administrative issues. Apart from the names above, my gratitude extends to all the colleagues from NovAM, FAME, NPM2, SEE and DEMO, Ad van Well, Baukje Terpstra, Ben Harrison, Chris Duif, Erik Kelder, Ernst van der Wal, Esther Bijl, Frans Ooms, Iulian Dugulan, Jeroen Plomp, Johan Bijleveld, Katia Pappas, Marnix Wagemaker, Michel Thijs, Pedro Braga Groszewicz, Santiago Garcia, Stephan Eijt, Steven Parnell, Swapna Ganapathy, Theo Rekveldt, Xuehang Wang, and Yinglu Tang.

Huifang Lan, Shuai Tang, Lishuai Zong, Xue Wang, and Cong Li, I sincerely value the beautiful moments and the hearty dinners we had together. Needless to say, I have learnt much from you as a new researcher, but more importantly, you made me feel at home during my first year. Huifang, my heartfelt thanks goes to you for assuring me that I will always be needed. Suxia Guo and Ying Li, I deeply appreciate our reunion in Japan in the summer of 2019, which has somehow given me the feeling that we are under the same sky despite the distance between us. This feeling has supported me through the craziness of Covid. Suxia, it was also you who inspired and encouraged me to take the step to be a PhD candidate. Kelly Greene, thank you for sparing your time speaking Dutch with me. It was not only Dutch, but also much life wisdom

that I have learnt from you. You are a friend who is open-minded and deep in thought. Nathan Chan, for a while you were the only person, apart from my supervisors, I spoke English with. Thank you for slowing down the retrogression rate of my English. Thanks to Jin Chang and Peng Zhuo, who helped me a lot during my application for the position. Thanks to Shuhong, for the many emotional moments we shared. Thanks to Qiyao, for the dinner on Chinese New Year. Thanks to Lois, Abi, Babara and other people from Globe Café in Nottingham. Meeting you again was the best thing happened during covid. Langzi, Ze Chang & Lu Cheng, Zhaoying, Shan Qu, Wenting, Changrang, Tingting, Xinxin, Qingru, Wenxiu, Xueqing, Yu Zhang, and the names I might have forgotten to mention, thank you for making my life in Delft so colourful.

Last but not least, it is to my family that I owe my deepest gratitude. Thanks to my amazing father and mother. With your endless and unconditional love, I have had the courage to handle anything knowing it is OK if I fail. You have given me not only the willingness to explore the world and the passion to excavate the unknown, but also the ability to listen to and empathise with people. I hope I can do as well as you with my own children. Weiwei, thank you for accepting who I am and for supporting me in every step during my journey through the years. I would never have been able to pursue my dream without you being my rock and my comfort. Now, let *our* dreams begin.

5. **Y. Fu**, H. Fang, F. Monaco, P. Cloetens, F.D. Tichelaar, J.G. van Meel, E. Brück, S. van der Zwaag, N.H. van Dijk, Self healing of creep-induced damage in Fe-3Au-4W by multiple healing agents studied by synchrotron X-ray nano-tomography, submitted.

4 **Y. Fu**, S. van der Zwaag, N.H. van Dijk, Modelling the growth and filling of creep-induced grain-boundary cavities in self-healing alloys, J. Mater. Sci. 57 (2022) 12034–12054.

3 Z. Zhang, S. Zhang, Z. Yao, M. Oleksandr, X. Cao, P. Zhang, **Y. Fu**, N. H. van Dijk, S. van der Zwaag, Precipitation of supersaturated solute in H ion irradiated Fe-Au and Fe-Au-W alloys studied by positron annihilation spectroscopy, Nucl. Instrum Methods Phys. Res. B 505 (2021) 50-57.

2 **Y. Fu**, C. Kwakernaak, W.G. Sloof, F.D. Tichelaar, E. Brück, S. van der Zwaag, N.H. van Dijk, Competitive Healing of Creep-Induced Damage in a Ternary Fe-3Au-4W Alloy, Metall. Mater. Trans. A 51(9) (2020) 4442-4455.

1 **Y. Fu**, C. Kwakernaak, J.C. Brouwer, W.G. Sloof, E. Brück, S. van der Zwaag, N.H. van Dijk, Surface precipitation of supersaturated solutes in a ternary Fe–Au–W alloy and its binary counterparts, J. Mater. Sci. 56(8) (2020) 5173-5189.

CURRICULUM VITAE

YIFAN FU

02-08-1988   Born in Benxi, China

EDUCATION

2006 – 2010   Bachelor of Science in Materials Physics
                          Dalian University of Technology, China

2010 - 2013   Master of Engineer in Materials Science and Technology
                          Dalian University of Technology, China

2016 - 2017   Master of Science in Advanced Materials
                          University of Nottingham, UK

2018 - 2022   PhD candidate
                          Delft University of Technology

WORKING EXPERIENCE

2013 - 2018   Metallurgical Engineer
                          Shenyang Liming Aero-Engine Group CO., LTD., Aviation
                          Industry Corporation of China (AVIC).